Physics of dry snow metamorphism : from microstructure to macroscopic properties

Neige Calonne

UNIVERSITÉ DE GRENOBLE

THÈSE

Pour obtenir le grade de

DOCTEUR DE L'UNIVERSITÉ DE GRENOBLE

Spécialité : **Matériaux, Mécanique, Génie civil, Electrochimie**

Arrêté ministériel : 7 août 2006

Présentée par

Neige CALONNE

Thèse dirigée par **Christian GEINDREAU**
et codirigée par **Frédéric FLIN**

préparée au sein du **CNRM–GAME/Centre d'Études de la Neige, Météo-France–CNRS**
et du **Laboratoire Sols, Solides, Structures, Risques**
dans **l'École Doctorale IMEP²**

Physique des métamorphoses de la neige sèche : de la microstructure aux propriétés macroscopiques

Thèse soutenue publiquement le **14 novembre 2014**,
devant le jury composé de :

Sylvain DRAPIER
Professeur, Ecole Nationale Supérieure des Mines de Saint-Étienne, St Etienne, France, Président
Benoît GOYEAU
Professeur, Ecole Centrale Paris, Paris, France, Rapporteur
Martin SCHNEEBELI
Directeur de recherche, WSL/SLF, Davos, Suisse, Rapporteur
Ian BAKER
Professeur, Thayer School of Engineering at Dartmouth, Hanover, USA, Examinateur
Luc SALVO
Professeur, Grenoble INP, SIMaP, Grenoble, France, Examinateur
Christian GEINDREAU
Professeur, Univ. Joseph Fourier, Grenoble, France, Directeur de thèse
Frédéric FLIN
Chargé de recherche, CNRM-GAME/CEN, Grenoble, France, Co-Directeur de thèse

Remerciements

Je tiens tout d'abord à remercier mes deux directeurs de thèse, Frédéric Flin et Christian Geindreau. Merci de m'avoir fait confiance, en premier lieu, puis merci pour votre grande disponibilité et implication au cours de ces trois années. J'ai beaucoup apprécié de travailler avec vous.

I would like to thank the members of my committee Martin Schneebeli, Benoit Goyeau, Luc Salvo, Ian Baker and Sylvain Drapier for their clear interest in my research work and for attending my PhD defense.

Avec le stage de master, j'ai passé quasiment 4 ans au CEN... je tiens à remercier tous mes collègues pour leur accueil et la bonne ambiance de travail, ainsi que leur aide précieuse en informatique, démarches administratives..., ou lors de nos manips.

Bernard et Anne, quel plaisir de travailler avec vous ! Merci pour votre bonne humeur et l'ambiance chaleureuse que vous apportez. Que de bons souvenirs en manip, sous chloronaphtalène par -30°C, à pomper et pomper, ou à coincer la bulle ! Merci à Jacques qui, un peu malgré lui, a fait partie de la fine équipe !

Pour tous les supers moments passés au labo ou ailleurs, un grand merci à ma bande : Carlo, Xi, Luc, Pierre, Matthieu, Camille, Alexander, Jésus, Matthieu le Grec, Vincent, Laura, Lilly... Merci pour votre soutien ces derniers mois !

Merci à ma famille et à mes amis. J'ai tellement de chance de vous avoir...

Résumé

L'objectif général de la thèse est de contribuer à l'amélioration de nos connaissances sur les métamorphoses de la neige sèche et sur sa description physique, à l'échelle microscopique (grains de glace et pores) et macroscopique (couche de neige). Dans un premier temps, la méthode d'homogénéisation basée sur les développements asymptotiques à échelles multiples est appliquée à la physique des métamorphoses de la neige sèche. On présente ainsi les descriptions macroscopiques équivalentes du transport de vapeur et de chaleur dérivées à partir de la description de la physique à micro-échelle. On considère à l'échelle des grains la diffusion, la conduction, et la convection forcée, couplées aux changements de phase (sublimation et déposition). Dans un second temps, les propriétés effectives de transport impliquées dans les descriptions macroscopiques (conductivité thermique effective, coefficient effectif de diffusion de vapeur et perméabilité intrinsèque) sont estimées à l'aide d'images 3D de neige couvrant toute la gamme de masse volumique et de types de neige. Enfin, on s'intéresse au suivi temporel des métamorphoses. Les liens entre la microstructure et les propriétés effectives d'une couche de neige sont mis en évidence au cours d'une métamorphose de gradient de température en utilisant des images 3D. On présente ensuite une cellule cryogénique que nous avons mise au point pour le suivi grains à grains par tomographie des évolutions d'un échantillon de neige au cours des métamorphoses, et qui s'utilise à température ambiante.

Mots-clés : Neige, Métamorphose, Transport de masse et de chaleur, Changement de phase, Modélisation multi-échelles, Tomographie RX, Images 3D, Microstructure, Propriétés effectives

Abstract

The main objective of the thesis is to improve our knowledge about dry snow metamorphism and its physical description, at the microscopic (ice grains and pores) and macroscopic (snow layer) scales. First, the homogenization method of multiple scale expansions is applied for the first time to the physics involved in dry snow metamorphism. This way, we present the equivalent macroscopic descriptions of heat and vapor transfers derived from the physical description at micro-scale. We consider at the grain scale diffusion, conduction, and forced convection, coupled to phase changes (sublimation and deposition). Second, the effective properties of transport arising in the macroscopic descriptions (effective thermal conductivity, effective coefficient of vapor diffusion, and intrinsic permeability) are estimated from 3D images of snow spanning the whole range of density and snow types. Finally, the monitoring of metamorphism with time is considered. The relationship between the microstructure and the effective properties of a snow layer are investigated during temperature gradient metamorphism using 3D images. We present then a new cryogenic cell that we developed to monitor the grain to grain evolution of a snow sample by time-lapse tomography during the metamorphism, and which operates at room temperature.

Keywords: Snow, Metamorphism, Heat and mass transfer, Phase change, Multiscale modeling, RX tomography, 3D images, Microstructure, Effective properties

Introduction générale

A l'échelle microscopique, une couche de neige sèche est un milieu hétérogène constitué d'air humide et de glace. Les évolutions de cette microstructure au cours du temps sous des contraintes thermodynamiques sont appelées "métamorphoses de la neige sèche". Elles constituent un mécanisme important à l'origine de l'évolution du manteau neigeux. La physique principale impliquée dans ces métamorphoses est le transport de chaleur et de vapeur d'eau couplé au changement de phase vapeur-glace. D'autres mécanismes, tels que la croissance anisotrope du cristal de glace ou la diffusion de surface, interviennent également. Leur quantification fait encore l'objet de nombreuses investigations. Un outil intéressant pour l'étude de la physique à cette échelle est notamment la tomographie par rayons X, qui permet d'obtenir des images 3D de la microstructure de la neige.

A l'échelle macroscopique, la description des phénomènes de transport est nécessaire aux modèles d'évolution des propriétés du manteau neigeux. Ces modèles répondent à des enjeux sociétaux tels que la prévision du risque d'avalanche, les études climatiques, la disponibilité des ressources en eau... A cette échelle, une couche de neige est vue comme un milieu homogène équivalent. Différentes formulations du transport macroscopique ont été proposées, principalement développées par une approche phénoménologique, et peuvent varier d'un modèle à l'autre. D'autre part, les propriétés effectives impliquées dans la description macroscopique des transferts sont souvent estimées à partir de paramétrisations expérimentales dérivées de mesures dispersées, et peuvent donc également varier d'une étude à l'autre.

Dans ce contexte, cette thèse vise à améliorer nos connaissances sur les métamorphoses de la neige sèche et sur sa description physique, à la fois à l'échelle microscopique et à l'échelle macroscopique. Le travail s'appuie sur de la modélisation théorique (méthode d'homogénéisation), de l'imagerie 3D (tomographie, expériences en chambre froide, instrumentation) et de la simulation numérique.

Contents

Chapter

1 Les métamorphoses de la neige sèche

Sommaire

1.1 Introduction

En moyenne, 25 % de la surface de la terre est recouverte par de la neige et de la glace, et plus particulièrement, 9 % est recouverte d'un manteau neigeux saisonnier [*Wallace and Hobbs*, 2006]. La neige, et plus généralement la cryosphère, est donc une composante importante du système terrestre. Dans cette section, on explique les principales connaissances à avoir concernant la neige et le manteau neigeux.

1.1.1 Formation et structure du manteau neigeux

Lors d'une chute de neige, les cristaux de glace créés dans l'atmosphère se déposent au sol par gravité et forment progressivement une couche de neige. Cette couche correspond à une structure de glace connectée dans laquelle l'air circule. Une couche de neige fraîche peut contenir jusqu'à 95 % d'air. La neige est donc un milieu poreux constitué principalement d'air et de glace. L'eau est présente également sous forme de vapeur d'eau dans l'air et d'eau liquide quand la température atteint 0°C. Chaque nouvel épisode neigeux crée une nouvelle couche de neige en surface. L'empilement des couches de neige constitue le manteau neigeux. Lorsque la neige est à des températures négatives, on parle de neige sèche car elle ne contient pas d'eau liquide. A l'inverse, lorsque la neige est à 0°C, l'eau liquide est présente et on parle de neige humide. Le manteau neigeux peut être saisonnier, i.e. fond totalement au printemps pour se former à nouveau l'hiver suivant, comme dans les Alpes par exemple, ou pluri-annuel en haute montagne ou dans les zones polaires où la fonte n'est que partielle.

Lorsque que l'on réalise une coupe verticale sur toute l'épaisseur du manteau neigeux, on observe une stratification où différentes couches de neige sont identifiables (cf Figure 1.1). Ces strates correspondent principalement à d'anciennes couches de neige de surface enfouies progressivement lors des épisodes neigeux suivants. Elle sont souvent bien distinguables car elles présentent des caractéristiques différentes les unes des autres, par exemple, la forme et/ou la taille des structures de glace, la proportion d'air, la dureté... A l'œil, on détecte une variation de texture et/ou de couleur. En fonction de la forme et de la taille des structures de glace, la classification internationale pour la neige saisonnière au sol [*Fierz et al.*, 2009] définit différents types de neige. On distingue six types principaux, comme illustré dans la Figure 1.2. Pour des raisons pratiques, on parle de grains de neige pour désigner les particules de glace que l'on observe lorsque l'on désagrège mécaniquement la structure de la neige.

1.1.2 Evolution du manteau neigeux

Les différences observées entre couches de neige témoignent d'une évolution morphologique différente au cours du temps. La structure initiale dite de "neige fraîche" (cristaux de glace venant de se déposer) se transforme en des structures dites "évoluées". Les causes principales de ces évolutions sont (1) les métamorphoses, (2) le tassement et (3) les événements météorologiques. Ce dernier point comprend principalement le vent, qui remobilise les grains des couches de surface puis les redépose en modifiant sensiblement leur

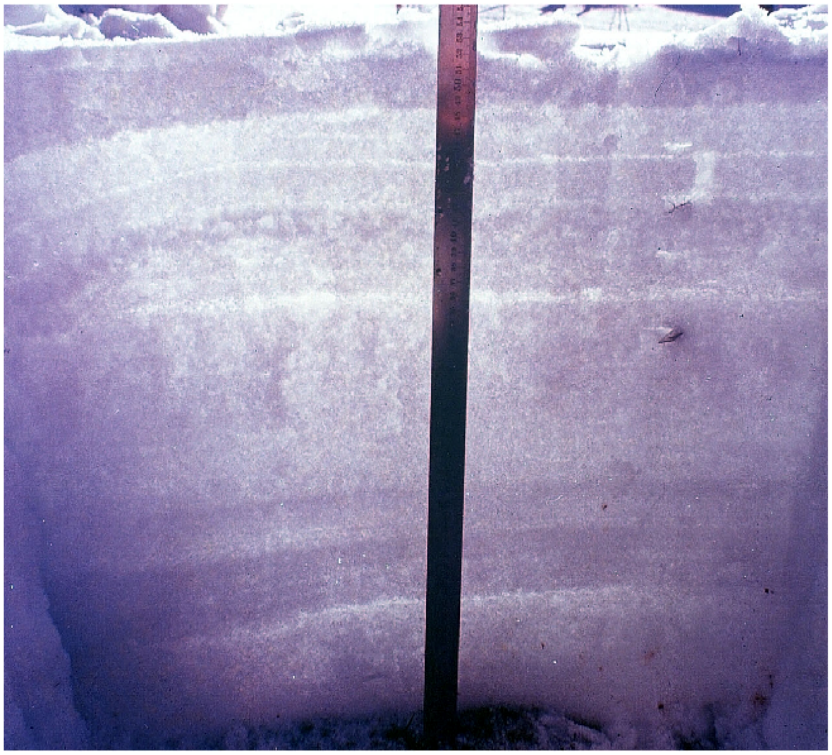

Figure 1.1: Photographie d'une coupe verticale d'un manteau neigeux au col de Porte. A l'oeil nu, les couches de neige sont distinguables entre elles par une différence de couleur et de texture. L'ensemble de ces couches forment la stratigraphie du manteau neigeux.

forme et leur taille, ou encore la pluie, l'arrivée d'une masse d'air humide... Le tassement s'opère par ré-arrangement des grains entre eux et par compaction des strates de neige sous le poids des couches supérieures. D'une manière générale, les couches de neige sont de plus en plus denses en allant de la surface vers la base du manteau neigeux. Enfin, les métamorphoses de la neige désignent les évolutions d'une couche de neige liées aux conditions de température auxquelles elle est soumise. Dans les zones tempérées, à la base du manteau neigeux, le sol reste proche de 0°C tout l'hiver grâce à un flux de chaleur terrestre vers la surface. La température de l'air en surface du manteau neigeux est, quant à elle, très variable. En fonction de cette température de l'air et du bilan thermique des strates voisines, différents régimes thermiques peuvent être imposés à une couche de neige, ce qui engendre différents types de métamorphoses, i.e. différentes évolutions de la structure de glace. On distingue classiquement la métamorphose de neige humide, lorsque la neige est à 0°C, des métamorphoses de neige sèche, lorsque la neige est à des températures négatives. Dans ce dernier cas, la température au sein d'une couche de neige peut être assez uniforme (on parle alors d'isothermie) ou, au contraire, varier suivant un gradient vertical. L'évolution de la neige est très différente selon ces deux cas. On parle respectivement de métamorphose d'équi-température (ou d'isothermie) et de métamorphose de gradient de température.

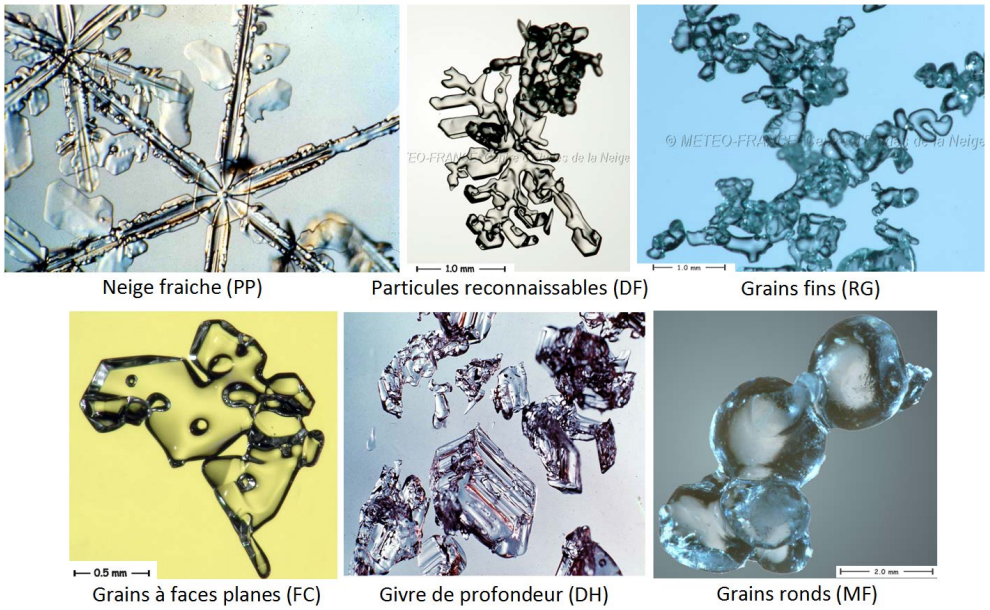

Figure 1.2: Photographie au microscope optique des six types de grains de neige principaux.

1.2 A l'échelle des grains et pores : la microstructure

L'étude de la neige et des métamorphoses à l'échelle des grains de glace, qui est de l'ordre du micromètre, s'est développée à partir du milieu du XXème siècle. Aujourd'hui, la physique locale impliquée dans les métamorphoses de la neige sèche est en grande partie connue [e.g. *Colbeck*, 1983a; *Libbrecht*, 2005]. Ainsi, différents modèles physiques de métamorphoses ont été proposés à l'échelle des grains sur des microstructures réelles [*Flin et al.*, 2003; *Flin and Brzoska*, 2008; *Kaempfer and Plapp*, 2009] ou simplifiées [*Christon et al.*, 1994; *Miller et al.*, 2003; *Miller and Adams*, 2009; *Barrett et al.*, 2012]. L'objectif de ces modèles est de simuler l'évolution temporelle de la structure de la neige à micro-échelle. Ils permettent, par confrontation à des observations expérimentales, de valider ou d'infirmer les phénomènes physiques pris en compte. Dans cette section, les différents moyens d'observation de la microstructure de la neige sont tout d'abord présentés. On décrit ensuite les deux principaux moteurs thermodynamiques des métamorphoses de la neige sèche, ainsi que les principales caractéristiques des deux types de métamorphoses qui en découlent. Enfin, on relie ces descriptions qualitatives à la physique impliquée dans les métamorphoses à micro-échelle.

1.2.1 Évolution de la microstructure : outils d'analyse

Bien que déjà observée à l'œil nu ou à la loupe, la microstructure de la neige n'est réellement devenue accessible qu'avec l'utilisation du microscope optique. Celui-ci a permis de photographier et d'analyser des cristaux isolés de neige fraîche ou évolués [*Bentley*, 1904; *Nakaya*, 1954; *Akitaya*, 1974; *Marbouty*, 1980; *Lesaffre et al.*, 1998; *Gay et al.*, 2002] (Figures 1.2 et 1.3 (a)), ainsi que des coupes minces d'échantillons de neige obtenues par microtomie [*Brzoska et al.*, 1998; *Arnaud et al.*, 1998; *Pfeffer and Mrugala*, 2002; *Satyawali*

et al., 2003; *Satyawali and Singh*, 2008; *Arakawa et al.*, 2009]. Dans ce cas, la structure de la neige telle qu'elle se compose dans la couche est observable en deux dimensions (Figure 1.3(b)). En photographiant une à une les coupes sériées d'un échantillon, il est possible de reconstituer l'images 3D du volume de neige [*Good*, 1987; *Brzoska et al.*, 1999b; *Theile and Schneebeli*, 2011]. La résolution verticale de ces reconstitutions 3D est néanmoins limitée par l'épaisseur minimale de la section qui peut être coupée (typiquement de l'ordre de quelques dizaines de microns).

L'utilisation du microscope électronique à balayage a permis l'observation de la surface d'échantillons de neige avec une précision pouvant atteindre le nanomètre, tel qu'illustré par la Figure 1.3(c), [*Wergin et al.*, 1996; *Dominé et al.*, 2003; *Erbe et al.*, 2003]. Ce microscope est donc notamment utilisé pour caractériser finement la surface de glace [e.g. *Chen and Baker*, 2010; *Wang and Baker*, 2013].

Durant ces quinze dernières années, la tomographie par rayons X est devenue un outil incontournable pour l'étude de la microstructure de la neige [*Brzoska et al.*, 1999a; *Schneebeli*, 2000; *Coléou et al.*, 2001; *Lundy et al.*, 2002]. Cette méthode non destructive permet de reconstituer l'image 3D d'un échantillon de neige de taille centimétrique avec une précision de l'ordre du micromètre, comme montré dans les Figures 1.3(d) et 1.5. On peut ainsi analyser en détail l'arrangement 3D de la structure de glace. A partir de ces images, une large gamme de calculs numériques peut être réalisée pour caractériser la microstructure ou estimer les propriétés physiques effectives de l'échantillon de neige, si celui-ci est de taille suffisante pour être représentatif.

Avec cette technique, il est également possible de suivre les évolutions morphologiques de la microstructure de la neige au cours du temps, soit par une méthode dite "statique" [e.g. *Brzoska et al.*, 1999a; *Coléou et al.*, 2001; *Flin et al.*, 2004; *Heggli et al.*, 2009], soit par une méthode dite "dynamique" ou "in vivo" [e.g. *Schneebeli and Sokratov*, 2004; *Pinzer and Schneebeli*, 2009a; *Chen and Baker*, 2010]. Brièvement, la méthode statique consiste à suivre l'évolution d'une couche de neige supposée homogène en prélevant à intervalles de temps réguliers un échantillon de neige dans la couche. La série d'échantillons est tomographiée par la suite. La méthode in vivo permet quant à elle de suivre l'évolution grains à grains d'un même échantillon de neige contenu dans une cellule cryogénique par des tomographies successives [*Schneebeli and Sokratov*, 2004; *Pinzer and Schneebeli*, 2009b; *Chen and Baker*, 2010]. Les cellules cryogéniques utilisées ne fonctionnent actuellement qu'en chambre froide avec un tomographe dédié, ce qui peut constituer une limitation en termes de techniques d'imagerie, de résolution, de vitesse d'acquisition... L'imagerie de haute technologie, telle que proposée par les instruments des synchrotrons, n'est donc pas accessible à l'approche in vivo.

1.2.2 Moteurs des métamorphoses : déséquilibres thermodynamiques

Comme expliqué précédemment, la métamorphose d'une couche de neige correspond à l'évolution morphologique de la microstructure de la neige. La redistribution de la matière (glace et vapeur) s'effectue principalement par changement de phase (de la glace se sublime en vapeur d'eau et de la vapeur d'eau se dépose en glace), couplé au transport de vapeur

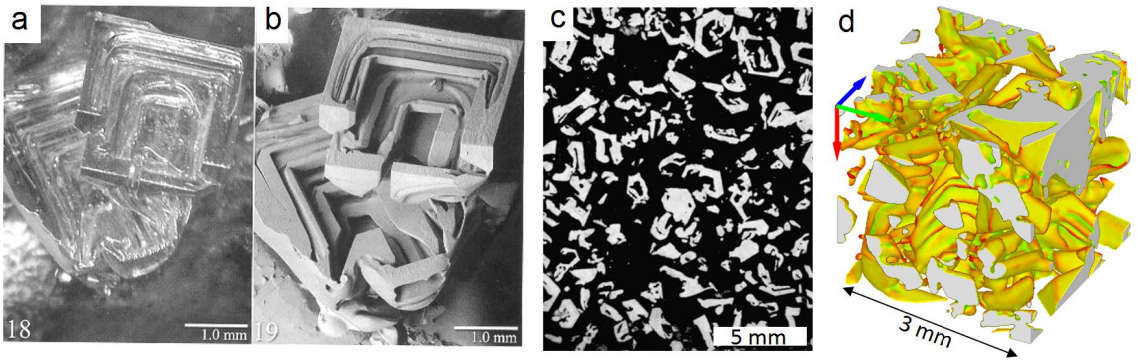

Figure 1.3: Givre de profondeur observé par différentes méthodes. (a) Microscope optique [*Erbe et al.*, 2003], (b) Microscope électronique à balayage [*Erbe et al.*, 2003], (c) Coupe mince binarisée obtenue au microscope optique [*Arakawa et al.*, 2009], et (d) Image 3D obtenue par micro-tomographie aux rayons X (1 pixel = 9.6 μm) [*Calonne et al.*, 2014a].

dans les pores (cf. section 1.2.5). Bien que ces phénomènes s'effectuent à l'échelle des molécules d'eau, ils ont un effet visible significatif sur la forme et la taille des grains de glace lorsqu'ils se produisent suffisamment longtemps et avec suffisamment d'intensité. La variable qui contrôle ces changements de phase est la pression partielle de vapeur d'eau saturante dans l'air. Elle correspond à la valeur de pression partielle de vapeur d'eau dans l'air à l'équilibre. L'équilibre est défini par l'absence de changement de phase. Dans ce manuscrit, pour faire le parallèle avec la masse volumique de la glace, on a choisi d'exprimer la pression partielle saturante sous la forme de la masse volumique de vapeur d'eau saturante dans l'air, noté ρ_{vs} en $\mathrm{kg\,m^{-3}}$. Ainsi, en considérant un volume d'air proche d'une surface de glace comportant une masse volumique de vapeur ρ_v,

- si $\rho_v > \rho_{vs}$, il y a sursaturation de vapeur d'eau et la vapeur va se déposer en glace (condensation solide ou dépôt) pour tendre vers l'équilibre $\rho_v = \rho_{vs}$.
- si $\rho_v < \rho_{vs}$, il y a sous-saturation de vapeur d'eau et la glace va se sublimer (sublimation) pour augmenter la masse volumique de vapeur dans l'air.

Pour qu'il y ait changement de phase, et donc métamorphose de la neige, il faut donc que la masse volumique de vapeur "locale" (ρ_v) dans l'air proche de l'interface de glace soit différente de la masse volumique de vapeur saturante (ρ_{vs}). Ce déséquilibre est provoqué dans la neige par une variation de température et/ou par une variation de courbure de la surface de glace, comme illustré par les schémas de la Figure 1.4. L'advection d'air plus ou moins humide peut également modifier l'équilibre thermodynamique de la neige.

Variation de la vapeur saturante avec la température La valeur de masse volumique de vapeur saturante dans l'air proche d'une surface plane de glace augmente avec la température T selon l'équation de Clausius-Clapeyron :

$$\rho_{vs}(T) = \rho_{vs}^{\mathrm{ref}}(T^{\mathrm{ref}}) \exp\left[\frac{L_{sg} m}{\rho_i k T}\left(\frac{T}{T^{\mathrm{ref}}} - 1\right)\right] \tag{1.1}$$

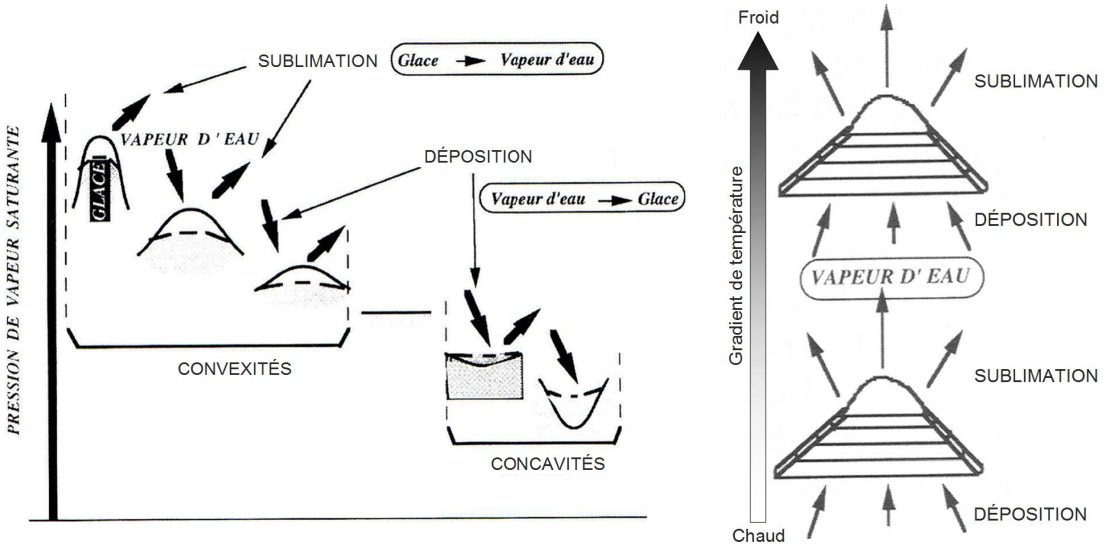

Figure 1.4: Transfert de la vapeur d'eau par effet de courbure à gauche et par effet de température à droite (cas d'un gradient vertical de température). Schémas d'après *Sergent et al.* [1998].

où ρ_{vs}^{ref} est une valeur de référence de masse volumique de vapeur d'eau à pression atmosphérique et à une température de référence T^{ref}, L_{sg} est la chaleur latente de sublimation (J m^{-3}), ρ_i est la masse volumique de la glace, k est la constante de Boltzmann ($1{,}38\times10^{-23}$ J K^{-1}), et m est la masse d'une molécule d'eau (cf Tableau 2.1).

Variation de la vapeur saturante avec la courbure de surface La masse volumique de vapeur saturante d'un volume d'air proche d'une surface de glace est aussi influencée par la courbure de cette surface. En se plaçant en isothermie, la relation de Gibbs-Thomson, aussi appelée équation de Kelvin, donne en un point de l'interface de courbure K :

$$\rho_{vs}(K) = \rho_{vs}^{\text{ref}}(T^{\text{ref}}) \exp\left[d_0 K\right] \tag{1.2}$$

où d_0 est la longueur capillaire (m). De façon synthétique, plus la surface de glace est concave, plus ρ_{vs} est faible. A l'inverse, plus la surface de glace est convexe, plus ρ_{vs} est élevée. Pour une surface parfaitement plate, il n'y a pas d'effet de courbure sur la valeur de ρ_{vs}.

Lorsque l'on linéarise la relation de Gibbs-Thomson (1.2) pour d_0K petit, l'effet de variation de courbure et de température peuvent être combinés pour donner la relation de Gibbs-Thomson généralisée [*Kaempfer and Plapp*, 2009] à l'interface :

$$\rho_{vs}(T, K) \approx \rho_{vs}(T)(1 + d_0 K) \tag{1.3}$$

où $\rho_{vs}(T)$ est définie par la relation de Clausius-Clapeyron.

Comme expliqué précédemment, lorsque la neige est soumise à une température quasi-isotherme, l'effet de courbure donne lieu à la métamorphose d'équi-température. L'effet de température devient en revanche prédominant lorsqu'un gradient de température est

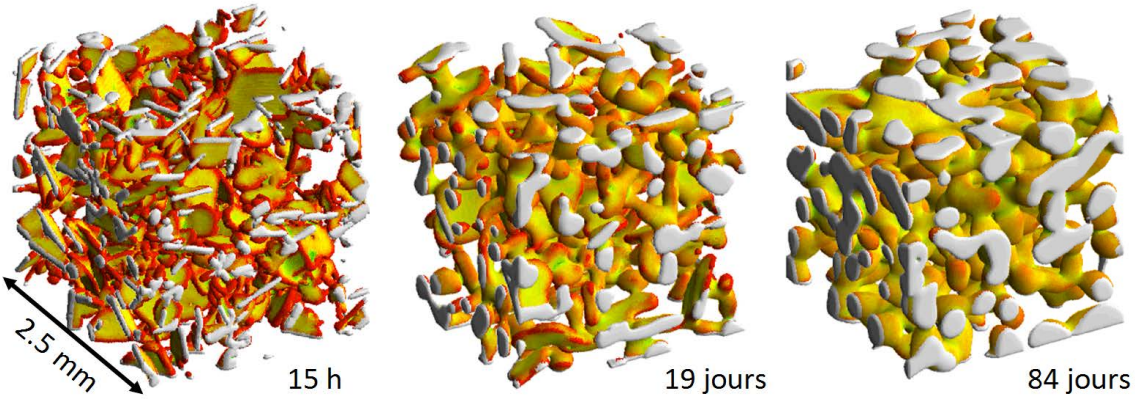

Figure 1.5: Images 3D, obtenues par tomographie X, d'échantillons de neige prélevés régulièrement dans une couche soumise à une métamorphose d'isothermie à -2°C [*Flin et al.*, 2004].

présent et engendre la métamorphose de gradient de température. Notons que les effets de courbure et de température sont toujours présents en simultané dans le manteau neigeux, mais l'un devient prédominant sur l'autre en fonction des conditions thermiques du manteau, du type de neige considéré (rayon de courbure)...

1.2.3 La métamorphose d'équi-température

La métamorphose d'équi-température de la neige est observée lorsque la neige est proche de l'isothermie. Cette métamorphose est caractérisée par un arrondissement général de la structure de glace [*Flin et al.*, 2004; *Kaempfer and Schneebeli*, 2007; *Chen and Baker*, 2010]. La Figure 1.5 est un exemple de cette évolution en 3D au cours du temps. L'effet principal de cette métamorphose est illustré par le schéma de gauche de la Figure 1.4 : les convexités se subliment tandis que les concavités sont peu à peu comblées par dépôt de glace. Cette métamorphose se produit essentiellement par transport de vapeur et changement de phase. Elle donne lieu à des particules reconnaissables (DF) et à des grains fins (RG).

1.2.4 La métamorphose de gradient de température

La métamorphose de gradient de température correspond à l'évolution micro-structurale de la neige sous l'effet d'un gradient de température. Cette condition se produit typiquement les nuits claires et froides où le manteau neigeux rayonne et se refroidit fortement en surface. Un gradient de température vertical entre la base du manteau neigeux à 0°C et le sommet plus froid se crée. Un transfert de vapeur principalement vertical se produit alors par sublimation des molécules d'eau au niveau des zones de glace les plus chaudes et dépôt de ces molécules dans les zones de glace les plus froides, tel que schématisé par la Figure 1.4. Le terme de "hand-to-hand delivery" est utilisé pour décrire intuitivement le transfert de matière de grain à grain [*Yosida et al.*, 1955].

L'intensité et le type d'évolution de la structure de neige varient avec la valeur du gradient de température imposé ainsi qu'avec la température moyenne [*Akitaya*, 1974; *Marbouty*, 1980]. On considère classiquement deux régimes de métamorphose de gradient

de température [e.g. *Colbeck*, 1983a]. Si le gradient est compris entre environ 5 et 20 $\mathrm{K\,m^{-1}}$, le type de neige créé est le cristal facetté, caractérisé par des faces planes (FC) aux contours anguleux. Si le gradient est supérieur à 20 $\mathrm{K\,m^{-1}}$, après un passage temporaire par le stade de faces planes (FC), du givre de profondeur (DH) se forme, caractérisé par des formes "pyramidales" de glace et une surface striée assez complexe, tel que montré dans la Figure 1.3. Il faut garder à l'esprit que ces seuils sont des valeurs moyennes basées sur des observations et qu'ils peuvent varier en fonction de la température moyenne, du type et de la masse volumique de la neige, du temps et des outils d'observation, de l'observateur... Par exemple, *Flin et al.* [2007] ont observé la formation de facettes pour un gradient de 3 $\mathrm{K\,m^{-1}}$ à partir d'images 3D de neige. D'autre part, *Pinzer and Schneebeli* [2009a] ont récemment étudié l'effet d'un gradient de température dont le signe change périodiquement au cours du temps à l'aide d'images 3D. Ils concluent que ce type de sollicitation n'aboutit pas à la formation de cristaux facettés ou de givre de profondeur, mais à des grains fins tels qu'observés après une métamorphose d'équi-température. Cette étude, cohérente avec d'autres travaux [e.g. *Flin and Brzoska*, 2008], contrebalance la vision jusque-là classiquement adoptée pour la formation des grains.

1.2.5 Processus physiques et modélisations des métamorphoses

Les métamorphoses de neige sèche se produisent sous l'effet des déséquilibres thermodynamiques exposés dans la section 1.2.2. On a alors décrit qualitativement les deux types d'évolution qui s'observent dans les sections 1.2.3 et 1.2.4. On présente ici la physique de ces métamorphoses à micro-échelle. Comme déjà mentionné, celle-ci correspond principalement au transport de la chaleur et de la matière (glace et vapeur) couplé au changement de phase, au sein de la microstructure de la neige. Afin de décrire correctement les métamorphoses, il faut également considérer la physique liée à la nature cristalline de la glace.

Transport de chaleur et de matière couplé au changement de phase

- Le transport de chaleur dans la neige se fait principalement par conduction dans la glace et l'air. Néanmoins, certaines études ne considèrent que la conduction de la glace et négligent celle de l'air [*Kaempfer et al.*, 2005; *Shertzer and Adams*, 2011] vu le rapport 100 de conductivité entre ces deux matériaux. D'autre part, le changement de phase (glace-vapeur) modifie la température locale aux interfaces par effet de chaleur latente. La sublimation constitue un puits de chaleur tandis que la condensation solide en constitue une source.

- Le transport de matière (glace et vapeur) est la cause directe de l'évolution de la microstructure de la neige. On peut distinguer le transport de vapeur et le transport "solide". Le transport de vapeur se fait par la diffusion de vapeur dans l'air contenu dans l'espace poreux de la neige et constitue un phénomène important des métamorphoses [*Hobbs and Mason*, 1964; *Colbeck*, 1983a; *Flin et al.*, 2003; *Flin and Brzoska*, 2008]. Trois processus ont été proposés pour le transport "solide" :

la diffusion de surface, la diffusion de volume, et la diffusion aux joints de grains. Leurs contributions aux évolutions morphologiques font encore l'objet de nombreuses études mais semblent de second ordre pour la plupart des conditions fréquemment rencontrées [e.g. *Kuroiwa*, 1961; *Kingery*, 1960; *Maeno and Ebinuma*, 1983; *Kaempfer and Schneebeli*, 2007]. Il est donc fréquent de réduire le transport de matière au transport de vapeur seulement. A l'interface des grains, le changement de phase fait varier la masse de glace et de vapeur dans l'air. La sublimation constitue une source de vapeur (puits de glace) et inversement pour la condensation solide.

- La chaleur et la vapeur peuvent être également transportées par un écoulement d'air dans les pores. Ce mouvement peut être créé par la convection naturelle due à un gradient de température [*Powers et al.*, 1985; *Brun and Touvier*, 1987; *Sturm and Johnson*, 1991; *Akitaya*, 1974], ou par convection forcée par du vent en surface, appelée également "windpumping" [*Colbeck*, 1989; *Albert and McGilvary*, 1992]. L'étude de ces phénomènes par des moyens expérimentaux reste délicate. Le travail théorique d'*Albert and McGilvary* [1992] montre l'effet significatif que peut avoir la convection forcée sur le transport de vapeur et de chaleur.

Si on définit un volume de neige Ω où la glace occupe le domaine Ω_i et l'air le domaine Ω_a, séparés par l'interface des grains Γ de normale $\mathbf{n_i}$ pointant vers les pores, la description microscopique du transport de chaleur et de vapeur au cours des métamorphoses peut s'écrire [*Kaempfer and Plapp*, 2009] :

$$\rho_i C_i \frac{\partial T_i}{\partial t} - \operatorname{div}(\kappa_i \, \mathbf{grad}\, T_i) = 0 \quad \text{dans } \Omega_i \tag{1.4}$$

$$\rho_a C_a \frac{\partial T_a}{\partial t} - \operatorname{div}(\kappa_a \, \mathbf{grad}\, T_a) = 0 \quad \text{dans } \Omega_a \tag{1.5}$$

$$\frac{\partial \rho_v}{\partial t} - \operatorname{div}(D_v \, \mathbf{grad}\, \rho_v) = 0 \quad \text{dans } \Omega_a \tag{1.6}$$

$$T_i = T_a \quad \text{sur } \Gamma \tag{1.7}$$

$$\kappa_i \, \mathbf{grad}\, T_i \cdot \mathbf{n_i} - \kappa_a \, \mathbf{grad}\, T_a \cdot \mathbf{n_i} = L_{sg} \mathbf{w} \cdot \mathbf{n_i} \quad \text{sur } \Gamma \tag{1.8}$$

$$D_v \, \mathbf{grad}\, \rho_v \cdot \mathbf{n_i} = (\rho_i - \rho_v) \mathbf{w} \cdot \mathbf{n_i} \quad \text{sur } \Gamma \tag{1.9}$$

avec t le temps (s), T la température (K), κ la conductivité thermique ($\mathrm{W\,m^{-1}\,K^{-1}}$), ρ la densité ($\mathrm{kg\,m^{-3}}$), C la capacité thermique spécifique ($\mathrm{J\,kg^{-1}\,K^{-1}}$), L_{sg} la chaleur latente de sublimation ($\mathrm{J\,m^{-3}}$), $\mathbf{w}$ la vitesse de croissance de l'interface de glace ($\mathrm{m\,s^{-1}}$), ρ_v la masse volumique partielle de vapeur dans l'air ($\mathrm{kg\,m^{-3}}$), et D_v le coefficient de diffusion de vapeur d'eau dans l'air ($\mathrm{m^2\,s^{-1}}$). Les opérateurs de divergence et de gradient exprimés en fonction des variables d'espace sont notés div et **grad**, respectivement. Les propriétés physiques de l'air et de la glace, désignées par les indices "a" et "i", sont supposées isotropes.

Remarques :

- Dans les équations (1.8) et (1.9), les termes $L_{sg}\mathbf{w} \cdot \mathbf{n_i}$ et $(\rho_i - \rho_v)\mathbf{w} \cdot \mathbf{n_i}$ sont des termes sources ou puits de chaleur et de vapeur, respectivement, qui proviennent du

changement de phase à l'interface (sublimation et dépôt) et qui sont donc liés à la vitesse de croissance de la structure de glace considérée **w**.

- L'expression de ce terme **w**, donnée dans la suite, fait intervenir la masse volumique de vapeur d'eau à saturation estimée à partir de la température (relation de Clausius-Clapeyron (1.1)). Le système d'équations (1.4) à (1.9) est donc un système fortement couplé, notamment par les effets se produisant aux interfaces.
- Le transport de chaleur et de vapeur par convection de l'air n'est pas décrit dans les équations (1.4) à (1.9), mais sera étudié dans le Chapitre 3.

Croissance d'un cristal de glace

A pression et température standard, les molécules d'eau qui composent la glace sont arrangées en un réseau cristallin de type hexagonal. Comme tout cristal hexagonal, on peut distinguer les deux faces basales des six faces prismatiques (Figure 1.7). Cette structure à l'échelle moléculaire se reflète parfois à micro-échelle sur la forme du cristal avec notamment l'observation de facettes et d'angles à 120°.

La première contrainte évidente pour la croissance de la glace est le respect du réseau cristallin. La localisation préférentielle du changement de phase à l'interface d'une surface de glace à l'échelle moléculaire est contrôlée par la physique des énergies de surface. Ces phénomènes sont à l'origine de l'effet de facettage et/ou d'arrondissement observé pour les différents types de neige (cf Figures 1.2 et 1.3). Le schéma du cristal de Kossel [*Markov*, 1995; *Mutaftschiev*, 2001] de la Figure 1.6 illustre ces effets.

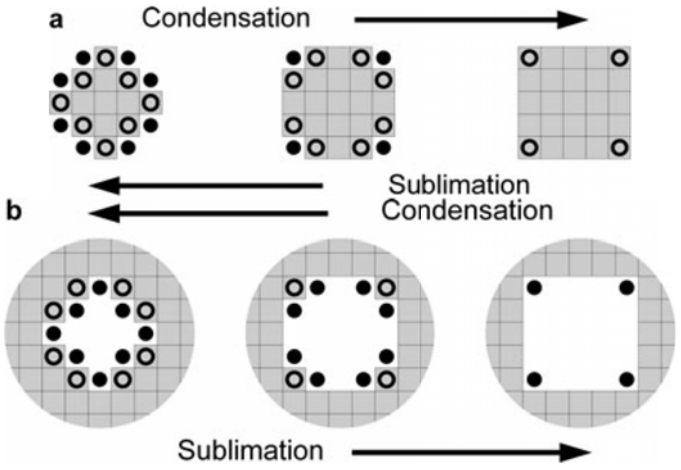

Figure 1.6: Modèle de facettage et d'arrondissement basé sur l'explication du cristal de Kossel. Les cercles et les points correspondent aux sites préférentiels de sublimation et de condensation, respectivement. (a) Pour les surfaces convexes, la condensation conduit à un facettage des grains, tandis que la sublimation génère un arrondissement . (b) Pour les surfaces concaves, le comportement inverse est observé [*Flin and Brzoska*, 2008].

En plus de la contrainte d'évolution liée au réseau cristallin, la croissance d'un cristal de glace est contrôlée par des phénomènes de "réactivité" à sa surface. Tout d'abord, à valeur

de sursaturation de vapeur d'eau égale, les changements de phase se font d'autant plus rapidement que la température de la neige est élevée. En outre, la vitesse de croissance va également varier en fonction de la face du cristal considérée (face prismatique ou basale). Ces propos sont illustrés par le diagramme de Nakaya (Figure 1.7), qui montre les différents types de cristaux observés en fonction de la température et de la sursaturation. On voit par exemple qu'entre -4°C et -10°C, la croissance des faces basales est privilégiée, tandis que, pour une même valeur de sursaturation, entre -10°C et -22°C, se sont les faces prismatiques qui croissent préférentiellement, aboutissant ainsi à des plaquettes. Ces différences de croissance entre faces sont liées à l'état de surface de la glace, qui influe sur sa réactivité, i.e. sa "capacité" à changer de phase. Les différents états de la surface de glace (couche quasi-liquide, surface rugueuse, surface lisse...) ont des caractéristiques propres qui font encore l'objet de beaucoup d'études [e.g. *Furukawa et al.*, 1987; *Wettlaufer and Worster*, 2006; *Sazaki et al.*, 2012] et qui peuvent varier d'une face cristalline à l'autre en fonction de la température et de la sursaturation [*Furukawa and Kohata*, 1993; *Nelson and Knight*, 1998]. Cette anisotropie de croissance se voit nettement avec les cristaux de neige fraîche, comme illustré dans la Figure 1.7, mais affecte de la même manière la croissance des grains de glace au sein d'une couche de neige.

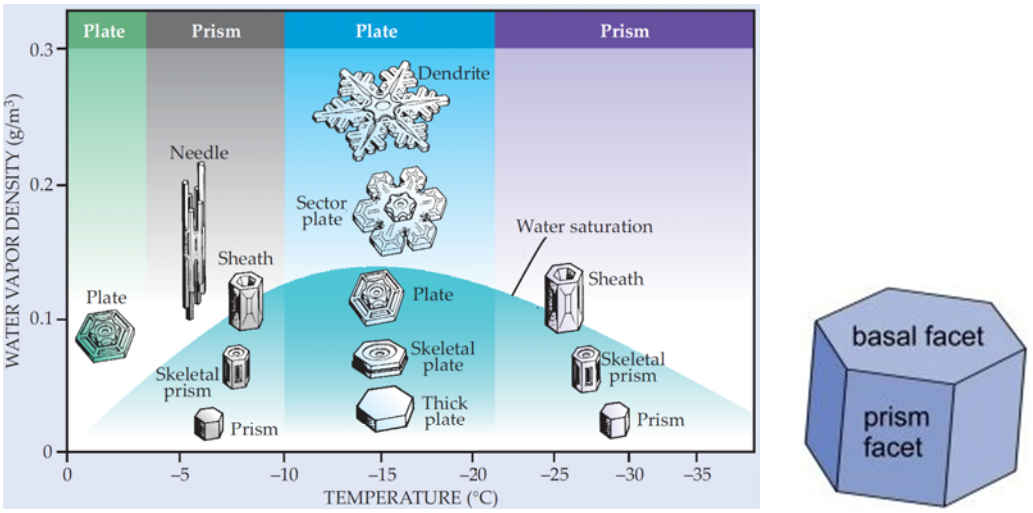

Figure 1.7: A gauche : diagramme de Nakaya qui illustre l'influence de la température et de la sursaturation sur la croissance des faces des cristaux de glace aboutissant à des cristaux de type plaquette ou de type prisme [*Furukawa and Wettlaufer*, 2007]; à droite : schéma d'un cristal hexagonal de glace.

La modélisation des métamorphoses à micro-échelle nécessiterait de reproduire les effets de facettage et d'arrondissement des grains liés au réseau cristallin, ainsi que l'anisotropie de croissance des faces liée à l'état de surface que l'on vient de décrire. Néanmoins, ces phénomènes sont encore peu connus et restent difficiles à simuler. Ils nécessitent par ailleurs des informations précises sur l'orientation cristalline des grains de glace. L'accès à de telles informations (axes c et a) en 3D n'est actuellement fourni que par peu d'études et seulement pour certains types de neige [*Rolland du Roscoat et al.*, 2011]. L'autre contrainte est la difficulté de quantifier les différences de croissance entre faces de manière précise.

Les modélisations actuelles sont principalement basées sur la formule de Hertz-Knudsen [*Saito*, 1996; *Libbrecht*, 2005; *Kaempfer and Plapp*, 2009] pour décrire la vitesse de croissance normale à la surface d'un cristal de glace, qui croit par dépôt de vapeur :

$$\mathbf{w} \cdot \mathbf{n_i} = \frac{1}{\beta} \frac{\rho_v - \rho_{vs}(T, K)}{\rho_{vs}(T)} \quad \text{sur } \Gamma \tag{1.10}$$

où β est le coefficient cinétique d'interface ($\mathrm{s\,m^{-1}}$), qui représente les phénomènes de réactivité de surface, et le terme de gauche représente le déséquilibre de vapeur par rapport à la valeur de saturation. En utilisant la relation de Gibbs-Thomson généralisée (1.3), cette équation peut se ré-écrire :

$$\mathbf{w} \cdot \mathbf{n_i} = \frac{1}{\beta} \left[\frac{\rho_v - \rho_{vs}(T)}{\rho_{vs}(T)} - d_0 K \right] \quad \text{sur } \Gamma \tag{1.11}$$

Cette équation complète le système d'équations (1.4)-(1.9) en couplant le transfert de vapeur et de chaleur avec les phénomènes aux interfaces. Le coefficient cinétique est lié au coefficient de condensation solide α_d par la relation suivante :

$$\beta = \frac{1}{\alpha_d} \frac{\rho_i}{\rho_{vs}(T)} \sqrt{\frac{2\pi m}{kT}} \tag{1.12}$$

où m est la masse d'une molécule d'eau (kg) et k la constante de Boltzmann égale à $1{,}38{\times}10^{-23}$ J $\mathrm{K^{-1}}$. Le coefficient de condensation solide α_d représente la façon dont les molécules d'eau sont incorporées au réseau cristallin de la glace. Il est défini tel que si les molécules de vapeur frappant la surface de glace sont directement incorporées, alors $\alpha_d = 1$; autrement, $\alpha_d < 1$. Pour modéliser l'anisotropie de croissance expliquée ci-dessus, le coefficient de condensation solide doit prendre des valeurs différentes en fonction de l'orientation cristalline de la surface de glace considérée et varier avec la température et la sursaturation [*Barrett et al.*, 2012]. Des expériences pour mesurer ce coefficient ont été réalisées mais elles restent très délicates [e.g. *Beckmann and Lacmann*, 1982; *Gonda and Koike*, 1982; *Libbrecht*, 2003; *Libbrecht and Arnold*, 2009]. Actuellement, les valeurs de β utilisées dans les modèles microscopiques de métamorphoses varient typiquement entre 10^4 et 10^9 $\mathrm{s\,m^{-1}}$ [*Kaempfer and Plapp*, 2009].

Pour conclure sur cette section, la physique des métamorphoses est en grande partie bien connue et implique, au premier ordre, le transport de vapeur et de chaleur couplé au changement de phase. Néanmoins, des incertitudes persistent concernant des processus plus fins qui pourraient permettre d'améliorer la description des métamorphoses, tels que la diffusion "solide" (diffusion de surface, joints de grains...) ou la convection naturelle, pour le transport de chaleur et de matière, mais aussi des phénomènes liés à la nature cristalline de la glace, comme l'anisotropie des vitesses de croissance. La prise en compte du facettage et de l'arrondissement des grains dans les modélisations 3D des métamorphoses est ainsi un sujet encore non résolu. En outre, certains des aspects évoqués ci-dessus nécessitent des informations sur l'orientations cristalline des grains de glace encore difficiles d'accès à l'échelle d'un échantillon de neige. La méthode in vivo de suivi des métamorphoses, présentée dans la section 1.2.1, semble être un outil prometteur pour avancer sur toutes ces

thématiques. Elle permettrait entre autres (i) l'observation 3D de différents phénomènes à micro-échelle lors d'expériences contrôlées, mais aussi (ii) la confrontation entre l'évolution de la microstructure de la neige prévue par les modèles 3D existants à celle obtenue expérimentalement.

1.3 A l'échelle d'une couche de neige ou du manteau neigeux

Depuis cinquante ans, on s'est intéressé à modéliser une couche de neige comme un milieu homogène équivalent afin de faciliter la simulation et la prévision des propriétés du manteau neigeux au cours du temps, telles que les propriétés mécaniques, optiques, thermiques... nécessaires à différentes applications comme la prévision du risque d'avalanche, du climat ou des ressources en eau... L'intérêt bien sûr est que la physique à cette échelle macroscopique est beaucoup plus facile à résoudre qu'à micro-échelle en considérant toutes les hétérogénéités. Dans cette section, on présente les principes de base du passage d'une description physique à l'échelle des grains à celle à l'échelle de la couche. Les principes de fonctionnement des différents modèles macroscopiques actuels sont ensuite présentés. Enfin, on décrit l'état de l'art sur les propriétés effectives impliquées dans ces modèles macroscopiques ainsi que leurs moyens d'estimations.

1.3.1 Passage de l'échelle des grains à l'échelle de la couche

A l'échelle microscopique, la neige est un matériau hétérogène constitué d'air et de glace. A l'échelle macroscopique, on peut assimiler la neige à un milieu continu homogène équivalent, c'est-à-dire qu'on ne "voit" plus les hétérogénéités, dont le comportement équivaut "en moyenne" à celui du comportement microscopique. La difficulté de cette approche réside dans la description de ce comportement équivalent, qui doit reproduire le mieux possible la physique locale. L'idée générale du passage de l'échelle des grains à l'échelle de la couche de neige est schématisé par la Figure 1.8. L'expression d'un matériau hétérogène en tant que matériau homogène fait apparaître entre autres les propriétés effectives du matériau, qui sont analogues aux propriétés locales des hétérogénéités mais en représentent une moyenne. Prenons l'exemple de la conductivité thermique. A micro-échelle, on doit prendre en compte la conductivité thermique de la glace et de l'air. A macro-échelle, on ne "voit" plus ni les grains de glace ni les pores d'air, mais on considère une conductivité thermique effective de la neige qui doit représenter "une moyenne" de la conductivité thermique des hétérogénéités au sein de la microstructure considérée (agencement, porosité...). Il existe différentes approches pour ce passage de la micro à la macro-échelle [*Bornert et al.*, 2001; *Auriault et al.*, 2009].

Si la détermination du comportement du matériau homogène équivalent s'effectue directement à l'échelle macroscopique, c'est-à-dire ici à l'échelle de la couche de neige, on parle généralement *d'approche phénoménologique*. Cette approche que l'on peut qualifier d'inductive est sans aucun doute la plus utilisée. La description macroscopique est souvent basée sur des observations et mesures à macro-échelle. Cette approche ne permet

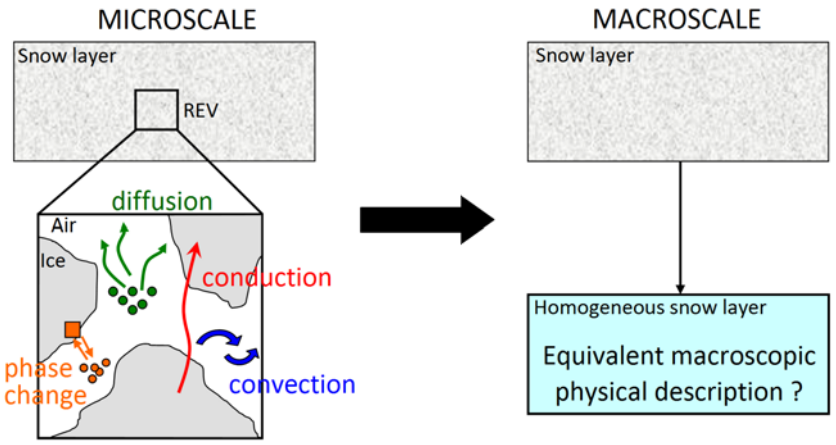

Figure 1.8: Illustration de la problématique du passage d'une description physique à l'échelle des grains à une description équivalente à l'échelle d'une couche de neige.

pas toujours d'établir la relation entre la description microscopique et la description macroscopique.

Si par contre, le comportement macroscopique est obtenu par un passage de la description microscopique à la description macroscopique homogène équivalente, on parle généralement *d'homogénéisation*. Cette approche peut être qualifiée de déductive, car plus prédictive dès lors que l'on modifie les propriétés ou l'agencement des hétérogénéités (microstructure) par exemple. Il existe de nombreuses méthodes de changement d'échelle. Dans le domaine des milieux poreux, la méthode des moyennes [*Whitaker*, 1969, 1998] et la méthode des développements à échelles multiples [*Bensoussan et al.*, 1978; *Sanchez-Palencia*, 1980; *Auriault*, 1991; *Auriault et al.*, 2009] sont les plus utilisées. Ces méthodes permettent de faire le lien entre les équations de bilans à l'échelle microscopique et macroscopique, et fournissent la définition des propriétés effectives impliquées. D'autres méthodes d'homogénéisation basées sur des microstructures simplifiées (assemblages de particules sphériques, ellipsoïdales...) peuvent aussi être utilisées, notamment lorsque l'on souhaite estimer des propriétés effectives. Par exemple, la méthode auto-cohérente [*Bruggeman*, 1935; *Hill*, 1965; *Budiansky*, 1965; *Hashin*, 1968], s'avère très efficace pour estimer les propriétés effectives à partir d'informations minimales sur la microstructure (concentration, propriétés des hétérogénéités).

En pratique, l'approche phénoménologique et l'homogénéisation sont bien évidemment complémentaires : la description microscopique, point de départ de l'homogénéisation, est souvent elle-même le résultat d'une approche phénoménologique.

1.3.2 Les phénomènes de transport dans les modèles macroscopiques

La modélisation macroscopique des phénomènes de transport de chaleur et de vapeur dans la neige sèche est nécessaire à la simulation de différentes propriétés du manteau neigeux. Ces phénomènes constituent une partie de l'ensemble des processus modélisés par les modèles complets d'évolution des propriétés du manteau neigeux [e.g. *Brun et al.*, 1989; *Jordan*, 1991; *Bartelt and Lehning*, 2002; *Lehning et al.*, 2006; *Vionnet et al.*, 2012],

utilisés pour différentes applications telles la prévision du risque d'avalanche, les ressources en eau et l'hydrologie, les études climatiques, les écosystèmes de montagne, le tourisme de montagne... Dans ces modèles, le manteau neigeux est représenté comme un empilement de couches de neige homogènes au sein duquel le bilan d'énergie et de matière est résolu verticalement en 1D.

Le transport de chaleur et de vapeur dans la neige sèche, sans considérer les bilans de surface neige/atmosphère et neige/sol, est généralement décrit à macro-échelle par deux équations de transport couplées (chaleur et vapeur) qui s'écrivent sous la forme schématique suivante [*Albert and McGilvary*, 1992; *Colbeck*, 1993; *Albert and Hardy*, 1995]:

$$\text{Transitoire} + \text{Diffusif} + \text{Convectif} = \text{Terme source} \tag{1.13}$$

où le terme source décrit l'apport ou la perte de chaleur et/ou de vapeur dû au changement de phase. En pratique, la formulation des phénomènes de transport dans les modèles de manteau neigeux actuels est souvent simplifiée et est principalement basée sur une approche phénoménologique. La description de la physique du transport en neige sèche des différents modèles proposés peut présenter des disparités, comme illustré dans les paragraphes suivants.

Phénomènes physiques En fonction du modèle considéré, certains processus physiques peuvent ne pas être pris en compte, sans qu'il y ait toujours de justification. Par exemple, les modèles Crocus [*Brun et al.*, 1989, 1992; *Vionnet et al.*, 2012] et SNOWPACK [*Bartelt and Lehning*, 2002; *Lehning et al.*, 2006] ne simulent pas la masse volumique de vapeur d'eau et donc son transfert au sein du manteau neigeux. Par ailleurs, peu de modèles prennent en compte le transfert de chaleur et de vapeur par convection/advection d'air, bien que ce processus puisse parfois avoir une influence significative [*Colbeck*, 1989; *Sturm and Johnson*, 1991; *Albert and McGilvary*, 1992]. *Lehning et al.* [2002a] propose une paramétrisation pour la prise en compte du "wind-pumping", mais dans le transport de chaleur uniquement. Cet effet n'est pas ajouté en tant que processus physique indépendant mais inclus dans la définition de la conductivité thermique.

Termes sources A l'échelle microscopique, le changement de phase par dépôt/sublimation à l'interface air-glace constitue une source de chaleur et de vapeur (équations (1.8) et (1.9)). La prise en compte ainsi que la formulation de ces termes sources à l'échelle macroscopique est également variable dans les modèles. A titre d'exemple, le modèle Crocus ne simule pas l'effet de chaleur latente de sublimation au sein d'une couche de neige sèche, tandis que le modèle SNOWPACK inclut des termes sources issus de ce changement de phase. Certains modèles [e.g. *Jordan*, 1991] décrivent quant à eux l'effet du changement de phase dans la définition des propriétés effectives et non par un terme source à part entière. C'est le cas, par exemple, dans le modèle de manteau neigeux de *Sun et al.* [1999] : "The contribution of vapor phase change and diffusion is included by an effective thermal conductivity in the energy balance equation".

Propriétés effectives Les composantes clés des termes diffusifs et convectifs des équations de bilan d'énergie et de masse à l'échelle macroscopique sont les propriétés effectives. Encore une fois, la définition de ces propriétés dans les modèles n'est pas homogène. La conductivité thermique effective est souvent paramétrée en fonction de la masse volumique uniquement, en utilisant par exemple la régression linéaire de *Yen* [1981] ou de *Sturm et al.* [1997] basée sur des mesures (Figure 1.9). Comme mentionné ci-dessus, sa description est parfois ajustée afin de prendre en compte les effets de certains processus physiques, comme la convection, ou de changement de phase. Le coefficient effectif de diffusion de vapeur dans la neige est quant-à-lui sujet à polémique [*Pinzer et al.*, 2012] et son estimation reste variable en fonction des modèles. Les difficultés liées à l'estimation des propriétés effectives de transport constituent une problématique majeure de la thèse et sont discutées de façon détaillée dans la section suivante.

Pour conclure, les descriptions macroscopiques des phénomènes de transport de chaleur et de vapeur d'eau peuvent différer les uns des autres, tant sur les phénomènes considérés que sur la définition de leurs termes sources ou de leurs propriétés effectives. A notre connaissance, les méthodes de changement d'échelle n'ont pas été appliquées à la physique du transport de chaleur et de vapeur dans la neige. Ces méthodes pourraient contribuer à mieux formaliser les relations entre la description physique microscopique (équations de bilan, propriétés physiques locales) et la description physique macroscopique (équations de bilan, propriétés effectives).

1.3.3 Les propriétés physiques effectives impliquées

A l'échelle des grains de glace, le transport de chaleur et de masse se fait principalement par conduction/diffusion, ainsi que par convection si un écoulement d'air dans les pores de la neige est présent, couplé au changement de phase air-glace. A l'échelle macroscopique, ces phénomènes sont contrôlés par des propriétés effectives de transport que sont la conductivité thermique effective, le coefficient effectif de diffusion et la perméabilité intrinsèque d'une couche de neige.

Conductivité thermique effective Elle caractérise la capacité d'une couche de neige à conduire la chaleur par conduction pure. Pour répondre aux besoins de différentes applications, plusieurs paramétrisations de la conductivité thermique effective en fonction de la masse volumique de la neige ont été proposées, par exemple par *Yen* [1981] et *Sturm et al.* [1997]. Ces paramétrisations, basées sur des mesures, présentent une dispersion de valeurs importante et diffèrent largement entre elles, comme illustré par la Figure 1.9. Ceci peut s'expliquer par le fait qu'il existe différentes méthodes de mesure de la conductivité thermique et aussi que chaque mesure présente une incertitude pouvant être significative. En plus de l'incertitude liée à la mesure elle-même, les méthodes de mesure actuelles fournissent une conductivité thermique apparente, i.e. que tous les processus de transfert de chaleur peuvent potentiellement être pris en compte et pas uniquement la conduction pure. On n'obtient donc pas des mesures de conductivité thermique effective au sens strict.

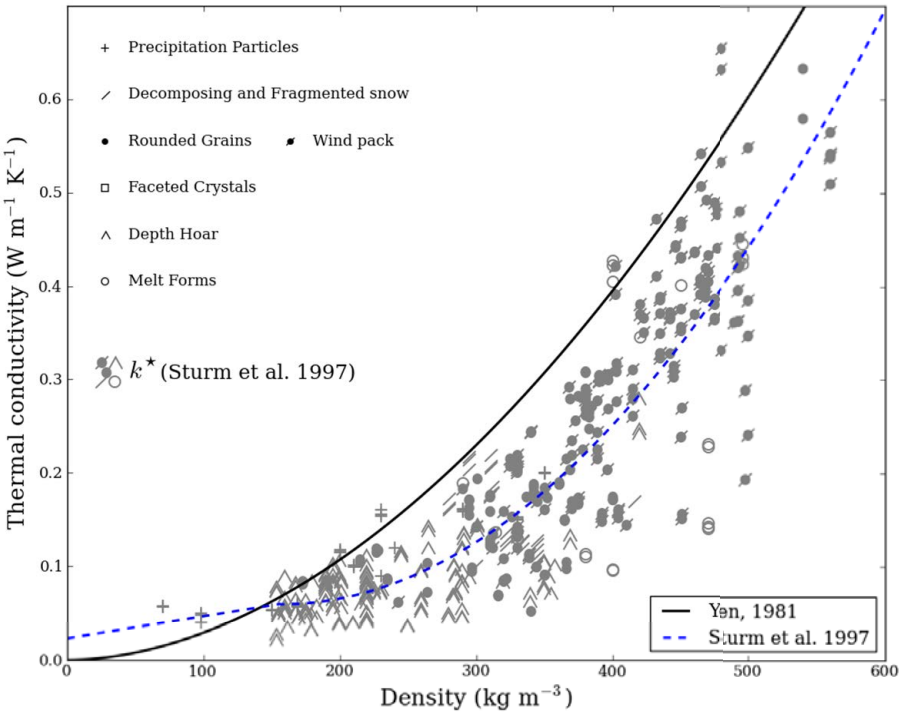

Figure 1.9: Conductivité thermique en fonction de la masse volumique. Les mesures obtenues par aiguille chauffante (symboles) et la régression correspondante (courbe en pointillés) de *Sturm et al.* [1997] sont montrées, ainsi que la régression de *Yen* [1981] (courbe en trait plein). La dispersion des mesures ainsi que la différence entre deux paramétrisations sont clairement illustrées.

D'autre part, elles font l'hypothèse que le milieu est isotrope, ou bien ne fournissent que la composante verticale de la conductivité [*Yen*, 1981; *Sturm et al.*, 1997; *Morin et al.*, 2010; *Riche and Schneebeli*, 2010]. L'étude de *Kaempfer et al.* [2005] propose une estimation de la conductivité thermique effective basée sur un calcul numérique de conduction pure à partir d'une image 3D de neige. Néanmoins, leur calcul ne considère pas la conduction dans l'air mais uniquement dans la glace et fournit une estimation de la composante verticale de la conductivité uniquement.

Perméabilité intrinsèque Elle caractérise la capacité d'une couche de neige à laisser l'air s'écouler à travers elle. La perméabilité a été estimée pour différentes applications liées aux échanges chimiques [*Freitag et al.*, 2002; *Neumann*, 2003; *Grannas et al.*, 2007; *Domine et al.*, 2008], aux métamorphoses de la neige et du névé [*Albert et al.*, 2004; *Hörhold et al.*, 2009] ou encore à l'écoulement d'eau liquide à travers le manteau neigeux [*Colbeck*, 1975, 1976; *Waldner et al.*, 2004; *Katsushima et al.*, 2009; *Yamaguchi et al.*, 2010]. Elle est classiquement exprimée en fonction de la masse volumique et d'une "taille de grains de glace" [*Bader*, 1939; *Shimizu*, 1970; *Sommerfeld and Rocchio*, 1993; *Jordan et al.*, 1999b; *Arakawa et al.*, 2010]. Comme pour la conductivité thermique, ces paramétrisations proviennent de mesures de perméabilité assez dispersées et sont parfois significativement différentes. Ces observations peuvent s'expliquer d'une part par la mesure qui est délicate à réaliser [*Sommerfeld and Rocchio*, 1993], d'autre part par la définition ambigüe de la

"taille d'un grain de glace" qui, en fonction de la définition et de la méthode de mesure utilisée, peut prendre des valeurs nettement différentes pour une même neige [*Jordan et al.*, 1999b]. L'estimation de la perméabilité intrinsèque a été effectuée à partir d'images 3D de névé par *Freitag et al.* [2002] et *Courville et al.* [2007]. Plus récemment, *Zermatten et al.* [2011] présentent des estimations réalisées sur des images de neige. L'étude se limite néanmoins à cinq images et à des calculs dans une seule direction de l'espace.

Coefficient effectif de diffusion de vapeur d'eau Il reflète la capacité d'une couche de neige à laisser la vapeur d'eau se diffuser au travers. Plusieurs études ont tenté d'estimer cette propriété et donnent des résultats très variables [e.g. *Yosida et al.*, 1955; *Sokratov and Maeno*, 2000]. Les mesures demeurent délicates et il n'existe pas actuellement de protocole "validé" [*Pinzer et al.*, 2012]. Dans la littérature, deux résultats opposés sont présentés : *Yosida et al.* [1955]; *Colbeck* [1993]; *Sturm et al.* [1997], et *Satyawali* [2000] suggèrent un coefficient effectif de diffusion de la vapeur d'eau dans la neige supérieur à celui dans l'air libre avec le concept de "enhanced diffusion", tandis que *Sokratov and Maeno* [2000] et *Pinzer et al.* [2012] présentent un coefficient non amplifié. Les paramétrisations proposées sont donc très controversées mais dépendent généralement de la masse volumique de la neige et du coefficient de diffusion de vapeur d'eau dans l'air. A notre connaissance, aucune estimation de ce coefficient à partir d'images 3D de neige n'a encore été réalisée.

En conclusion, l'estimation de ces propriétés effectives pour différentes applications telles que les modèles de manteau neigeux reste encore source d'incertitudes. Comme le montre la Figure 1.9, pour une même valeur de masse volumique, la conductivité thermique mesurée peut varier d'un facteur 4. Ainsi, le rôle de la microstructure sur ces propriétés, en plus de celui de la masse volumique, devrait être investigué, notamment pour les neiges dont la structure de glace est fortement anisotrope [e.g. *Sturm and Johnson*, 1991; *Schneebeli and Sokratov*, 2004]. Comme initiés par *Freitag et al.* [2002]; *Kaempfer et al.* [2005]; *Courville et al.* [2007]; *Zermatten et al.* [2011] et *Pinzer et al.* [2012], des calculs numériques "de référence" à l'aide d'images 3D de neige semblent nécessaires pour confronter et valider les paramétrisations, mesures et modèles actuels.

1.4 Quelques limites et verrous

L'étude de la physique des métamorphoses de la neige sèche à l'échelle des grains et à l'échelle d'une couche de neige s'est récemment accélérée, notamment avec le développement de nouveaux outils de mesure, d'observation ou informatiques. Néanmoins, comme présenté dans les sections 1.2 et 1.3, il reste encore des obstacles à la bonne compréhension et modélisation de la neige. Cette section synthétise certaines problématiques actuelles :

Modélisations macroscopiques des phénomènes de transport Les modèles actuels ont été établis en suivant une approche principalement phénoménologique, et par conséquent ne permettent pas toujours de mettre en évidence la relation entre la physique locale à l'échelle des grains et la physique macroscopique simulée. Par ailleurs,

leur description peut varier d'un modèle à l'autre tant sur les phénomènes considérés que sur la définition de leurs termes sources ou de leurs propriétés effectives, sans réelle justification physique mais souvent par souci de simplification dans la résolution numérique. Les questions qu'on peut donc se poser sont : pour une physique microscopique donnée, quelle(s) est (sont) la (les) description(s) macroscopique(s) équivalente(s) correspondante(s) (équations de bilan, termes sources et propriétés effectives) ? Quel est son domaine de validité (en fonction de la physique locale considérée, telle que l'intensité de l'écoulement d'air, du gradient de température) ?

Évaluation des propriétés effectives et lien avec la microstructure Les mesures des propriétés effectives lié aux transports de chaleur et de vapeur dans la neige restent délicates et aboutissent à des valeurs dispersées. Ceci peut s'expliquer en partie par la difficulté de découpler les phénomènes physiques en jeu. Néanmoins, à partir des mesures, différentes paramétrisations basées sur la masse volumique de la neige ont été proposées et sont largement utilisées, notamment dans les modèles macroscopiques de manteau neigeux. Quelle est donc la validité de ces paramétrisations (notamment lorsqu'on s'intéresse à des neiges anisotropes de type givre de profondeur, comme soulevé par des études récentes) ? Peut-on estimer ces propriétés effectives par des modèles analytiques simples basés sur des informations de la microstructure ?

Meilleure compréhension des métamorphoses à micro-échelle La physique impliquée à l'échelle des grains de glace lors des métamorphoses est en grande partie connue. Néanmoins, de nombreuses interrogations persistent sur des processus plus fins, telle que la diffusion "solide", l'anisotropie des vitesses de croissance... Leur prise en compte pourrait améliorer la description physique microscopique et avoir des répercussions à plus grande échelle. L'observation des métamorphoses et la caractérisation des microstructures de neige par imagerie 3D semblent être un moyen efficace pour avancer sur ces problématiques et permettre une meilleure compréhension des phénomènes microscopiques et leur modélisation.

1.5 Objectifs et organisation du manuscrit

1.5.1 Objectifs

L'objectif général de cette thèse est de contribuer à l'amélioration de nos connaissances sur les métamorphoses de neige sèche et sur sa description physique, aux échelles microscopique et macroscopique. La thèse repose à la fois sur de la modélisation théorique, de l'expérimentation (tomographie, instrumentation, chambre froide...), et de la simulation numérique.
Ce travail s'appuie notamment sur (i) l'utilisation de la méthode d'homogénéisation basée sur les développements asymptotiques à échelles multiples, qui permet d'exprimer mathématiquement une description macroscopique équivalente à partir de la description physique à l'échelle des grains de glace (cf Section 1.3.1), et sur (ii) de l'imagerie 3D de la

microstructure de la neige, qui permet, entre autres, d'estimer numériquement différentes propriétés structurales et effectives présentes dans les modèles macroscopiques (cf Section 1.2.1).

A l'aide de ces outils, les objectifs principaux de la thèse sont de :

- Développer un modèle macroscopique équivalent pour le transport de chaleur et de vapeur impliqué dans les métamorphoses de neige sèche, en utilisant la méthode d'homogénéisation. L'idée est de fournir des modèles macroscopiques "de référence", où tous les termes apparaissant sont définis (équations de bilan, propriétés effectives, termes sources...) en fonction de l'intensité des phénomènes locaux considérés (faible ou fort gradient de température, écoulement ou non d'air...)
- Estimer les propriétés effectives associées à ces modèles macroscopiques à l'aide d'images 3D de neige. Les propriétés visées sont la conductivité thermique effective, le coefficient effectif de diffusion, et la perméabilité intrinsèque. L'objectif est d'étudier leur relation avec la microstructure, masse volumique incluse.
- Suivre l'évolution 3D des métamorphoses de neige sèche par tomographie, notamment grâce au développement d'un nouvel instrument pour le suivi in vivo. L'idée est de contribuer à l'amélioration de nos connaissances de la physique à micro-échelle par l'acquisition et l'analyse d'image 3D de résolution micrométrique.

1.5.2 Plan du manuscrit

Le manuscrit suit un ordre logique mais ne décrit pas les travaux dans l'ordre chronologique dans lequel ils ont été effectués. Il est composé de trois parties qui regroupent des études liées à une même thématique :
- Partie I, la modélisation macroscopique des phénomènes de transport.
- Partie II, l'étude des propriétés effectives de transport.
- Partie III, le suivi des métamorphoses au cours du temps.

Partie I
Dans cette partie, on utilise la méthode d'homogénéisation pour exprimer le modèle macroscopique équivalent à partir de la description microscopique du transport de chaleur et de vapeur, couplé au changement de phase vapeur-glace. La description microscopique utilisée est différente entre les chapitres 2 et 3.

- **Chapitre 2**
  Dans cette étude on considère localement les phénomènes de conduction et de diffusion, ainsi que le changement de phase. Ce chapitre est constitué de l'article *Macroscopic modeling for heat and water vapor transfer in dry snow by homogenization*, actellement publié en version ASAP dans *Journal of Physical Chemistry B* en 2014.

- **Chapitre 3**
  On considère ici un écoulement d'air dans les pores à micro-échelle. Le transport de vapeur et de chaleur se fait donc par diffusion/conduction mais aussi par convection.

Partie II
La Partie II est consacrée à l'estimation des propriétés effectives de transport de chaleur et de vapeur d'eau impliquées dans les métamorphoses de la neige sèche à partir d'images 3D couvrant toute la gamme de masses volumiques et de types de neige.

- **Chapitre 4**
  Ce chapitre se focalise sur la conductivité thermique effective et est constitué de l'article *Numerical and experimental investigations of the effective thermal conductivity of snow*, publié dans *Geophysical Research Letters* en 2011.

- **Chapitre 5**
  Ce chapitre se consacre à l'étude de la perméabilité intrinsèque. Il est constitué de l'article *3-D image-based numerical computations of snow permeability: links to specific surface area, density, and microstructural anisotropy*, publié dans *The Cryosphere* en 2012.

Partie III
La Partie III est constituée de deux études dédiées à l'évolution de la neige au cours du temps, i.e. lors des métamorphoses.

- **Chapitre 6**
  On étudie ici l'évolution des propriétés microstructurales et effectives d'une couche de neige au cours d'une métamorphose de gradient de température à l'aide d'images 3D. Ce chapitre est constitué de l'article *Study of a temperature gradient metamorphism of snow from 3-D images: time evolution of microstructures, physical properties and their associated anisotropy*, soumis à *The Cryosphere*.

- **Chapitre 7**
  Dans ce chapitre, on présente une cellule cryogénique opérant à température ambiante qui permet le suivi grain à grain des métamorphoses d'un échantillon de neige par tomographie au cours du temps. Il est constitué de l'article *CellIVM: a room temperature operating cryogenic cell for the in vivo monitoring of snow metamorphism by X-ray microtomography* (soumis).

Conclusion générale et perspectives
On rappelle les principaux résultats obtenus dans le cadre du travail de thèse et quelques perspectives sont proposées.

Part I

Equivalent macroscopic modelings of heat and vapor transport by homogenization

Introduction Part I

As mentioned in Chapter 1, the physical description of the heat and vapor transfers of the current snowpack models have been proposed in a phenomenological way. The different physical phenomena (thermal conduction, water vapor diffusion, convection, source terms due to phase change, etc) involved in these models vary from one model to another, as well as the definition of the effective properties (enhanced effective properties due to the phase change, etc).

In this part, we derive rigorously the macroscopic modeling for the heat and water vapor transport through a snow layer from the physics involved at the grain scale using an upscaling method, namely the homogenization of multiple scale expansions [*Bensoussan et al.*, 1978; *Sanchez-Palencia*, 1980; *Auriault*, 1991; *Geindreau and Auriault*, 2001; *Auriault et al.*, 2009]. Under the condition of separation of scales, the macroscopic equivalent modeling is obtained without any prerequisite at the macroscopic scale and is intrinsic to the geometry of the medium and the phenomenon. The formulation of such macroscopic modeling is driven by an analysis of the relative importance of the physical phenomena considered at the grain scale. It includes the exact expression of the effective properties, source terms, etc. To our knowledge, this upscaling approach has never been applied to snow physics.

Part I includes mathematical developments to derive the macroscopic modeling from the description of the physics at the micro scale, as well as numerical simulations using the finite element code Comsolmultiphysics. Those simulations were performed on a 2D geometry to illustrate and evaluate the macroscopic modelings with respect to the "real" physics operating at the micro-scale. This part is divided in two chapters. In Chapter 2, we suppose that the heat and water vapor transfer at the grain scale are driven by conduction, diffusion and phase changes at the ice grain interface. In Chapter 3, the microscopic description is enriched by adding the heat and vapor convection by an air flow through the pore spaces.

Chapter

2 Macroscopic modeling for heat and water vapor transfer in dry snow by homogenization

Contents

This chapter corresponds to the paper entitled *Macroscopic modeling for heat and water vapor transfer in dry snow by homogenization* by Calonne N., Geindreau C. and Flin F., published in the "as soon as publishable" version of the *Journal of Physical Chemistry B*, 2014 (doi:10.1021/jp5052535).

Abstract

Dry snow metamorphism, involved in several topics related to cryospheric sciences, is mainly linked to heat and water vapor transfers through snow including sublimation and deposition at the ice-pore interface. In this paper, the macroscopic equivalent modeling of heat and water vapor transfers through a snow layer was derived from the physics at the pore scale using the homogenization of multiple scale expansions. The microscopic phenomena under consideration are heat conduction, vapor diffusion, sublimation, and deposition. The obtained macroscopic equivalent model is described by two coupled transient diffusion equations including a source term arising from phase change at the pore scale. By dimensional analysis, it was shown that the influence of such source terms on the overall transfers can generally not be neglected, except typically under small temperature gradients. The precision and the robustness of the proposed macroscopic modeling were illustrated through 2D numerical simulations. Finally, the effective vapor diffusion tensor arising in the macroscopic modeling was computed on 3D images of snow. The self-consistent formula offers a good estimate of the effective diffusion coefficient with respect to the snow density, within an average relative error of 10%. Our results confirm recent work that the effective vapor diffusion is not enhanced in snow.

2.1 Introduction

The macroscopic modeling of heat and water vapor transfer through a snowpack is important to describe dry snow metamorphism and has important applications in snowpack stability [*Schweizer et al.*, 2003], transport of chemical species[*Grannas et al.*, 2007], snow energy balance [*Sokratov and Barry*, 2002]... Currently, the numerical resolution at the pore scale of the heat and water vapor transfer including phase change processes at the ice-pore interface is possible over small volumes only [*Christon et al.*, 1994; *Flin et al.*, 2003; *Kaempfer et al.*, 2005; *Brzoska et al.*, 2008; *Flin and Brzoska*, 2008; *Kaempfer and Plapp*, 2009; *Vetter et al.*, 2010]. At the scale of a snow layer, a macroscopic equivalent model is more relevant.

In the literature, different macroscopic models have been proposed to describe such phenomena. Using a phenomenological approach, *Albert and McGilvary* [1992] proposed to describe the heat and water vapor transfer through the snowpack by two coupled advection-diffusion equations including a source term due to the sublimation and deposition. Thanks to these equations, they investigated thermal effects due to air flow and vapor transport for different snow types and conditions. Following this work, *Neumann et al.* [2009] performed several experiments in a cold room to determine the mass transfer coefficient that arises in the source term and plays an important role on the coupling between the temperature and the water vapor fields. In this way, they proposed an empirical expression of the mass transfer coefficient.

In parallel, several models [*Jordan*, 1991; *Brun et al.*, 1992; *Lehning et al.*, 1999] have been also developed in order to simulate the physical phenomena of the snowpack. As an example, in the Crocus model [*Vionnet et al.*, 2012] the effective vapor diffusion is not described and the temperature is determined in dry snowpacks from a classical heat

transfer equation without taking into account the latent heat due to phase change. The effective thermal conductivity is assumed constant within a snow layer and estimated with respect to density using the parametrization of *Yen* [1981]. In the SNOWPACK model [*Lehning et al.*, 2002b], the effective vapor flux is simulated using an enhanced diffusion coefficient of snow (=8.5×10^{-5} $m^2\,s^{-1}$, http://models.slf.ch).

As already mentioned, the above models have been established in a phenomenological way. Consequently the link between these macroscopic modelings (e.g. effective properties or geometrical parameters involved) and the physical phenomena occurring at the pore scale is not always clearly established. As fully explained in *Pinzer et al.* [2012], the macroscopic description of the water vapor transfer in such models remains controversial. Studies by *Yosida et al.* [1955]; *Colbeck* [1993]; *Sturm et al.* [1997], and *Satyawali* [2000] indicate that the effective vapor diffusion in snow is greater than in a free air space, whereas *Sokratov and Maeno* [2000] and *Pinzer et al.* [2012] suggest a nonenhanced coefficient. In particular, from measurements and numerical simulations *Pinzer et al.* [2012] indicate that the macroscopic vapor transfer through snow is not significantly influenced by the ice structure but mainly depends on the temperature field.

In this paper, we propose to derive the macroscopic equivalent modeling of the heat and vapor transfer through snow from its description at the pore scale (at the representative elementary volume (REV) scale) using the homogenization of multiple scale expansions [*Bensoussan et al.*, 1978; *Sanchez-Palencia*, 1980; *Auriault*, 1991; *Geindreau and Auriault*, 2001; *Auriault et al.*, 2009]. Under the condition of separation of scales, the macroscopic equivalent modeling is obtained without any prerequisite at the macroscopic scale and is intrinsic to the geometry of the medium and the phenomenon. The method also provides the definitions of the effective parameters arising at macro scale and the domains of validity of the macroscopic modeling, given by the order of magnitude of the dimensionless numbers that characterize the intensity of the physical phenomena at the pore scale.

The paper is organized as follows: a step by step description of the homogenization method applied to the heat and water vapor transfer through snow is presented in the first section. The obtained macroscopic equivalent modeling is discussed. In a second section, the precision and robustness of the proposed macroscopic equivalent modeling is evaluated. For that purpose, a comparison of the numerical results for the heat and vapor transfer through a 2D snow layer obtained in the case of a fine scale modeling (i.e., by taking into account all the heterogeneities) and in the case of the corresponding macroscopic equivalent modeling is performed. Finally, the influence of the snow microstructure on the effective vapor diffusion tensor arising in the macroscopic modeling is investigated by performing numerical simulations on 3D images of different snow types.

2.2 Derivation of the macroscopic modeling

2.2.1 Upscaling method

Physical phenomena in heterogeneous media such as snow can be homogenized; i.e., they can be modeled by a continuous macroscopic equivalent description, if the condition of

separation of scales is satisfied [*Bensoussan et al.*, 1978; *Sanchez-Palencia*, 1980; *Auriault*, 1991; *Auriault et al.*, 2009]. This fundamental condition may be expressed as

$$\varepsilon = \frac{l}{L} \ll 1 \tag{2.1}$$

where l and L are the characteristic lengths of the heterogeneities at the pore scale and of the macroscopic sample or excitation, respectively. This condition implies the existence of a REV of size l of both the material and the excitation. In the following, the macroscopic equivalent model is obtained from the description at the heterogeneity scale, i.e., the REV scale, by using the homogenization technique of multiple scale expansions [*Bensoussan et al.*, 1978; *Sanchez-Palencia*, 1980] and by following the methodology presented in *Auriault* [1991]. More precisely, the macroscopic equivalent modeling of heat and water vapor transfer through a snow layer is obtained from the description of the physics at the pore scale by (i) assuming the medium to be periodic, without loss of generality because the condition (2.1) is fulfilled [*Auriault*, 2011]; (ii) writing the local description in a dimensionless form; (iii) evaluating the obtained dimensionless numbers with respect to the coefficient of separation of scale ε; (iv) looking for the unknown fields in the form of asymptotic expansions in powers of ε; (v) solving the successive boundary-value problems that are obtained after introducing these expansions in the local dimensionless description. The macroscopic equivalent model is obtained from compatibility conditions that are the necessary conditions for the existence of solutions to the boundary-value problems.

2.2.2 Description of the physics at the microscopic scale

Let us assume that a snowpack can be represented by a collection of spatially periodic representative elementary volume (REV) with a characteristic length l, such that the scale parameter $\varepsilon = l/L \ll 1$ (Figure 7.1). Within the REV of snow Ω, the domains occupied by

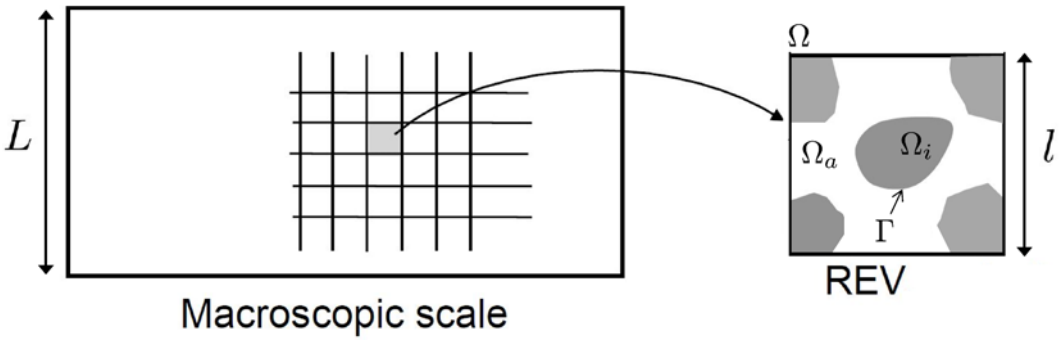

Figure 2.1: Macroscopic sample, i.e., a snow layer, and representative elementary volume (REV) with period Ω.

the ice and the air are denoted by Ω_i and Ω_a respectively. The interface of ice is denoted by Γ and $\mathbf{n_i}$ is the unit outward vector of Ω_i. Neglecting the air convection and snow densification, the phenomena involved in dry snow metamorphism considered are (i) the heat conduction through ice and air, (ii) the water vapor diffusion in air, and (iii) the sublimation of ice and deposition of vapor at the ice-pore interface, which is characterized

by the interface growth velocity [*Kaempfer and Plapp*, 2009; *Barrett et al.*, 2012; *Libbrecht*, 2005]. In what follows, the subscripts "i" or "a" are related to quantities defined in Ω_i and Ω_a, respectively. Assuming that the properties of air and ice are isotropic, these physical phenomena at the pore scale are described by the following set of equations:

$$\rho_i C_i \frac{\partial T_i}{\partial t} - \mathrm{div}(\kappa_i \mathbf{grad} T_i) = 0 \quad \text{in } \Omega_i \tag{2.2}$$

$$\rho_a C_a \frac{\partial T_a}{\partial t} - \mathrm{div}(\kappa_a \mathbf{grad} T_a) = 0 \quad \text{in } \Omega_a \tag{2.3}$$

$$\frac{\partial \rho_v}{\partial t} - \mathrm{div}(D_v \mathbf{grad} \rho_v) = 0 \quad \text{in } \Omega_a \tag{2.4}$$

$$T_i = T_a \quad \text{on } \Gamma \tag{2.5}$$

$$\kappa_i \mathbf{grad} T_i \cdot \mathbf{n_i} - \kappa_a \mathbf{grad} T_a \cdot \mathbf{n_i} = L_{sg} \mathbf{w} \cdot \mathbf{n_i} \quad \text{on } \Gamma \tag{2.6}$$

$$D_v \mathbf{grad} \rho_v \cdot \mathbf{n_i} = (\rho_i - \rho_v) \mathbf{w} \cdot \mathbf{n_i} \simeq \rho_i \mathbf{w} \cdot \mathbf{n_i} \quad \text{on } \Gamma \tag{2.7}$$

where t is the time (s), T is the temperature (K), κ is the thermal conductivity ($\mathrm{W\,m^{-1}\,K^{-1}}$), ρ is the density ($\mathrm{kg\,m^{-3}}$), C is the specific heat capacity ($\mathrm{J\,kg^{-1}\,K^{-1}}$), L_{sg} is the latent heat of sublimation ($\mathrm{J\,m^{-3}}$), $\mathbf{w}$ is the interface growth velocity ($\mathrm{m\,s^{-1}}$), ρ_v is the partial density of water vapor in air ($\mathrm{kg\,m^{-3}}$), D_v is the water vapor diffusion coefficient in air ($\mathrm{m^2\,s^{-1}}$) and, div and **grad** are the divergence and gradient operators with respect to the physical space variable $\mathbf{X}$, respectively. At the interface, the heat and mass transfer are coupled through the normal interface growth velocity $w_n = \mathbf{w} \cdot \mathbf{n_i}$ (Eq. (2.6) and (2.7)), which is given by the Hertz-Knudsen equation:

$$w_n = \mathbf{w} \cdot \mathbf{n_i} = \frac{1}{\beta} \left[\frac{\rho_v - \rho_{vs}(T_a)}{\rho_{vs}(T_a)} - d_0 K \right] \quad \text{on } \Gamma \tag{2.8}$$

where β is the interface kinetic coefficient ($\mathrm{s\,m^{-1}}$), ρ_{vs} is the saturation water vapor density in air ($\mathrm{kg\,m^{-3}}$), d_0 is the capillary length (m), and K is the interface mean curvature ($\mathrm{m^{-1}}$). Let us remark that the interface kinetic coefficient β is linked to the deposition coefficient α_d by $\beta = (1/\alpha_d)(\rho_i/\rho_{vs}(T_a))((2\pi m)/(kT_a))^{1/2}$, where m is the mass of a water molecule (kg) and k is the Boltzmann's constant equal to $1.38{\times}10^{-23}$ J K^{-1}. Accurate experimental measurements of α_d, i.e. β, remain a challenge. In the literature [*Kaempfer and Plapp*, 2009], β ranges from 10^4 to 10^9 $\mathrm{s\,m^{-1}}$. On the basis of Equation (2.8), w_n is positive when the ice surface grows and negative when the ice surface sublimates. The saturation vapor density ρ_{vs} is given by the Clausius-Clapeyron's law:

$$\rho_{vs}(T_a) = \rho_{vs}^{\mathrm{ref}}(T^{\mathrm{ref}}) \exp\left[\frac{L_{sg} m}{\rho_i k} \left(\frac{1}{T^{\mathrm{ref}}} - \frac{1}{T_a} \right) \right] \tag{2.9}$$

The reference values T^{ref} and $\rho_{vs}^{\mathrm{ref}}(T^{\mathrm{ref}})$ are equal here to 273 K and $2.173{\times}10^{-3}$ $\mathrm{kg\,m^{-3}}$ respectively. In what follows, for the sake of simplicity, we will suppose that all material properties (ρ, C, κ, D_v, β, m) do not depend on the temperature.

2.2.3 Dimensionless pore scale description: normalization

Following the methodology presented in *Auriault* [1991], let us introduce into the set of Eq. (2.2)-(2.7) the following representation of all dimensional variables φ: $\varphi = \varphi_c \varphi^*$, where the subscript "c" denotes characteristic quantities (constant) and the asterisk "*" denotes the dimensionless microscopic variables. So we have: $\rho_i = \rho_{i_c}\rho^*, C_i = C_{i_c}C_i^*, \kappa_i = \kappa_{i_c}\kappa_i^*, T_i = T_{i_c}T_i^*, t = t_c t^*$, and so on. In the following, the microscopic length l is chosen as characteristic length ($l_c = l$), i.e., the so-called microscopic point of view is adopted [*Auriault*, 1991]. The gradient and the divergence operator are thus replaced by $(1/l)\mathbf{grad}^*$ and $(1/l)\mathbf{div}^*$. Consequently, the formal dimensionless set that describes the physics at the pore scale is written:

$$\left[\mathrm{F}_i^T\right] \rho_i^* C_i^* \frac{\partial T_i^*}{\partial t^*} - \mathrm{div}^*(\kappa_i^* \mathbf{grad}^* T_i^*) = 0 \quad \text{in } \Omega_i \tag{2.10}$$

$$\left[\mathrm{F}_a^T\right] \rho_a^* C_a^* \frac{\partial T_a^*}{\partial t^*} - \mathrm{div}^*(\kappa_a^* \mathbf{grad}^* T_a^*) = 0 \quad \text{in } \Omega_a \tag{2.11}$$

$$[\mathrm{F}_a^\rho] \frac{\partial \rho_v^*}{\partial t^*} - \mathrm{div}^*(D_v^* \mathbf{grad}^* \rho_v^*) = 0 \quad \text{in } \Omega_a \tag{2.12}$$

$$T_i^* = T_a^* \quad \text{on } \Gamma \tag{2.13}$$

$$[\mathrm{K}]\, \kappa_i^* \mathbf{grad}^* T_i^* \cdot \mathbf{n_i} - \kappa_a^* \mathbf{grad}^* T_a^* \cdot \mathbf{n_i} = [\mathrm{H}]\, L_{sg}^* \mathbf{w}^* \cdot \mathbf{n_i} \quad \text{on } \Gamma \tag{2.14}$$

$$D_v^* \mathbf{grad}^* \rho_v^* \cdot \mathbf{n_i} = [\mathrm{W}]\, \rho_i^* \mathbf{w}^* \cdot \mathbf{n_i} \quad \text{on } \Gamma \tag{2.15}$$

This dimensionless pore scale description introduces six dimensionless numbers that characterize the intensity of the physical phenomena at the pore scale. These dimensionless numbers are defined as

$$\left[\mathrm{F}_i^T\right] = \frac{l^2 \rho_{i_c} C_{i_c}}{t_c \kappa_{i_c}}, \quad \left[\mathrm{F}_a^T\right] = \frac{l^2 \rho_{a_c} C_{a_c}}{t_c \kappa_{a_c}}, \quad [\mathrm{F}_a^\rho] = \frac{l^2}{D_{v_c} t_c} \tag{2.16}$$

$$[\mathrm{K}] = \frac{\kappa_{i_c}}{\kappa_{a_c}}, \quad [\mathrm{H}] = \frac{l L_{sg_c} w_{n_c}}{\kappa_{a_c} T_{a_c}}, \quad [\mathrm{W}] = \frac{l \rho_{i_c} w_{n_c}}{D_{v_c} \rho_{v_c}}. \tag{2.17}$$

Dimensionless numbers $\left[\mathrm{F}_i^T\right]$ and $\left[\mathrm{F}_a^T\right]$ correspond to the inverse of the Fourier number in Ω_i and Ω_a, respectively. These numbers characterize the ratio between the rate of thermal energy storage and the heat conduction rate. $[\mathrm{F}_a^\rho]$ is an analogous inverse Fourier number for the transient water vapor transfer by diffusion in Ω_a. Dimensionless numbers [K], [H], and [W] are defined on the ice-pore interface. In particular, [H] characterizes the ratio between the heat flux induced by phase changes and the heat flux from heat conduction in the air phase. Similarly, [W] is defined as the ratio between the vapor flux from phase changes and the vapor flux from vapor diffusion in pores.

2.2.4 Estimation of the dimensionless numbers

The next important step of the homogenization process consists of estimating the above six dimensionless numbers with respect to the scale parameter $\varepsilon = l/L$. In practice, l and L correspond typically to the order of magnitude of the ice grain size and the thickness of a snow layer, respectively. In what follows, we assumed that $l \approx 5 \times 10^{-4}$ m

and $L \approx 0.1$ m, leading to $\varepsilon = 5 \times 10^{-3}$. The characteristic values of each variable arising in the dimensionless numbers (2.16)-(2.17) are summarized in Table 2.1. These values were evaluated for a temperature of -10°C and come from the literature [*Massman*, 1998; *Kaempfer and Plapp*, 2009]. According to these characteristic values, it can be first shown that the thermal diffusivity in the ice phase $\alpha_{i_c} = \kappa_{i_c}/(C_{i_c}\rho_{i_c})$ and in the air phase $\alpha_{a_c} = \kappa_{a_c}/(C_{a_c}\rho_{a_c})$, are of the same order of magnitude than the vapor diffusion coefficient D_{v_c}. Thus, the characteristic time t_c associated with these transfers through the snowpack are of the same order of magnitude: $t_c = \mathcal{O}(L^2/\alpha_{i_c}) = \mathcal{O}(L^2/\alpha_{i_a}) = \mathcal{O}(L^2/D_{v_c})$. Consequently, from (2.16), we get

$$\left[\mathrm{F}_i^T\right] = \mathcal{O}\left(\left[\mathrm{F}_a^T\right]\right) = \mathcal{O}\left([\mathrm{F}_a^\rho]\right) = \mathcal{O}(\varepsilon^2) \tag{2.18}$$

At the ice-pore interface, from (2.17), we have $[\mathrm{K}] = \mathcal{O}(1)$. Dimensionless numbers [H] and [W] depend on the intensity of the interface normal growth velocity w_{n_c}, which corresponds to an averaged value $\langle w_n \rangle$ over the REV. In practice, w_n varies widely locally inside a REV, depending on the temperature gradient, temperature, kinetic and curvature effects, etc. Nevertheless, several experimental and numerical studies [*Colbeck*, 1983a; *Fukuzawa and Akitaya*, 1993; *Sturm et al.*, 1997; *Flin and Brzoska*, 2008; *Libbrecht and Rickerby*, 2011] showed that w_n ranges from 0 to 10^{-9} m s^{-1} for temperature gradients between 0 and 500 K m^{-1}. Taking into account these results, Figure 2.2 shows that [H] and [W] can take different order of magnitude according to the value of w_{n_c}. Typically, several cases can be considered:

- Case 0: when $w_{n_c} \approx 10^{-10}$ m s^{-1}, $[\mathrm{H}] = \mathcal{O}(\varepsilon^2)$ and $[\mathrm{W}] = \mathcal{O}(\varepsilon)$;
- Case 1: when $w_{n_c} \approx 10^{-11}$ m s^{-1}, $[\mathrm{H}] = \mathcal{O}(\varepsilon^2)$ and $[\mathrm{W}] = \mathcal{O}(\varepsilon^2)$;
- Case 2: when $w_{n_c} \approx 10^{-12}$ m s^{-1}, $[\mathrm{H}] = \mathcal{O}(\varepsilon^3)$ and $[\mathrm{W}] = \mathcal{O}(\varepsilon^2)$;
- Case 3: when $w_{n_c} \lesssim 10^{-13}$ m s^{-1}, $[\mathrm{H}] \leqslant \mathcal{O}(\varepsilon^3)$ and $[\mathrm{W}] \leqslant \mathcal{O}(\varepsilon^3)$;

In what follows, we will not investigate the Case 0, which corresponds to the case of very large temperature gradients and is characterized by interfaces rapidly moving into vapor fields and significant latent heat effects. Only Cases 1, 2, and 3 are considered. Moreover, we will show that Cases 2 and 3 can be easily deduced from Case 1.

2.2.5 Asymptotic analysis

The next step is to introduce multiple-scale coordinates [*Bensoussan et al.*, 1978; *Sanchez-Palencia*, 1980; *Auriault*, 1991]. The two characteristic lengths L and l introduce two dimensionless space variables, $\mathbf{x}^* = \mathbf{X}/L$ and $\mathbf{y}^* = \mathbf{X}/l$, where $\mathbf{X}$ is the physical space variable. The macroscopic (or slow) dimensionless space variable $\mathbf{x}^*$ is related to the microscopic (or fast) dimensionless space variable $\mathbf{y}^*$ by $\mathbf{x}^* = \varepsilon\mathbf{y}^*$. When l is used as the characteristic length, the dimensionless derivative operator $\mathbf{grad}^*$ becomes $(\mathbf{grad}_{y^*} + \varepsilon\mathbf{grad}_{x^*})$, where the subscripts $_{x^*}$ and $_{y^*}$ denote the derivatives with respect to the variables $\mathbf{x}^*$ and $\mathbf{y}^*$, respectively. Following the multiple-scale expansion technique [*Bensoussan*

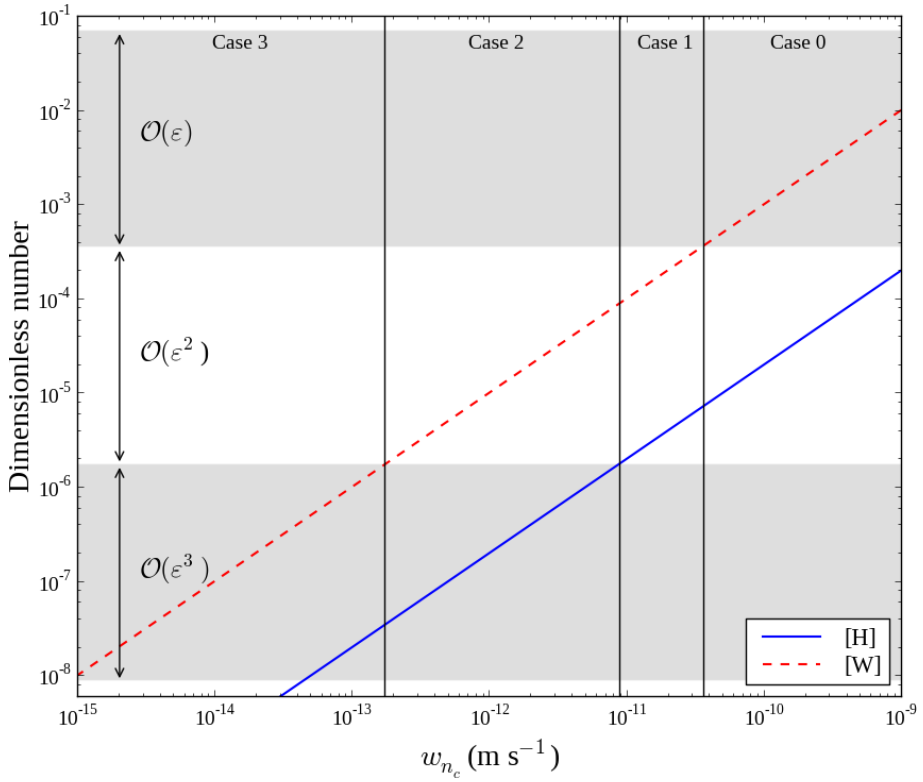

Figure 2.2: Estimation of dimensionless numbers [H] and [W] versus the characteristic interface normal growth velocity w_{n_c}, from characteristic values given in Table 2.1.

et al., 1978; *Sanchez-Palencia*, 1980; *Auriault*, 1991], the ice temperature T_i^*, the air temperature T_a^*, and the water vapor ρ_v^* are sought in the form of asymptotic expansions of powers of ε:

$$\varphi^*(\mathbf{x}^*, \mathbf{y}^*, t) = \varphi^{*(0)}(\mathbf{x}^*, \mathbf{y}^*, t) + \varepsilon\varphi^{*(1)}(\mathbf{x}^*, \mathbf{y}^*, t) + \varepsilon^2\varphi^{*(2)}(\mathbf{x}^*, \mathbf{y}^*, t) + ... \tag{2.19}$$

where $\varphi^* = T_i^*, T_a^*, \rho_v^*$ and the corresponding $\varphi^{*(i)}$ are periodic functions of period Ω with respect to the space variable $\mathbf{y}^*$. Substituting these expansions in the set (2.10)-(2.15) gives, by identification of like powers of ε, successive boundary value problems to be investigated. All the details concerning this asymptotic analysis of the Case 1 are presented in the Appendix A1. The main results are summarized in the following section.

2.2.6 Macroscopic equivalent description

According to the order of magnitude of the dimensionless numbers in the Case 1, $\left[\mathrm{F}_i^T\right] = \mathcal{O}\left(\left[\mathrm{F}_a^T\right]\right) = \mathcal{O}\left([\mathrm{F}_a^\rho]\right) = \mathcal{O}(\varepsilon^2)$, $[\mathrm{K}] = \mathcal{O}\left(1\right), [\mathrm{H}] = \mathcal{O}\left(\varepsilon^2\right), [\mathrm{W}] = \mathcal{O}\left(\varepsilon^2\right)$, the asymptotic analysis presented in the Appendix A1 shows that the heat transfer and the water vapor diffusion at the macroscopic scale are described by the equations (A.48) and (A.51). Retuning in dimensional variables, the macroscopic model is written

$$(\rho C)^{\text{eff}}\frac{\partial T^{(0)}}{\partial t} - \text{div}(\mathbf{k}^{\text{eff}}\mathbf{grad}\ T^{(0)}) = \text{SSA}_\text{V} L_{sg} w_n^{(0)} \tag{2.20}$$

$$\phi\frac{\partial \rho_v^{(0)}}{\partial t} - \text{div}(\mathbf{D}^{\text{eff}}\mathbf{grad}\ \rho_v^{(0)}) = -\text{SSA}_\text{V}\rho_i w_n^{(0)} \tag{2.21}$$

Table 2.1: Characteristic values of the properties evaluated at -10°C from the literature [*Massman*, 1998; *Kaempfer and Plapp*, 2009].

symbol	description	value
T_{i_c}, T_{a_c}	temperature of ice, air	263 K
κ_{i_c}	heat conductivity of ice	2.3 $\mathrm{W\,m^{-1}\,K^{-1}}$
κ_{a_c}	heat conductivity of air	0.024 $\mathrm{W\,m^{-1}\,K^{-1}}$
C_{i_c}	specific heat capacity of ice	2000 $\mathrm{J\,kg^{-1}\,K^{-1}}$
C_{a_c}	specific heat capacity of air	1005 $\mathrm{J\,kg^{-1}\,K^{-1}}$
L_{sg_c}	latent heat of sublimation of ice	2.60×10^9 $\mathrm{J\,m^{-3}}$
w_{n_c}	normal interface velocity	10^{-14} to 10^{-8} $\mathrm{m\,s^{-1}}$
D_{v_c}	water vapor diffusion coefficient in air	2.036×10^{-5} $\mathrm{m^2\,s^{-1}}$
ρ_{v_c}	water vapor density in air	0.002 $\mathrm{kg\,m^{-3}}$
ρ_{i_c}	ice density	917 $\mathrm{kg\,m^{-3}}$
ρ_{a_c}	air density	1.335 kg $\mathrm{m^{-3}}$
l	microscopic length	$5{\times}10^{-4}$ m
L	macroscopic length	0.1 m

where $w_n^{(0)}$ is given by the Hertz-Knudsen equation (A.47) and the Clausius-Clapeyron's law (A.43)

$$w_n^{(0)} = \frac{1}{\beta}\left[\frac{\rho_v^{(0)} - \rho_{vs}^{(0)}(T^{(0)})}{\rho_{vs}^{(0)}(T^{(0)})} - d_0 K\right] \tag{2.22}$$

$$\rho_{vs}^{(0)}(T^{(0)}) = \rho_{vs}^{\mathrm{ref}} \exp\left[\frac{L_{sg} m}{\rho_i k}\left(\frac{1}{T^{\mathrm{ref}}} - \frac{1}{T^{(0)}}\right)\right] \tag{2.23}$$

and where ϕ is the porosity, $\mathrm{SSA_V} = |\Gamma|/|\Omega|$ is the specific surface area defined as the ice surface area over the snow volume in $\mathrm{m^{-1}}$, $(\rho C)^{\mathrm{eff}}$ is the effective thermal capacity (A.49), $\mathbf{k}^{\mathrm{eff}}$ is the effective thermal conductivity tensor (A.50), and $\mathbf{D}^{\mathrm{eff}}$ is the effective diffusion tensor (A.52). These effective properties are defined as

$$(\rho C)^{\mathrm{eff}} = (1-\phi)\rho_i C_i + \phi \rho_a C_a \tag{2.24}$$

$$\mathbf{k}^{\mathrm{eff}} = \frac{1}{|\Omega|}\left(\int_{\Omega_\mathrm{a}} \kappa_\mathrm{a}(\mathbf{grad}\ \mathbf{t}_a + \mathbf{I})\mathrm{d}\Omega + \int_{\Omega_\mathrm{i}} \kappa_\mathrm{i}(\mathbf{grad}\ \mathbf{t}_i + \mathbf{I})\mathrm{d}\Omega\right) \tag{2.25}$$

$$\mathbf{D}^{\mathrm{eff}} = \frac{1}{|\Omega|}\int_{\Omega_a} D_v(\mathbf{grad}\ \mathbf{g}_v + \mathbf{I})\mathrm{d}\Omega \tag{2.26}$$

where $\mathbf{t}_a$ and $\mathbf{t}_i$ are two periodic vectors solution of the following boundary value problem over the REV (A.20)-(A.24):

$$\mathrm{div}(\kappa_i(\mathbf{grad}\ \mathbf{t}_i + \mathbf{I})) = 0 \quad \text{in } \Omega_i \tag{2.27}$$

$$\mathrm{div}(\kappa_a(\mathbf{grad}\ \mathbf{t}_a + \mathbf{I})) = 0 \quad \text{in } \Omega_a \tag{2.28}$$

$$\mathbf{t}_i = \mathbf{t}_a \quad \text{on } \Gamma \tag{2.29}$$

$$(\kappa_i(\mathbf{grad}\ \mathbf{t}_i + \mathbf{I}) - \kappa_a(\mathbf{grad}\ \mathbf{t}_a + \mathbf{I})) \cdot \mathbf{n_i} = 0 \quad \text{on } \Gamma \tag{2.30}$$

$$\frac{1}{|\Omega|}\int_{\Omega}(\mathbf{t}_\mathrm{a} + \mathbf{t}_\mathrm{i})\mathrm{d}\Omega = \mathbf{0} \tag{2.31}$$

and where $\mathbf{g}_v$ is a periodic vector solution of the following boundary value problem over the REV (A.35)-(A.37):

$$\mathrm{div}(D_v(\mathbf{grad}\ \mathbf{g}_v + \mathbf{I})) = 0 \quad \text{in } \Omega_a \tag{2.32}$$

$$D_v(\mathbf{grad}\ \mathbf{g}_v + \mathbf{I}) \cdot \mathbf{n_i} = 0 \quad \text{on } \Gamma \tag{2.33}$$

$$\frac{1}{|\Omega|}\int_{\Omega_a}\mathbf{g}_v\mathrm{d}\Omega = \mathbf{0} \tag{2.34}$$

In Case 1, the above macroscopic equivalent description shows that at the first order:

- the heat transfer through the snowpack is described by a transient heat transfer equation () with a source term $Q_T = \mathrm{SSA_V}\ L_{sg}\ w_n^{(0)}$ induced by the phase change process occurring at the pore scale on the ice-pore interface Γ.
- the mass transfer is governed by a transient water vapor diffusion equation (2.21) including a source term $Q_v = -\mathrm{SSA_V}\ \rho_i\ w_n^{(0)}$ induced by the phase change process occurring on Γ. Let us remark that $\rho_v^{(0)}$ is the vapor density per unit volume of fluid.
- both source terms are defined by the Hertz-Knudsen equation (2.22) and the Clausius Clapeyron's law (2.23), but expressed with respect to the two macroscopic variables $T^{(0)}$ and $\rho_v^{(0)}$.

Finally, from the asymptotic analysis presented in the Appendix A1, it can be easily shown that in the Case 2, i.e. when $[\mathrm{H}] = \mathcal{O}(\varepsilon^3)$ and $[\mathrm{W}] = \mathcal{O}(\varepsilon^2)$, the macroscopic modeling is the same as the one obtained in the Case 1, but Q_T is negligible. Similarly, in the Case 3, i.e. when $[\mathrm{H}] \leqslant \mathcal{O}(\varepsilon^3)$ and $[\mathrm{W}] \leqslant \mathcal{O}(\varepsilon^3)$, both Q_T and Q_v become negligible at the macroscopic scale.

2.3 2D numerical example

2.3.1 Problem definition

To evaluate the obtained macroscopic modeling, we propose in this section to compare the numerical results for the heat and water vapor transfer through a snow layer obtained in the case of a fine scale modeling (i.e., by taking into account all the heterogeneities) and in the case of the corresponding macroscopic equivalent modeling. For that purpose, finite element numerical simulations have been preformed on the same 2D vertical snow layer of 10 cm length and 0.5 cm width (Figure 3.4) using the finite element code ComsolMultiphysics. At the top and the bottom of the snow layer, the temperatures T_{top} and T_{bottom} are imposed and, by this way, the vapor density, which is supposed to be equal to the saturation vapor density, $\rho_{vs}(T_{\mathrm{top}})$ and $\rho_{vs}(T_{\mathrm{bottom}})$ using Equation (2.9). Symmetry conditions are imposed

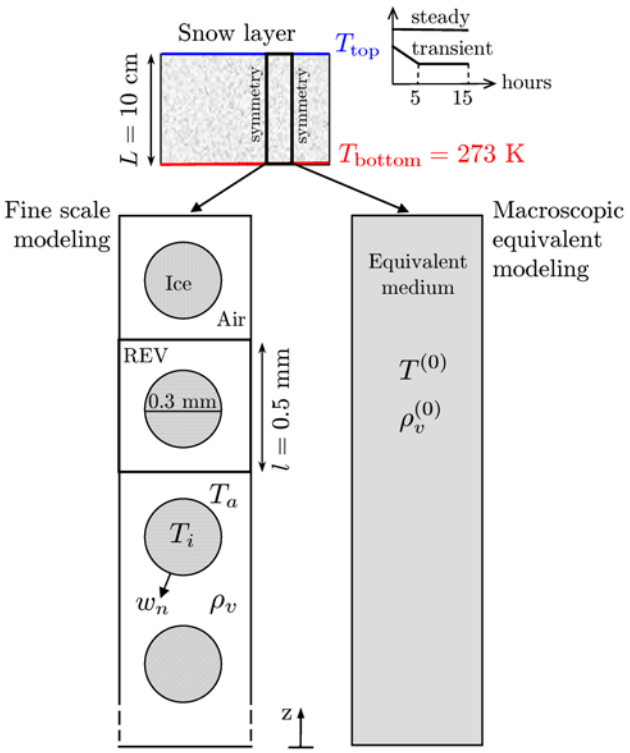

Figure 2.3: Illustration of the 2D geometry for the fine scale modeling and the macroscopic equivalent modeling.

on the lateral sides of the snow layer. In what follows, curvature effects are neglected ($d_0 K = 0$), and the interface kinetic coefficient β is taken constant and equal to $5.5{\times}10^5$ s m^{-1}, as in the study of *Kaempfer and Plapp* [2009].

In the case of the fine scale modeling, the snow layer microstructure consists in 200 periodic cells of $0.5{\times}0.5$ mm^2; each periodic cell (REV) is composed by an ice grain of diameter 0.3 mm surrounded by air. Thus, the porosity is equal to 0.71, which corresponds to a snow density of 266 kg m^{-3}. In this case, the heat and the mass transfer within this layer are described by the set of equations (2.2) – (2.9) where T_i, T_a, and ρ_v are the unknowns. This set of equations has been numerically solved using the material parameter values presented in Table 1.

In the case of the macroscopic equivalent modeling, the snow layer is seen as a continuous equivalent medium. The heat and the mass transfer are now described by the set of equations (2.2.6) – (2.23) where $T^{(0)}$ and $\rho_v^{(0)}$ are the macroscopic unknowns. This macroscopic description requires us to compute some parameters or effectives properties over the REV. The porosity ϕ and the specific surface area $\mathrm{SSA_V}$ involved in the macroscopic modeling can be easily deduced from the geometry of the REV. The effective heat capacity $(\rho C)^{\mathrm{eff}}$, effective thermal conductivity $\mathbf{k}^{\mathrm{eff}}$ and effective vapor diffusion $\mathbf{D}^{\mathrm{eff}}$ were computed using relations (2.24), (2.25), and (2.26), respectively. For that purpose, the boundary values problems (2.27)-(2.31) and (2.32)-(2.34) have been solved numerically over the REV. Due to the symmetry of the REV, tensors $\mathbf{D}^{\mathrm{eff}}$ and $\mathbf{k}^{\mathrm{eff}}$ are both isotropic and can be written $\mathbf{D}^{\mathrm{eff}} = D^{\mathrm{eff}}\mathbf{I}$ and $\mathbf{k}^{\mathrm{eff}} = k^{\mathrm{eff}}\mathbf{I}$, where $\mathbf{I}$ is the identity tensor. The parameters and

Table 2.2: Macroscopic properties computed over the REV of the considered 2D geometry, using κ_a=0.024 W m^{-1} K^{-1}, κ_i=2.3 W m^{-1} K^{-1} and D_v= 2.036 × 10^{-5} m^2 s^{-1}.

porosity, ϕ	0.71
surface area, SSA_V	3770 m^{-1}
effective thermal capacity, $(\rho C)^{eff}$	5.328×10^5 J m^{-3} K^{-1}
effective thermal conductivity, k^{eff}	0.04243 W m^{-1} K^{-1}
effective diffusion, D^{eff}	1.156×10^{-5} m^2 s^{-1}

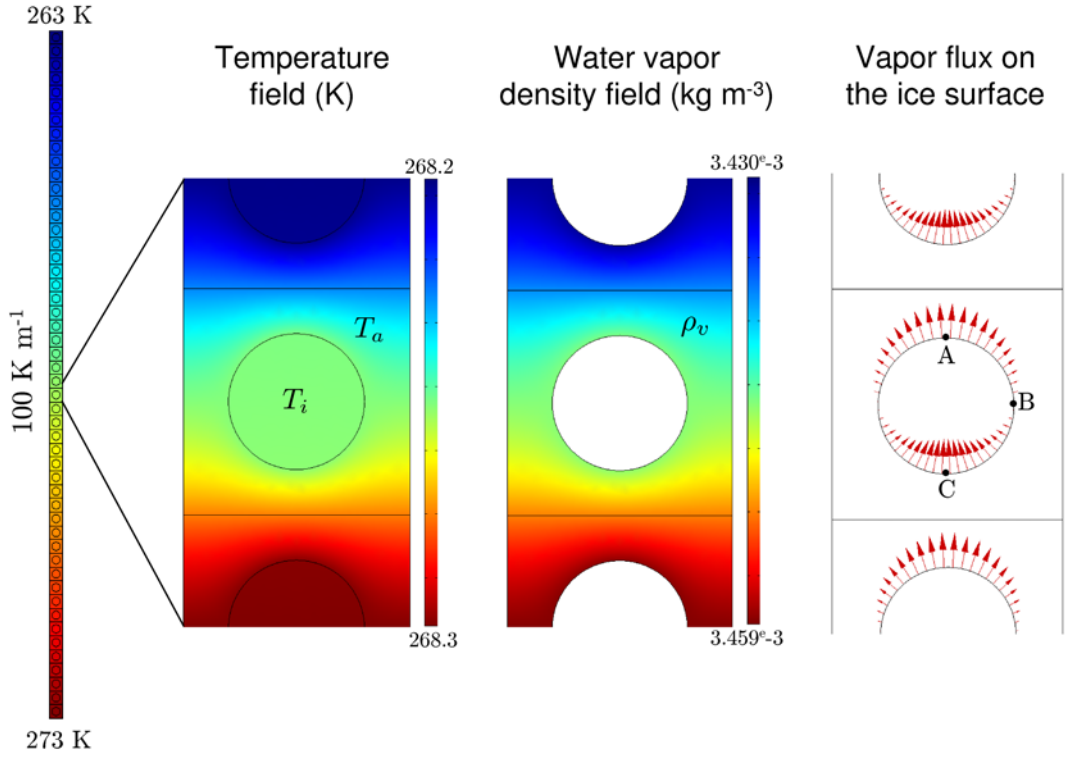

Figure 2.4: Microscopic field of temperature, water vapor density, and vapor density flux computed within the cell at midheight of the snow layer that experiences a constant temperature gradient of 100 K m^{-1}.

the effective properties deduced from the REV scale are summarized in Table 2.2.

2.3.2 Results

Figure 2.4 shows the temperature field and vapor density field as well as the vapor density flux at the interface computed within the cell at midheight of the snow layer using the fine scale modeling when T_{top} = 263 K and T_{bottom} = 273 K, in the steady state. At the pore scale, the temperature gradient is mainly concentrated in air due to the ratio κ_i/κ_a, which is around 100. The vapor flux varies widely along the interface and the sign is opposite between the upper (sublimation) and lower (deposition) parts of the grain.

The vertical profiles of the temperature and vapor density through the snow layer obtained in the case of a fine scale modeling (marks) and in the case of the corresponding

macroscopic equivalent modeling (solid line) are presented in Figures 2.5 and 2.6. In the case of the fine scale modeling, the average values of each microscopic variable over the cell have been reported, expressed as

$$\langle T \rangle = \frac{1}{\Omega}\left(\int_{\Omega_i} T_i d\Omega + \int_{\Omega_a} T_a d\Omega\right), \quad \langle \rho_v \rangle = \frac{1}{\Omega_a}\int_{\Omega_a} \rho_v d\Omega$$

Figure 2.5 shows the obtained results in steady state, when $T_{\text{bottom}} = 273$ K and $T_{\text{top}} = 268, 263$, and 248 K successively, which leads to a temperature gradient of 50, 100, and 250 $\mathrm{K\,m^{-1}}$, respectively. Under such conditions, temperature profiles are mostly linear; by contrast, vapor density profile are strongly nonlinear. Moreover, this figure shows that overall the temperature and water vapor profiles deduced from the fine scale modeling and the macroscopic equivalent modeling are close. In detail, the macroscopic equivalent description underestimates the temperature and vapor density; as shown in Figure 2.5, the maximum relative difference between both modelings does not exceed 0.24 % for the temperature and 5.44 % for the vapor density in the middle of the snow layer and for $T_{\text{top}} = 248$ K. This figure also underlines that a small error on the temperature field may lead to a large error on the water vapor field when the temperature gradient increases.

Figure 2.6 shows the temperature and vapor density profiles in the case of a transient analysis. The snow layer is initially at a temperature of 273 K; then T_{top} decreases to reach 263 K in 5 h and remains constant until 15 h. The value of T_{bottom} is constant and equal to 273 K. The profiles at six different times are shown. Once again, we can observe a good agreement between the numerical results of both modelings. Under such conditions, the maximum relative error is obtained at t = 6 h and reaches -0.14 % for the temperature profile and -3.35 % for the vapor density profile.

Finally, the temperature and water vapor profiles (dashed lines) obtained if the source term is supposed to be negligible in the macroscopic heat transfer equation (Case 2) are also reported in Figure 2.5. These results show that for low to moderate temperature gradients (typically lower than 100 $\mathrm{K\,m^{-1}}$), the relative difference between both modelings remains lower than 0.1% for the temperature and lower than 2.2 % for the water vapor density. For large temperature gradients (typically larger than 200 $\mathrm{K\,m^{-1}}$), these relative differences strongly increase and show that the source term in the heat transfer equation is not negligible. These results are consistent with the dimensionless analysis and are directly linked to the evolution of the normal growth velocity with respect to the temperature gradient.

Figure 2.7 presents the evolution of the normal growth velocity at the midheight of the snow layer deduced from the fine scale modeling (w_n at the top (point A), base (point C), and midheight (point B) of the ice grain as well as the average value $\langle w_n \rangle$ over the REV, Figure 2.4) and from the macroscopic equivalent modeling ($w_n^{(0)}$) for a temperature gradient within the range 0 to 250 $\mathrm{K\,m^{-1}}$. As expected, the normal growth velocity increases with increasing temperature gradient. At the top and the base of the ice grain, w_n is negative (sublimation) and positive (deposition), respectively, and ranges typically from 10^{-11} to 10^{-9} $\mathrm{m\,s^{-1}}$, whereas at the midheight of the grain w_n ranges from 10^{-15} to 10^{-12} $\mathrm{m\,s^{-1}}$. Figure 2.7 shows that the average value $\langle w_n \rangle$ over the REV presents a similar trend and

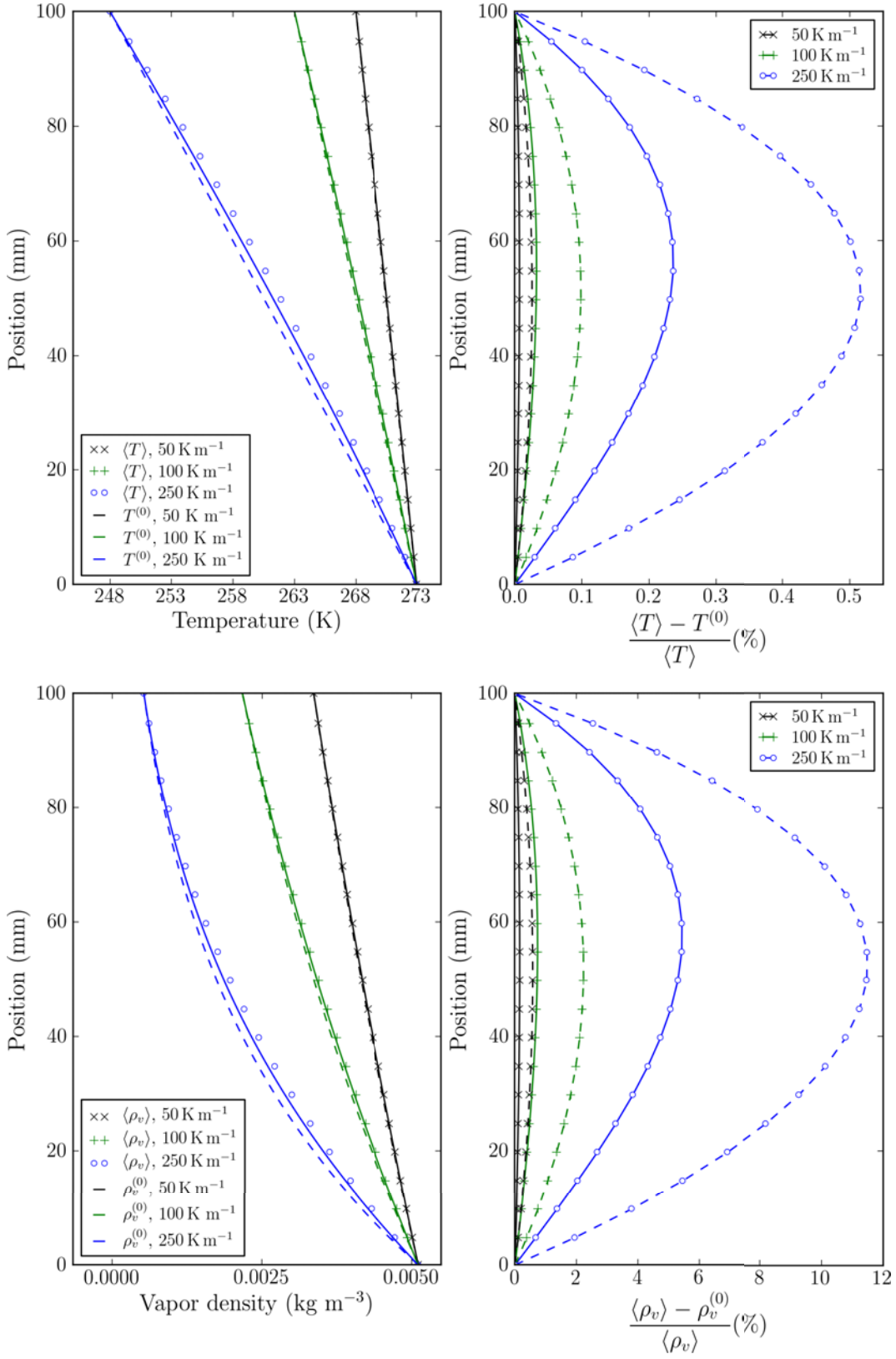

Figure 2.5: Comparison between fine scale (marks) and macroscopic equivalent (solid line) modeling (Case 1) in the steady state: vertical profile of temperature and vapor density and relative errors for a temperature gradient of 50, 100, and 250 K m^{-1}. Dashed lines correspond to Case 2: the source term is supposed to be negligible in the macroscopic heat transfer equation.

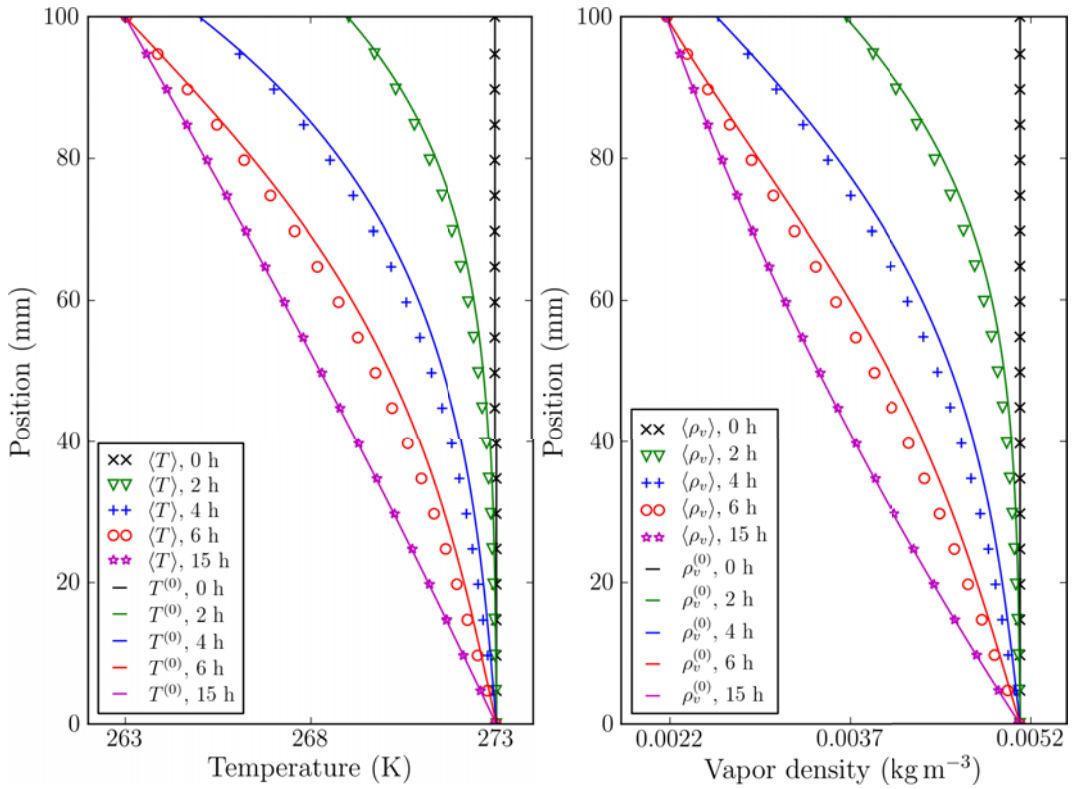

Figure 2.6: Comparison between fine scale (marks) and macroscopic equivalent (continuous lines) modeling in the case of transient analysis: vertical profile of temperature and water vapor density within the snow layer at 6 different times.

also ranges from 10^{-15} to 6×10^{-12} m s^{-1}. The averaged growth velocity over the particle interface is low, but positive, meaning that the deposition predominates slightly over the sublimation. This is due to the nonlinear relationship between the temperature and the saturation vapor density. The evolution of the "macroscopic equivalent normal velocity" $w_n^{(0)}$ is consistent with $\langle w_n \rangle$. This evolution of the normal velocity versus the temperature gradient confirms that the dimensionless numbers [H] and [W] may extend over several orders of magnitude as already discussed. For large temperature gradients, $[\mathrm{H}] = \mathcal{O}(\varepsilon^2)$ and $[\mathrm{W}] = \mathcal{O}(\varepsilon^2)$ which corresponds to Case 1, i.e the macroscopic modeling including a source term in both the heat and mass transfer equation.

2.4 Effective diffusion tensors from 3D images of snow

In practice, the macroscopic equivalent modeling given by the set of equations (2.2.6) – (2.23) requires the knowledge of the effective thermal conductivity tensor $\mathbf{k}^{\mathrm{eff}}$ and the effective vapor diffusion tensor $\mathbf{D}^{\mathrm{eff}}$, which can be computed not only on a simple microstructure as previously but also on 3D images of snow obtained by X-ray microtomography. The effective thermal conductivity tensor has been already computed on 3D images in *Calonne et al.* [2011] (see Part III, chapter 3). Following this work, the effective vapor diffusion tensor was computed by solving the specific boundary value problem (2.32) - (2.34) over REVs extracted from 3D images using the software Geodict (see www.geodict.de/DiffuDict.php).

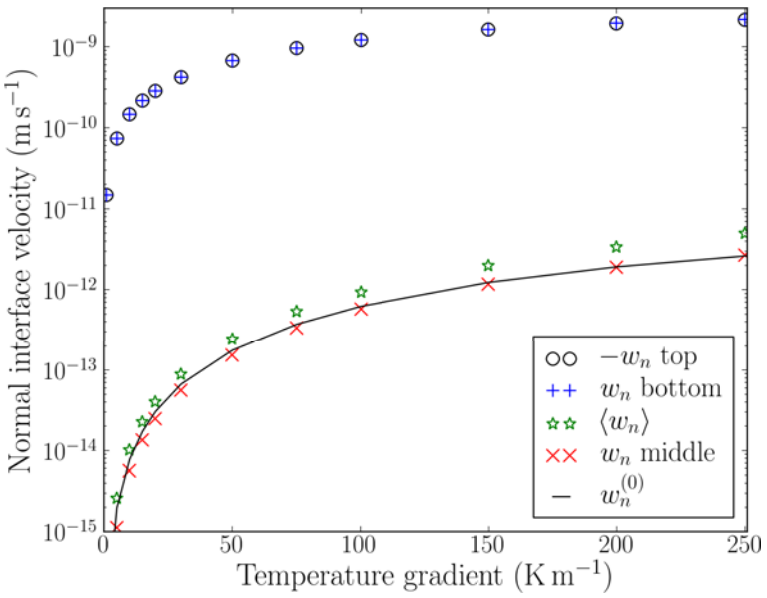

Figure 2.7: Evolution of the normal growth velocity in the midheight of the 2D snow layer deduced from the fine scale modeling (w_n at the top, base and middle of the ice grain as well as the average value $\langle w_n \rangle$ over the REV) and from the macroscopic equivalent modeling ($w_n^{(0)}$) for a temperature gradient within the range 0−250 K m^{-1}.

First, we estimated the size of the REVs following *Calonne et al.* [2011] (auxiliary material) by computing the effective vapor diffusion tensor over subvolumes of increasing sizes. The effective vapor diffusion tensor has been determined on 35 images of snow spanning the different snow types and a large range of snow density (more information about the 3D images can be found in the auxiliary materials of *Calonne et al.* [2012]). Three subvolumes of the 3D images used are shown in Figure 2.8. Each image has been defined in a frame (x, y, z), where z is the vertical direction of the snow layer. In the following, we only present the diagonal components of the tensor $\mathbf{D}^{\text{eff}}$, because the nondiagonal ones are negligible.

Figure 2.9 shows the evolution of the vertical and horizontal components of $\mathbf{D}^{\text{eff}}$ normalized by the vapor diffusion coefficient in the air (D_v) as a function of the snow density. These values are given in Appendix A2. Horizontal components correspond to the average of the x-value and y-value of $\mathbf{D}^{\text{eff}}$. In the figure, the vertical and horizontal components are represented by the tips and horizontal bars of the 'T' shapes, respectively. Let us remark that $\mathbf{D}^{\text{eff}}/D_v = \phi\boldsymbol{\tau}_{\mathbf{a}}$, where $\boldsymbol{\tau}_{\mathbf{a}}$ is the tortuosity tensor associated to the air phase and ϕ is the porosity. The normalized effective vapor diffusion decreases linearly with increasing density and ranges from 0.17 to 0.76, which correspond to non-normalized values from 3.46×10^{-6} to 1.55×10^{-5} m^2 s^{-1}, if we consider $D_v = 2.036\times10^{-5}$ m^2 s^{-1}.

We quantified the anisotropic behavior of the effective vapor diffusion of snow by using an anisotropy coefficient. This coefficient is defined as the vertical component over the horizontal component of the diagonal terms of the tensor $\mathbf{D}^{\text{eff}}$. Figure 2.10 shows the anisotropy coefficient of the effective vapor diffusion versus the anisotropy coefficient of the effective thermal conductivity. The latter comes from the study of *Calonne et al.* [2011]. The anisotropy coefficient of the effective vapor diffusion ranges from 0.86 for a natural

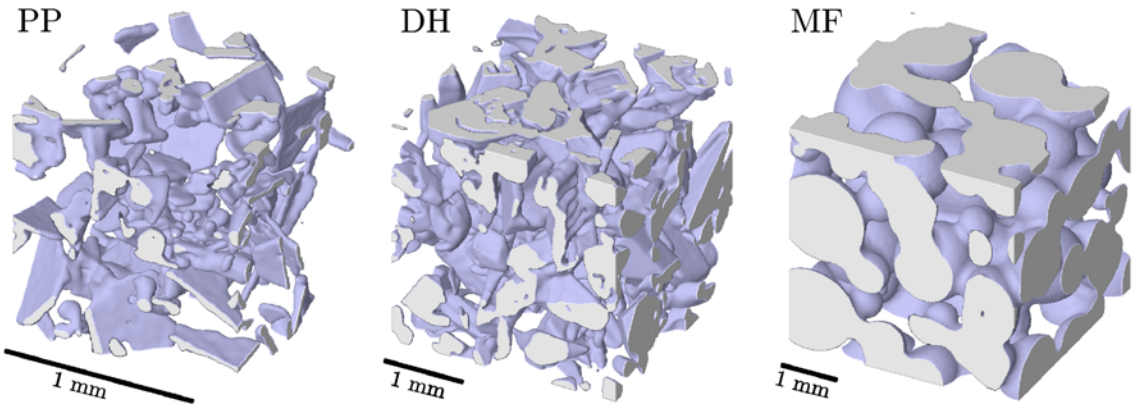

Figure 2.8: Representation of 3D images (subvolumes) of three different snow types obtained by X-ray tomography: precipitation particles (PP), depth hoar (DH), and melt forms (MF), from left to right.

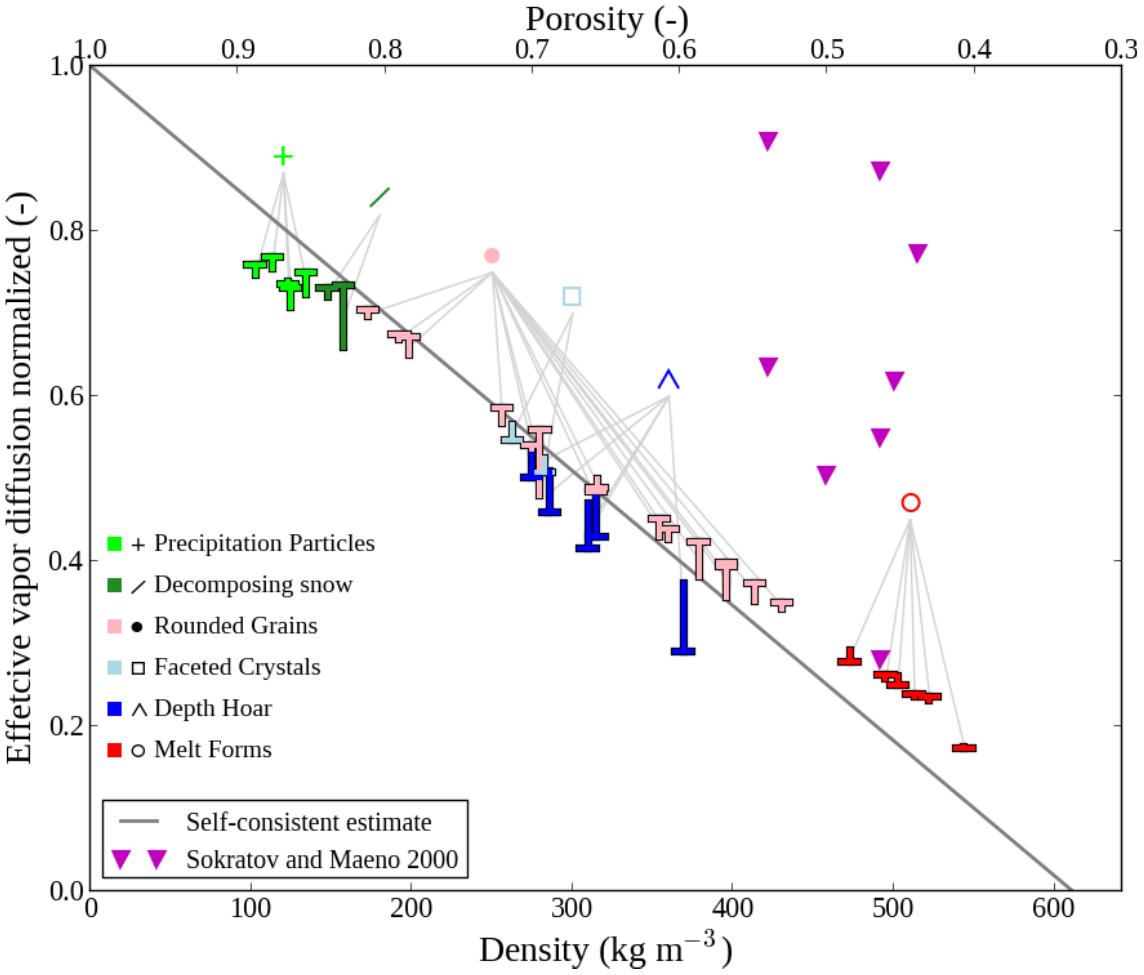

Figure 2.9: Normalized effective vapor diffusion versus snow density. Tips and horizontal bars of the "T" shapes represent the vertical and horizontal components of $\mathbf{D}^{\text{eff}}$. Colors correspond to the ICSSG [*Fierz et al.*, 2009]. Measurements from *Sokratov and Maeno* [2000] are shown in purple and the self-consistent estimate is plotted in gray.

snow sample of rounded grains collected in depth to 1.29 for a particularly evolved depth hoar sample obtained in cold room. In contrast with the coefficient of the effective thermal

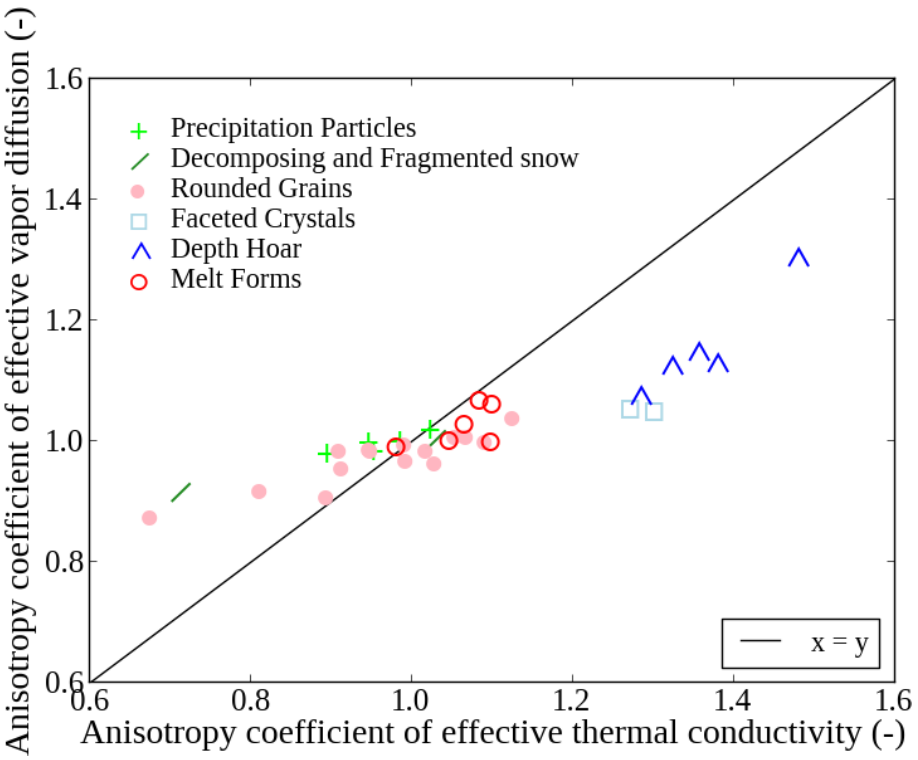

Figure 2.10: Anisotropy coefficients of effective vapor diffusion versus the anisotropy coefficients of effective thermal conductivity. The latter come from *Calonne et al.* [2011]. Colors and symbols correspond to the ICSSG [*Fierz et al.*, 2009].

conductivity, the anisotropy coefficient of the effective vapor diffusion does not separate systematically the depth hoar and faceted crystals from the other snow types. Overall, the effective vapor diffusion shows a more isotropic behavior (values centered around 1) than the effective thermal conductivity.

Finally, in Figure 2.9 we have also reported (i) the cold-room measurements of the effective vapor diffusion in snow performed by *Sokratov and Maeno* [2000] and (ii) the self-consistent estimate of the effective diffusion for spherical inclusions [*Auriault et al.*, 2009]: $D^{\mathrm{SC}} = D_v(3\phi - 1)/2$. The experimental values of *Sokratov and Maeno* [2000], which are smaller than 1 and tend to indicate that there is no enhancement of the effective vapor diffusion in snow, are in overall much higher than our numerical values. The self-consistent formula offers a good estimate of our numerical results, within an averaged relative error of $\pm$ 10%.

2.5 Discussion

In the presented paper, the macroscopic equivalent modeling of heat and water vapor transfer through snow has been derived from the physics at the pore scale by using an upscaling method. In the absence of convection and densification, we have shown that this macroscopic equivalent modeling strongly depends on the order of magnitude of dimensionless numbers defined at the ice-pore interface ([H] and [W]). In the most general case (Case 1: $[\mathrm{H}] = \mathcal{O}(\varepsilon^2)$ and $[\mathrm{W}] = \mathcal{O}(\varepsilon^2)$), the heat and mass transfer

are described by two coupled equations including a source term $Q_T = \mathrm{SSA_V}\ L_{sg}\ w_n^{(0)}$ and $Q_v = -\mathrm{SSA_V}\ \rho_i\ w_n^{(0)}$, where $w_n^{(0)}$ is given by the Clausius-Clapeyron's law and the Hertz-Knudsen equation expressed in terms of macroscopic variables. The obtained macroscopic modeling is similar to the one presented by *Albert and McGilvary* [1992] in a phenomenological way. By contrast, the homogenization process also provides the definition of the effectives properties and of the domain of validity of the modeling via the dimensionless numbers.

The macroscopic description was derived for a condition of scale $\varepsilon = 5 \times 10^{-3}$. This corresponds to a "medium" separation of scale and higher values will indicate that microscopic and macroscopic scales cannot be separated; the homogenization method will thus not be applicable. Inversely, as shown by Equation (2.19), the smaller the condition of the scale, the closer the macroscopic description with respect to the microscopic one. In that case, the source terms at the interface will have less influence on the macroscopic profile of vapor and heat.

On the basis of the definition of Q_v and Q_T, the mass transfer coefficient at the interface h_m, which is expressed in the source terms presented by *Albert and McGilvary* [1992], is perfectly defined as

$$h_m = \frac{\rho_i}{\beta\, \rho_{vs}^{(0)}(T^{(0)})} \tag{2.35}$$

Figure 2.11 shows the mass transfer coefficient as a function of the temperature and for three values of β. The gray zone corresponds to the range of values of h_m measured by *Neumann et al.* [2009]. The mass-transfer coefficient decreases with increasing temperature and its order of magnitude strongly depends on β. To be in agreement with the experimental data of *Neumann et al.* [2009], the mass transfer must be computed with a value of β around $1{\times}10^9\ \mathrm{s\,m^{-1}}$.

In all modeling cases, the effect of phase changes occurring at the micro scale is larger on the macroscopic vapor field than in the macroscopic temperature field, as suggested in Figure 2.2. Indeed, the relative errors observed for the temperature profiles of Figure 2.5 remain small with and without taking into account Q_T in the macroscopic modelings. This observation is consistent with the parametric study performed by *Albert and McGilvary* [1992]. Nevertheless, the above considerations are counterbalanced by the fact that, because the evolution of the saturation vapor density over ice is exponential with respect to the temperature, a small error in the macroscopic temperature induces a large error in the macroscopic vapor density. This error is enhanced for the large temperature gradients. In conclusion, the effect of phase changes at the macro scale should be taken into account via Q_T and Q_v for a better precision, and especially when snow experiences large temperature gradients.

In agreement with *Sokratov and Maeno* [2000] and *Pinzer et al.* [2012], our theoretical developments and 3D image-based computations of the effective vapor diffusion tensor $\mathbf{D}^{\mathrm{eff}}$ indicate that there is no enhancement of the effective vapor diffusion in snow. In the absence of convection, the sublimation and deposition over the ice surface, which can be viewed as a mechanism that enhances the vapor transfer, is reflected by the macroscopic source term Q_v and not by $\mathbf{D}^{\mathrm{eff}}$. The good agreement of the vapor density profiles of the

2D snow layer between the microscopic and macroscopic modeling strengthens the above considerations. Our results of effective vapor diffusion are overall smaller than the values of *Sokratov and Maeno* [2000], who first present a non-enhanced effective vapor diffusion based on experimental results. The scatter of the data of *Sokratov and Maeno* [2000] highlights the difficulty of performing such measurements.

Further developments are required concerning the following points: (i) Case 0, i.e, when $[\mathrm{H}] = \mathcal{O}(\varepsilon^2)$ and $[\mathrm{W}] = \mathcal{O}(\varepsilon)$ has not been investigated in the present work. This case corresponds typically to snow layers under very large temperature gradients. These gradients may lead to a macroscopic length associated with the phenomena (ratio between the average temperature over the temperature gradient) smaller than the geometric one associated with the thickness of the snow layer, and consequently to a poor separation of scales [*Auriault et al.*, 2005]. In that case, the macroscopic modeling can be formulated by investigating the following superior order of approximation in the asymptotic analysis. (ii) A poor separation of scales can also occur when the thickness of the snow layer L is very small. Such a particular case can be studied as in the Case 0, by investigating the following superior order of approximation in the asymptotic analysis. (iii) In the present modeling, the air convection, which can be induced by wind-pumping [*Albert and Shultz*, 2002] for example, has been neglected. These effects must be included in the microscopic description to quantify their influences (convection, dispersion, etc) on the macroscopic modeling. (iv) Monitored experiments might be carried out to evaluate the macroscopic modeling with respect to measurements.

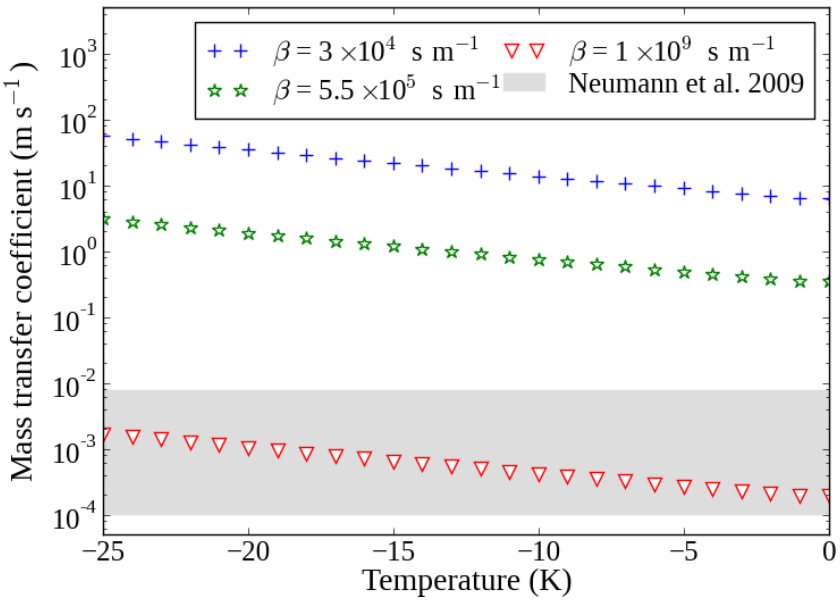

Figure 2.11: Mass transfer coefficient as a function of temperature, computed with Equation (2.35) using three values of the interface kinetic coefficient β. Values of $\rho_{vs}^{(0)}$ are computed using the Clausius-Clapeyron law (see Eq. (2.23)) and ρ_i is equal to 917 kg m^{-3}. The range of values corresponding to the measurements of *Neumann et al.* [2009] are shown by the gray area.

2.6 Conclusion

In this paper, we derived the macroscopic equivalent modeling of the heat and water vapor transfer through snow from its description at the pore scale using the homogenization of multiple scale expansions [*Bensoussan et al.*, 1978; *Sanchez-Palencia*, 1980; *Auriault*, 1991; *Auriault et al.*, 2009]. In contrast with more phenomenological models, the homogenization method provides the exact expression of the effective properties and the source terms (i.e. the mass-transfer coefficient) at the macroscopic scale. The formulation of the macroscopic equivalent modeling is driven by the order of magnitude of the dimensionless numbers that characterize the physics at the pore scale, and thus constitute the domain of validity of the modeling.

In the most general case, the macroscopic modeling is described by two coupled equations of heat and vapor transfer including a source term. These source terms arise from the phase changes at the ice-air interface. The upscaling process clearly shows that these phase changes do not appear in the definition of the effective properties (effective diffusion, effective thermal conductivity, etc), in contradiction with some macroscopic models presented in the literature [*Sun et al.*, 1999; *Boone and Etchevers*, 2001].

The precision and the robustness of the obtained macroscopic equivalent modeling were evaluated by comparing the results of numerical simulations of the heat and the water vapor transfer through a snow layer obtained in the case of a fine scale modeling (i.e., taking into account all the heterogeneities) and in the case of the corresponding macroscopic modeling, for temperature gradients ranging from 50 to 250 $\mathrm{K\,m^{-1}}$. This study points out that (i) the temperature field is estimated by the obtained macroscopic modeling within a smaller error than the water vapor density field (both errors increase with increasing temperature gradients) and (ii) the macroscopic source term of heat and vapor is required in the macroscopic modeling especially for snow which experiences large temperature gradients.

Finally, the effective diffusion tensor involved in the macroscopic modeling has been computed using the result of the homogenization method on 3D images of different snow types. The effective diffusion coefficients of snow are lower than the one of air, decrease gradually with increasing density, and exhibit a slight anisotropy for some snow samples. The self-consistent formula provides a good estimation of our coefficients with respect to the snow density. Our theoretical developments and numerical results indicate that the vapor diffusion is not enhanced in snow.

Chapter

3 Influence of the convection on the macroscopic modeling of heat and water vapor transfer in dry snow

Contents

3.1 Introduction

At the grain scale, air convection can occur through the pore spaces and can be divided in two types: the forced convection and the natural convection. The first one is due to wind at the surface of the snowpack that creates a "wind-pumping" ventilation through the snow layers, especially through those close to the surface [*Albert and McGilvary*, 1992; *Albert and Shultz*, 2002]. The second one is created by temperature gradients through air and seems potentially more important for snow that exhibits large pores [*Sturm and Johnson*, 1991]. Despite the fact that the relative importance of both convections through snow is still controversial, it is recognized that such processes might significantly impact snow metamorphism [e.g. *Akitaya*, 1974; *Powers et al.*, 1985; *Brun and Touvier*, 1987; *Albert et al.*, 2004]. From a modeling point of view, *Albert and McGilvary* [1992] presented a phenomenological description of the heat and mass transport at macro-scale coupled to a forced convection to investigate the influence of such an air flow on the temperature and vapor profiles. Based on their results, *Lehning et al.* [2002a] improved their snowpack model to take into account the effect of wind-pumping on the heat transport by parameterizing the effective thermal conductivity.

In this chapter, following the work of *Albert and McGilvary* [1992], we investigated the influence of air convection (forced convection) on the macroscopic model of heat and vapor transport presented in Chapter 2. For that, the macroscopic models are derived from the physics at the pore scale using the homogenization. As in Chapter 2, 2D numerical simulations are performed in order to illustrate and evaluate the proposed models.

3.2 Derivation of the macroscopic modeling

3.2.1 Description of the physics at the microscopic scale

As in Chapter 2, let us assume that a snow layer can be represented by a collection of spatially periodic representative elementary volumes (REV) with a characteristic length l, such that the scale parameter $\varepsilon = l/L \ll 1$ (Figure 7.1). Within the REV of snow Ω, the domains occupied by ice and air are denoted by Ω_i and Ω_a respectively. The interface of ice is denoted by Γ and $\mathbf{n_i}$ is the outward unit vector of Ω_i. The phenomena considered at micro-scale are now (i) the steady state air flow within the pores. The air velocity in

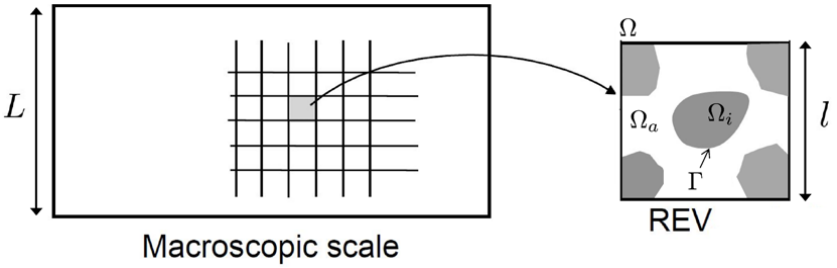

Figure 3.1: Macroscopic sample, i.e. a snow layer, and Representative Elementary Volume (REV) with period Ω.

the pores is typically lower than 0.1 $\mathrm{m\,s^{-1}}$ [*Albert and McGilvary*, 1992; *Albert*, 1993], and thus the Mach number defined as the ratio of the air velocity over the sound velocity is much smaller than 0.3. Consequently, at the pore scale, the air flow is assumed to be incompressible and is described by the Navier-Stokes equation; (ii) the heat transfer by conduction in ice and by conduction-convection in air; (iii) the water vapor transfer by diffusion-convection in air; (iv) the sublimation of ice and deposition of vapor at the ice-pore interface. In what follows, the subscripts $(_i)$ or $(_a)$ are related to quantities defined in Ω_i and Ω_a, respectively. Assuming that the properties of air and ice are isotropic, these physical phenomena at the pore scale are described by the following set of equations:

$$\rho_a \mathbf{v}_a \,\mathbf{grad}\, \mathbf{v}_a = \mu_a \Delta \mathbf{v}_a - \mathbf{grad}\, p_a \quad \text{in } \Omega_a \tag{3.1}$$

$$\mathrm{div}\, \mathbf{v}_a = 0 \quad \text{in } \Omega_a \tag{3.2}$$

$$\rho_i C_i \frac{\partial T_i}{\partial t} - \mathrm{div}(\kappa_i \,\mathbf{grad}\, T_i) = 0 \quad \text{in } \Omega_i \tag{3.3}$$

$$\rho_a C_a \frac{\partial T_a}{\partial t} + \rho_a C_a \mathbf{v}_a \cdot \mathbf{grad}\, T_a - \mathrm{div}(\kappa_a \,\mathbf{grad}\, T_a) = 0 \quad \text{in } \Omega_a \tag{3.4}$$

$$\frac{\partial \rho_v}{\partial t} + \mathbf{v}_a \cdot \mathbf{grad}\, \rho_v - \mathrm{div}(D_v \,\mathbf{grad}\, \rho_v) = 0 \quad \text{in } \Omega_a \tag{3.5}$$

$$T_i = T_a \quad \text{on } \Gamma \tag{3.6}$$

$$\mathbf{v_a} \cdot \mathbf{t_i} = 0 \quad \text{on } \Gamma \tag{3.7}$$

$$\rho_a(\mathbf{w} - \mathbf{v_a}) \cdot \mathbf{n_i} = \rho_i \mathbf{w} \cdot \mathbf{n_i} \quad \text{on } \Gamma \tag{3.8}$$

$$\kappa_i \,\mathbf{grad}\, T_i \cdot \mathbf{n_i} - \kappa_a \,\mathbf{grad}\, T_a \cdot \mathbf{n_i} = L_{sg} \mathbf{w} \cdot \mathbf{n_i} \quad \text{on } \Gamma \tag{3.9}$$

$$D_v \,\mathbf{grad}\, \rho_v \cdot \mathbf{n_i} = (\rho_i - \rho_v) \mathbf{w} \cdot \mathbf{n_i} \quad \text{on } \Gamma \tag{3.10}$$

where t is the time (s), $\mathbf{v}_a$ is the air velocity ($\mathrm{m\,s^{-1}}$), p_a is the air pressure (Pa), μ_a is the air dynamic viscosity ($\mathrm{Pa\,s^{-1}}$), T is the temperature (K), κ is the thermal conductivity ($\mathrm{W\,m^{-1}\,K^{-1}}$), ρ is the density ($\mathrm{kg\,m^{-3}}$), C is the specific heat capacity ($\mathrm{J\ kg^{-1}\,K^{-1}}$), L_{sg} is the latent heat of sublimation ($\mathrm{J\,m^{-3}}$), $\mathbf{w}$ is the interface growth velocity ($\mathrm{m\ s^{-1}}$), ρ_v is the partial density of water vapor in air ($\mathrm{kg\,m^{-3}}$), D_v is the water vapor diffusion coefficient in air ($\mathrm{m^2\,s^{-1}}$) and, div and **grad** are the divergence and gradient operators with respect to the physical space variable $\mathbf{X}$ respectively. At the interface, the heat and mass transfer are still coupled through the normal interface growth velocity $w_n = \mathbf{w} \cdot \mathbf{n_i}$ (Eq. (3.9) and (3.10)), which is given by the Hertz-Knudsen equation:

$$w_n = \mathbf{w} \cdot \mathbf{n_i} = \frac{1}{\beta} \left[\frac{\rho_v - \rho_{vs}(T_a)}{\rho_{vs}(T_a)} - d_0 K \right] \quad \text{on } \Gamma \tag{3.11}$$

where β is the interface kinetic coefficient ($\mathrm{s\,m^{-1}}$), ρ_{vs} is the saturation water vapor density in air ($\mathrm{kg\,m^{-3}}$), d_0 is the capillary length (m), K is the interface mean curvature ($\mathrm{m^{-1}}$). w_n is positive when the ice surface grows and negative when the ice surface sublimates. The saturation vapor density ρ_{vs} is given by the Clausius-Clapeyron's law:

$$\rho_{vs}(T_a) = \rho_{vs}^{\mathrm{ref}}(T^{\mathrm{ref}}) \exp\left[\frac{L_{sg} m}{\rho_i k} \left(\frac{1}{T^{\mathrm{ref}}} - \frac{1}{T_a} \right) \right] \tag{3.12}$$

The reference values T^{ref} and $\rho_{vs}^{\text{ref}}(T^{\text{ref}})$ are equal here to 273 K and 2.173×10^{-3} kg m^{-3} respectively. In what follows, for the sake of simplicity, we will suppose that all material properties (μ_a, ρ, C, κ, D_v, β, m) do not depend on the temperature.

3.2.2 Dimensionless pore scale description: normalization

As in Chapter 2, following the methodology presented in *Auriault* [1991], we introduce in the set of Eq. (3.1)-(3.10) the following representation of all dimensional variables φ: $\varphi = \varphi_c\varphi^*$. The subscript 'c' denotes characteristic quantities (constant) and the superscript '*' denotes the dimensionless microscopic variables. Note that the microscopic length l is chosen as the characteristic length ($l_c = l$), i.e. the so-called microscopic point of view is adopted [*Auriault*, 1991]. Consequently, the formal dimensionless set that describes the physics at the pore scale is written:

$$[\text{Re}]\,\rho_a^*\mathbf{v_a}^*\,\mathbf{grad}^*\,\mathbf{v_a}^* = \mu_a^*\Delta^*\mathbf{v_a}^* - [\text{Q}]\,\mathbf{grad}^*\,p_a^* \quad \text{in } \Omega_a \tag{3.13}$$

$$\text{div}^*\,\mathbf{v_a}^* = 0 \quad \text{in } \Omega_a \tag{3.14}$$

$$\left[\text{F}_\text{i}^\text{T}\right]\rho_i^*C_i^*\frac{\partial T_i^*}{\partial t^*} - \text{div}^*(\kappa_i^*\mathbf{grad}^*T_i^*) = 0 \quad \text{in } \Omega_i \tag{3.15}$$

$$\left[\text{F}_\text{a}^\text{T}\right]\rho_a^*C_a^*\frac{\partial T_a^*}{\partial t^*} + \left[\text{Pe}^\text{T}\right]\rho_a^*C_a^*\mathbf{v_a}^*\cdot\mathbf{grad}^*\,T_a^* - \text{div}^*(\kappa_a^*\mathbf{grad}^*T_a^*) = 0 \quad \text{in } \Omega_a \tag{3.16}$$

$$[\text{F}_\text{a}^\rho]\,\frac{\partial\rho_v^*}{\partial t^*} + [\text{Pe}^\rho]\,\mathbf{v_a}^*\cdot\mathbf{grad}^*\,\rho_v^* - \text{div}^*(D_v^*\mathbf{grad}^*\rho_v^*) = 0 \quad \text{in } \Omega_a \tag{3.17}$$

$$T_i^* = T_a^* \quad \text{on } \Gamma \tag{3.18}$$

$$\mathbf{v_a}^*\cdot\mathbf{t_i} = 0 \quad \text{on } \Gamma \tag{3.19}$$

$$\rho_a^*([\text{M}]\,\mathbf{w}^* - \mathbf{v_a}^*)\cdot\mathbf{n_i} = -\,[\text{N}]\,\rho_i^*\mathbf{w}^*\cdot\mathbf{n_i} \quad \text{on } \Gamma \tag{3.20}$$

$$[\text{K}]\,\kappa_i^*\mathbf{grad}^*T_i^*\cdot\mathbf{n_i} - \kappa_a^*\mathbf{grad}^*T_a^*\cdot\mathbf{n_i} = [\text{H}]\,L_{sg}^*\mathbf{w}^*\cdot\mathbf{n_i} \quad \text{on } \Gamma \tag{3.21}$$

$$D_v^*\mathbf{grad}^*\rho_v^*\cdot\mathbf{n_i} = [\text{W}]\,\rho_i^*\mathbf{w}^*\cdot\mathbf{n_i} \quad \text{on } \Gamma \tag{3.22}$$

This dimensionless pore scale description introduces 12 dimensionless numbers which characterize the intensity of the physical phenomena at the pore scale. These dimensionless numbers are defined as:

$$[\text{Re}] = \frac{l v_{a_c}\rho_{a_c}}{\mu_{a_c}}, \quad [\text{Q}] = \frac{p_{a_c}l}{\mu_{a_c}v_{a_c}} \tag{3.23}$$

$$\left[\text{F}_\text{i}^\text{T}\right] = \frac{l^2\rho_{i_c}C_{i_c}}{t_c\kappa_{i_c}}, \quad \left[\text{F}_\text{a}^\text{T}\right] = \frac{l^2\rho_{a_c}C_{a_c}}{t_c\kappa_{a_c}}, \quad [\text{F}_\text{a}^\rho] = \frac{l^2}{D_{v_c}t_c} \tag{3.24}$$

$$\left[\text{Pe}^\text{T}\right] = \frac{l\rho_{a_c}C_{a_c}v_{a_c}}{\kappa_{a_c}} = [\text{Pr}]\,[\text{Re}]\,, \quad [\text{Pe}^\rho] = \frac{v_{a_c}l}{D_{v_c}} = [\text{Sc}]\,[\text{Re}] \tag{3.25}$$

$$[\text{M}] = \frac{w_{n_c}}{v_{a_c}}, \quad [\text{N}] = \frac{\rho_{i_c}}{\rho_{a_c}} \tag{3.26}$$

$$[\text{K}] = \frac{\kappa_{i_c}}{\kappa_{a_c}}, \quad [\text{H}] = \frac{lL_{sg_c}w_{n_c}}{\kappa_{a_c}T_{a_c}}, \quad [\text{W}] = \frac{l\rho_{i_c}w_{n_c}}{D_{v_c}\rho_{v_c}}. \tag{3.27}$$

In the above set of equations, [Re] is the classical pore Reynolds number that characterizes the intensity of the flow in Ω_a, and [Q] is a dimensionless number that measures the ratio

Table 3.1: Characteristic values of the properties evaluated at -10°C from the literature [*Massman*, 1998; *Kaempfer and Plapp*, 2009].

Symbol	Description	Value, Reference
T_{i_c}, T_{a_c}	Temperature of ice, air	263 K
κ_{i_c}	Heat conductivity of ice	2.3 $\mathrm{W\,m^{-1}\,K^{-1}}$
κ_{a_c}	Heat conductivity of air	0.024 $\mathrm{W\,m^{-1}\,K^{-1}}$
C_{i_c}	Specific heat capacity of ice	2000 $\mathrm{J\,kg^{-1}\,K^{-1}}$
C_{a_c}	Specific heat capacity of air	1005 $\mathrm{J\,kg^{-1}\,K^{-1}}$
L_{sg_c}	Latent heat of sublimation of ice	2.60×10^9 $\mathrm{J\,m^{-3}}$
w_{n_c}	Normal interface velocity	10^{-14} to 10^{-8} $\mathrm{m\,s^{-1}}$
D_{v_c}	Water vapor diffusion coefficient in air	2.036×10^{-5} $\mathrm{m^2\,s^{-1}}$
ρ_{v_c}	Water vapor density in air	0.002 $\mathrm{kg\,m^{-3}}$
ρ_{i_c}	Ice density	917 $\mathrm{kg\,m^{-3}}$
ρ_{a_c}	Air density	1.335 kg $\mathrm{m^{-3}}$
l	Microscopic length	5×10^{-4} m
L	Macroscopic length	0.1 m
μ_{a_c}	Dynamic viscosity of air	1.7×10^{-5} $\mathrm{Pa\,s^{-1}}$
p_{a_c}	Air pressure	1.01325×10^5 Pa
v_{a_c}	Air velocity	10^{-8} to 10^{-3} $\mathrm{m\,s^{-1}}$

between the pressure and the viscous stress in Ω_a. As defined in Chapter 2, dimensionless numbers $\left[\mathrm{F_i^T}\right]$ and $\left[\mathrm{F_a^T}\right]$ correspond to the inverses of the Fourier numbers in Ω_i and Ω_a, respectively and $[\mathrm{F_a^\rho}]$ is an analogous inverse Fourier number for the transient water vapor transfer by diffusion in Ω_a. $\left[\mathrm{Pe^T}\right]$ and $[\mathrm{Pe}^\rho]$ are the Péclet numbers associated to the thermal and water vapor transfer in Ω_a. They measure the ratio between the transfer by convection over the transfer by conduction or diffusion. Let us remark that $\left[\mathrm{Pe^T}\right]$ can be expressed as the product of the Reynolds number [Re] and the Prandt number [Pr] equal to $(\mu_{a_c} C_{a_c})/\kappa_{a_c} \sim 0.71$. Similarly, $[\mathrm{Pe}^\rho]$ is written as the product of the Reynolds number [Re] and the Schmidt number [Sc] equal to $\mu_{a_c}/(\rho_{a_c} D_{v_c}) \sim 0.63$. Dimensionless numbers [M], [N], [K], [H] and [W] characterize the physical phenomena at the ice grain interface. In particular [M], and [N] characterize the continuity of the mass fluxes at the ice-air interface. As seen in Chapter 2, [H] characterizes the ratio between the heat flux induced by phase changes and the heat flux from heat conduction in the air phase. Similarly, [W] is defined as the ratio between the vapor flux from phase changes and the vapor flux from vapor diffusion in the air phase.

3.2.3 Estimation of the dimensionless numbers

The next step of the homogenization process consists at estimating the above 12 dimensionless numbers with respect to the scale parameter $\varepsilon = l/L$. In practice, l and L correspond to the order of magnitude of the ice grain size and the thickness of the snow layer, respectively. As in Chapter 2, for the following estimations, we assumed that $l \approx 5.10^{-4}$ m and $L \approx 0.1$ m, leading to $\varepsilon = 5.10^{-3}$. The characteristic time t_c is the time over which we intend to describe the heat and water vapor transfer through the snowpack, i.e. the characteristic time of observation. As in *Auriault and Adler* [1995] and *Auriault et al.* [2009], we can introduce two characteristics times: t^{di} and t^{co} associated with the diffusion/conduction and the convection phenomena, respectively. There are defined as:

$$t^{\mathrm{di}} = \mathcal{O}(L^2/\alpha_{i_c}) = \mathcal{O}(L^2/\alpha_{i_a}) = \mathcal{O}(L^2/D_{v_c}) \tag{3.28}$$

$$t^{\mathrm{co}} = \mathcal{O}(L/v_{a_c}) \tag{3.29}$$

where $\alpha_{i_c} = \kappa_{i_c}/(C_{i_c}\rho_{i_c})$ and $\alpha_{a_c} = \kappa_{a_c}/(C_{a_c}\rho_{a_c}\ )$ are the thermal diffusitivity of the ice and the air phase. Using these definitions, the Péclet numbers $\left[\mathrm{Pe}^{\mathrm{T}}\right]$ and $[\mathrm{Pe}^{\rho}]$, that characterize the ratio between the transfer by convection over the transfer by conduction or diffusion at the pore scale, can be rewritten as:

$$\left[\mathrm{Pe}^{\mathrm{T}}\right] = [\mathrm{Pe}^{\rho}] = \mathcal{O}(\varepsilon\ t^{\mathrm{co}}/t^{\mathrm{di}}) \tag{3.30}$$

All the characteristic values of each variable arising in the dimensionless numbers (3.23)-(3.27) are summarized in Table 2.1. The time t_c, the air velocity v_{a_c}, and the normal interface velocity w_{n_c} are likely to vary and different estimations are considered depending on their values.

Dimensionless numbers depending on t_c and v_{a_c} The inverses of Fourier numbers $\left[\mathrm{F}_{\mathrm{i}}^{\mathrm{T}}\right]$, $\left[\mathrm{F}_{\mathrm{a}}^{\mathrm{T}}\right]$, $[\mathrm{F}_{\mathrm{a}}^{\rho}]$ depend on the order of the characteristic time t_c, which can be the characteristic time of diffusion/conduction or convection. The characteristic time of convection is related to the characteristic intensity of the air flow v_{a_c} (Eq. (3.29)). The Péclet numbers $\left[\mathrm{Pe}^{\mathrm{T}}\right]$ and $[\mathrm{Pe}^{\rho}]$ and the pore Reynolds number [Re] are the same order of magnitude (since the Prandt and Schmidt numbers are both of the order of one) and also depend on v_{a_c}. This variable corresponds to an averaged value $\langle v_a \rangle$ over the REV. During wind pumping, the air velocity within a snow layer varies typically between 10^{-7} to 10^{-1} m s^{-1} [*Albert and McGilvary*, 1992; *Albert*, 1993]. Taking into account these results, Figure 3.2 shows that [Re], $\left[\mathrm{Pe}^{\mathrm{T}}\right]$ and $[\mathrm{Pe}^{\rho}]$ can take different order of magnitude according to the value of v_{a_c}. Consequently, three cases can be considered:

- Case A: when $v_{a_c} \lesssim 10^{-5}$ m s^{-1}, diffusion dominates at the macroscopic scale: $t^{\mathrm{di}} = \varepsilon t^{\mathrm{co}}$ ($t^{\mathrm{di}} \ll t^{\mathrm{co}}$). To investigate this case, we use the diffusion characteristic time as our characteristic time: $t_c = t^{\mathrm{di}}$. This means that $\left[\mathrm{F}_{\mathrm{i}}^{\mathrm{T}}\right] = \left[\mathrm{F}_{\mathrm{a}}^{\mathrm{T}}\right] = [\mathrm{F}_{\mathrm{a}}^{\rho}] = \mathcal{O}\left(\varepsilon^2\right)$ and $[\mathrm{Re}] = \left[\mathrm{Pe}^{\mathrm{T}}\right] = [\mathrm{Pe}^{\rho}] \leqslant \mathcal{O}\left(\varepsilon^2\right)$;

- Case B: when 10^{-5} m s$^{-1} \lesssim v_{a_c} \lesssim 10^{-3}$ m s^{-1}, diffusion and convection are the same order of magnitude at the macroscopic scale: $t^{\mathrm{di}} = t^{\mathrm{co}}$. To investigate this case, we use $t_c = t^{\mathrm{di}} = t^{\mathrm{co}}$ as our characteristic time. This means that $\left[\mathrm{F}_{\mathrm{i}}^{\mathrm{T}}\right] = \left[\mathrm{F}_{\mathrm{a}}^{\mathrm{T}}\right] = [\mathrm{F}_{\mathrm{a}}^{\rho}] = \mathcal{O}(\varepsilon^2)$ and $[\mathrm{Re}] = \left[\mathrm{Pe}^{\mathrm{T}}\right] = [\mathrm{Pe}^{\rho}] = \mathcal{O}(\varepsilon)$;
- Case C: when 10^{-3} m s$^{-1} \lesssim v_{a_c} \lesssim 10^{-1}$ m s^{-1}, convection dominates at the macroscopic scale: $t^{\mathrm{di}} = \varepsilon^{-1} t^{\mathrm{co}}$ ($t^{\mathrm{di}} \gg t^{\mathrm{co}}$). To investigate this case, we use the convection characteristic time as our characteristic time: $t_c = t^{\mathrm{co}}$. This means that $\left[\mathrm{F}_{\mathrm{i}}^{\mathrm{T}}\right] = \left[\mathrm{F}_{\mathrm{a}}^{\mathrm{T}}\right] = [\mathrm{F}_{\mathrm{a}}^{\rho}] = \mathcal{O}(\varepsilon)$ and $[\mathrm{Re}] = \left[\mathrm{Pe}^{\mathrm{T}}\right] = [\mathrm{Pe}^{\rho}] = \mathcal{O}(1)$.

The fluid flow is also characterized by the dimensionless number [Q]. It can be shown [*Auriault*, 1991] by following a physical reasoning that $[\mathrm{Q}] = \mathcal{O}(\varepsilon^{-1})$.

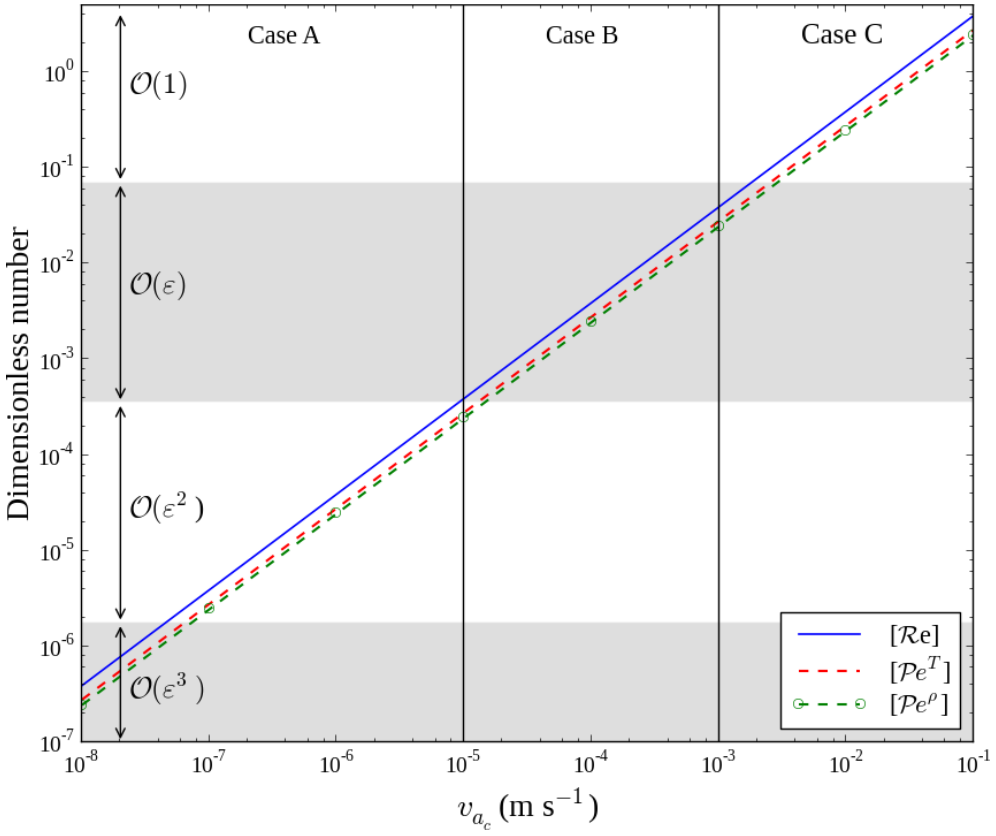

Figure 3.2: Estimation of dimensionless numbers [Re], $\left[\mathrm{Pe}^{\mathrm{T}}\right]$, and $[\mathrm{Pe}^{\rho}]$ versus the characteristic air velocity v_{a_c}, from characteristic values given in Table 3.1.

Dimensionless numbers depending on w_{n_c} As in Chapter 2, dimensionless numbers [H] and [W] depend on the intensity of the interface normal growth velocity w_{n_c}, which corresponds to an averaged value $\langle w_n \rangle$ over the REV. In practice, w_n varies widely locally inside a REV, depending on the temperature gradient, temperature, kinetic and curvature effects... Nevertheless, several experimental and numerical studies [*Colbeck*, 1983a; *Fukuzawa and Akitaya*, 1993; *Sturm et al.*, 1997; *Kamata and Sato*, 2006; *Flin and Brzoska*, 2008; *Libbrecht and Rickerby*, 2011] have shown w_n values ranging from 0 to 10^{-9}

m s^{-1} for temperature gradients between 0 and 500 K m^{-1}. Thus several cases can be considered depending on the order of w_{n_c} [*Calonne et al.*, 2014b]:

- Case 0: when $w_{n_c} \approx 10^{-10}$ m s^{-1}, $[\mathrm{H}] = \mathcal{O}(\varepsilon^2)$ and $[\mathrm{W}] = \mathcal{O}(\varepsilon)$;
- Case 1: when $w_{n_c} \approx 10^{-11}$ m s^{-1}, $[\mathrm{H}] = \mathcal{O}(\varepsilon^2)$ and $[\mathrm{W}] = \mathcal{O}(\varepsilon^2)$;
- Case 2: when $w_{n_c} \approx 10^{-12}$ m s^{-1}, $[\mathrm{H}] = \mathcal{O}(\varepsilon^3)$ and $[\mathrm{W}] = \mathcal{O}(\varepsilon^2)$;
- Case 3: when $w_{n_c} \lesssim 10^{-13}$ m s^{-1}, $[\mathrm{H}] \leqslant \mathcal{O}(\varepsilon^3)$ and $[\mathrm{W}] \leqslant \mathcal{O}(\varepsilon^3)$;

As in Chapter 2, the Case 0 will not be investigated in the following.

Other dimensionless numbers Finally, at the ice-pore interface, we have $[\mathrm{K}] = \mathcal{O}(1)$ and $[\mathrm{N}] = \mathcal{O}(\varepsilon^{-1})$. The last dimensionless number [M] is defined as the ratio of w_{n_c} and v_{a_c}. Consequently, the order of magnitude of [M] depends simultaneously on the Case A, B, C and the Case 1, 2, 3 under consideration.

To conclude, 9 different cases must be considered a priori. The order of magnitude of all the dimensionless numbers corresponding to these different cases are summarized in Figure 3.3. However, it can be shown that only three cases are of interest: Case A1, B1, and C1. The other ones can be viewed as particular cases of these three main cases. Moreover, in Case A1, when $[\mathrm{Re}] = \left[\mathrm{Pe}^{\mathrm{T}}\right] = [\mathrm{Pe}^{\rho}] \leqslant \mathcal{O}(\varepsilon^2)$, the intensity of air flow is very small, and it can be shown that convection effects on the macroscopic heat and mass transfer are negligible. Thus, Case A1 corresponds to the local physics already studied in Chapter 2. We have shown that at the macroscopic scale, both heat and mass transfer are described by a classical conduction (or diffusion) equation. The Case B1 and Case C1 that correspond to the case of moderate and strong convection, respectively, are investigated in the following.

3.2.4 Asymptotic analysis

The next step is to introduce multiple-scale coordinates [*Bensoussan et al.*, 1978; *Sanchez-Palencia*, 1980; *Auriault*, 1991]. The two characteristic lengths L and l introduce two dimensionless space variables, $\mathbf{x}^* = \mathbf{X}/L$ and $\mathbf{y}^* = \mathbf{X}/l$, where $\mathbf{X}$ is the physical space variable. The macroscopic (or slow) dimensionless space variable $\mathbf{x}^*$ is related to the microscopic (or fast) dimensionless space variable $\mathbf{y}^*$ by $\mathbf{x}^* = \varepsilon \mathbf{y}^*$. When l is used as the characteristic length, the dimensionless derivative operator $\mathbf{grad}^*$ becomes $(\mathbf{grad}_{y^*} + \varepsilon \mathbf{grad}_{x^*})$, where the subscripts $_{x^*}$ and $_{y^*}$ denote the derivatives with respect to the variables $\mathbf{x}^*$ and $\mathbf{y}^*$, respectively. Following the multiple-scale expansion technique [*Bensoussan et al.*, 1978; *Sanchez-Palencia*, 1980; *Auriault*, 1991], the air velocity ${\mathbf{v_a}}^*$, the air pressure p_a^*, the ice temperature T_i^*, the air temperature T_a^* and the water vapor ρ_v^* are sought in the form of asymptotic expansions of powers of ε:

$$\varphi^*(\mathbf{x}^*, \mathbf{y}^*, t) = \varphi^{*(0)}(\mathbf{x}^*, \mathbf{y}^*, t) + \varepsilon \varphi^{*(1)}(\mathbf{x}^*, \mathbf{y}^*, t) + \varepsilon^2 \varphi^{*(2)}(\mathbf{x}^*, \mathbf{y}^*, t) + ... \tag{3.31}$$

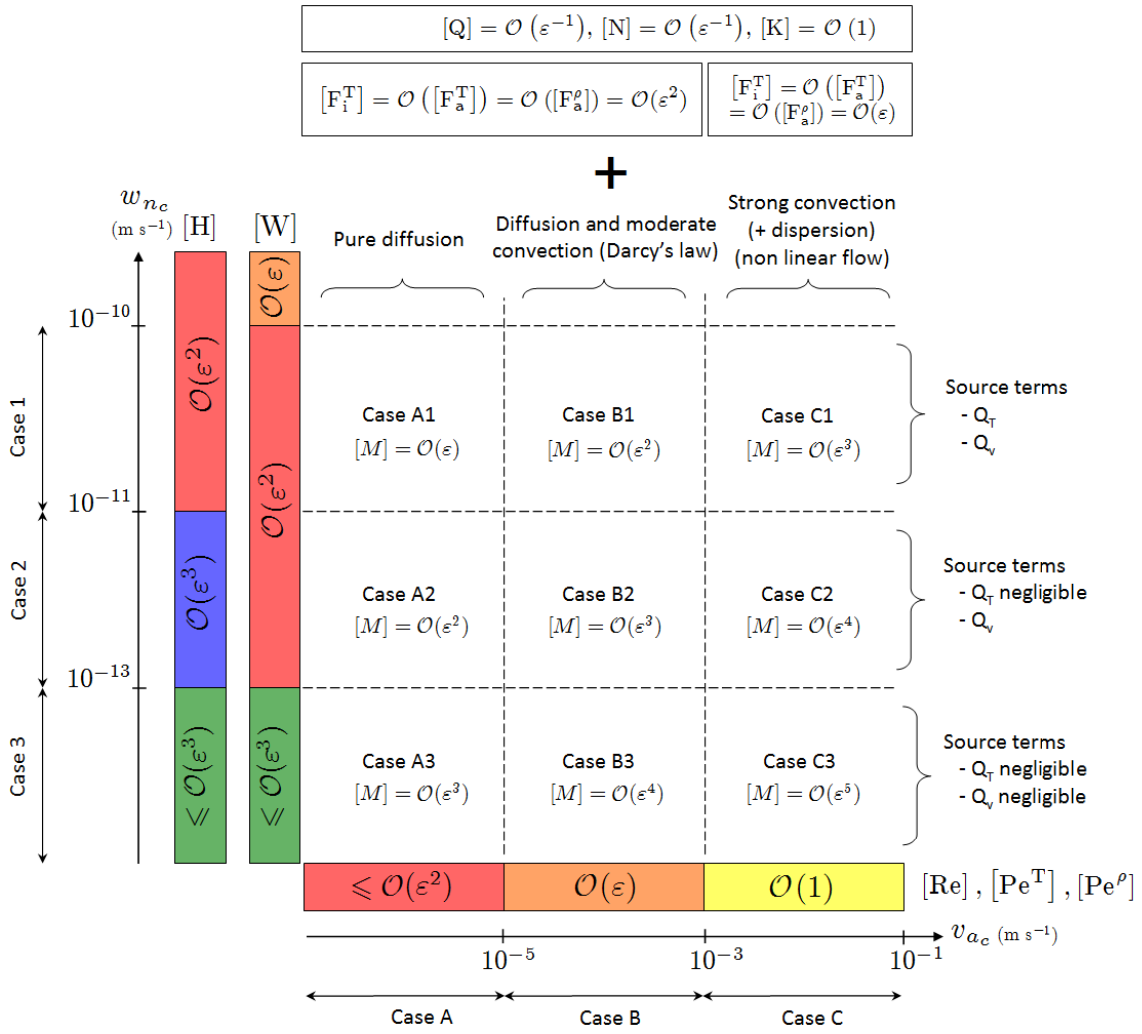

Figure 3.3: Synthesis of the different cases of dimensionless estimations, corresponding to different models, depending on the characteristic values considered in the description of the physics at the pore scale.

where $\varphi^* = \mathbf{v_a}^*, p_a^*, T_i^*, T_a^*, \rho_v^*$ and the corresponding $\varphi^{*(i)}$ are periodic functions of period Ω with respect to the space variable $\mathbf{y}^*$. Substituting these expansions in the set (3.13)-(3.22) gives, by identification of like powers of ε, successive boundary value problems to be investigated. All the details concerning this asymptotic analysis in the Case B1 and the Case C1 are presented in Appendix B.

3.2.5 Macroscopic equivalent descriptions

According to the order of magnitude of the dimensionless numbers, the heat and water vapor transfer through the snowpack are described by the following three main different macroscopic models (A1, B1 and C1).

3.2.5.1 Case A1 (A2 and A3): conduction/diffusion + source terms

In the Case A1, convection effects on the heat and water vapor transfers are negligible at the macroscopic scale. Thus, as in the Chapter 2, these transfers are described by the following set of equations (A.48, A.51):

$$(\rho C)^{\text{eff}} \frac{\partial T^{(0)}}{\partial t} - \text{div}(\mathbf{k}^{\text{eff}} \mathbf{grad}\ T^{(0)}) = \text{SSA}_{\text{V}} L_{sg} w_n^{(0)} \tag{3.32}$$

$$\phi \frac{\partial \rho_v^{(0)}}{\partial t} - \text{div}(\mathbf{D}^{\text{eff}} \mathbf{grad}\ \rho_v^{(0)}) = -\text{SSA}_{\text{V}} \rho_i w_n^{(0)} \tag{3.33}$$

where $w_n^{(0)}$ is given by the Hertz-Knudsen equation (A.47) and the Clausius Clapeyron's law (A.43)

$$w_n^{(0)} = \frac{1}{\beta} \left[\frac{\rho_v^{(0)} - \rho_{vs}^{(0)}(T^{(0)})}{\rho_{vs}^{(0)}(T^{(0)})} - d_0 K \right] \tag{3.34}$$

$$\rho_{vs}^{(0)}(T^{(0)}) = \rho_{vs}^{\text{ref}} \exp\left[\frac{L_{sg} m}{\rho_i k} \left(\frac{1}{T^{\text{ref}}} - \frac{1}{T^{(0)}} \right) \right] \tag{3.35}$$

and where $T^{(0)}$ is the macroscopic temperature, $\rho_v^{(0)}$ is the macroscopic vapor density in the air volume, ϕ is the porosity, $\text{SSA}_{\text{V}} = |\Gamma|/|\Omega|$ is the specific surface area, $(\rho C)^{\text{eff}}$ is the effective thermal capacity (A.49), $\mathbf{k}^{\text{eff}}$ is the effective thermal conductivity tensor (A.50) and $\mathbf{D}^{\text{eff}}$ is the effective diffusion tensor (A.52). These effective properties are defined as:

$$(\rho C)^{\text{eff}} = (1-\phi)\rho_i C_i + \phi \rho_a C_a \tag{3.36}$$

$$\mathbf{k}^{\text{eff}} = \frac{1}{|\Omega|} \left(\int_{\Omega_{\text{a}}} \kappa_{\text{a}} (\mathbf{grad}\ \mathbf{t}_a + \mathbf{I}) \text{d}\Omega + \int_{\Omega_{\text{i}}} \kappa_{\text{i}} (\mathbf{grad}\ \mathbf{t}_i + \mathbf{I}) \text{d}\Omega \right) \tag{3.37}$$

$$\mathbf{D}^{\text{eff}} = \frac{1}{|\Omega|} \int_{\Omega_a} D_v (\mathbf{grad}\ \mathbf{g}_v + \mathbf{I}) \text{d}\Omega \tag{3.38}$$

where $\mathbf{t}_a$ and $\mathbf{t}_i$ are two periodic vectors solution of the following boundary value problem over the REV (A.20)-(A.24):

$$\text{div}(\kappa_i (\mathbf{grad}\ \mathbf{t}_i + \mathbf{I})) = 0 \quad \text{in } \Omega_i \tag{3.39}$$

$$\text{div}(\kappa_a (\mathbf{grad}\ \mathbf{t}_a + \mathbf{I})) = 0 \quad \text{in } \Omega_a \tag{3.40}$$

$$\mathbf{t}_i = \mathbf{t}_a \quad \text{on } \Gamma \tag{3.41}$$

$$(\kappa_i (\mathbf{grad}\ \mathbf{t}_i + \mathbf{I}) - \kappa_a (\mathbf{grad}\ \mathbf{t}_a + \mathbf{I})) \cdot \mathbf{n_i} = 0 \quad \text{on } \Gamma \tag{3.42}$$

$$\frac{1}{|\Omega|} \int_{\Omega} (\mathbf{t}_{\text{a}} + \mathbf{t}_{\text{i}}) \text{d}\Omega = \mathbf{0} \tag{3.43}$$

and where $\mathbf{g}_v$ is a periodic vector solution of the following boundary value problem over the REV (A.35)-(A.37):

$$\text{div}(D_v (\mathbf{grad}\ \mathbf{g}_v + \mathbf{I})) = 0 \quad \text{in } \Omega_a \tag{3.44}$$

$$D_v (\mathbf{grad}\ \mathbf{g}_v + \mathbf{I}) \cdot \mathbf{n_i} = 0 \quad \text{on } \Gamma \tag{3.45}$$

$$\frac{1}{|\Omega|} \int_{\Omega_a} \mathbf{g}_v \text{d}\Omega = \mathbf{0} \tag{3.46}$$

In the Case A1, the heat and water vapor transfers are described by two coupled equations, including a source term of heat $Q_T = \mathrm{SSA_V} L_{sg} w_n^{(0)}$, and a source term of vapor $Q_v = -\mathrm{SSA_V} \rho_i w_n^{(0)}$. In the Case A2, the source term Q_T arising in the heat transfer equation is negligible. In the Case A3, the sources terms Q_T and Q_v arising in both equations are negligible.

3.2.5.2 Case B1 (B2 and B3): conduction/diffusion and moderate convection + source terms

In that case, the heat and water vapor transfer are described by two coupled equations including convection effects. Returning in dimensional variables, the macroscopic model (B.27, B.28, B.50, B.64) is summarized as follows:

$$\mathrm{div}_x \langle \mathbf{v}_a^{(0)} \rangle + \left(1 - \frac{\rho_i}{\rho_a}\right) \mathrm{SSA}_V \; w_n^{(0)} = 0 \tag{3.47}$$

$$\langle \mathbf{v}_a^{(0)} \rangle = -\frac{\mathbf{K}^{\mathrm{eff}}}{\mu_a} \mathbf{grad} \; p_a^{(0)} \tag{3.48}$$

$$(\rho C)^{\mathrm{eff}} \frac{\partial T^{(0)}}{\partial t} + \rho_a C_a \langle \mathbf{v}_a^{(0)} \rangle \cdot \mathbf{grad} T^{(0)} - \mathrm{div}(\mathbf{k}^{\mathrm{eff}} \mathbf{grad} \; T^{(0)}) = \mathrm{SSA_V} L_{sg} w_n^{(0)} \tag{3.49}$$

$$\phi \frac{\partial \rho_v^{(0)}}{\partial t} + \langle \mathbf{v}_a^{(0)} \rangle \cdot \mathbf{grad} \rho_v^{(0)} - \mathrm{div}(\mathbf{D}^{\mathrm{eff}} \mathbf{grad} \; \rho_v^{(0)}) = -\mathrm{SSA_V} \rho_i w_n^{(0)} \tag{3.50}$$

where $\langle \mathbf{v}_a^{(0)} \rangle$ is the Darcy's velocity, $\mathbf{K}^{\mathrm{eff}}$ is the intrinsic permeability defined as (B.29)

$$\mathbf{K}^{\mathrm{eff}} = \frac{1}{|\Omega|} \int_{\Omega_a} \mathbf{k} \, \mathrm{d}\Omega \tag{3.51}$$

where $\mathbf{k}$ is a periodic second order tensor, solution of the following boundary value problem (B.21, B.22, B.23) over the REV:

$$\mu_a \Delta \mathbf{k} - \mathbf{grad} \, \mathbf{b} - \mathbf{I} = 0 \quad \text{in } \Omega_a \tag{3.52}$$

$$\mathbf{grad} \, \mathbf{k} = 0 \quad \text{in } \Omega_a \tag{3.53}$$

$$\mathbf{k} = 0 \quad \text{on } \Gamma \tag{3.54}$$

$$\frac{1}{|\Omega|} \int_{\Omega_a} \mathbf{b} \mathrm{d}\Omega = \mathbf{0} \tag{3.55}$$

All the other parameters involved in this model are the same as the ones defined in the Case A1.

At the macroscopic scale, in the Case B1, the heat and water vapor transfers are described by two coupled equations of diffusion/conduction and convection, including a source term induced by the phase change. The air flow is described by the classical Darcy's law (3.48), however the mass balance (3.47) presents also a source term due to the mass loss or gain induced by the phase change. Once again, it can be shown that in the Case B2, the source term arising in the heat transfer equation and in the mass balance is negligible. Only the source term of vapor is significant. In the Case B3, the sources terms arising in all the equations are negligible.

3.2.5.3 Case C1 (C2 and C3): strong convection + dispersion + source terms

In that case, according to the order of magnitude of the dimensionless numbers, the heat and the water vapor transfers are governed by convection at the first order of approximation. Returning in dimensional variables, the macroscopic model (C.23, C.24, C.34, C.59) is summarized as follows:

$$\mathrm{div}\langle \mathbf{v}_a^{(0)} \rangle = 0 \tag{3.56}$$

$$\langle \mathbf{v}_a^{(0)} \rangle = -\mathbf{F}(\mathbf{grad} p_a^{(0)}, \text{microstructure}, \rho_a, \mu_a) \tag{3.57}$$

$$(\rho C)^{\text{eff}} \frac{\partial T^{(0)}}{\partial t} + \rho_a C_a \langle \mathbf{v}_a^{(0)} \rangle \cdot \mathbf{grad} T^{(0)} = 0 \tag{3.58}$$

$$\phi \frac{\partial \rho_v^{(0)}}{\partial t} + \langle \mathbf{v}_a^{(0)} \rangle \cdot \mathbf{grad} \rho_v^{(0)} = 0 \tag{3.59}$$

where $\mathbf{F}$ is the flow law which is a non-linear function of the macroscopic gradient of pressure (to take into account inertial effects) and depends on the microstructure and the physical properties of the fluid (ρ_a, μ_a). This function $\mathbf{F}$ can be determined by solving over the REV the boundary value problem (C.15) - C.18). At the first order of approximation, at the macroscopic scale, the heat and water vapor transfers are described by convection. These two equations do not include source terms induced by the phase change. This set of equations is valid for the Case C1, C2 and C3.

Remark 1: In presence of strong convection, the above macroscopic modeling shows that the macroscopic flow law $\mathbf{F}$ becomes strongly non-linear. During the last decades, several theoretical and numerical works (see for example *Mei and Auriault* [1991]; *Skjetne and Auriault* [1999]; *Lasseux et al.* [2011] and references therein) have been performed in order to find a general expression of $\mathbf{F}$ whatever the porous media (isotropic or anisotropic). As recently shown by *Lasseux et al.* [2011], due to the non linearity, in general there is a strong coupling between the flow and the microstructure of the porous media. Consequently, the mean velocity is not necessarily collinear to the macroscopic pressure gradient as in the case of Darcy's law. As a consequence, in the case of orthotropic porous media for example, the knowledge of this relationship within the principal axis, as it as been performed on 3D images of snow by *Zermatten et al.* [2014], is not sufficient to describe the flow for any orientation of the pressure gradient with respect to the microstructure.

Remark 2: In porous media, it is well known that when the Péclet number at the pore scale is larger than 1 [*Bear*, 1972], the transfers through the porous media are usually driven by convection and dispersion. As shown in *Auriault and Adler* [1995], the interplay between diffusion and convection will appear by investigating the first corrector (i.e the next order of the asymptotic expansion) of the above macroscopic modeling. In the present case, following *Auriault and Adler* [1995]; *Geindreau and Auriault* [2001], and *Auriault et al.* [2009], it can be shown that at the second order of approximation, returning in dimensional variables, the macroscopic model (C.53, C.71) for the heat and the water vapor transfer is written:

$$(\rho C)^{\text{eff}} \frac{\partial \langle T \rangle}{\partial t} + \rho_a C_a \langle \mathbf{v}_a \rangle \cdot \mathbf{grad} \langle T \rangle - \mathrm{div}(\mathbf{k}^{\text{disp}} \mathbf{grad} \langle T \rangle) = \mathrm{SSA}_V L_{sg} w_n^{(0)} \tag{3.60}$$

$$\phi\frac{\partial\langle\rho_v\rangle_a}{\partial t}+\langle\mathbf{v}_a\rangle\cdot\mathbf{grad}\langle\rho_v\rangle_a-\mathrm{div}(\mathbf{D}^{\mathrm{disp}}\mathbf{grad}\langle\rho_v\rangle_a)=-\mathrm{SSA}_V\rho_i w_n^{(0)} \tag{3.61}$$

where $\langle T\rangle$, $\langle\rho_v\rangle_a$ and $\langle\mathbf{v}_a\rangle$ are the macroscopic temperature, water vapor density and fluid velocity, respectively, and $\mathbf{k}^{\mathrm{disp}}$ (C.51) and $\mathbf{D}^{\mathrm{disp}}$ (C.69) are the the effective thermal dispersion tensor and effective dispersion tensor, respectively. The notations $\langle\cdot\rangle_a$ and $\langle\cdot\rangle$ represent the mean over the air phase and over the REV, respectively. These tensors depends on the local velocity field and are defined as:

$$\mathbf{k}^{\mathrm{disp}}=\frac{1}{|\Omega|}\left(\int_{\Omega_{\mathrm{a}}}\kappa_a(\mathbf{grad}\ \mathbf{m}_a+\mathbf{I})+\mathbf{v}_a^{(0)}\otimes\mathbf{m}_a\mathrm{d}\Omega+\int_{\Omega_{\mathrm{i}}}\kappa_i(\mathbf{grad}\ \mathbf{m}_i+\mathbf{I})\mathrm{d}\Omega\right) \tag{3.62}$$

$$\mathbf{D}^{\mathrm{disp}}=\frac{1}{|\Omega|}\int_{\Omega_a}D_v(\mathbf{grad}\ \mathbf{h}_v+\mathbf{I})+\mathbf{v}_a^{(0)}\otimes\mathbf{h}_v\mathrm{d}\Omega \tag{3.63}$$

where $\mathbf{m}_a$ and $\mathbf{m}_i$ are periodic vectors solution of the boundary value problem (C.41 - C.44) over the REV:

$$-\beta\langle\mathbf{v}_a^{(0)}\rangle-\mathrm{div}(\kappa_i(\mathbf{grad}\ \mathbf{m}_i+\mathbf{I}))=\mathbf{0}\quad\text{in }\Omega_i \tag{3.64}$$

$$(-\gamma+\rho_aC_a)\langle\mathbf{v}_a^{(0)}\rangle+\mathbf{v}_a^{(0)}\cdot\mathbf{grad}\ \mathbf{m}_a-\mathrm{div}(\kappa_a(\mathbf{grad}\ \mathbf{m}_a+\mathbf{I}))=\mathbf{0}\quad\text{in }\Omega_a \tag{3.65}$$

$$\mathbf{m}_i=\mathbf{m}_a\quad\text{on }\Gamma \tag{3.66}$$

$$(\kappa_i(\mathbf{grad}\ \mathbf{m}_i+\mathbf{I})-\kappa_a(\mathbf{grad}\ \mathbf{m}_a+\mathbf{I}))\cdot\mathbf{n_i}=0\quad\text{on }\Gamma \tag{3.67}$$

$$\frac{1}{|\Omega|}\int_{\Omega}(\mathbf{m}_{\mathrm{a}}+\mathbf{m}_{\mathrm{i}})\mathrm{d}\Omega=\mathbf{0} \tag{3.68}$$

where $\beta=(\rho_aC_a)\times(\rho_iC_i)/(\rho C)^{\mathrm{eff}}$ and $\gamma=(\rho_aC_a)^2/(\rho C)^{\mathrm{eff}}$. Similarly, $\mathbf{h}_v$ is a periodic vector solution of the boundary value problem (C.63 - C.64) over the REV

$$(-\phi^{-1}\langle\mathbf{v}_a^{(0)}\rangle+\mathbf{v}_a^{0)})+\mathbf{v}_a^{(0)}\cdot\mathbf{grad}\ \mathbf{h}_v-\mathrm{div}(D_v(\mathbf{grad}\ \mathbf{h}_v+\mathbf{I}))=0\quad\text{in }\Omega_a \tag{3.69}$$

$$D_v(\mathbf{grad}\ \mathbf{h}_v+\mathbf{I})\cdot\mathbf{n_i}=0\quad\text{on }\Gamma \tag{3.70}$$

$$\frac{1}{|\Omega|}\int_{\Omega_a}\mathbf{h}_v\mathrm{d}\Omega=\mathbf{0} \tag{3.71}$$

These two boundary value problems clearly underline the strong coupling between the diffusion and the convection phenomena at the REV scale, and consequently at the macroscopic scale through the dispersion tensors.

3.3 2D numerical illustration

3.3.1 Problem definition

As in Chapter 2, in order to illustrate and evaluate the obtained macroscopic modeling, we propose to compare the numerical results for the heat and water vapor transfer through a snow layer obtained in the case of a fine scale modeling (i.e. by taking into account all the heterogeneities) and in the case of the macroscopic equivalent modeling. We focus on Case B1.

For that purpose, numerical simulations have been preformed on the same 2D vertical snow layer of 10 cm length and 0.5 mm width (Figure 3.4) using the finite element code

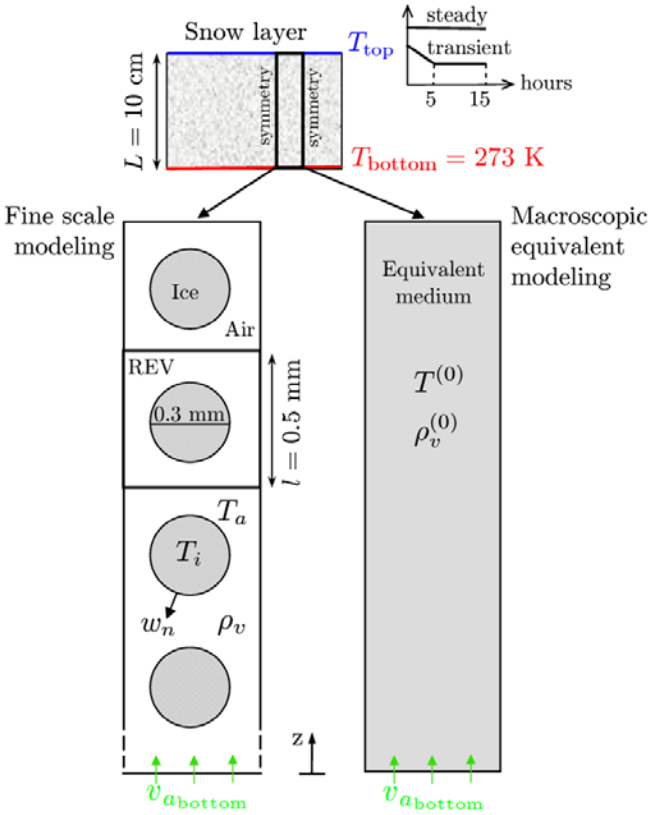

Figure 3.4: Illustration of the 2D geometry for the fine scale modeling and the macroscopic equivalent modeling.

ComsolMultiphysics. The separation of scales remains $\varepsilon = 5 \times 10^{-3}$. At the base of the snow layer, the temperature $T_{\text{bottom}} = 273$ K, the vapor density $\rho_{vs}(T_{\text{bottom}}) = 5.113 \times 10^{-3}$ kg m^{-3}, which is supposed to be equal to the saturation vapor density using Equation (3.12), and the input flow of velocity $v_{a_{\text{bottom}}}$ are imposed. At the top of the snow layer, the temperature T_{top}, the air pressure $p_{a_{\text{top}}} = 1$ Pa are imposed. The vapor density is not imposed at the outlet as in *Albert and McGilvary* [1992]. The boundary conditions that we modified are T_{top}, to control the temperature gradient through the snow layer, and $v_{a_{\text{bottom}}}$ to control the intensity of the air flow through the snow layer. At the ice interface the no slip condition is put for the air flow. Symmetry conditions are imposed on the lateral sides of the snow layer. The above boundary conditions are similar to the ones defined in the study of *Albert and McGilvary* [1992]. In what follows, curvature effects are neglected ($d_0 K = 0$), and the interface kinetic coefficient β is taken constant and equal to 5.5×10^5 s m^{-1}, as in the study of *Kaempfer and Plapp* [2009]. Moreover, for the sake of simplicity, the simulations do not reflect the evolution of the microstructure (air-ice interface motion), i.e. the geometry is not updated with time.

In the case of the fine scale modeling, the snow layer microstructure consists of 200 periodic cells of 0.5×0.5 mm^2; each periodic cell (REV) is composed of an ice grain of diameter 0.3 mm surrounded by air. Thus, the porosity is equal to 0.71, which corresponds to a snow density of 266 kg m^{-3}. The heat and the mass transfer within this layer are described by the set of equations (3.1) – (3.12) where p_a, v_a, T_i, T_a and ρ_v are the unknowns.

Table 3.2: Macroscopic properties computed over the REV of the considered 2D geometry, using κ_{a}=0.024 $\mathrm{W\,m^{-1}\,K^{-1}}$, κ_{i}=2.3 $\mathrm{W\,m^{-1}\,K^{-1}}$ and D_v= 2.036×10^{-5} $\mathrm{m^2\,s^{-1}}$.

Porosity, ϕ	0.71
Surface area, $\mathrm{SSA_V}$	3770 $\mathrm{m^{-1}}$
Intrinsic permeability K^{eff}	2.71×10^{-9} $\mathrm{m^{-2}}$
Effective thermal capacity, $(\rho C)^{\mathrm{eff}}$	5.3×10^{6} $\mathrm{J\,m^2\,K^{-1}}$
Effective thermal conductivity, k^{eff}	0.04243 $\mathrm{W\,m^{-1}\,K^{-1}}$
Effective diffusion, D^{eff}	1.156×10^{-5} $\mathrm{m^2\,s^{-1}}$

This set of equations has been numerically solved using the material parameter values presented in Table 3.1.

In the case of the macroscopic equivalent modeling, the snow layer is seen as a continuous equivalent medium. We simulated the Case B1, i.e. the heat and the mass transfer are described by the set of equations (3.47) – (3.50), (3.34) and (3.35) where $p_a^{(0)}$, $v_a^{(0)}$, $T^{(0)}$ and $\rho_v^{(0)}$ are the macroscopic unknowns. This macroscopic description requires computation of some parameters or effective properties over the REV. The porosity ϕ and the specific surface area $\mathrm{SSA_V}$ involved in the macroscopic modeling can be easily deduced from the geometry of the REV. The intrinsic permeability $\mathbf{K}^{\mathrm{eff}}$, effective heat capacity $(\rho C)^{\mathrm{eff}}$, effective thermal conductivity $\mathbf{k}^{\mathrm{eff}}$ and effective vapor diffusion $\mathbf{D}^{\mathrm{eff}}$ were computed using relations (3.51), (3.36), (3.37), and (3.38), respectively. For that purpose, the boundary value problems (3.52)-(3.55), (3.39)-(3.43) and (3.44)-(3.46) have been solved numerically over the REV. Due to the symmetry of the REV, tensors $\mathbf{K}^{\mathrm{eff}}$, $\mathbf{D}^{\mathrm{eff}}$ and $\mathbf{k}^{\mathrm{eff}}$ are isotropic and can be written $\mathbf{K}^{\mathrm{eff}} = K^{\mathrm{eff}}\mathbf{I}$, $\mathbf{D}^{\mathrm{eff}} = D^{\mathrm{eff}}\mathbf{I}$ and $\mathbf{k}^{\mathrm{eff}} = k^{\mathrm{eff}}\mathbf{I}$, where $\mathbf{I}$ is the identity tensor. The parameters and the effective properties deduced from the REV scale are summarized in Table 3.2.

3.3.2 Results

Figure 3.5 shows the velocity field, temperature field, vapor density field, with the corresponding flux (black arrows), as well as the vapor density flux at the interface. These variables are computed within two cells of the snow layer using the fine scale modeling when $T_{\mathrm{top}} = 248$ K, in steady state. For the temperature field and the vapor density field, we use a color map defined as the average temperature over the cell ± 0.15 K and the average vapor density $\pm 0.03 \times 10^{-3}$ kg $\mathrm{m^{-3}}$, respectively. The vapor fluxes at the interface are represented by red arrows that are proportional to the flux intensity. In this way, the intensity of the gradients and of the interfacial vapor flux of each caption can be compared.

- First, when a very slow flow is simulated ($v_{a_{\mathrm{bottom}}} = 10^{-8}$ m $\mathrm{s^{-1}}$, i.e. $[\mathrm{Re}] = \left[\mathrm{Pe^T}\right] = [\mathrm{Pe}^{\rho}] = \mathcal{O}\left(\varepsilon^3\right)$), the gradients of temperature and vapor density are similar between the cell at the top and bottom of the layer; only the values are different. The small difference of the gradient intensity along the snow layer is due to the nonlinear

relationship between temperature and saturation vapor density. The heat transfer is clearly higher in the ice phase. Locally, the fluxes of vapor and heat are influenced by the phase changes, in addition to the macroscopic temperature gradient imposed. Along the interface, the vapor fluxes are due to sublimation on the upper part of the grain and condensation on the lower part.

- When we consider the simulations with a high air flow velocity ($v_{a_{\text{bottom}}} = 10^{-3}$ m s^{-1}, i.e. $[\text{Re}] = \left[\text{Pe}^{\text{T}}\right] = [\text{Pe}^{\rho}] \leqslant \mathcal{O}(\varepsilon^2)$), the gradients are different between the top and base of the snow layer. For the cell located at the bottom, the temperature and vapor density are quasi homogeneous. Conversely, the cell located at the top exhibits large gradients of temperature and vapor density. This configuration is due to the input air flow at the bottom of the layer that transfers the heat and mass toward the top; the gradients are thus concentrated in this area. The heat and vapor fluxes are identical to those of the air flow, i.e. the transfer is driven by the air flow, in addition to the macroscopic temperature gradient imposed, and the effect of phase changes is not observable. At the base of the snow layer, because the temperature gradient is low, the vapor flux at the interface due to phase change is also very low.

The above comments show the strong influence of the air flow on the temperature field and, as it is coupled, on the vapor density field at the microscopic scale. This effect is also observed at the macro scale by Figure 3.6 that shows the vertical profile of the intensity of local temperature gradients induced by a macroscopic temperature gradient of 100 K m^{-1} and under three different values of $v_{a_{\text{bottom}}}$. As expected, when low flow velocities are considered, the snow layer is submitted to a constant vertical temperature gradient equal to the macroscopic one imposed; but when a strong convection occurs, the snow undergoes locally temperature gradients that increase along the flow direction from the base to the top of the layer. In the case of Figure 3.6, the local gradients range from about 0 to 500 K m^{-1} for a macroscopic temperature gradient of 100 K m^{-1}.

The vertical profiles of the temperature and vapor density through the snow layer obtained in the case of a fine scale modeling (marks) and in the case of the corresponding macroscopic equivalent modeling (solid line) are presented in Figure 3.7 to Figure 3.10. In the case of the fine scale modeling, the average values of each microscopic variable over the cell have been expressed as:

$$\langle T \rangle = \frac{1}{\Omega}\left(\int_{\Omega_i} T_i d\Omega + \int_{\Omega_a} T_a d\Omega\right), \quad \langle \rho_v \rangle = \frac{1}{\Omega_a}\int_{\Omega_a} \rho_v d\Omega$$

Figures 3.7, 3.8 and 3.9 show the results obtained in steady state, when $T_{\text{bottom}} = 273$ K and $T_{\text{top}} = 268, 263$ and 248 K, which leads to a temperature gradient of 50, 100 and 250 K m^{-1} respectively. For each figure, the velocity of the input air flow at the base of the snow layer $v_{a_{\text{bottom}}}$ is equal to $10^{-8}, 10^{-5}, 10^{-4}$ and 10^{-3} m s^{-1} successively. An air flow above 10^{-4} m s^{-1}, i.e. $[\text{Re}] = \left[\text{Pe}^{\text{T}}\right] = [\text{Pe}^{\rho}] \geqslant \mathcal{O}(\varepsilon)$, significantly modifies the temperature and vapor profile, as expected by the dimensionless numbers analysis.

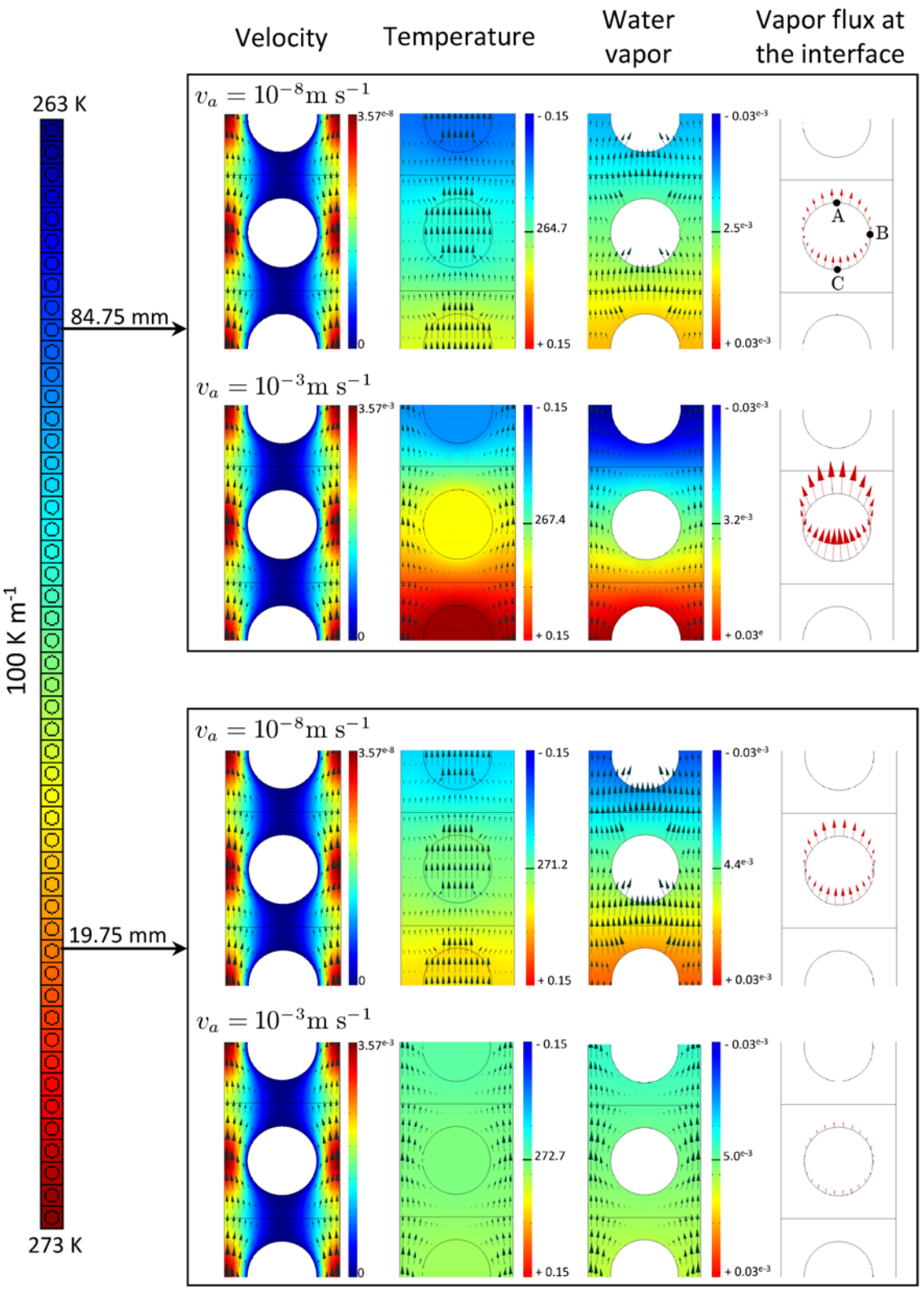

Figure 3.5: Microscopic field of air velocity, temperature, water vapor density, and vapor density flux at the ice interface, computed within two cells at 19.75 mm and 84.75 mm height of the snow layer, respectively, that experience a constant temperature gradient of 100 K m^{-1} and an input air flow $v_{a_{\text{bottom}}} = 10^{-3}$ m s^{-1} or 10^{-8} m s^{-1}. The black arrows show the corresponding flux.

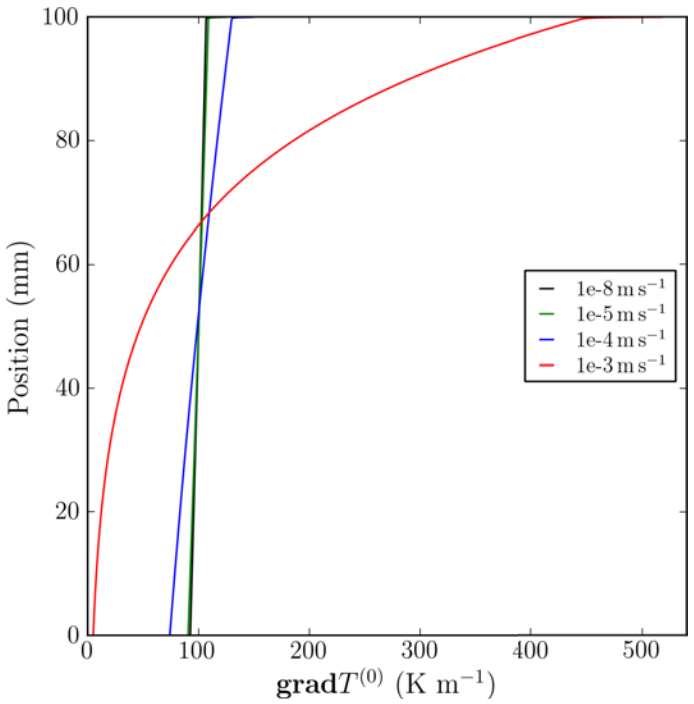

Figure 3.6: Vertical profile of the local temperature gradient depending on the input air velocity.

Below this value, the profiles are the same as the ones presented in Chapter 2 with no convection. Overall, profiles deduced from the fine scale modeling and the macroscopic equivalent modeling are close. The maximum relative error is reached in the upper part of the snow layer for $v_{a_{\text{bottom}}} = 10^{-3}$ m s^{-1} and a temperature gradient of 250 K m^{-1} and is equal to -0.39 % for the temperature and -9.4 % for the vapor density. These errors are in absolute value larger and of opposite sign to the ones obtained when no convection is considered (see Chapter 2) or similar in the present case when $v_{a_{\text{bottom}}} = 10^{-8}$ m s^{-1}.

Figure 3.10 and 3.11 show the temperature and vapor density profiles for a temperature gradient of 100 K m^{-1} with $v_{a_{\text{bottom}}} = 10^{-3}$ and 10^{-8} m s^{-1}, respectively, when the heat and mass transfer are solved in transient state and the fluid flow are solved in steady state. The snow layer is initially at a temperature of 273 K; then T_{top} decreases to reach 263 K in 5 hours and remains constant until 15 hours. The value of T_{bottom} is constant and equal to 273 K. The profiles at 5 different times are shown in both figures, similar to Figure 2.6 of Chapter 2. Once again, we can observe a good agreement between the numerical results of both modelings. Under such conditions, the maximum relative error is obtained at t = 6 hours and reaches -0.14 % for the temperature profile and -3.35 % for the vapor density profile.

Finally, Figure 3.12 presents the evolution of the normal growth velocity in two cells positioned at the upper and lower part of the snow layer deduced from the fine scale modeling (w_n at the top (point A), base (point C), and midheight (point B) of the

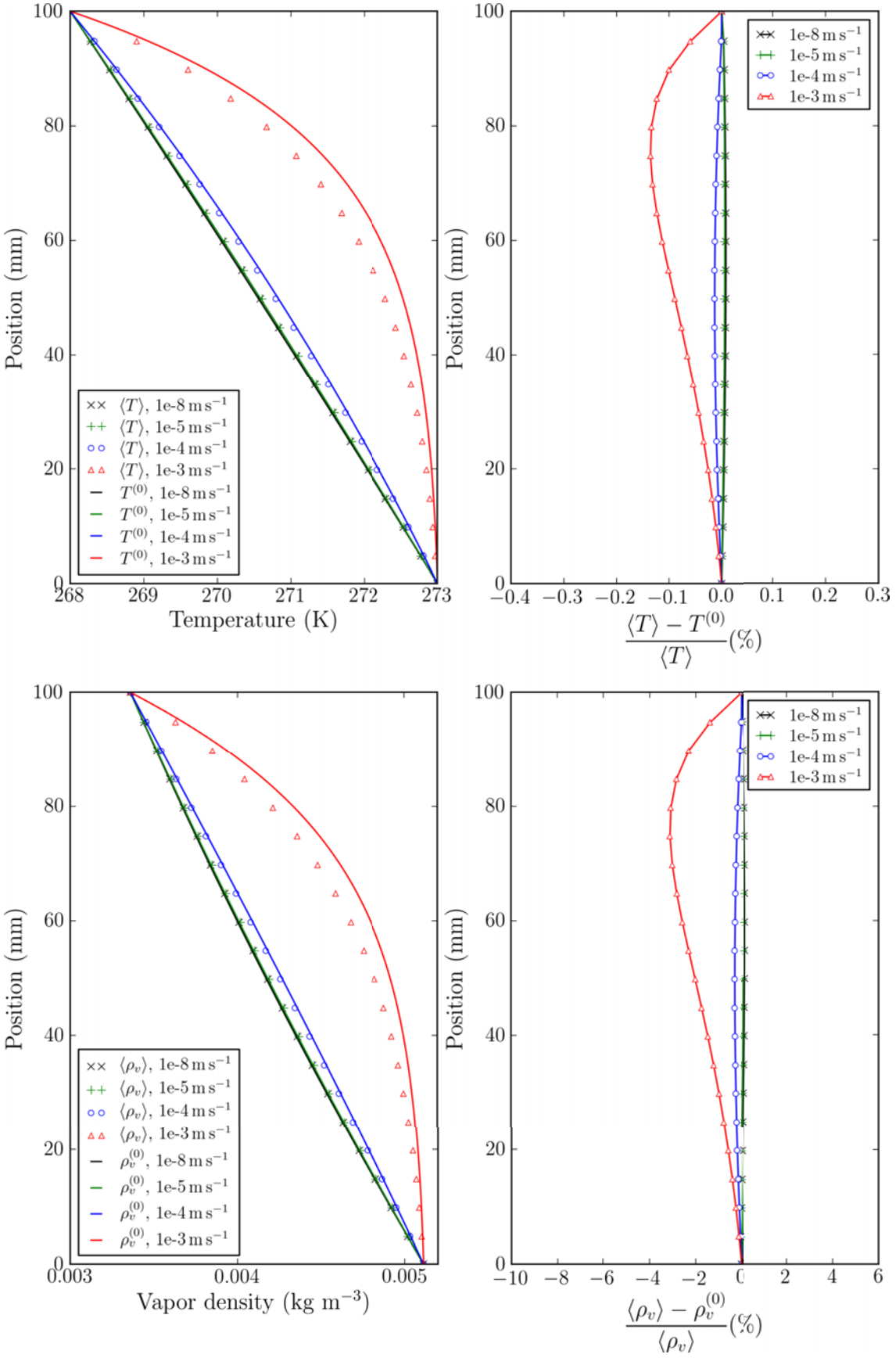

Figure 3.7: Comparison between fine scale (marks) and macroscopic equivalent (solid line) modeling in steady state and for a temperature gradient of 50 K m^{-1}: vertical profile of temperature and vapor density and relative errors for an input air velocity $v_{a_{\text{bottom}}}$ of 10^{-8}, 10^{-5}, 10^{-4}, and 10^{-3} m s^{-1}.

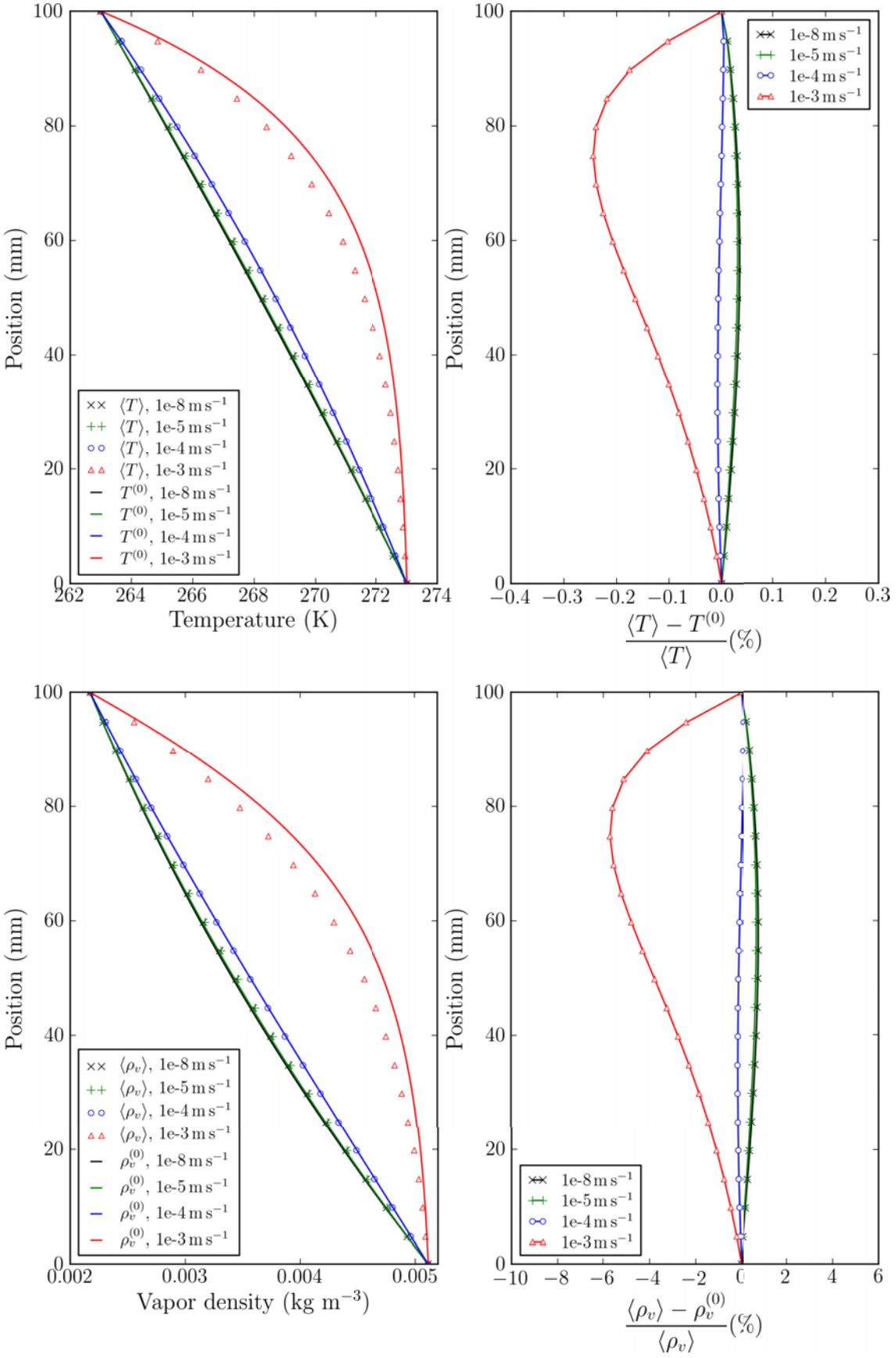

Figure 3.8: Comparison between fine scale (marks) and macroscopic equivalent (solid line) modeling in steady state and for a temperature gradient of 100 K m^{-1}: vertical profile of temperature and vapor density and relative errors for an input air velocity $v_{a_{\text{bottom}}}$ of 10^{-8}, 10^{-5}, 10^{-4}, and 10^{-3} m s^{-1}.

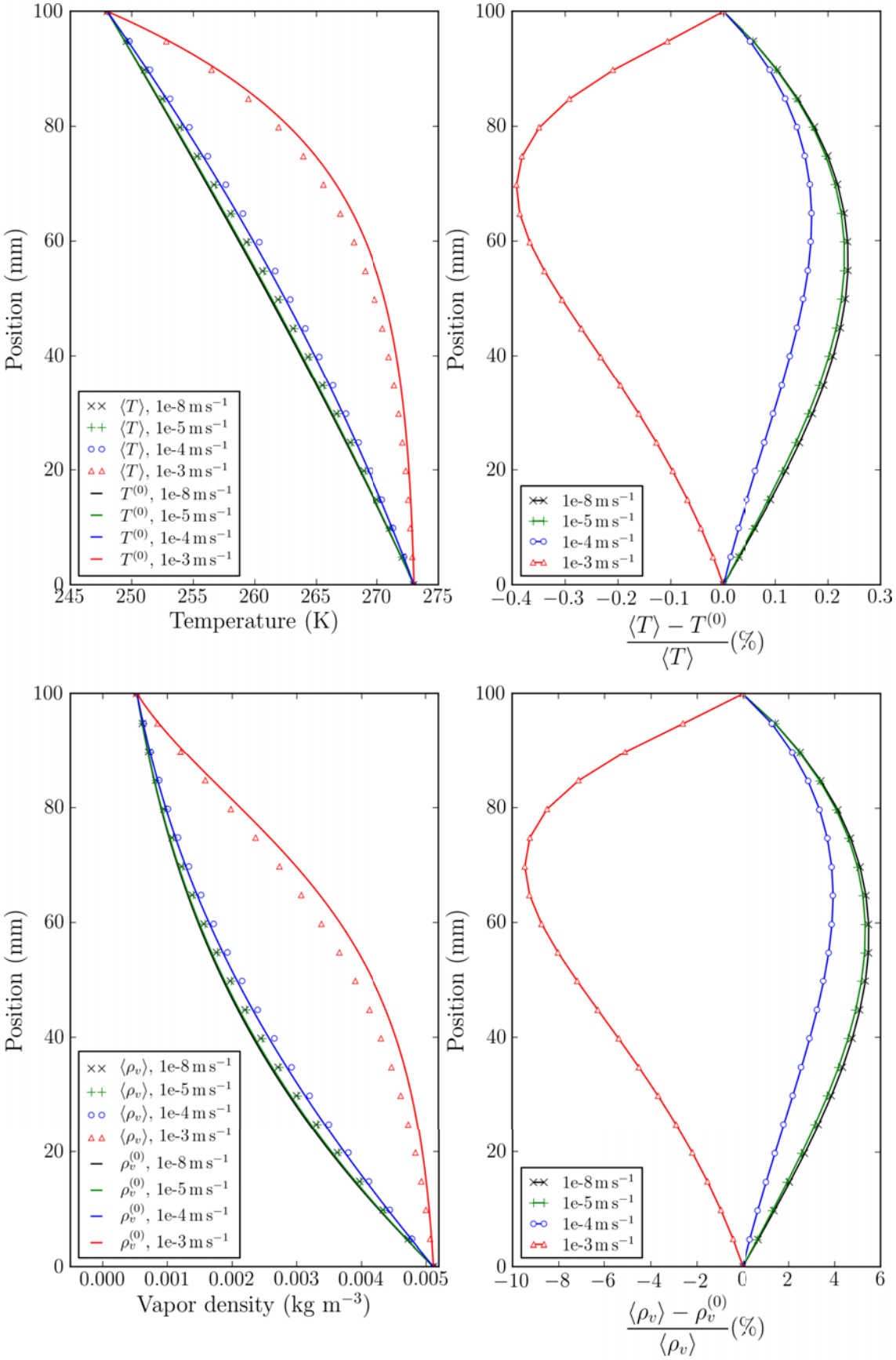

Figure 3.9: Comparison between fine scale (marks) and macroscopic equivalent (solid line) modeling in steady state and for a temperature gradient of 250 K m^{-1}: vertical profile of temperature and vapor density and relative errors for an input air velocity $v_{a_{\text{bottom}}}$ of 10^{-8}, 10^{-5}, 10^{-4}, and 10^{-3} m s^{-1}.

ice grain as well as the average value $\langle w_n \rangle$ over the REV, Figure 3.5) and from the macroscopic equivalent modeling ($w_n^{(0)}$) for a temperature gradient within the range 0 to 250 $\mathrm{K\,m^{-1}}$ and $v_{a_{\mathrm{bottom}}}$ of 10^{-8} and 10^{-3} $\mathrm{m\,s^{-1}}$. The values of w_n at the top of the grain are negative and presented in terms of the absolute value in the figure. As expected, the normal growth velocity increases with increasing temperature gradient and is related to the local temperature gradients presented in Figure 3.6. For the upper cell, the local temperature gradients can be strongly enhanced compared to the macroscopic gradient imposed. In spite of this, the average value $\langle w_n \rangle$ of this cell does not exceed 2×10^{-11} $\mathrm{m\,s^{-1}}$ ($[\mathrm{W}] = [\mathrm{H}] \simeq \mathcal{O}(\varepsilon^2)$). For both cells, w_n is negative (sublimation) and positive (deposition) at the top and the base of the ice grain, respectively, and ranges typically from 10^{-11} to 10^{-9} $\mathrm{m\,s^{-1}}$, whereas at the midheight of the grain w_n ranges from 10^{-15} to 10^{-11} $\mathrm{m\,s^{-1}}$. The averaged growth velocity over the particle interface is low, but positive, meaning that the deposition predominates slightly over the sublimation. This is due to the nonlinear relationship between the temperature and the saturation vapor density. The evolution of the "macroscopic equivalent normal velocity" $w_n^{(0)}$ is consistent with $\langle w_n \rangle$.

3.4 Discussion and conclusion

We derived the macroscopic equivalent modeling of the heat and water vapor transfer through snow from its description at the pore scale using the homogenization of multiple scale expansions [*Bensoussan et al.*, 1978; *Sanchez-Palencia*, 1980; *Auriault*, 1991; *Auriault et al.*, 2009]. In contrast to Chapter 2, air flow is also considered in the definiton of the physics at the pore scale. The formulation of the macroscopic equivalent modeling is driven by the order of magnitude of the dimensionless numbers that characterize the physics at the pore scale, and thus constitute the domain of validity of the modeling. The formulation includes the exact expression of the effective properties (effective thermal conductivity, effective vapor diffusion coefficient and intrinsic permeability) and of the source terms of heat and vapor arising from the phase change at the pore scale.

The different estimations of the dimensionless numbers lead to three main cases of macroscopic modeling:

- Case A1: when the air flow velocity $v_{a_c} \lesssim 10^{-5}$ m s^{-1}, i.e. $\left[\mathrm{F_i^T}\right] = \left[\mathrm{F_a^T}\right] = [\mathrm{F_a^\rho}] = \mathcal{O}(\varepsilon^2)$ and $[\mathrm{Re}] = \left[\mathrm{Pe^T}\right] = [\mathrm{Pe^\rho}] \leqslant \mathcal{O}(\varepsilon^2)$, the convection is negligible at the macroscopic scale. The physics at the scale of a snow layer is described by two coupled equations of heat and vapor diffusion/conduction including source terms (Q_T, Q_v), and corresponds to the one presented in Chapter 2.

- Case B1: when 10^{-5} m s^{-1} $\lesssim v_{a_c} \lesssim 10^{-3}$ m s^{-1}, i.e. $\left[\mathrm{F_i^T}\right] = \left[\mathrm{F_a^T}\right] = [\mathrm{F_a^\rho}] = \mathcal{O}(\varepsilon^2)$ and $[\mathrm{Re}] = \left[\mathrm{Pe^T}\right] = [\mathrm{Pe^\rho}] = \mathcal{O}(\varepsilon)$, the diffusion/conduction and convection are of the same order of magnitude at the macroscopic scale. The convection corresponds to a moderate flow that is described by Darcy's law. The macroscopic modeling includes two coupled equations of diffusion/conduction and convection of heat and vapor including source terms (Q_T, Q_v).

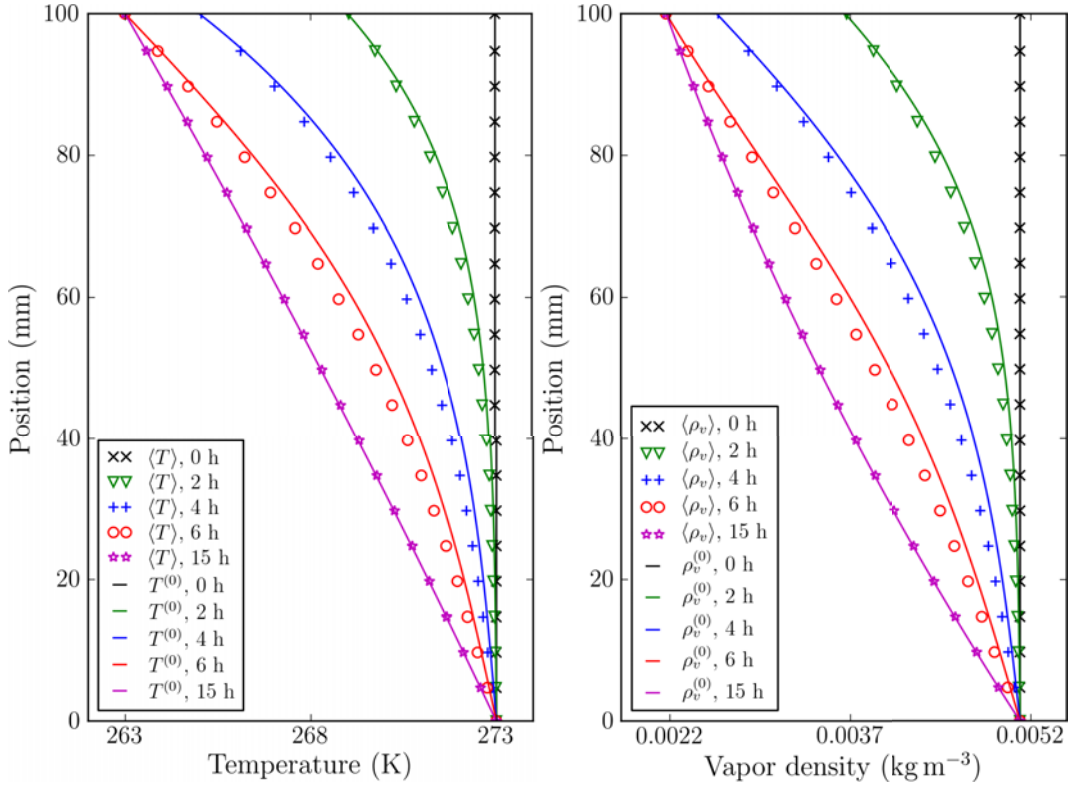

Figure 3.10: Comparison between fine scale (marks) and macroscopic equivalent (solid lines) modeling in the case of transient analysis for an input air velocity $v_{a_{\text{bottom}}}$ of 10^{-8} m s^{-1}: vertical profile of temperature and water vapor density within the snow layer at 5 different times.

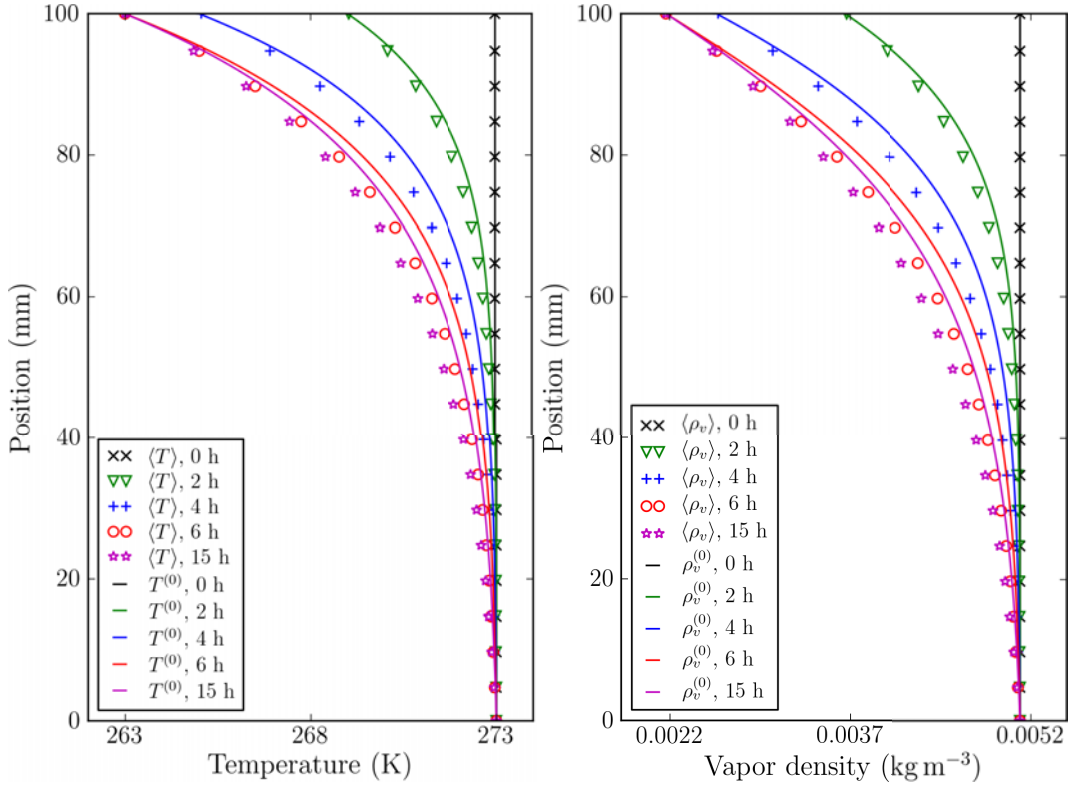

Figure 3.11: Comparison between fine scale (marks) and macroscopic equivalent (solid lines) modeling in the case of transient analysis for an input air velocity $v_{a_{\text{bottom}}}$ of 10^{-3} m s^{-1}: vertical profile of temperature and water vapor density within the snow layer at 5 different times.

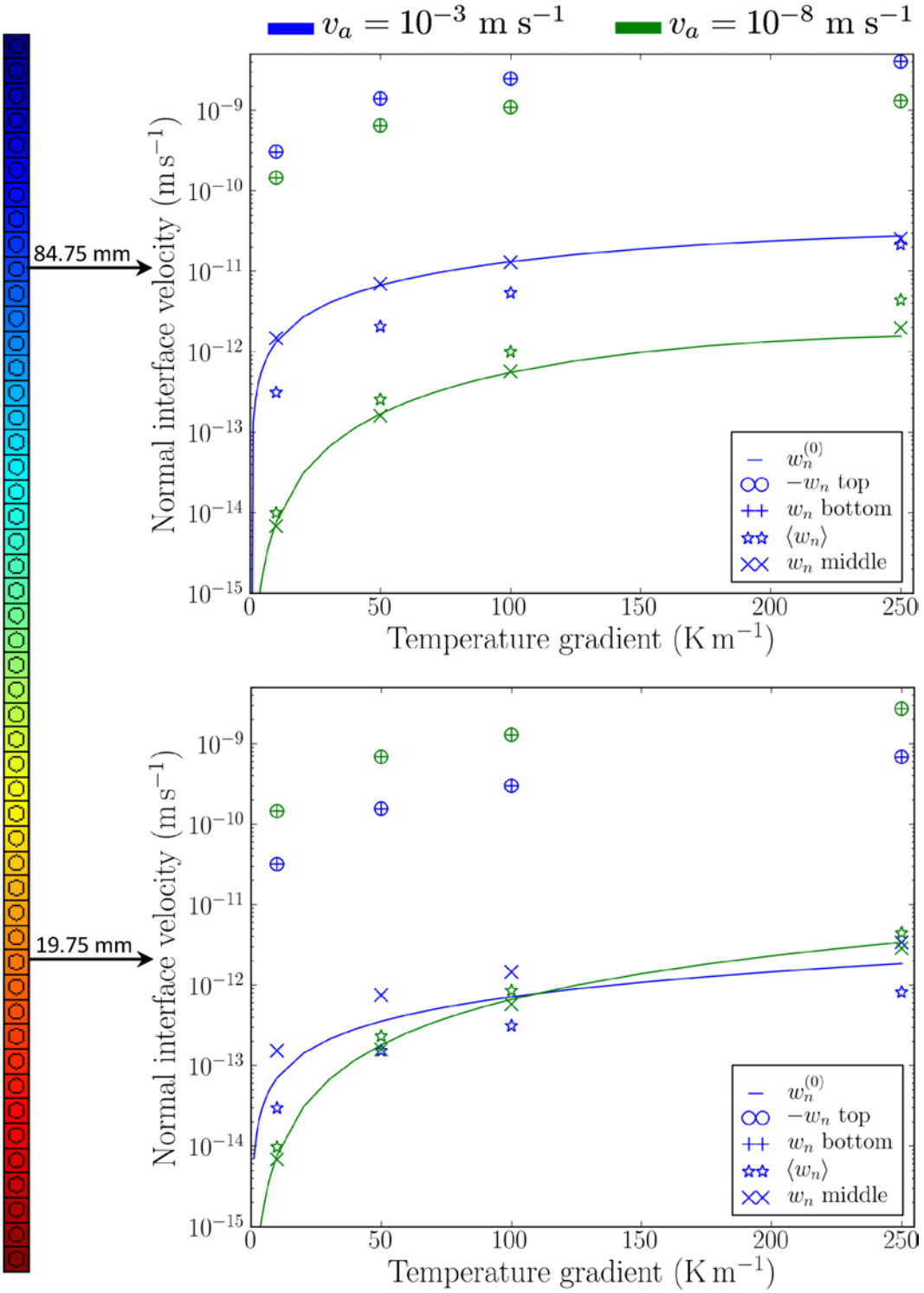

Figure 3.12: Evolution of the normal growth velocity in two cells positioned at the upper and lower part of the 2D snow layer deduced from the fine scale modeling (w_n at the top, base and middle of the ice grain as well as the average value $\langle w_n \rangle$ over the REV) and from the macroscopic equivalent modeling ($w_n^{(0)}$). Results for a temperature gradient within the range 0−250 K m^{-1} and for an input air velocity $v_{a_{\text{bottom}}}$ of 10^{-8} and 10^{-3} m s^{-1}.

- Case C1: when 10^{-3} m s$^{-1} \lesssim v_{a_c} \lesssim 10^{-1}$ m s^{-1}, i.e. $\left[\mathrm{F_i^T}\right] = \left[\mathrm{F_a^T}\right] = [\mathrm{F_a^\rho}] = \mathcal{O}(\varepsilon)$ and $[\mathrm{Re}] = \left[\mathrm{Pe^T}\right] = [\mathrm{Pe}^\rho] = \mathcal{O}(1)$, the macroscopic diffusion/conduction are negligible at the first order of approximation. The convection corresponds to a strong flow that is not described anymore by Darcy's law but by a non linear flow to take into account inertial effects. The heat and vapor transfers are described at the macroscopic scale by two equations of convection without source terms. However, we have shown that at the second order of approximation, the description of these transfers also included dispersion effects and source terms.

The sub-cases A2, A3, or B2, B3, or C2, C3, are particular cases of the three main cases described above: they correspond to simplifications of the source terms when the interface growth velocity is moderate to low, typically for $w_{n_c} \lesssim 10^{-11}$ m s^{-1}, i.e. $[\mathrm{H}] \leqslant \mathcal{O}(\varepsilon^3)$ and $[\mathrm{W}] \leqslant \mathcal{O}(\varepsilon^2)$.

The modeling B1 −when the diffusion/conduction and convection are of the same order of magnitude at the macroscopic scale− is similar to the model presented by *Albert and McGilvary* [1992]. The expression of their source terms involved a mass transfer coefficient h_m. According to our developments, h_m is perfectly defined and only depends on the macroscopic temperature as:

$$h_m = \frac{\rho_i}{\beta\, \rho_{vs}^{(0)}(T^{(0)})} \tag{3.72}$$

The experimental work of *Neumann et al.* [2009] presents measurements of h_m that indicate that it mainly depends on the air velocity through the snow sample, i.e. of the pore Reynold number. However, the mean temperature was not homogeneous within their sample. So, it seems not obvious to define a mean mass transfer coefficient from their measurement, except by performing an inverse analysis.

Finally, the 2D simulations of the physics at the pore scale and of the macroscopic modeling B1 illustrate the influence of the air flow on the overall heat and vapor transfer. If an air flow greater than about 10^{-4} m s^{-1} is applied, i.e. $[\mathrm{Re}] = \left[\mathrm{Pe^T}\right] = [\mathrm{Pe}^\rho] \geqslant \mathcal{O}(\varepsilon)$, the temperature field is significantly perturbed and the intensity of the temperature gradient vary widely locally. Despite the large local temperature gradients that can appear, the "macroscopic equivalent normal velocity" does not exceed $2{\times}10^{-11}$ m s^{-1}. Overall, the comparative study show the precision and the robustness of the resulting macroscopic equivalent modeling B1.

Conclusion Part I

In this Part, the macroscopic equivalent models of heat and water vapor transfers through a snow layer were derived from the physics at the pore scale using the homogenization of multiple scale expansions. Under the condition of separation of scales, these modelings are obtained without any prerequisites at the macroscopic scale and are intrinsic to the geometry of the medium and the phenomenon. The microscopic description of the heat and vapor transfers was described by the conduction, diffusion and phase changes in Chapter 2, and has been enriched by the forced convection in Chapter 3. The main contributions of these studies are summarized in the following.

- Three main macroscopic modelings of heat and vapor transfers were derived. The domain of validity of these models is given by the order of magnitude of the dimensionless numbers with respect to the separation of scales, here $\varepsilon = 5 \times 10^{-3}$. We have also shown that the modeling mainly depends on the intensity of the air flow, i.e. on the order of magnitude of the pore Reynolds number [Re] and the Péclet numbers $\left[\mathrm{Pe}^{\mathrm{T}}\right]$ and $[\mathrm{Pe}^{\rho}]$, and on the temperature gradient imposed to the layer, i.e. on the order of magnitude of [W] and [H]. The precision and the robustness of the modelings were illustrated through 2D numerical simulations.
- The definition of the effective properties (effective diffusion tensor, effective thermal conductivity tensor, intrinsic permeability tensor...) arising in the macroscopic modelings of transport are provided by the homogenization method. More precisely, the effective properties can be estimated by solving specific boundary value problems over representative elementary volumes of snow. Let us remark that, although the macroscopic heat and vapor transfers are described by two coupled equations, these effective properties can be obtained in general by solving uncoupled problems, except in the case of the dispersion tensor.
- The macroscopic source terms of heat and vapor, induced by sublimation/deposition at the pore scale, are perfectly defined by the homogenization method. In the present case, we have shown that the mass transfer coefficient introduced by *Albert and McGilvary* [1992] depends only on temperature.
- Our theoretical developments show that the effective diffusion tensor of vapor is not enhanced in snow, as suggested by previous studies. This effective diffusion tensor was estimated over 3D images spanning the whole range of snow types and density.

Based on our work, further work can be considered:
(i) Monitored experiments might be carried out to evaluate the macroscopic modeling with respect to measurements.
(ii) If the microscopic description is enriched by other physical phenomena (anisotropic growth, natural convection, etc) one can follow the presented method to derive the new corresponding macroscopic modeling.
(iii) A poor separation of scales might arise when very large temperature gradients or very thin snow layers are considered. In that case, the macroscopic modeling can be derived by investigating the following superior order of approximation in the asymptotic analysis.

Part II

Effective properties of transport phenomena

Introduction Part II

The previous part was dedicated to the description of the macroscopic modeling of heat and vapor transport through dry snow, in which the effective tensor of vapor diffusion, the effective thermal conductivity tensor, the intrinsic permeability tensor, and the effective dispersion tensor are implied. This latter one, which arises in the macroscopic modeling when a strong air flow is present, will not investigated in this thesis. Parameterizations based on measurements are often used to estimate these properties as a function of the snow density but can vary largely from one study to another. The estimations of the effective properties remain thus a source of uncertainty.

In order to improve these estimations, this part is dedicated to estimate the effective properties of transport from 3D images of snow, as initiated by *Kaempfer et al.* [2005] and *Zermatten et al.* [2011]. For that, the specific boundary value problems presented in Part I arising from the homogenization method are solved over representative elementary volumes (REV) using the software Geodict. The REV are extracted from about thirty 3D images of snow spanning the full range of seasonal snow types and density. These 3D images come from previous field samplings and cold-room experiments combined to tomography performed during the last 10 years at the CEN, but also from an experiment carried out during the thesis (cf Chapter 6). The obtained estimations of effectives properties are expressed with respect to snow density and compared to measurements, parameterizations, models and analytical estimates from the literature. We also study for the first time the anisotropy coefficient of each effective property.

The study of the effective coefficient diffusion was presented in Chapter 2 of Part II, as we keep the structure of the published paper. The investigation of the effective thermal conductivity and of the intrinsic permeability are now carried out in Chapter 4 and Chapter 5, respectively.

Chapter

4 Numerical and experimental investigations of the effective thermal conductivity of snow

Contents

This chapter corresponds to the paper entitled *Numerical and experimental investigations of the effective thermal conductivity of snow* by Calonne N., Flin F., Morin S., Lesaffre B., Rolland du Roscoat S. and Geindreau C., published in *Geophysical Research Letters*, 2011.

Abstract

We carried out numerical simulations of the conductivity of snow using microtomographic images. The full tensor of the effective thermal conductivity ($\mathbf{k}^{\text{eff}}$) was computed from 30 three-dimensional images of the snow microstructure, spanning all types of seasonal snow. Only conduction through ice and interstitial air were considered. The obtained values are strongly correlated to snow density. The main cause for the slight scatter around the regression curve to snow density is the anisotropy of $\mathbf{k}^{\text{eff}}$: the vertical component of $\mathbf{k}^{\text{eff}}$ of facetted crystals and depth hoar samples is up to 1.5 times larger than the horizontal component, while rounded grains sampled deeply in the snowpack exhibit the inverse behavior. Results of simulations neglecting the conduction in the interstitial air indicate that this phase plays a vital role in heat conduction through snow. The computed effective thermal conductivity is found to increase with decreasing temperature, mostly following the temperature dependency of the thermal conductivity of ice. The results are compared to experimental data obtained either with the needle-probe technique or using combined measurements of the vertical heat flux and the corresponding temperature gradient. Needle-probe measurements are systematically significantly lower than those from the two other techniques. The observed discrepancies between the three methods are investigated and briefly discussed.

4.1 Introduction

Snow on the ground is a complex porous medium made of air and up to three phases of water (ice, water vapor and liquid water). Understanding heat and mass transfer through the snowpack is critical to assess the climatic and hydrological role of snow in the cryosphere. It is also needed to predict morphological changes in snow crystals [*Brzoska et al.*, 2008; *Flin and Brzoska*, 2008; *Kaempfer and Plapp*, 2009; *Pinzer and Schneebeli*, 2009a], the vertical distribution of which governs, for example, the surface energy balance and the mechanical stability of the snowpack [*Armstrong and Brun*, 2008].

Heat transfer through snow proceeds by conduction through ice and air, but is also potentially affected by phase change effects, water vapor diffusion and air convection in the pores [*Arons and Colbeck*, 1995; *Sturm et al.*, 1997]. Defining in a physically sound manner the thermal conductivity of snow, i.e. the tensor ($\mathbf{k}$) linking the macroscopic temperature gradient ($\boldsymbol{\nabla} T$) and the heat flux ($\mathbf{F}$) through the Fourier's law ($\mathbf{F} = -\mathbf{k}\boldsymbol{\nabla} T$), is thus challenging because conductive and non-conductive processes both contribute to heat transfer through snow. From experimental relationships between $\boldsymbol{\nabla} T$ and $\mathbf{F}$, many investigators have derived an apparent thermal conductivity $\mathbf{k}^{\star}$, which in general is treated as a scalar, $k^{\star}$, either assuming the medium to be isotropic, or at most focusing on its vertical component [*Yen*, 1981; *Sturm et al.*, 1997; *Kaempfer et al.*, 2005; *Morin et al.*, 2010; *Riche and Schneebeli*, 2010].

To meet the needs of applications that require the thermal properties of snow to be estimated based on other physical variables (e.g., numerical snowpack models), experimental fits between $k^{\star}$ and snow density (ρ_s) have been proposed [*Yen*, 1981; *Sturm et al.*, 1997; *Domine et al.*, 2011]. Such regression curves differ widely: there is up to a factor of two

difference between the regression curve of *Sturm et al.* [1997] and *Yen* [1981]. In addition, a considerable scatter of measured $k^\star$ values is found around the best fitting curve between $k^\star$ and ρ_s [*Sturm et al.*, 1997]. Both of these issues highlight the need for a re-assessment of the variables related to $k^\star$, the partitioning between the various physical processes involved in heat transfer, and the experimental methods used to infer $k^\star$.

To contribute to this effort, we carried out numerical simulations of the conductivity of snow from its microstructure. This was done using 30 different 3D images of snow obtained by means of microtomography [*Brzoska et al.*, 1999a; *Coléou et al.*, 2001; *Schneebeli and Sokratov*, 2004; *Kaempfer et al.*, 2005]. Only conduction through ice and air was considered in the heat transfer, leading to computing the true effective thermal conductivity tensor of snow ($\mathbf{k}^{\text{eff}}$) from a material science perspective [*Rolland du Roscoat et al.*, 2008]. This work follows the pioneering developments of *Kaempfer et al.* [2005], who first reported computations of the vertical component of $\mathbf{k}^{\text{eff}}$ from tomographic images and compared them to experimental data. The main differences lie in the fact that our study considers a wide range of snow types, uses the periodic homogenization method [*Auriault et al.*, 2009] and evaluates the anisotropy of $\mathbf{k}^{\text{eff}}$. In addition, it includes thermal conduction in interstitial air, which was neglected by *Kaempfer et al.* [2005] and, more recently, by *Shertzer and Adams* [2011].

4.2 Methods

4.2.1 Snow samples

The numerical analyses were performed on 30 tomographic 3D images obtained from previous experiments or field sampling, spanning most snow types of seasonal snow, i.e. Precipitation Particles (PP), Decomposing and Fragmented precipitation particles (DF), Rounded Grains (RG), Faceted Crystals (FC), Depth Hoar (DH) and Melt Forms (MF), according to the International Classification for Seasonal Snow on the Ground [ICSSG; *Fierz et al.*, 2009]. Most snow samples were impregnated with 1-chloronaphthalene prior to 3D imaging, as described by *Flin et al.* [2003]. A few other samples were prepared using a previously developed technique (diethyl-orthophthalate soaking, followed by iso-octane rinsing just before tomography [*Coléou et al.*, 2001]).

One third of the snow samples were directly collected in the field: 10 snow specimens (PP, DF and RG) were sampled at increasing depths in the snowpack of the Girose glacier (Écrins, French Alps) [*Flin et al.*, 2011]. Another PP snow sample was collected at Col de Porte (Chartreuse, French Alps). The remaining snow samples were obtained during controlled cold-room experiments: a first series (PP, DF and RG) was obtained under isothermal conditions at 271 K directly from deposited natural snow [*Flin et al.*, 2004]. Another sample (RG) was obtained under similar conditions, but after sieving. Four samples were obtained from different experiments where the snow evolved under a fixed temperature gradient ranging between 16 and 100 $\mathrm{K\,m^{-1}}$, at a temperature between 268 and 270 K. These specimens correspond to various stages of transformations into facetted crystals and depth hoar [*Coléou et al.*, 2001; *Flin and Brzoska*, 2008]. A series of wet

snow samples (MF) were obtained by grain coarsening in water-saturated snow using the method of *Raymond and Tusima* [1979] followed by draining of their liquid water content [*Coléou et al.*, 2001; *Flin et al.*, 2011]. Additional information concerning the samples are given in a table provided in Appendix C.

4.2.2 Computation of the effective thermal conductivity of snow

Let us consider heterogeneous systems such as porous media where l and L are the characteristic lengths of the heterogeneities at the pore scale and of the macroscopic sample or excitation, respectively. Physical phenomena in such systems can be modeled by an equivalent continuous macroscopic description, provided that the condition of separation of scales is satisfied [*Auriault*, 1991; *Auriault et al.*, 2009], i.e. L is sufficiently large compared to l. This condition implies the existence of a Representative Elementary Volume (REV) of size l for the material. We provide here the main steps concerning the derivation of the macroscopic heat transfer equation from the physics at the pore scale using the homogenization method for periodic structures [*Bensoussan et al.*, 1978; *Auriault*, 1991].

Without loss of generality, the medium is assumed to be Ω-periodic. The period, i.e. the REV, is defined by Ω, where Ω_i and Ω_a are the domains occupied by the ice and the air respectively. The common boundary of Ω_i and Ω_a is denoted Γ. The size of the periodic cell Ω is l. Neglecting convection, phase change and under steady state conditions, heat transfers at the microscopic scale are described by:

$$\boldsymbol{\nabla} \cdot (\kappa_i \boldsymbol{\nabla} T_\mathrm{i}) = 0 \quad \text{in } \Omega_\mathrm{i} \tag{4.1}$$

$$\boldsymbol{\nabla} \cdot (\kappa_a \boldsymbol{\nabla} T_\mathrm{a}) = 0 \quad \text{in } \Omega_\mathrm{a} \tag{4.2}$$

$$T_\mathrm{i} - T_\mathrm{a} = 0 \quad \text{on } \Gamma \tag{4.3}$$

$$(\kappa_a \boldsymbol{\nabla} T_\mathrm{a} - \kappa_i \boldsymbol{\nabla} T_\mathrm{i}) \cdot \mathbf{n} = 0 \quad \text{on } \Gamma \tag{4.4}$$

where $\mathbf{n}$ is the normal to Γ. T refers to the temperature and κ to the thermal conductivity (considered isotropic) of the phases denoted in subscripts. Using the homogenization method for periodic structures, it can be shown that the corresponding macroscopic description is [*Auriault et al.*, 2009]:

$$\boldsymbol{\nabla} \cdot (\mathbf{k}^\mathrm{eff} \boldsymbol{\nabla} T) = 0, \tag{4.5}$$

where $\mathbf{k}^\mathrm{eff}$ is the effective thermal conductivity tensor defined as:

$$\mathbf{k}^\mathrm{eff} = \frac{1}{|\Omega|} \left(\int_{\Omega_\mathrm{a}} \kappa_a (\boldsymbol{\nabla} \mathbf{t}_\mathrm{a} + \mathbf{I}) \mathrm{d}\Omega + \int_{\Omega_\mathrm{i}} \kappa_i (\boldsymbol{\nabla} \mathbf{t}_\mathrm{i} + \mathbf{I}) \mathrm{d}\Omega \right) \tag{4.6}$$

where $\mathbf{I}$ is the identity tensor, and where the two Ω-periodic vectors $\mathbf{t}_\mathrm{i}$ and $\mathbf{t}_\mathrm{a}$ are solutions of the following boundary value problem over the REV:

$$\boldsymbol{\nabla} \cdot (\kappa_i (\boldsymbol{\nabla}\ \mathbf{t}_\mathrm{i} + \mathbf{I})) = \mathbf{0} \quad \text{in } \Omega_\mathrm{i} \tag{4.7}$$

$$\boldsymbol{\nabla} \cdot (\kappa_a (\boldsymbol{\nabla}\ \mathbf{t}_\mathrm{a} + \mathbf{I})) = \mathbf{0} \quad \text{in } \Omega_\mathrm{a} \tag{4.8}$$

$$\mathbf{t}_\mathrm{i} - \mathbf{t}_\mathrm{a} = \mathbf{0} \quad \text{on } \Gamma \tag{4.9}$$

$$(\kappa_a (\boldsymbol{\nabla}\ \mathbf{t}_\mathrm{a} + \mathbf{I}) - \kappa_i (\boldsymbol{\nabla}\ \mathbf{t}_\mathrm{i} + \mathbf{I})) \cdot \mathbf{n} = \mathbf{0} \quad \text{on } \Gamma \tag{4.10}$$

$$\frac{1}{|\Omega|} \int_\Omega (\mathbf{t}_\mathrm{a} + \mathbf{t}_\mathrm{i}) \mathrm{d}\Omega = \mathbf{0} \tag{4.11}$$

In what follows, this boundary value problem has been numerically solved on REVs extracted from 3D images of snow by using the commercial software Geodict [*Thoemen et al.*, 2008].

Computations were carried out for all samples using the thermal properties of ice and air at 271 K ($\kappa_a = 0.024$ W m^{-1} K^{-1} and $\kappa_i = 2.107$ W m^{-1} K^{-1}). Computations were also carried out for a few selected samples, using thermal properties of ice and air at 203 K, i.e. κ_a and κ_i values are 0.019 W m^{-1} K^{-1} and 2.900 W m^{-1} K^{-1}, respectively [*Yen*, 1981; *Sturm et al.*, 1997]. Finally, calculations were also performed for some samples, neglecting conduction in air, i.e. setting $\kappa_a = 0$ W m^{-1} K^{-1}. We refer to k^{eff} as the average value of the three diagonal terms of $\mathbf{k}^{\text{eff}}$, k_z^{eff} its vertical component, and k_{xy}^{eff} the average of its two horizontal components.

4.2.3 Computation of other variables from 3D images

The representative elementary volume (REV) constitutes the smallest fraction of the sample volume from which a variable representative of the whole can be determined. For all snow samples, attention was paid to ensure that computations of the thermal conductivity and the density were carried out on a REV. It can be estimated by calculating values of a given variable from several sub-volumes of increasing sizes. The REV is reached as soon as values do not vary significantly when sub-volumes of computation increase. Note that the REV size depends on the variable and on the sample studied. For the considered study, REVs for thermal conductivity estimation range from about 2.5 mm (PP) to 5.5 mm (MF). Calculations performed on a lower volume than the REV were disregarded. Snow density was estimated from the tomographic images using a standard voxel counting algorithm.

4.2.4 Experimental data

In parallel to the numerical experiments described above, an experiment was carried out to compare thermal conductivities obtained numerically to those measured experimentally on the same samples. A snow slab (area: 1 m^2, thickness: 0.14 m) was exposed in a cold room to a high vertical temperature gradient (43 K m^{-1}) maintained by two horizontal copper plates thermally regulated at 272 and 266 K, at the bottom and top, respectively. The experiment lasted for three weeks, during which the snow, originally sieved rounded grains with a density of 300 kg m^{-3}, transformed into depth hoar, with an insignificant change in density. Two of the snow samples used for numerical computations originate from this experiment. In addition, the thermal conductivity of snow was measured using a needle-probe following the method of *Morin et al.* [2010]. Briefly, a needle (Hukseflux TP02) with a diameter of 1.5 mm and a heated length of 10 cm was inserted in the snow at half-height and remained there for the whole experiment. The needle was heated with a constant power of 0.4 W m^{-1} once a day for 100 s, and the temperature rise in the middle of the needle was monitored and used to determine the apparent thermal conductivity $k^{\star}_{\text{needle}}$ relevant to this experimental approach [*Sturm et al.*, 1997; *Morin et al.*, 2010]. In parallel, the heat-flux at the bottom of the snow slab was measured continuously using two Hukseflux HFP01 sensors (accuracy of ± 5 %), and divided by the temperature gradient measured

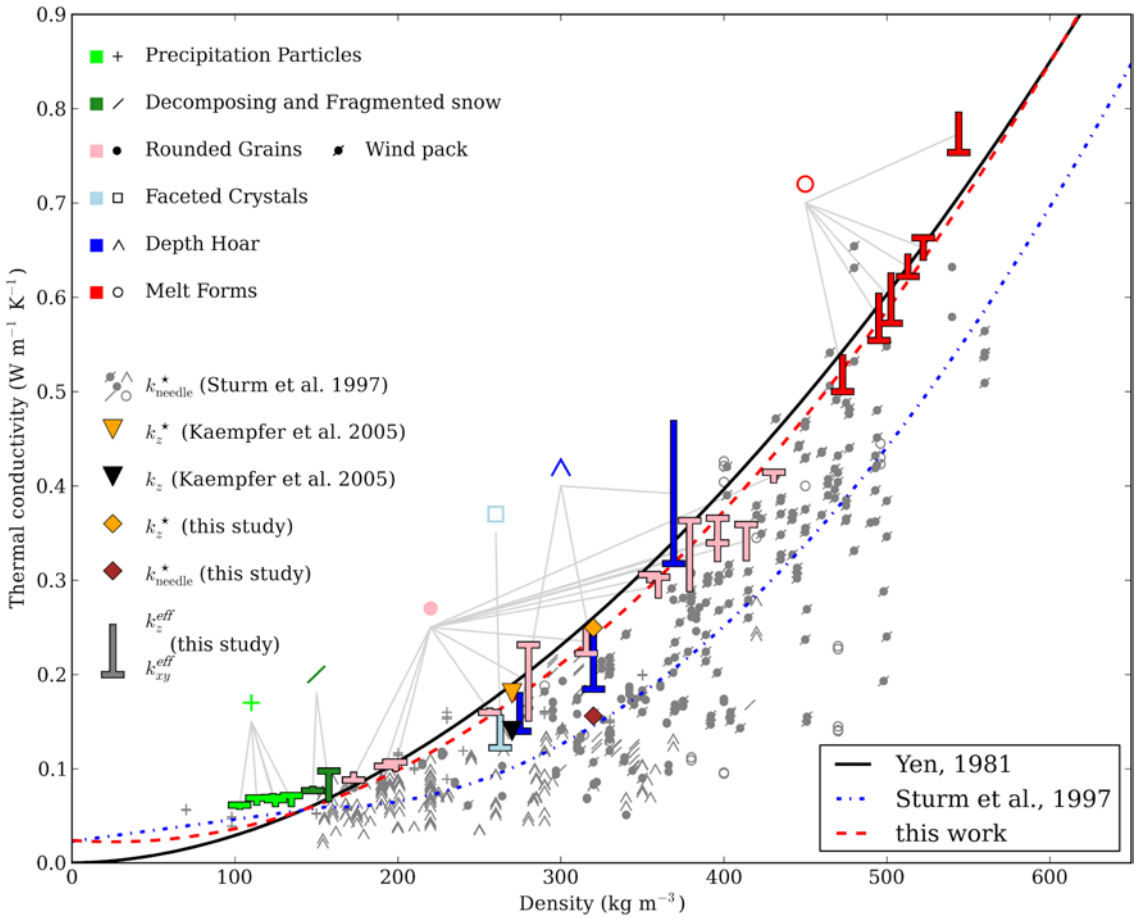

Figure 4.1: Effective thermal conductivity vs. snow density (ρ_s). The k_z^{eff} and k_{xy}^{eff} components of the computed $\mathbf{k}^{\text{eff}}$ data are provided ("T" shape symbols pointing to the k_z^{eff} value) and compared to (i) needle-probe measurements by *Sturm et al.* [1997], using gray symbols corresponding to the ICSSG [*Fierz et al.*, 2009], (ii) numerical and experimental data from *Kaempfer et al.* [2005] using inverted triangles in black and yellow, respectively and (iii) experimental data from this study using diamonds. Also shown are the regression curves from *Yen* [1981], *Sturm et al.* [1997] and the quadratic equation derived in this study. See text for a full description of the notations used.

using Pt100 temperature probes, to determine independently the vertical component of the apparent thermal conductivity of snow ($k_z^{\star}$).

4.3 Results

4.3.1 Effective thermal conductivity versus snow density

Figure 4.1 shows the two components k_z^{eff} and k_{xy}^{eff} of the effective thermal conductivity of snow, computed from all the 3D images considered in this work, as a function of snow density (ρ_s). Non-diagonal terms of $\mathbf{k}^{\text{eff}}$ are more than 100 times lower than diagonal terms and can be neglected (the image axes x, y and z correspond to the principal directions of the microstructure, z being along the direction of gravity and the macroscopic temperature gradient, which are similar in our cases). The figure shows that both components (k_z^{eff} and

k_{xy}^{eff}) of $\mathbf{k}^{\text{eff}}$ are strongly correlated to snow density, and covary with it. The lowermost k^{eff} values are obtained for fresh snow, exhibiting values as low as 0.06 $\mathrm{W\,m^{-1}\,K^{-1}}$ ($k_z^{\text{eff}} \simeq k_{xy}^{\text{eff}}$) at a density of 103 $\mathrm{kg\,m^{-3}}$. Refrozen wet snow shows the largest values, with k^{eff} values near 0.77 $\mathrm{W\,m^{-1}\,K^{-1}}$ at a density of 544 $\mathrm{kg\,m^{-3}}$. The values of k^{eff} were fitted to snow density leading to the following equation:

$$k^{\text{eff}} = 2.5 \times 10^{-6}\,\rho_s^2 - 1.23 \times 10^{-4}\,\rho_s + 0.024 \tag{4.12}$$

This fit has been chosen such as k^{eff} corresponds to the thermal conductivity of air when snow density is zero. The correlation coefficient for the 30 samples is 0.985, which is best represented by the fact that standard deviation of the residuals to the regression curve is only 0.025 $\mathrm{W\,m^{-1}\,K^{-1}}$. The regression curve is the same whether k_z^{eff} or k^{eff} is used to derive Eq. (4.12). We also note that our data show an excellent agreement with the regression curve proposed by *Yen* [1981]: $k^{\text{eff}} = 2.22362 \times (\rho_{\text{snow}}/\rho_{\text{water}})^{1.885}$.

4.3.2 Anisotropy

As displayed on Figure 4.1, several samples show a strong difference between the vertical and horizontal component of $\mathbf{k}^{\text{eff}}$. Rounded grains (RG) samples collected in the field, at a depth of several tens of cm below the surface, exhibit k_{xy}^{eff} values higher than k_z^{eff}. The ratio $k_z^{\text{eff}}/k_{xy}^{\text{eff}}$ can be as low as 0.7. In contrast, several facetted (FC) and depth hoar (DH) samples exhibit an inverse behavior, where the $k_z^{\text{eff}}/k_{xy}^{\text{eff}}$ ratio can be as high as 1.5. This anisotropy induces a slight scatter around the overall correlation between k^{eff} and ρ_s (Eq. 4.12). We note that our anisotropy results are consistent with the recent study by *Shertzer and Adams* [2011], who estimated the effective thermal conductivity using microstructural parameters computed from 3D images. The granular approach used [*Batchelor and O'Brien*, 1977], was applied to two series of snow samples obtained during experiments under high temperature gradient. Although their computations are based on 2D slices of the full images and neglect heat conduction in air, the inception and build-up of anisotropy in terms of effective thermal conductivity of snow during temperature gradient metamorphism is in agreement with our results obtained on different snow types.

4.3.3 Influence of temperature and conduction in interstitial air

In this section, for the sake of brevity, we focus on the vertical component k_z^{eff} of $\mathbf{k}^{\text{eff}}$. However, the k_z^{eff} results can be extended to the whole tensor $\mathbf{k}^{\text{eff}}$ without any loss of generality.

Figure 4.2 shows that k_z^{eff} increases with decreasing temperature in a non-linear manner depending on snow type. Although ice and air display opposite variations with temperature (κ_i increases while κ_a decreases with decreasing temperature), this result indicates that much of the variations in $\mathbf{k}^{\text{eff}}$ stem from variations in κ_i. The effect is more pronounced in denser snow: snow with very high porosity, made mostly of air, shows almost no variation with temperature. Such results are opposite to the experimental findings of *Pitman and Zuckerman* [1967], who observed a decrease of $k_z^{\star}$ with decreasing temperature.

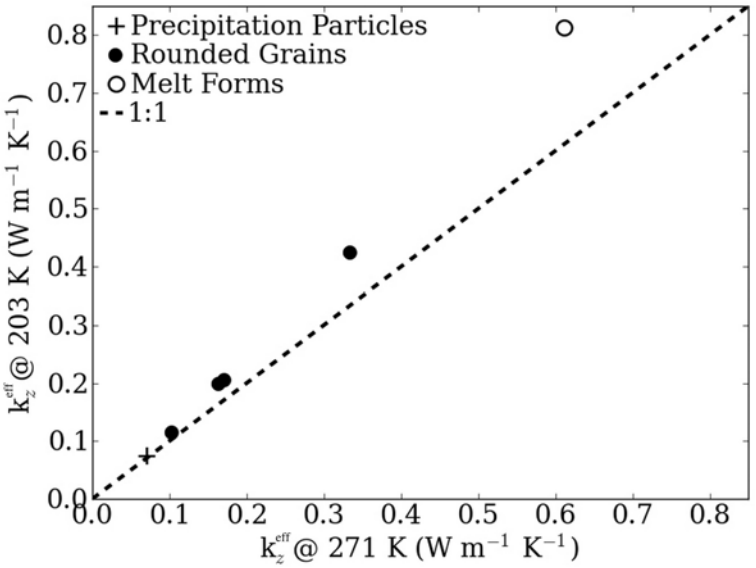

Figure 4.2: Impact of temperature on the effective thermal conductivity of snow. Computations were made using the thermal conductivity of air and ice at 271 and 203 K, respectively. Symbols correspond to the ICSSG [*Fierz et al.*, 2009].

Table 4.1: Impact of interstitial air conduction on the effective thermal conductivity of snow. The absence of conduction in interstitial air was assessed by setting $\kappa_a = 0$ W m^{-1} K^{-1}.

Sample	Type	ρ_s kg m^{-3}	k_z^{eff} W m^{-1} K^{-1}	
			air cond.	no air cond.
I01	PP	103	0.06	0.006
I23	RG	256	0.16	0.10
4A	DH	315	0.25	0.18

The numerical experiments summarized in Table 4.1 demonstrate that conduction in interstitial air plays a vital role in heat transfer through snow. Indeed, ignoring heat conduction in air leads to underestimating k_z^{eff} by a factor 10 for precipitation particles (see Table 4.1). Even in denser snow such as depth hoar or rounded grains, neglecting conduction in air lowers by up to a factor 2 the effective thermal conductivity of snow. This result stems from the fact that, by setting κ_a to zero, even the smallest gaps in the network of ice grains may lead to no heat transfer at all. The impact of dead-ends within the microstructure is therefore greatly enhanced when conduction in air is neglected. *Kaempfer et al.* [2005] carried out a simulation of k_z^{eff} on a rounded grain snow sample with a density of 268 kg m^{-3}, held at 265 K, where they used a value for κ_i of 2.29 W m^{-1} K^{-1}. They found a value for k_z^{eff} of 0.15 $\pm$ 0.01 W m^{-1} K^{-1}, by neglecting conduction in the pores. This value is consistent with our results, as it falls in between the two k_z^{eff} values of one of our RG sample (see Table 4.1) featuring a similar density (256 kg m^{-3}), by taking into account, or not, heat conduction in interstitial air.

4.3.4 Comparison to experimental methods

Figure 4.1 compares data from different methods to determine the effective or apparent thermal conductivity of snow, in the (k, ρ_s) space. Values of $\mathbf{k}^{\text{eff}}$ determined from 3D images are provided from *Kaempfer et al.* [2005] and this study. Data from needle-probe measurements ($k^{\star}_{\text{needle}}$) stem from the large compilation of *Sturm et al.* [1997], and also from measurements carried out during our own cold room experiment. Finally, data originating from experiments where the heat-flux and the temperature gradient were ratioed ($k^{\star}_z$) are given for our experiment and from *Kaempfer et al.* [2005]. The data indicate that, overall, the measurements from needle-probes are systematically significantly lower than other methods. Experimental data from flux/gradient measurements correspond better to k^{eff}_z computations although discrepancies are also significant. We note that measurements by *Sturm et al.* [1997] and *Kaempfer et al.* [2005] were carried out at temperatures generally lower than the conditions of our simulations. Nevertheless, our results correspond to the upper bound of existing measurements, and computations carried out using conductive thermal properties of ice and air at lower temperatures indicate that $\mathbf{k}^{\text{eff}}$ components can only increase when temperature decreases. Neither the temperature dependency of κ_i and κ_a nor the snow anisotropy explain the observed discrepancy.

4.4 Discussion and conclusions

Riche and Schneebeli [2010] have recently advocated that needle-probe measurements of the apparent thermal conductivity of snow ($k^{\star}_{\text{needle}}$) were biased low because of microstructural disturbances induced by the insertion of the needle into the snow. However, this conclusion was reached using an inadequate choice of instrumental parameters, in particular the heating time and the time window used to infer $k^{\star}_{\text{needle}}$. Indeed, numerical modeling of the impact of an air gap around the needle has shown no significant effect on the estimation of $k^{\star}_{\text{needle}}$, provided that the first 30 s into the heating period are discarded [*Morin et al.*, 2010]. Experiments on the same issue have ruled out that the quality of the thermal contact was a significant cause of error [*M. Sturm, pers. commun.*, 2011]. However, in light of the discrepancy observed between the three available methods to measure the thermal properties of snow, it appears necessary to delve deeper into this conundrum. Firstly, it must be noted that the three methods (needle-probe, flux/gradient and numerical modeling) do not exactly probe the same variable. Needle-probe measurements are carried out under the assumption that the medium is homogeneous (i.e. the size of the REV is smaller than the typical radius of the cylinder of influence around the needle, i.e. about 10 mm in common snow types *Morin et al.*, 2010), isotropic (i.e. the vertical and horizontal components of $\mathbf{k}^{\star}$ are the same), and take place in transient mode, leading to the build-up of locally strong temperature gradients. Flux/gradient measurements focus only on the vertical component of $\mathbf{k}^{\star}$, in steady-state conditions. Last, as described above, numerical modeling considers only two out of the many processes potentially contributing to heat transfer in snow. It thus appears likely that the ability for the different techniques to provide convergent results strongly depends on snow type, and also on the temperature and

the temperature gradient, as the latent heat effects and water vapor diffusion undoubtedly depend on these variables. Effects from snow type and temperature may even interact in a nontrivial manner. It also seems likely that the latent heat effects and water vapor diffusion contribute to heat transfer in variable proportions depending on snow type, given that k_z^{eff} and $k_z^{\star}$ differ non systematically.

In light of the above-mentioned findings, we recommend purely conductive effects (i.e. conduction through ice and interstitial air) to be considered separately from non-conductive processes. At present, the only method able to unambiguously characterize the purely conductive effective thermal conductivity is numerical modeling based on microstructure 3D images. Our study, carried out on 30 snow samples spanning the full range of seasonal snow type, reveals that the effective thermal conductivity of snow is strongly correlated with snow density, and follows closely the regression curve proposed by *Yen* [1981]. Unexpectedly, this corroborates the use of this relationship in several snowpack models [e.g. Crocus, *Brun et al.*, 1989]. Work is needed to disentangle the impact of non-conductive processes on experimental methods meant to determine $\mathbf{k}^{\text{eff}}$, as well as to better account for such effects in terms of heat transfer through the snowpack. An appealing approach is to explicitly simulate heat transfer in snow, taking into account both conductive and non-conductive effects, based on the microstructure of snow. Only at this cost will significant improvements of the understanding and modeling of heat transfer in snow occur.

Chapter

5 3-D image-based numerical computations of snow permeability: links to specific surface area, density, and microstructural anisotropy

Contents

This chapter corresponds to the paper entitled *3-D image-based numerical computations of snow permeability: links to specific surface area, density, and microstructural anisotropy* by Calonne N., Geindreau C., Flin F., Morin S., Lesaffre B., Rolland du Roscoat S., and Charrier P., published in *The Cryosphere*, 2012.

Abstract

We used three-dimensional (3-D) images of snow microstructure to carry out numerical estimations of the full tensor of the intrinsic permeability of snow ($\mathbf{K}^{\text{eff}}$). This study was performed on 35 snow samples, spanning a wide range of seasonal snow types. For several snow samples, a significant anisotropy of permeability was detected and is consistent with that observed for the effective thermal conductivity obtained from the same samples. The anisotropy coefficient, defined as the ratio of the vertical over the horizontal components of $\mathbf{K}^{\text{eff}}$, ranges from 0.74 for a sample of decomposing precipitation particles collected in the field to 1.66 for a depth hoar specimen. Because the permeability is related to a characteristic length, we introduced a dimensionless tensor $\mathbf{K}^{\text{eff}*} = \mathbf{K}^{\text{eff}}/r_{\text{es}}^2$, where the equivalent sphere radius of ice grains (r_{es}) is computed from the specific surface area of snow (SSA) and the ice density (ρ_i) as follows: $r_{\text{es}} = 3/(\text{SSA} \times \rho_i)$. We define K^{eff} and $K^{\text{eff}*}$ as the average of the diagonal components of $\mathbf{K}^{\text{eff}}$ and $\mathbf{K}^{\text{eff}*}$, respectively. The 35 values of $K^{\text{eff}*}$ were fitted to snow density (ρ_s) and provide the following regression: $K^{\text{eff}} = (3.0 \pm 0.3)\, r_{es}^2 \exp\left((-0.0130 \pm 0.0003)\rho_s\right)$. We noted that the anisotropy of permeability does not affect significantly the proposed equation. This regression curve was applied to several independent datasets from the literature and compared to other existing regression curves or analytical models. The results show that it is probably the best currently available simple relationship linking the average value of permeability, K^{eff}, to snow density and specific surface area.

5.1 Introduction

The intrinsic permeability ($\mathbf{K}$) is an important physical property of snow. Defined in a tensorial way, $\mathbf{K}$ (m^2) links the pressure gradient $\boldsymbol{\nabla} p$ ($\text{Pa}\,\text{m}^{-1}$) and the discharge per unit area $\mathbf{q}$ ($\text{m}\,\text{s}^{-1}$) through the Darcy's law $\mathbf{q} = -(1/\mu)\mathbf{K}\boldsymbol{\nabla} p$, where μ is the dynamic viscosity of the fluid ($\text{kg}\,\text{m}^{-1}\,\text{s}^{-1}$). The intrinsic permeability is of particular interest to quantify transport properties of snow and firn, such as wind pumping processes [*Colbeck*, 1989, 1997], air convection [*Akitaya*, 1974; *Powers et al.*, 1985; *Brun and Touvier*, 1987; *Sturm and Johnson*, 1991; *Albert et al.*, 2004] and liquid water flow [*Colbeck*, 1975, 1976; *Waldner et al.*, 2004; *Katsushima et al.*, 2009; *Yamaguchi et al.*, 2010]. It is a key variable for a wide number of applications such as atmospheric and firn chemistry [*Freitag et al.*, 2002; *Neumann*, 2003; *Grannas et al.*, 2007; *Domine et al.*, 2008] or snow-firn metamorphism [*Albert*, 2002; *Hörhold et al.*, 2009]. Permeability has also been proposed as a means of characterization for quantitative snow classification [*Bader*, 1939; *Jordan et al.*, 1999b; *Arakawa et al.*, 2009]. Indeed, most physical properties of snow, including its permeability, are linked to the geometrical arrangement of ice, air, water vapor and sometimes liquid water, referred to as its microstructure.

The first quantitative investigations of snow permeability are attributed to *Bader* [1939]. *Shimizu* [1970], *Sommerfeld and Rocchio* [1993], *Jordan et al.* [1999b] and *Arakawa et al.* [2010] realized extensive experiments on seasonal snow and proposed parameterizations depending on grain size and density. However, these studies are characterized by a significant scatter in the results, which seems mainly due to experimental issues [*Sommerfeld and Rocchio*, 1993] and to sometimes ambiguous definitions of grain size [*Jordan et al.*,

1999b]. In addition existing field permeameters require snow samples to be several cm large (cylinder diameter on the order of 10 to 20 cm typically, and cylinder height from several to tens of cm) [*Shimizu*, 1970; *Albert et al.*, 2000; *Arakawa et al.*, 2009] which generally exceeds the size within which snow properties can reasonably be considered homogeneous [*Schneebeli et al.*, 1999; *Pielmeier and Schneebeli*, 2003; *Matzl and Schneebeli*, 2006, 2010; *Marshall and Johnson*, 2009].

More recently, the availability of 3-D images of snow and firn from X-ray tomography [*Brzoska et al.*, 1999a; *Coléou et al.*, 2001; *Freitag et al.*, 2004; *Schneebeli and Sokratov*, 2004; *Kaempfer et al.*, 2005; *Chen and Baker*, 2010] opened the way to numerical simulations, applying to snow the methods developed for porous media in general [*Spanne et al.*, 1994; *Ferreol and Rothman*, 1995; *Martys and Chen*, 1996; *Arns et al.*, 2001, 2004]. In particular, such techniques allow to estimate the permeability for snow samples much smaller than those used for experimental measurements, thereby reducing if not eliminating issues associated with the intrinsic heterogeneity of the samples probed. Recently, *Freitag et al.* [2002] and *Courville et al.* [2010] computed one component of the permeability of firn samples using Lattice-Boltzman modeling and *Zermatten et al.* [2011] performed direct pore-level simulations on five snow samples. While these numerical computations methods are particularly promising, the obtained results show only a qualitative agreement with previous experimental studies and theoretical models, and do not take into account the anisotropy of the permeability.

We carried out numerical estimations of the full 3-D tensor of intrinsic permeability ($\mathbf{K}^{\text{eff}}$) on 35 3-D images of seasonal snow obtained from microtomography. Computations were performed with the software Geodict [*Thoemen et al.*, 2008; *Koivu et al.*, 2009; *Calonne et al.*, 2011] and were based on the periodic homogenization method [*Auriault et al.*, 2009]. The main objective of this paper was to elaborate a parameterization of the snow permeability from other variables measurable in the field. For this purpose, we studied the relationship between the computed permeability, snow density and grain size, defined here as the equivalent sphere radius, at the scale of the representative elementary volume (REV). This relationship obtained using our data was compared to existing literature datasets as well as other equations from theoretical models and regressions. In addition, we focused on the anisotropy of permeability, available from the computed 3-D tensor of permeability.

5.2 Methods

5.2.1 Snow samples

Numerical computations were performed on 35 tomographic images obtained from previous experiments or field sampling [e.g. *Calonne et al.*, 2011], spanning most types of seasonal snow, i.e. precipitation particles (PP), decomposing and fragmented precipitation particles (DF), rounded grains (RG), faceted crystals (FC), depth hoar (DH) and melt forms (MF), according to the International Classification for Seasonal Snow on the Ground (ICSSG) [*Fierz et al.*, 2009].

Two-thirds of the snow samples come from controlled cold-room experiments: a first series (PP, DF and RG) was obtained by subjecting deposited natural snow to isothermal conditions at 271 K [*Flin et al.*, 2004]. Another RG sample was obtained under similar conditions, but after sieving. A second series (RG, FC and DH) was obtained under a temperature gradient of $43\,\mathrm{K\,m^{-1}}$ at 269 K and corresponds to various stages of metamorphism of the initial sieved snow (RG) into FC then DH. Two other similar experiments, with a gradient of 16 and $100\,\mathrm{K\,m^{-1}}$ at 268 and 270 K, provided two samples (FC and DH) [*Coléou et al.*, 2001; *Flin and Brzoska*, 2008]. A series of MF samples was obtained by grain coarsening in water-saturated snow using the method of *Raymond and Tusima* [1979] followed by draining their liquid water content [*Coléou et al.*, 2001; *Flin et al.*, 2011].

The remaining snow samples were directly collected in the field: 10 snow specimens (PP, DF and RG) were sampled at increasing depths in the snowpack of the Girose glacier (Écrins, French Alps) [*Flin et al.*, 2011]. Another PP sample was collected at Col de Porte (Chartreuse, French Alps).

All 3-D images considered in this study are cubic, have an edge size ranging from 2.51 to 9.66 mm, and a resolution between 4.91 micrometer (μm) and 10 μm, depending on the snow type. Additional information are indicated in Table 1 of Appendix D.

5.2.2 Computations of snow permeability

Auriault [1991, 2011] has shown that physical phenomena in random and in periodic medium can be modeled by a similar equivalent continuous macroscopic description, provided that the condition of separation of scales is satisfied. This fundamental condition may be expressed as $\varepsilon \ll 1$, where ε represents the separation of scale and is defined as $\varepsilon = l/L$, in which l and L are the characteristic lengths of the heterogeneities at the pore scale and of the macroscopic sample or excitation, respectively. This condition implies the existence of a representative elementary volume (REV) of size l of the material and the physical phenomena. The REV constitutes the smallest fraction of the sample volume from which a variable representative of the whole can be determined. In practice, periodic boundary conditions are thus widely used to compute effective properties of random media [*Kanit et al.*, 2003; *Bernard et al.*, 2005; *Koivu et al.*, 2009; *Calonne et al.*, 2011]. Assuming for snow that $\varepsilon \ll 1$, we applied the homogenization method for periodic structures to derive the Darcy's law from the physics at the pore scale [*Ene and Sanchez-Palencia*, 1975], as described in the following. Let us consider a rigid porous matrix, which is periodic with period Ω, i.e. the size of the REV, and is fully saturated by an incompressible Newtonian fluid of density ρ_a and viscosity μ_a. Ω_i and Ω_a are the domains occupied by the solid and the fluid, respectively. The common boundary of Ω_i and Ω_a is denoted Γ. The porosity is defined as $\phi = |\Omega_a|/|\Omega|$. At the pore scale, the steady state flow is described by

$$\mu_a \triangle \mathbf{v}_a - \boldsymbol{\nabla} p_a = \rho_a (\mathbf{v}_a \cdot \boldsymbol{\nabla}) \mathbf{v}_a \qquad \text{within } \Omega_a \tag{5.1}$$

$$\boldsymbol{\nabla} \cdot \mathbf{v}_a = 0 \qquad \text{within } \Omega_a \tag{5.2}$$

$$\mathbf{v}_a = \mathbf{0} \qquad \text{on } \Gamma \tag{5.3}$$

where $\mathbf{v}_a$ and p_a are the velocity and the pressure of the fluid, respectively. Using the homogenization method, it can be shown that the corresponding macroscopic description strongly depends on the order of magnitude of the pore Reynolds number, $R_{\text{el}} = |\rho_a(\mathbf{v}_a \cdot \boldsymbol{\nabla})\mathbf{v}_a|/|\mu_a \triangle \mathbf{v}_a| = \mathcal{O}(\rho_a v_{a_c} l/\mu)$ where v_{a_c} is a characteristic value of fluid velocity. When $R_{\text{el}} < \mathcal{O}(1)$, the macroscopic flow is described by Darcy's law, otherwise non-linearities appear at the macroscopic scale [*Mei and Auriault*, 1991]. In what follows, it is assumed that $R_{\text{el}} < \mathcal{O}(1)$, which is typically the case if we consider airflow through snow and firn induced by moderate winds ($< 6\,\text{m}\,\text{s}^{-1}$) over the snowpack surface [*Albert*, 2002]. Under such conditions, the macroscopic description is written:

$$\langle \mathbf{v}_a \rangle = -\frac{\mathbf{K}^{\text{eff}}}{\mu_a} \boldsymbol{\nabla} p_a, \quad \boldsymbol{\nabla} \cdot \langle \mathbf{v}_a \rangle = 0, \quad \text{with } \langle \mathbf{v}_a \rangle = \frac{1}{\Omega} \int_{\Omega_a} \mathbf{v}_a \, \mathrm{d}\Omega \tag{5.4}$$

where $\langle \mathbf{v} \rangle = \mathbf{q}$ represents the Darcy's velocity and $\mathbf{K}^{\text{eff}}$ is the intrinsic permeability tensor of the porous media. This tensor, which is symmetric and positive, is defined as $K_{ij} = \langle k_{ij} \rangle$. The second order tensor $\mathbf{k}$ is the solution of the following boundary value problem over the REV,

$$\mu_a \triangle \mathbf{v}_a - \boldsymbol{\nabla} \tilde{p}_a - \boldsymbol{\nabla} p_a = \mathbf{0} \quad \text{within } \Omega_a \tag{5.5}$$

$$\boldsymbol{\nabla} \cdot \mathbf{v}_a = 0 \quad \text{within } \Omega_a \tag{5.6}$$

$$\mathbf{v}_a = \mathbf{0} \quad \text{on } \Gamma \tag{5.7}$$

where $\mathbf{v}_a = -(1/\mu_a)\mathbf{k}\boldsymbol{\nabla} p_a$, the pressure fluctuation $\tilde{p}_a$ (with $\langle \tilde{p}_a \rangle = 0$) are the periodic unknowns and $\boldsymbol{\nabla} p_a$ is a given macroscopic gradient of pressure. The components of the permeability tensor $\mathbf{K}^{\text{eff}}$ were estimated by solving the above boundary value problem (Eqs. 3a–3c) on a REV extracted from tomographic images (see Sect. 5.3.6), using the software Geodict (`http://www.geodict.de`). The boundary value problem is solved by using the finite difference method. Within this method a staggered grid (voxel) is used. The values of velocity and pressure are defined at center points of the faces and volume of the cubic unit cells, respectively. The partial differential equations for incompressible Stokes flow (Eqs. 3a–3c) are solved by using the FFF-Stokes solver based on fast Fourier transform. Periodic boundary conditions are applied on the external boundaries of each volume (see *Wiegmann* [2007] for more details).

Before carrying out the computations, voxels that are part of the network of interconnected pores were detected by image analysis, allowing to determine the ratio between closed and open porosity and to check that it was very small (less than 0.004 for all the samples). This means that it is correct to consider that air can flow through the whole porosity of the REVs for all of our samples.

In the following, the non-diagonal terms of the tensor $\mathbf{K}^{\text{eff}}$, about 50 times lower than diagonal terms, are not presented (the x-, y- and z-axes of 3-D images correspond to the principal directions of the microstructure, z being along the direction of the gravity). We note K_x^{eff}, K_y^{eff} and K_z^{eff} the diagonal term of the permeability tensor computed in the x-, y- and z-direction, respectively, K^{eff} the average value of the three terms, and K_{xy}^{eff} the average value of K_x^{eff} and K_y^{eff}. In the following, we mostly use K_z^{eff}, K_{xy}^{eff} and K^{eff}, i.e.

the vertical component, the average of the two horizontal components, and the average value of the three components of the permeability tensor, respectively.

5.2.3 Dimensionless permeability

The intrinsic permeability is strongly linked to a characteristic length of the microstructure of the medium considered [*Boutin and Geindreau*, 2010]. Because the dimension of the permeability is a square length, $\mathbf{K}^{\text{eff}}$ is often normalized by a characteristic length to the square, leading to a dimensionless tensor that we note $\mathbf{K}^{\text{eff}*}$.

Among various existing length metrics for snow [*Fierz et al.*, 2009], we focus on the equivalent sphere radius of snow (r_{es}, in m) [*Sommerfeld and Rocchio*, 1993; *Luciano and Albert*, 2002], also called the optical radius, optical-equivalent grain size or OGS [e.g. *Grenfell and Warren*, 1999; *Painter et al.*, 2006; *Fierz et al.*, 2009; *Brucker et al.*, 2011]. It is a characteristic length of the ice grains at the microscopic scale, which corresponds to the radius of a monodisperse collection of spheres having the same specific surface area (SSA) value than the sample considered. The snow SSA is defined as the total surface area of the air–ice interface per unit mass and can be quantitatively estimated by various means experimentally [e.g. *Matzl and Schneebeli*, 2006; *Domine et al.*, 2008; *Gallet et al.*, 2009; *Arnaud et al.*, 2011] and numerically using 3-D images [e.g. *Flin et al.*, 2011]. The equivalent sphere radius and snow SSA[a] are related by the following equation:

$$r_{\text{es}} = \frac{3}{\text{SSA} \times \rho_i} \tag{5.8}$$

where $\rho_i = 917\,\text{kg}\,\text{m}^{-3}$ is the ice density. In the following, $\mathbf{K}^{\text{eff}*}$ thus corresponds to $\mathbf{K}^{\text{eff}}/r_{\text{es}}^2$ and we keep the notation $K^{\text{eff}*}$, $K_z^{\text{eff}*}$ and $K_{xy}^{\text{eff}*}$ for the average, vertical and horizontal components of $\mathbf{K}^{\text{eff}*}$, respectively.

One could also choose to normalize $\mathbf{K}^{\text{eff}}$ by a characteristic length corresponding to the pore space and use the hydraulic radius (r_{h}), commonly applied to flow through pipes and open channels. This normalization is equivalent to using r_{es}, because these two radii are linked by the simple relationship: $r_{\text{h}} = r_{\text{es}}(1-\phi)/(3\phi)$ [*Bear*, 1972], where ϕ represents snow porosity. The granulometric analysis is another possible way to estimate a characteristic length [*Zermatten et al.*, 2011]. However, this approach is less convenient since it cannot be performed in the field, but only using 3-D images.

5.2.4 Microstructural properties

Snow porosity (ϕ), and thus snow density ($\rho_s = \rho_i\,(1-\phi)$, in $\text{kg}\,\text{m}^{-3}$), were estimated from 3-D images using a standard voxel counting algorithm.

The specific surface area (SSA, in $\text{m}^2\,\text{kg}^{-1}$) was computed from 3-D images using a stereological method as described by *Flin et al.* [2011] where this quantity is obtained by averaging SSA estimations computed along 3 orthogonal directions (x, y, z). The equivalent sphere radius was then computed from SSA using Eq. (5.8).

[a] The SSA is defined here per unit of mass in $\text{kg}\,\text{m}^{-2}$ and is linked to SSA_V (per unit of snow volume), presented in Chapter 2 and 3, by $\text{SSA} = \text{SSA}_\text{V} \,/\, \rho_s$, where ρ_s is the snow density. In the folowing, we also define SSA_I (per unit of ice volume), which is equal to SSA $\times \rho_i$.

The anisotropy coefficient of permeability, $A(\mathbf{K}^{\text{eff}})$, was computed from numerical estimations of the permeability tensor such as $A(\mathbf{K}^{\text{eff}}) = K_z^{\text{eff}}/K_{xy}^{\text{eff}}$.

The full tensor of the effective thermal conductivity ($\mathbf{k}^{\text{eff}}$, in $\mathrm{W\,m^{-1}\,K^{-1}}$) of the 35 snow samples considered was computed using the periodic homogenization. The effective thermal conductivity of most snow samples presented here were already described and included in a previous study [*Calonne et al.*, 2011]. Computations were extended to a few samples additionally considered in the present study. The coefficient of anisotropy of the effective thermal conductivity $A(\mathbf{k}^{\text{eff}})$ was defined similarly to that of intrinsic permeability, by ratioing the vertical and horizontal components of the tensor.

5.2.5 Representative elementary volume

The representative elementary volume (REV) of our samples was estimated by calculating values of a given variable from several sub-volumes of increasing sizes within the same sample. The size of the REV was assumed to be reached once values did not vary significantly when the size of the sub-volumes of computation increased. Note that the REV size depends on the variable and on the sample studied: REVs with respect to permeability are generally equal to or larger than those for other variables, such as density, SSA or the effective thermal conductivity [*Kanit et al.*, 2003; *Rolland du Roscoat et al.*, 2007]. Thus, a special attention must be paid to ensure that computations are carried out on a sufficiently large volume.

5.3 Results and discussion

5.3.1 Overview of the numerical calculations

The average value of the three components of the intrinsic permeability of snow, noted K^{eff}, ranges from 4×10^{-10} to $6 \times 10^{-9}\,\mathrm{m^2}$ for the 35 samples considered in this study. This range of values is consistent with previous experimental and numerical estimates of snow permeability [e.g. *Sommerfeld and Rocchio*, 1993; *Albert et al.*, 2000; *Luciano and Albert*, 2002; *Domine et al.*, 2008; *Arakawa et al.*, 2009; *Courville et al.*, 2010; *Zermatten et al.*, 2011]. Density and SSA span from 103 to $544\,\mathrm{kg\,m^{-3}}$ and from 4 to $56\,\mathrm{m^2\,kg^{-1}}$, respectively. For each sample, detailed values are provided in Table 2 of Appendix D.

Figure 5.1 provides an overview of the above results for the 35 samples of this study, showing the vertical ($K_z^{\text{eff}*}$) and horizontal ($K_{xy}^{\text{eff}*}$) components of the dimensionless permeability vs. snow density. PP samples exhibit the largest values of $K^{\text{eff}*}$ (1.05 for $\rho_s = 103\,\mathrm{kg\,m^{-3}}$), while the lowermost values are obtained for MF samples (2.16×10^{-3} for $\rho_s = 544\,\mathrm{kg\,m^{-3}}$). The figure clearly shows that $K_z^{\text{eff}*}$, $K_{xy}^{\text{eff}*}$ and thus $K^{\text{eff}*}$ decrease with increasing ρ_s.

5.3.2 Anisotropy

As shown by Fig. 5.1, values of the vertical ($K_z^{\text{eff}*}$) and horizontal ($K_{xy}^{\text{eff}*}$) components of the dimensionless permeability are not identical, and some samples exhibit significant

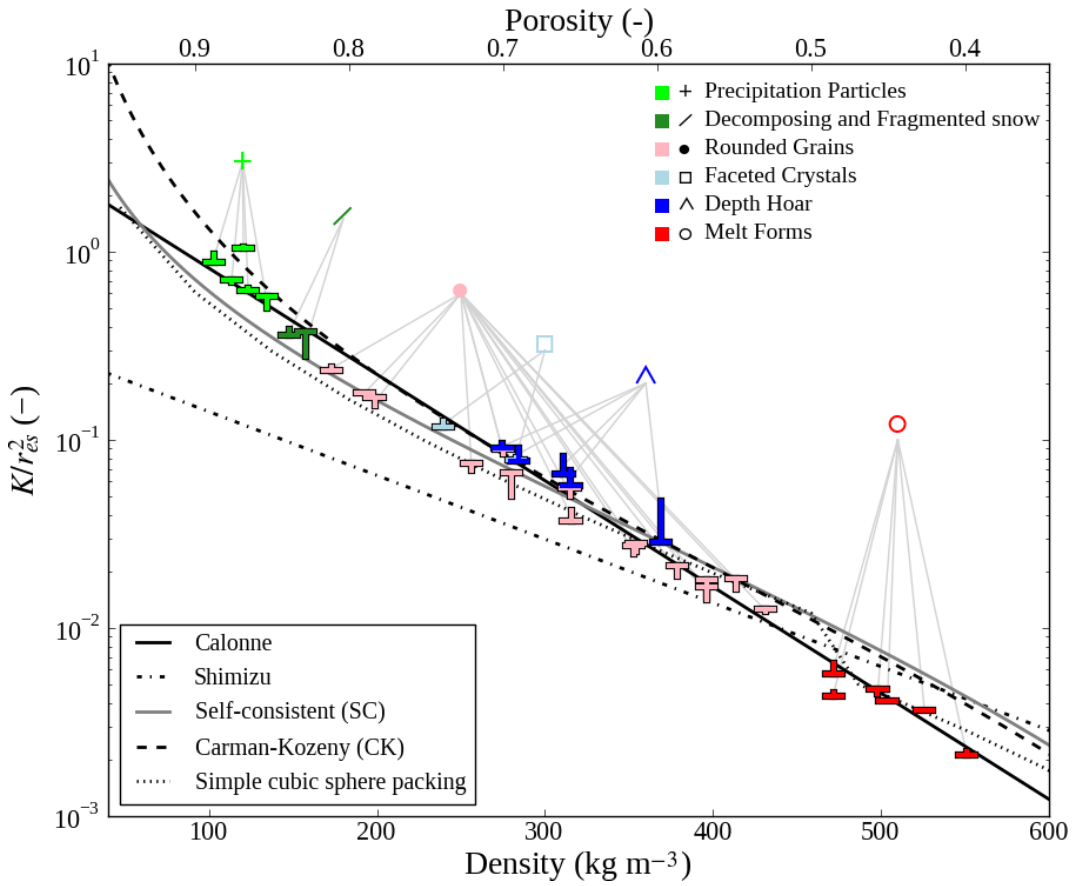

Figure 5.1: Dimensionless permeability vs. snow density. "T" symbols indicate the values obtained by our numerical computations. Tips and horizontal bars of the "T" shapes represent the vertical ($K_z^{\text{eff}*}$) and horizontal ($K_{xy}^{\text{eff}*}$) components of $\mathbf{K}^{\text{eff}*}$, respectively. Colors correspond to the ICSSG [*Fierz et al.*, 2009]. Analytical models, numerical computations and fits are also plotted.

differences. Indeed, the anisotropy coefficients of permeability ($A(\mathbf{K}^{\text{eff}})$) range from 0.74 for a DF sample collected in the field, to 1.66 for a particularly evolved DH sample obtained in cold room. We note that this range of $A(\mathbf{K}^{\text{eff}})$ values is consistent with the values between 0.75 and 1.9 measured by *Luciano and Albert* [2002] on firn collected from 1 to 13 m depth at Summit, Greenland.

For our snow specimen exhibiting a $A(\mathbf{K}^{\text{eff}})$ value of 1.66, Fig. 5.2 shows the air flow through the sample induced by a pressure drop along the vertical (left) and horizontal (right) direction. The flow, constrained by the snow microstructure, is clearly higher in the vertical than in the horizontal direction, leading to a high K_z^{eff} value. Note that the value of 1.66 is of the same order of magnitude as the analytical coefficient of anisotropy for a network of vertical cylinders [*Boutin*, 2000].

Figure 5.3 shows the relationship between the anisotropy coefficient computed for the intrinsic permeability ($A(\mathbf{K}^{\text{eff}})$) and for the effective thermal conductivity ($A(\mathbf{k}^{\text{eff}})$) of snow. The good relationship between these two variables indicates that the microstructure influences both variables in a similar manner. Nevertheless, some discrepancies can be observed depending on density, snow type and microstructure. In addition, Fig. 5.3 shows

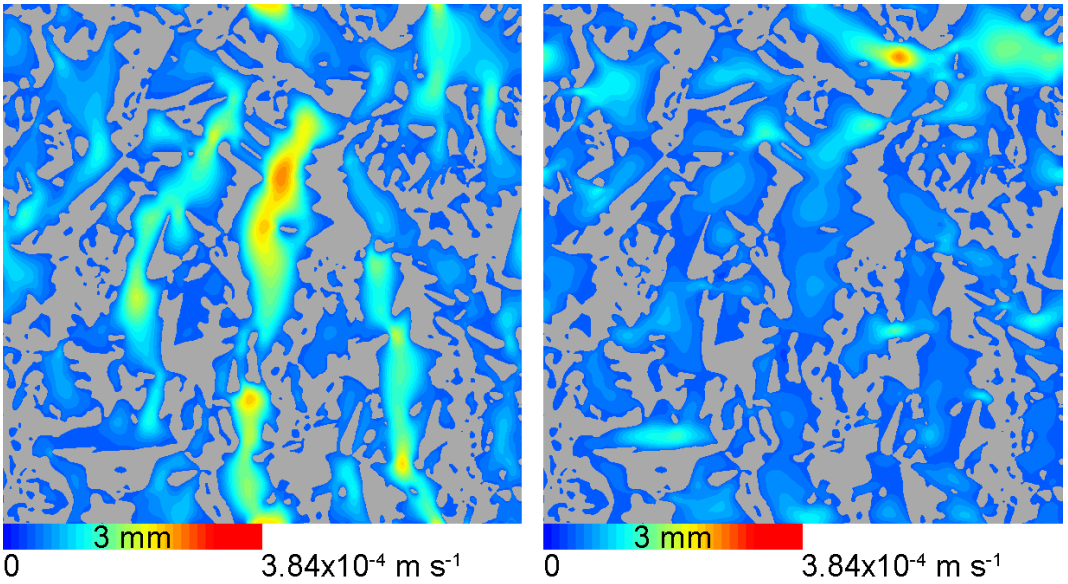

Figure 5.2: Vertical cross section (plane (y,z)) of an evolved DH sample. The color levels of the images correspond to the fluid velocity (intensity) computed for a pressure drop of 2×10^{-2} Pa along the z (left) and y (right) direction, and for a dynamic viscosity of air of $1.8 \times 10^{-5}\,\mathrm{Pa\,s^{-1}}$. The ice matrix of the microstructure is represented in gray. The length of the color bar corresponds to 3 mm.

that the anisotropy coefficients, and especially $A(\mathbf{k}^{\mathrm{eff}})$, enable the differentiation of the DH and FC samples (highest values) from other snow types. This result suggests that the anisotropy coefficients may be helpful for quantitative classification of snow. However, due to the thin layered nature of the snowpack [e.g. *Schneebeli et al.*, 1999; *Matzl and Schneebeli*, 2006, 2010; *Marshall and Johnson*, 2009], macroscopic measurements seem particularly challenging to access such information except in special cases where the investigated material is sufficiently homogeneous [e.g. *Luciano and Albert*, 2002].

5.3.3 Regression analysis

The numerical data presented in Sect. 5.3.1 were used to build a regression curve allowing to infer the intrinsic permeability from snow density and equivalent sphere radius. Following the pioneering work of *Shimizu* [1970], a regression of this form was seeked:

$$K^{\mathrm{eff}}/r_{\mathrm{es}}^2 = a\,\exp\left(b\,\rho_s\right). \tag{5.9}$$

Other mathematical forms of equations were tested and none of them proved better than Eq. (5.9). For the 35 samples studied, the parameters a and b in Eq. (5.9) were calculated using the nonlinear least-squares Marquardt-Levenberg fitting algorithm, from the numerical estimates of permeability, r_{es} and ρ_s. Note that these computations were performed separately for each diagonal component of $\mathbf{K}^{\mathrm{eff}}$, as well as for the average value K^{eff}. The fitting algorithm used provides estimates of the uncertainty pertaining to the parameters a and b, in the form of "asymptotic standard errors". These constitute an indication of the fit's accuracy.

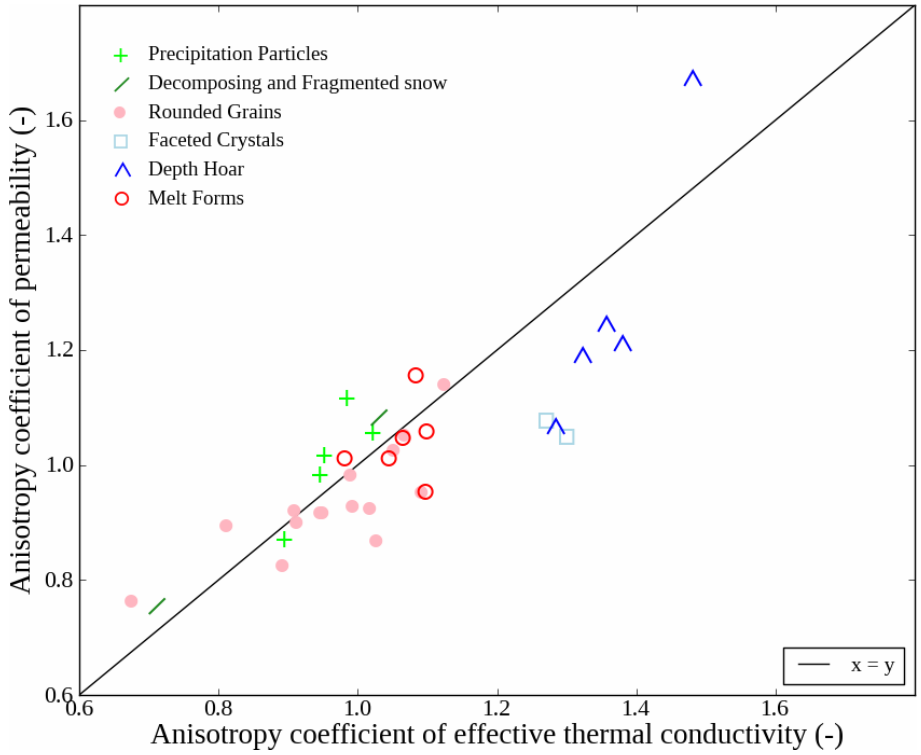

Figure 5.3: Anisotropy coefficient computed for the intrinsic permeability $A(\mathbf{K}^{\text{eff}})$ vs. that for the effective thermal conductivity $A(\mathbf{k}^{\text{eff}})$ for the 35 samples considered in this study. Symbols and colors correspond to the ICSSG [*Fierz et al.*, 2009].

Table 5.1 shows an overview of the fit parameters a and b computed using the values of K_x^{eff}, K_y^{eff}, K_z^{eff} and K^{eff}, with the associated "asymptotic standard errors". For the whole computation, the "asymptotic standard errors" values are small (on the order of 10 % and 2 % for a and b, respectively), indicating a strong correlation between permeability, density and r_{es}. Moreover, the table indicates that the parameters obtained from the four different values of $\mathbf{K}^{\text{eff}}$ are insignificantly different from each other. The regression is thus not affected by the anisotropy of $\mathbf{K}^{\text{eff}}$ presented in the previous section. Based on our numerical estimates of $\mathbf{K}^{\text{eff}}$, r_{es} and ρ_s, which span a wide range of snow types, we propose the following regression to infer an average permeability value K^{eff} from r_{es} and ρ_s:

$$K^{\text{eff}} = (3.0 \pm 0.3)\, r_{\text{es}}^2 \exp\left((-0.0130 \pm 0.0003)\, \rho_s\right). \tag{5.10}$$

This regression corresponds to the black solid line in Fig. 5.1. Providing a regression which reflects the anisotropy of permeability seems currently challenging and further investigations are needed. Nevertheless, we believe that it would require an additional variable representing the snow microstructure.

5.3.4 Test of the obtained regression curve against literature data

This section compares our numerical data and the obtained regression curve (Eq. 5.10) with K, r_{es} and ρ_s data from the literature. *Sommerfeld and Rocchio* [1993], *Arakawa*

Table 5.1: Regression parameters (a and b) of Eq. (5.9) for the three components of $\mathbf{K}^{\text{eff}}$, as well as for their mean value K^{eff}. "Asymptotic standard errors" ($\pm$) resulting from the fitting algorithm are given both in absolute units and as percentage values.

	a	$\pm$	$\pm$	b	$\pm$	$\pm$
	–	–	%	$\mathrm{m^3\,kg^{-1}}$	$\mathrm{m^3\,kg^{-1}}$	%
K_x^{eff}	3.1	0.3	9.0	−0.0130	0.0003	2.1
K_y^{eff}	2.9	0.2	8.5	−0.0129	0.0003	2.0
K_z^{eff}	2.9	0.3	11.6	−0.0129	0.0003	2.7
K^{eff}	3.0	0.3	9.1	−0.0130	0.0003	2.1

et al. [2009] and *Courville et al.* [2010] performed measurements of permeability using an air permeameter on fresh or equitemperature snow, in south-eastern Wyoming (USA), on naturally deposited dry snow in Hokkaido prefecture (Japan), and on polar firn (Antarctica), respectively. The SSA was estimated from photographs of snow section planes using a stereological method in the first two papers, while *Courville et al.* [2010] used tomographic images. Numerical computations of permeability involving 3-D images were carried out in two recent studies: *Courville et al.* [2010] used Lattice-Boltzman modeling to compute the permeability in one direction on polar firn, and *Zermatten et al.* [2011] determined the vertical component of the permeability for five snow samples using the direct pore-level simulations method. In both cases, SSA was estimated from the 3-D images.

Figure 5.4 provides a general view of the values of dimensionless permeability vs. density from the four datasets described above (colored symbols), as well as from our 35 computed values and the associated regression curve (in black). Data from the four studies are overall consistent with our computations, showing a similar relationship of dimensionless permeability with ρ_s, even if some discrepancies can be observed.

The predicted values of K^{eff} provided by the regression curve (Eq. 5.10) were compared to observed permeability data. Figure 5.5 displays the mean and standard deviation of the relative residuals of the regression curve against our own permeability data as well as the above-mentioned datasets. It indicates that our regression curve manages to estimate the intrinsic permeability of snow with a small relative bias on the order of 20 % maximum within a standard deviation on the order of 40 % maximum. This result shows that the numerical computations of *Courville et al.* [2010], *Zermatten et al.* [2011] and this study are in good agreement, although all three studies use different numerical methods and boundary conditions on the external faces of the sample. The only major deviation from a good performance of Eq. (5.10) against experimental and numerical data is encountered with the dataset of *Arakawa et al.* [2009], which exhibits an overall positive relative bias of 71 % with a standard deviation of 85 %, also seen in Fig. 5.4. At present, the exact reason(s) for this discrepancy is (are) not understood. This could be due to the difficulty of making reliable and reproducible measurements of permeability. A first source of error may be the physical damage of the sample caused during its sampling or its handling [*Sommerfeld and Rocchio*, 1993]. *Shimizu* [1970] and *Sommerfeld and Rocchio* [1993] also pointed out a bias linked to possible condensation/sublimation of the snow microstructure induced by the airflow imposed through the snow sample during the measurement. Sample

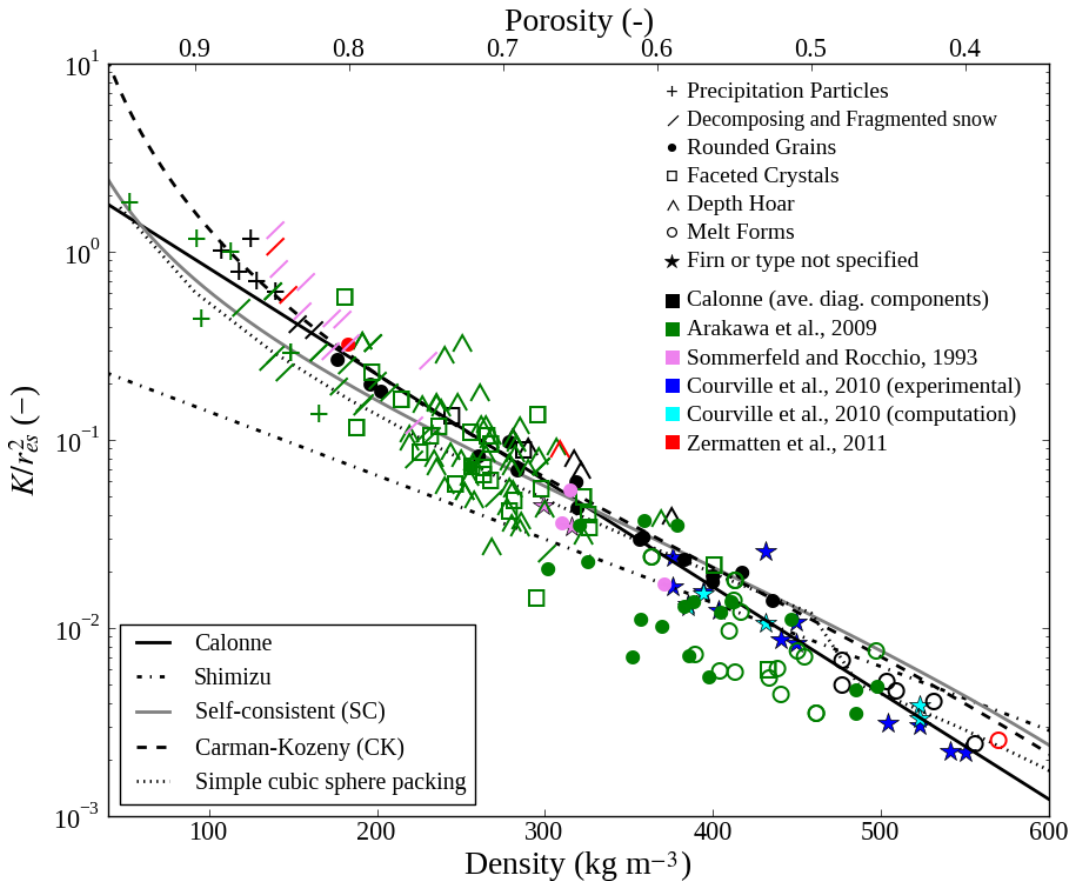

Figure 5.4: Dimensionless permeability vs. snow density. Our $K^{\text{eff}*}$ values (in black) are compared to results from other studies (in color). Symbols correspond to the ICSSG [*Fierz et al.*, 2009], excepting stars which are used when firn is considered or when the snow type is not specified in the paper. Analytical models and fits are also plotted.

heterogeneity could also be invoked.

Based on the mathematical equation of our proposed regression curve (Eq. 5.10), accounting for a 10 % uncertainty on the parameter a of the equation (here we neglect the uncertainty on the parameter b of the equation – see Table 5.1), and assuming that r_{es} and ρ_s both carry a measurement uncertainty on the order of 10 % [*Matzl and Schneebeli*, 2006; *Painter et al.*, 2006; *Gallet et al.*, 2009; *Conger and McClung*, 2009; *Arnaud et al.*, 2011], the propagation of these relative errors in terms of K adds up to about 50 %. This experimental error is of the same order of magnitude as the minimum and maximum deviation found when applying the regression curve to independent data (black points in Fig. 5.5).

5.3.5 Comparisons of the obtained regression curve to models and fits

This section compares the permeability estimates provided by our regression (Eq. 5.10) and by various classical equations proposed in the literature. We used the following regressions, analytical formulas or numerical computations (note that Figs. 5.1 and 5.4 show the

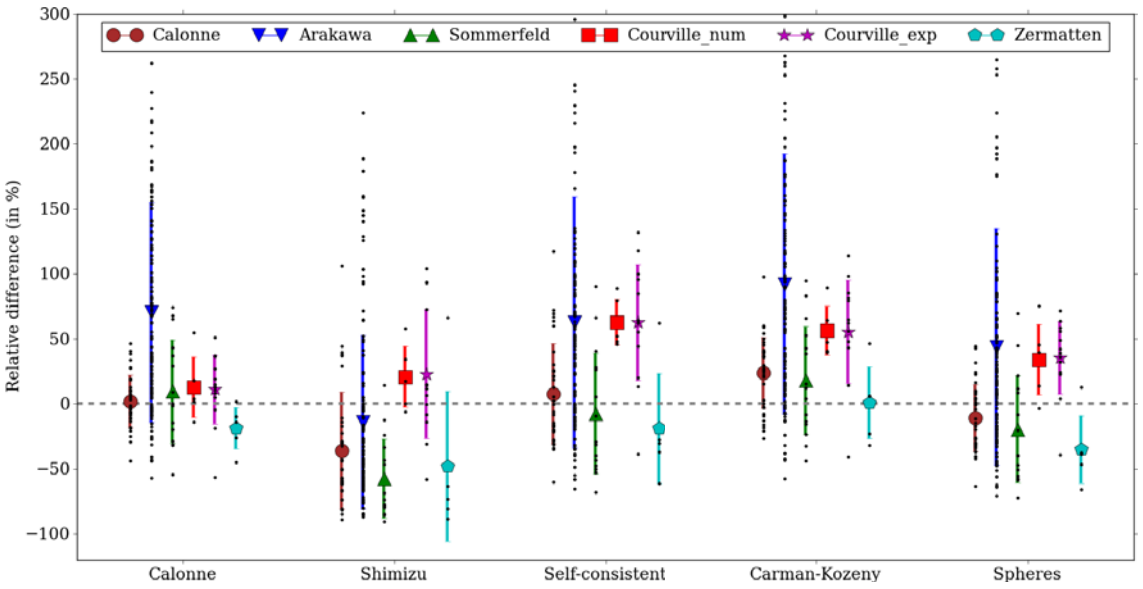

Figure 5.5: Overview of the relative differences between experimental or numerically computed values of the intrinsic permeability of snow from six datasets (colors) and their estimates based on the corresponding snow density and equivalent sphere radius using various regression or analytical curves (x-axis). Black dots refer to individual measurements of relative residual. The mean and standard deviation of the relative differences are indicated as symbols and error bars, respectively.

corresponding curves in terms of dimensionless permeability: $K^* = K/r_{\text{es}}^2$):

i. We recall the regression fit (Eq. 5.10) proposed in this study (referred to as "Calonne" in the relevant figures):

$$K_{\text{Cal}} = (3.0 \pm 0.3)\, r_{\text{es}}^2 \exp\left((-0.0130 \pm 0.0003)\, \rho_s\right).$$

ii. The well-known Shimizu's fit [*Shimizu*, 1970] is expressed as

$$K_{\text{Shi}} = 0.077 D^2 \times \exp\left(-0.0078 \rho_s\right), \text{ with } D = 2r_{\text{es}}.$$

iii. The self-consistent (SC) estimate was obtained assuming that the porous medium consists of a bicomposite spherical pattern made of an internal spherical grain and an external fluid shell that ensures fluid connectivity. The porous medium is defined using the most basic information, i.e. the porosity and the grain size. Using the SC method, *Boutin* [2000] showed that the above porous medium leads to the following estimate:

$$K_{\text{SC}} = [r_{\text{es}}^2/(3\beta^2)] \times [-1 + (2 + 3\beta^5)/(\beta(3 + 2\beta^5))],$$

where $\beta = (1 - \phi)^{(1/3)}$.

iv. In the Carman-Kozeny (CK) model, the medium is treated as a bundle of capillarity tubes of equal length. By solving the Stokes equations simultaneously for all the channels passing through a cross-section normal to the flow in the porous medium, the

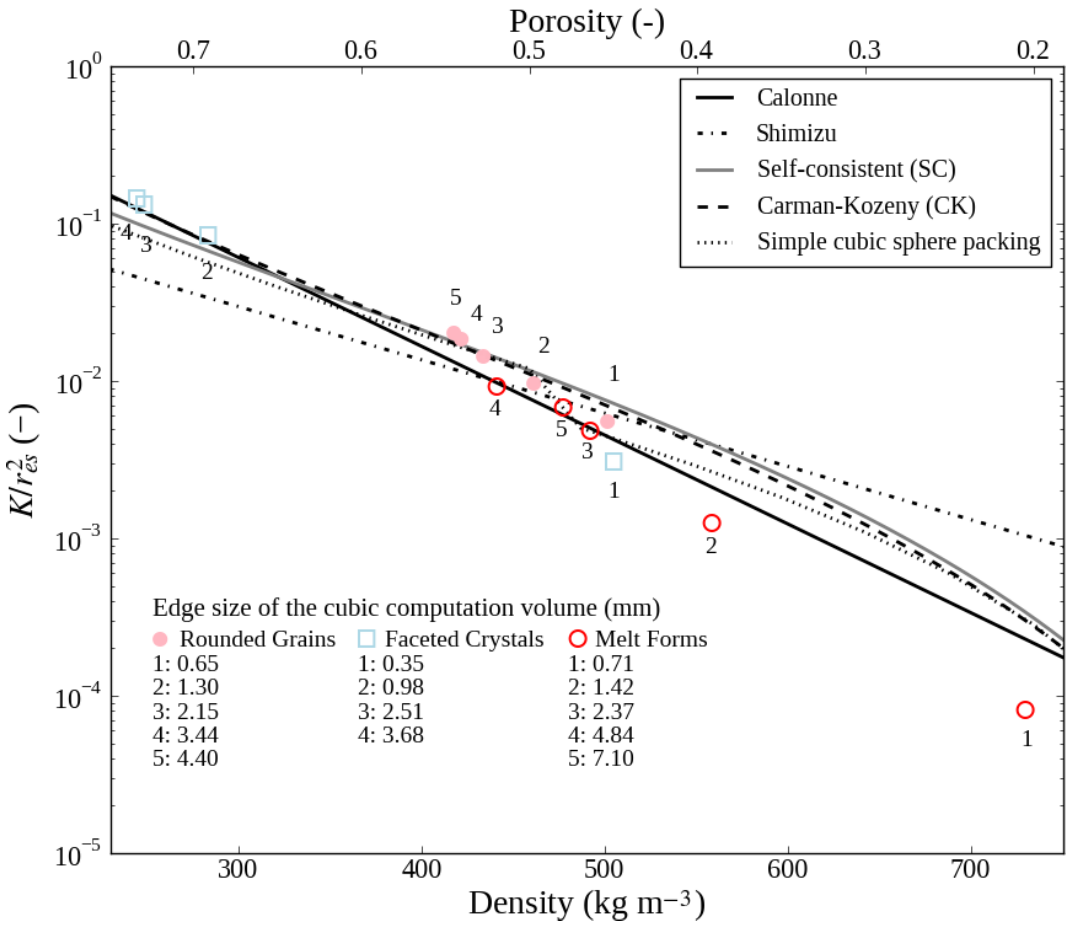

Figure 5.6: Dimensionless permeability versus snow density for three snow samples. Symbols and colors correspond to the ICSSG [*Fierz et al.*, 2009]. For a given sample, each symbol represents a particular volume from which $\mathbf{K}^{\text{eff}}$, SSA and ρ_s were computed. The largest volume corresponds to the total volume of the sample. Analytical models and fits are also plotted.

permeability is written as $K = (c \times \phi^3)/(\text{SSA}_\text{I}^2 \times (1-\phi)^2)$ where SSA_I is the specific surface area per unit of ice volume ($\text{SSA}_\text{I} = \text{SSA} \times \rho_i$, in m^{-1}) and c a coefficient which characterizes the geometry of the channels in the model. Empirically, c is found to be equal to 0.2 for many types of porous media [*Bear*, 1972]. The CK equation can thus be expressed as

$$K_{\text{CK}} = (4r_{\text{es}}^2 \times \phi^3)/(180(1-\phi)^2).$$

v. Numerical values of permeability (K_{sphere}) were computed using the periodic homogenization method and a finite element software, for a simple cubic packing of spheres [*Boutin and Geindreau*, 2010]. Note that at high density, where spheres interpenetrate, the SSA is computed from the effective surface formed by the sphere's assembly.

Figure 5.5 allows to investigate the performance of the above equations by comparing their estimates (K_{Cal}, K_{Shi}, K_{SC}, K_{CK} and K_{sphere}) against the independently observed

permeability data presented in Sect. 5.3.4. For each expression, the result is given in terms of average and standard deviation of the relative residuals (in color on Fig. 5.5). The whole set of the relative residual values is also shown by the black points. Note that in the case of the simple cubic packing of spheres, the corresponding K values, normalized by r_{es} and then expressed as a function of density, were interpolated to be able to compute K_{sphere} estimates for all values of density and r_{es}.

Figure 5.5 shows that the Carman-Kozeny (CK) model, self-consistent (SC) model, and the numerical computations for a simple cubic packing of spheres, predict the numerical values obtained in this study with a relative bias of the order of 20 % maximum within a factor 2 at most (maximum relative deviation of 40 %). These expressions are thus consistent with our proposed regression curve. In contrast, the regression fit proposed by *Shimizu* [1970] behaves poorly against our numerical values, showing a negative relative bias of −36 % within a relative deviation of 45 % (see Fig. 5.5). This situation is also true for other datasets, where the fit proposed by *Shimizu* [1970] underestimates K (relative bias between 21 % (± 23 %) and −57 % (± 31 %)). As pointed out by several studies [*Sommerfeld and Rocchio*, 1993; *Jordan et al.*, 1999b], we believe that this is largely due to the method used by *Shimizu* [1970] to estimate grain size. From snow cross-sections, he computed a grain diameter $D = 2\,r_{\mathrm{es}} = \sqrt{6\rho_s/\pi\rho_i n}$, where n, the number of ice grains appearing in the cross section per a unit area, is estimated by a counting process described as "a complicated-shaped grain having m remarkable constrictions was counted as $m + 1$ grains". This visual method is subjective and may lead to erroneous estimates of n and therefore of K^*.

Over the whole ensemble of tested datasets, Fig. 5.5 indicates that the best estimates are obtained using our regression (Eq. 5.10), showing very small average values of relative residuals, from +13 % for the numerical study of *Courville et al.* [2010] to −19 % for *Zermatten et al.* [2011]. Moreover, the set of values of relative residuals generally does not exceed ± 50 %. Again, the predicted values for the dataset reported by *Arakawa et al.* [2009] do not correspond to this situation, as discussed in Sect. 5.3.4.

The predicted values using a simple packing of spheres are also consistent with experimental and numerical estimates from snow samples. In particular, this latter model behaves better than the CK and SC approach for the MF samples, where these two models fail to reflect the snow microstructure and overestimate the permeability, as shown in Fig. 5.1. These results can be explained by the fact that at low density the airflow around a snow particle is little affected by flow around its neighbors. In contrast, at higher density, snow particles are close together and the flow around one of them disturbs the flow around the others. This last phenomenon is not captured by analytical models.

Finally, *Zermatten et al.* [2011] indicate significant differences between the CK model and their values, while Fig. 5.5 shows an excellent agreement between both (the CK model predicts their observed data with a relative bias of 0.8 % within a relative deviation of 27 %): they apparently plotted an erroneous CK equation, using the specific surface area per unit of snow volume ($\mathrm{SSA_V}$, in $\mathrm{m^{-1}}$) in the expression of $K = \phi^3/(5(1-\phi)^2\mathrm{SSA_I^2})$ instead of $\mathrm{SSA_I}$.

5.3.6 Representative elementary volume

Permeability estimations of the REV were performed on one sample of each snow type and their edge size range from 2.5 mm for the PP sample to 5.5 mm for the MF sample, which corresponds to volumes smaller or equal to those of our 3-D images (see Appendix D for further details).

For three snow samples (RG, FC and MF snow types), computations of $\mathbf{K}^{\text{eff}}$, SSA and ρ_s were performed on the total available 3-D image and on sub-volumes of different sizes. Figure 5.6 shows the obtained values of $K^{\text{eff}*}$ as a function of ρ_s. By increasing the volume size of calculation (from volume 1 to 4 or 5 in Fig. 5.6), the $K^{\text{eff}*}$ value is closer and closer to the result based on the previous volume, which is consistent with the definition of a REV. We can also see that if $\mathbf{K}^{\text{eff}}$, SSA and/or ρ_s are computed on a volume smaller than their REV, the relationship between $K^{\text{eff}*}$ and ρ_s remains consistent with the regression curve (Eq. 5.10) proposed in this study. This observation confirms the robustness of the relationship between $\mathbf{K}^{\text{eff}}$, SSA and ρ_s.

5.4 Conclusions

The intrinsic permeability tensor $\mathbf{K}^{\text{eff}}$ was computed on 35 tomographic images of various snow types by solving numerically a specific boundary value problem arising from the homogenization process on a representative elementary volume (REV). The equivalent sphere radius (r_{es}) was used as a characteristic length of the microstructure to reduce $\mathbf{K}^{\text{eff}}$ to a dimensionless tensor $\mathbf{K}^{\text{eff}*}$. A regression equation using the 35 computed values of mean permeability (K^{eff}), density (ρ_s) and equivalent sphere radius was proposed, such as: $K^{\text{eff}} = (3.0 \pm 0.3)\, r_{\text{es}}^2 \exp\left((-0.0130 \pm 0.0003)\, \rho_s\right)$ and compared to existing literature data. Our main conclusions are summarized below:

1. The intrinsic permeability of snow can be anisotropic depending on the snow microstructure. The anisotropy coefficients of permeability range from 0.74 for a sample of decomposing precipitation particles collected in the field, to 1.66 for a particularly evolved depth hoar specimen, and are consistent with the anisotropy coefficient of the effective thermal conductivity. It appears that the use of these coefficients could be helpful for the quantitative classification of snow, as it may enable to distinguish the depth hoar and the facetted crystals from other snow types.

2. Permeability, density and equivalent sphere radius, directly related to the specific surface area, are strongly correlated. The equivalent sphere radius is thus a relevant characteristic length for permeability, which in addition is rather easy to determine in the field or from 3-D images. However, this strong correlation between snow permeability, density and SSA precludes considering them as independent variables for the sake of objective snow classification.

3. The anisotropy of permeability does not affect the regression curve performed on the 35 snow samples. Indeed, very similar regression curves have been computed by

using each diagonal component of $\mathbf{K}^{\text{eff}}$ as well as the average of these three terms. Thus, the proposed regression allows estimating an average permeability value only.

4. Our numerical computations of permeability from 3-D images are consistent with datasets from other experimental and numerical studies. Moreover, our regression succeeds in estimating the permeability data of previous studies with a small relative bias on the order of 20 % maximum, within a factor ≈ 2 maximum relative deviation (40 %), except for the dataset of *Arakawa et al.* [2009] for which the agreement is lower (positive relative bias of 71 % with a standard deviation of 85 %). By comparing with other equations from theoretical models, fits and numerical data available in literature, our regression appears to be the best currently available simple relationship linking the average value of permeability to snow density and specific surface area. In particular, the well known fit proposed by *Shimizu* [1970] seems to significantly underestimate the permeability of snow for most of the tested datasets, most probably due to an inconsistency between the equivalent sphere radius derived from the specific surface area of snow and the empirically-defined snow grain size used by this author.

Conclusion Part II

The objective of this part was to improve the estimations of the effective properties arising in the macroscopic models of transport phenomena, and to better understand their relationship with the density. For that, we carried out numerical computations of the effective thermal conductivity and intrinsic permeability from about thirty 3D images of snow spanning the full range of seasonal snow types and density. The computations are based on the results of the homogenization method presented in Part I via the software Geodict. Our computed properties were compared to measurements, parameterizations, models and analytical estimates from the literature. Since our method of estimation provides the full tensor of the properties, we also studied their anisotropy.

The main contributions of these studies are summarized in the following.

- The effective thermal conductivity of snow computed from 3D images is strongly correlated with the snow density and follows closely the regression curve proposed by *Yen* [1981].
- Precautions must be paid because the three methods to estimate the thermal conductivity (needle-probe, flux/gradient and numerical modeling) do not exactly probe the same variable. Moreover our results indicate that the heated-needle probe measurements are likely biased low.
- The heat conduction through the air pores plays a vital role in the overall heat conduction of snow and should not be neglected in numerical computations.
- The anisotropy coefficients of the effective thermal conductivity, defined as the vertical component over the horizontal component of the tensor, range from 0.7 to 1.5 for the whole range of density depending on the snow type, i.e. microstructure.
- The intrinsic permeability can be reasonably inferred from specific surface area and density of snow, both measurable in the field.
- The intrinsic permeability of snow computed from 3D images is not in agreement with the regression curve proposed by *Shimizu* [1970]. A good correlation is found with the Carman-Kozeny model and the self-consistent estimate.
- The anisotropy coefficients of the intrinsic permeability agree with those of the effective thermal conductivity and span from 0.7 to 1.6 for the whole range of density depending on the snow type, i.e. microstructure.

Overall, these studies confirm that the effective properties are related to the snow density at the first order of approximation and provide their relationship based on estimations from 3D images. Nevertheless, we also pointed out an anisotropic behavior of the effective properties that can not be reflected, of course, by an isotropic variable as the density. The next part will notably contribute to investigate this issue.

Part III

Monitoring of dry snow metamorphism

Introduction Part III

Previously, we presented the effective properties of snow as a function of the density. In a complementary manner, we are interested here in studying the microstructure and properties of snow as a function of time, i.e. during the metamorphism. This part includes the main experimental work carried out during the thesis.

As pointed out in Part II, the effective properties strongly depends on the snow density, but should be also related to other parameters to reflect their anisotropic behavior for example. Further works on the link between the effective properties and the microstructure seem required, especially during the temperature gradient metamorphism where snow generally evolves at a constant density. Moreover, at the pore scale, some features of the physics involved in the dry snow metamorphism remain an issue. As the description of the physics at this scale constitutes the starting point for the modeling at a larger scale, efforts have to be done in this way. The monitoring of the evolution of snow metamorphism by tomography seems a useful tool to address both of the above issues.

Chapter 6 is dedicated to monitoring the evolution of a snow slab undergoing temperature gradient metamorphism, by collecting different snow samples at regular time intervals in the slab (static approach). This work is based on experiments and tomography sessions carried out during my master internship. From the time series of 3D images obtained, the three effective properties of transport were estimated based on the results of homogenization presented in Part I using the software Geodict. The structural properties were computed using algorithms previously developed at the CEN. We can thus investigate the link between microstructure and effective properties for that experiment. Moreover, we present simple analytical estimates of the effective properties, as well as their anisotropy coefficients, that are based on basic informations of the microstructure.

The next chapter 7 aims at monitoring the evolution of the same snow sample over time (in vivo approach). For that, we developed a cryogenic cell for the in vivo monitoring of snow metamorphism by time-lapse tomography. This cell operates in room temperature conditions and can be adapted to various tomographic scanners, in contrast to other existing cells operating in cold-rooms with a dedicated tomograph. At Grenoble, the cell can be used with the tomograph of the 3SR lab (precision until 5 μm) and to the ESRF instruments (high-resolution and high-speed scan, diffraction contrast tomography...). The acquisition of a shared nano-tomograph by several labs is also on going.

Chapter

6 Study of a temperature gradient metamorphism of snow from 3-D images: time evolution of microstructures, physical properties and their associated anisotropy

Contents

This chapter corresponds to the paper entitled *Study of a temperature gradient metamorphism of snow from 3-D images: time evolution of microstructures, physical properties and their associated anisotropy* by Calonne N., Flin F., Geindreau C., Lesaffre B., Rolland du Roscoat S., published in *The Cryosphere Discussion*, 2014.

Abstract

We carried out a study to monitor the time evolution of microstructural and physical properties of snow during temperature gradient metamorphism: a snow slab was subjected to a constant temperature gradient in the vertical direction for three weeks in a cold-room, and regularly sampled in order to obtain a series of 3-D images using X-ray microtomography. A large set of properties was then computed from this series of 3-D images: density, specific surface area, correlation lengths, mean and Gaussian curvature distributions, air and ice tortuosities, effective thermal conductivity, and intrinsic permeability. Whenever possible, specific attention was paid to assess these properties along the vertical and horizontal directions, and an anisotropy coefficient defined as the ratio of the vertical over the horizontal values was deduced. The time evolution of these properties, as well as their anisotropy coefficients, was investigated, showing the development of a strong anisotropic behavior during the experiment. Most of the computed physical properties of snow were then compared with two analytical estimates (Self consistent estimates and Dilutes bed of spheroids) based on the snow density, and the size and anisotropy of the microstructure through the correlation lengths. These models, which require only basic microstructural information, offer rather good estimates of the properties and anisotropy coefficients for our experiment without any fitting parameters. Our results highlight the interplay between the microstructure and physical properties, showing that the physical properties of snow subjected to a temperature gradient cannot be described accurately using only isotropic parameters such as the density and require more refined information. Furthermore, this study constitutes a detailed database on the evolution of snow properties under a temperature gradient, which can be used as a guideline and a validation tool for snow metamorphism models at the micro or macro scale.

6.1 Introduction

Natural snowpacks are frequently subjected to temperature gradients induced by their environment. Due to temperature differences in the snowpack, the morphology of snow at the microscale, i.e. the snow microstructure, quickly evolves with time. This metamorphism, called Temperature Gradient (TG) metamorphism, is mainly charaterized by the reorganization of ice along the gradient direction by sublimation of the warmest parts of the grains, water vapor transport across the air pores, and its deposition on the coldest zones of the ice matrix [*Yosida et al.*, 1955; *De Quervain*, 1973; *Colbeck*, 1997; *Flin and Brzoska*, 2008]. In terms of snow type, this leads to faceted crystals and depth hoar, which constitute often the weakest layers of the snowpack. Experimental and theoretical studies such as those of *Yosida et al.* [1955]; *De Quervain* [1973]; *Akitaya* [1974]; *Marbouty* [1980]; *Colbeck* [1983a, b]; *Fukuzawa and Akitaya* [1993] and *Satyawali et al.* [2008] provide a good base of knowledge on TG metamorphism, with descriptions of the evolution of the snow grains mostly based on photographs. With the development of X-ray microtomography for snow [*Brzoska et al.*, 1999a; *Schneebeli*, 2000; *Coléou et al.*, 2001; *Lundy et al.*, 2002; *Pinzer and Schneebeli*, 2009b; *Chen and Baker*, 2010], very precise studies related to TG metamorphism are now available. Up to now, two different approaches have been used: the

static approach, where the metamorphism of a homogeneous snow slab can be monitored by imaging different impregnated snow samples collected in the slab [*Flin and Brzoska*, 2008; *Srivastava et al.*, 2010], and the in vivo approach, that gives access to the grain to grain evolution of a same snow sample by time-lapse tomography [*Schneebeli and Sokratov*, 2004; *Pinzer and Schneebeli*, 2009a; *Pinzer et al.*, 2012]. They allow a better understanding of the mechanisms involved and highlight the impact of snow microstructure on its physical and mechanical properties.

In particular, snow properties are often expressed as functions of snow density such as for the effective thermal conductivity [*Yen*, 1981; *Sturm et al.*, 1997; *Calonne et al.*, 2011; *Löwe et al.*, 2013] or the intrinsic permeability [*Shimizu*, 1970; *Jordan et al.*, 1999a; *Courville et al.*, 2010; *Zermatten et al.*, 2011; *Calonne et al.*, 2012], leading to simple parameterizations that can be used to estimate properties in snowpack models, e.g. Crocus [*Brun et al.*, 1989] and Snowpack [*Lehning et al.*, 1999]. However, *Marbouty* [1980]; *Schneebeli and Sokratov* [2004] and *Satyawali et al.* [2008] have shown that during TG metamorphism, the effective thermal conductivity of snow evolves without significant changes in density, but only because of the ice/pores reorganization. Such studies suggest that there is a need to refine the parameterizations of snow properties, at least for snow subjected to temperature gradients. In addition, as recently shown for the effective thermal conductivity [*Calonne et al.*, 2011; *Shertzer and Adams*, 2011; *Riche and Schneebeli*, 2013] or the intrinsic permeability [*Calonne et al.*, 2012], this type of snow exhibits anisotropic behavior, and requires more systematic investigations. Recently, *Löwe et al.* [2013] proposed a refined parameterization of the effective thermal conductivity tensor of snow based on anisotropic second order bounds. Their results show the importance of taking into account the microstructural anisotropy for the estimation of the effective thermal conductivity during TG metamorphism.

We propose addressing these issues by studying the evolution of snow morphology together with several physical properties during a typical experiment of TG metamorphism. The main objective consists in better understanding the relationships between the snow microstructure and its properties. In this context, our paper focuses on the description of the time evolution of a snow slab of 294 $\mathrm{kg\,m^{-3}}$ subjected to a vertical temperature gradient of 43 $\mathrm{K\,m^{-1}}$ in a cold room at -4°C. The temperature and gradient values were chosen to observe a significant but not extreme evolution of the snow in a reasonable time (three weeks of experiment). Moreover, these experimental conditions are in the range of conditions frequently encountered by natural alpine snowpacks. Snow specimens were regularly sampled from the snow slab and, after treatment, scanned by X-ray microtomography to obtain a set of 3-D images showing the time evolution of the snow microstructure. Then, computations were performed on the 3-D images to estimate various geometrical and physical properties. Whenever possible, specific attention was paid to assess these properties in the x, y, and z directions, z being along the direction of gravity and of the macroscopic temperature gradient. In addition, following the approach of *Löwe et al.* [2013], we present two anisotropic analytical estimates for the determination of the physical properties of snow based on the knowledge of basic microstructural information (porosity,

correlation lengths in the x, y, and z directions). This offers interesting possibilities for the improvement of the parameterizations of snow properties.

The new contributions of this study lie in the following points: (i) a wide range of snow properties (mean and Gaussian curvature distributions, directional correlation lengths, specific surface area, air and ice tortuosities, intrinsic permeability, effective thermal conductivity) are investigated during the same experiment; (ii) the time evolution of most properties computed in the x, y, and z directions is provided, allowing monitoring the anisotropy of properties with time; and (iii) the physical properties computed on 3-D images are compared with those determined by anisotropic analytical estimates based on basic microstructural properties.

6.2 Materials and methods

6.2.1 Experimental setup and 3-D images

Natural snow was collected at Chamrousse (1800 m, French Alps) on 22 February 2011 and stored at $-20\,^{\circ}\mathrm{C}$ for two weeks. This snow was then sieved in a cold room at $-5\,^{\circ}\mathrm{C}$ to obtain a horizontal snow slab of length 100 cm, width 50 cm, and height 14 cm, composed of rounded grains [RG, *Fierz et al.*, 2009] at $300 \pm 15\ \mathrm{kg\,m^{-3}}$ (result from macroscopic density measurements). The snow slab was confined at the base and the top between two copper plates whose temperature was controlled by a thermo-regulated fluid circulation. The whole system was insulated by 8 cm thick polystyrene plates. An illustration of the experimental set-up is given in Fig. 6.1. Isothermal conditions at $-5\,^{\circ}\mathrm{C}$ were first applied to the snow slab during 24 h. This aimed at sintering snow grains whose bonds may have been destroyed by sieving. During the following three weeks, the temperature of the cold room was held at $-4\,^{\circ}\mathrm{C}$ and the upper and lower copper plates were maintained at $-1\,^{\circ}\mathrm{C}$ and $-7\,^{\circ}\mathrm{C}$, respectively, generating a steady vertical temperature gradient of $43\ \mathrm{K\,m^{-1}}$ through the snow slab.

The snow slab was sampled using a cylindrical core drill approximately every three days over the three weeks, leading to seven samples in total at the end of the experiment. Macro photographs of snow particles were also taken to characterize snow type. During the sampling operation, the temperature of the cold room was temporarily held at $-7\,^{\circ}\mathrm{C}$ (temperature of the upper copper plate) in order to minimize the change of boundary conditions of the snow slab. The polystyrene plates and the upper copper plate were then temporarily removed in order to access the snow slab. The samples were taken in the middle height of the layer and at a minimum distance of 5 cm from edges and from regions already sampled. The air gap created by the sampling was systematically refilled with freshly sieved snow to prevent strong modifications of the thermal field of the snow slab. Immediately after sampling, each snow specimen was put in a plastic box and impregnated with 1-chloronaphthalene. This organic product, in liquid state above $-15\,^{\circ}\mathrm{C}$, was poured along the box walls, filling slowly the open pores of snow. Then, the sample was frozen in an iso-octane bath cooled by dry ice ($-78\,^{\circ}\mathrm{C}$) to allow the solidification of the 1-chloronaphthalene. The impregnation is required to stop the metamorphism of the

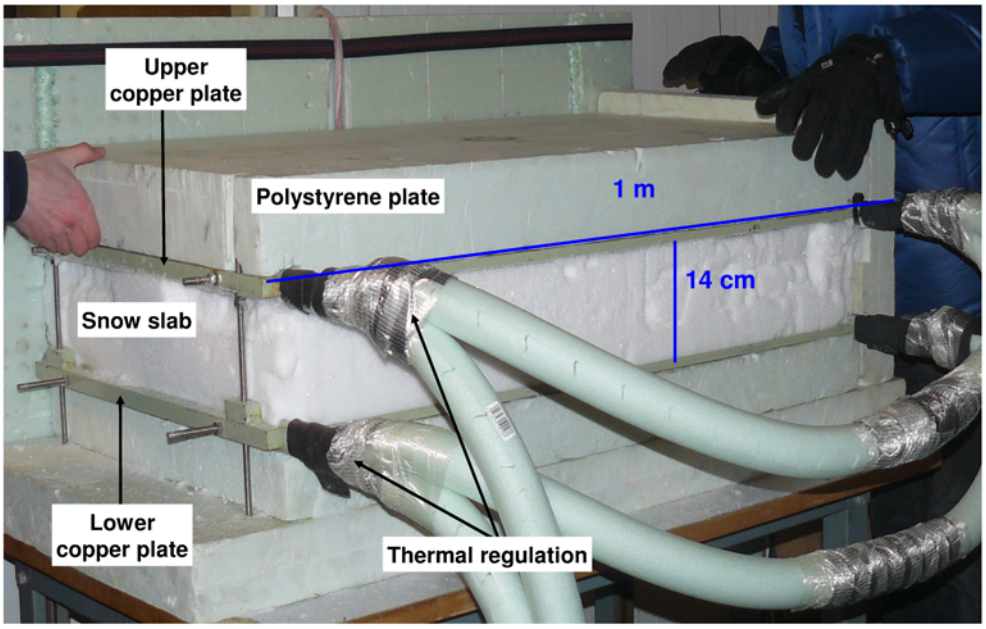

Figure 6.1: Photograph in cold room of the apparatus designed to control and monitor temperatures at the top and bottom of a snow slab. The front and left vertical polystyrene plates were removed from the device for visualization purposes.

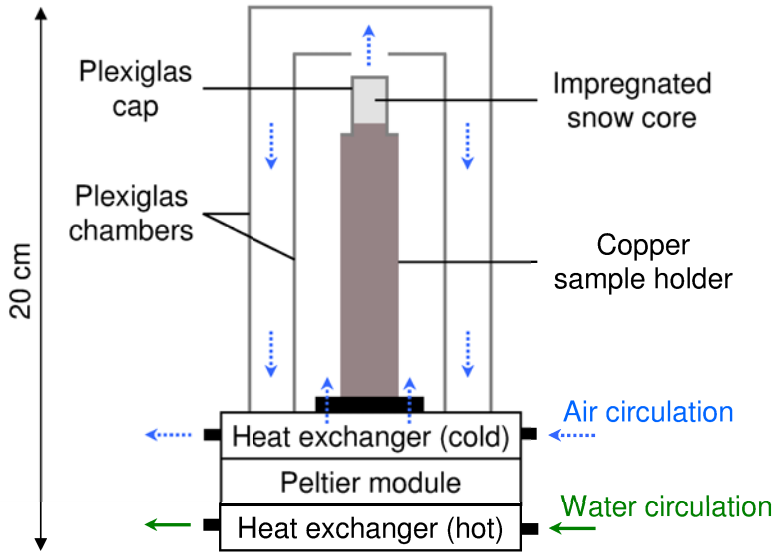

Figure 6.2: Illustration of the cryogenic cell used during the tomographic acquisition.

snow microstructure and consolidate the snow sample for further machining processes. The absorption properties of the ice, air and 1-chloronaphthalene ensure a good contrast between these three components for the X-ray tomographic acquisition. Cylindrical snow cores were extracted from the samples by machining with a press drill which is mounted on a lathe and operated in a cold room at $-30\,^{\circ}\mathrm{C}$. Each snow core was then glued on the upper part of a copper sample holder by a droplet of 1-chloronaphthalene and sealed into

a Plexiglas cap. The prepared samples were finally stored at −20 °C until the tomographic acquisitions.

Each core was scanned using the conical X-ray microtomograph of the 3S-R lab set with an acceleration voltage of 75 kV and a current intensity of 100 μA. As this microtomograph operates in an ambient temperature room, the snow core was placed in a specially designed cryogenic cell composed of a Peltier module, which maintains a regulated temperature of around −30 °C at the bottom part of the copper sample holder. Figure 6.2 shows a schematic of this cell. A continuous dry and cold air circulation between the sample holder and the double-wall Plexiglas chambers of the cell prevents the deposition or condensation of water vapor on their sides. In addition, the heat generated by the Peltier module is dissipated by water circulation. The whole system is able to rotate 360° during the acquisition. Each tomographic acquisition lasted around 2 h during which 1200 radiographies of the entire impregnated snow sample were taken. Horizontal cross sections of the sample were reconstructed from radiographies using DigiXCT[a] software. Image processing was then applied to the grayscale reconstructed images to obtain binary images representative of the ice-pore arrangement [*Flin et al.*, 2003; *Lesaffre et al.*, 2004; *Hagenmuller et al.*, 2013]. The method used consists of the following steps: (i) removing the remaining air bubbles and associating them with the pore phase, (ii) smoothing and thresholding, (iii) visual verifications and 3-D post processing. One can refer to the section "Three or more materials", pp 862-863 of *Hagenmuller et al.* [2013] for detailed information on the exact procedure applied. We finally obtained seven binary 3-D images, extracted in the middle of the whole reconstructed volumes and showing the microstructural evolution of the snow slab with time. The 3-D images have a voxel size of 8.4 or 9.7 μm and a volume size of 5.9^3, 9.2^3 or 9.7^3 mm^3. Detailed information for each image are given in Table 6.4.2.

6.2.2 Computation of structural properties

6.2.2.1 Density

Snow porosity ϕ (dimensionless), also called volume fraction of air, was estimated from 3-D images using a standard voxel counting algorithm. Snow density ρ_s (in $\mathrm{kg\,m^{-3}}$) was simply deduced from ϕ as $\rho_\mathrm{s} = \rho_\mathrm{i}\,(1-\phi)$ where ρ_i is the ice density equal to 917 $\mathrm{kg\,m^{-3}}$.

6.2.2.2 Specific surface area SSA

The specific surface area estimates along the x, y and z directions, denoted by SSA_x, SSA_y and SSA_z (in $\mathrm{m^2\,kg^{-1}}$), were computed from 3-D images, using a stereologic method [*Arakawa et al.*, 2009; *Flin et al.*, 2011]:

$$\mathrm{SSA}_x = \frac{2N_x}{L\rho_\mathrm{s}}, \quad \mathrm{SSA}_y = \frac{2N_y}{L\rho_\mathrm{s}}, \quad \text{and} \quad \mathrm{SSA}_z = \frac{2N_z}{L\rho_\mathrm{s}} \tag{6.1}$$

where N_x, N_y, and N_z are the total number of intersections between air and ice along parallel testing lines in the x, y, and z directions, respectively, through the entire volume,

[a] DigiXCT: `http://www.digisens3d.com/en/soft/3-DigiXCT.html`.

and L is the total length of the testing lines (in m). We recall that the z direction corresponds to the direction of gravity and of the macroscopic temperature gradient. In the following, we use the vector $\boldsymbol{SSA} = (\mathrm{SSA}_x, \mathrm{SSA}_y, \mathrm{SSA}_z)$, where SSA_z is called the vertical component while the average value of SSA_x and SSA_y, noted SSA_{xy}, is called the horizontal component. The orientation of this vector in the (x, y, z) coordinate system is thus a way to estimate the degree of anisotropy of the snow surfaces. In addition, averaging the three components of $\boldsymbol{SSA}$ yields a precise estimate of the usual scalar SSA [*Berryman*, 1998; *Flin et al.*, 2011] provided x, y, and z are aligned with the potential anisotropy axes of the sample.

6.2.2.3 Two-point probability function and correlation lengths

At a given time, within 3-D images of snow, we can define the following characteristic function of the air phase:

$$I^a(\mathbf{x}) = \begin{cases} 1 & \text{if} \quad \mathbf{x} \text{ lies in the air phase} \\ 0 & \text{if} \quad \mathbf{x} \text{ lies in the ice phase} \end{cases}$$

where $\mathbf{x}$ is a position vector within the sample. The one- and two-point probability functions for the air phase are then defined as:

$$S_1 = \langle I^a(\mathbf{x}) \rangle \tag{6.2}$$

$$S_2(\mathbf{r}) = \langle I^a(\mathbf{x}) I^a(\mathbf{x}+\mathbf{r}) \rangle \tag{6.3}$$

where $\mathbf{r}$ is a vector oriented in the x, y or z direction of the image and the angular brackets denote the volume average. $S_2(\mathbf{r})$ is also called the two-point correlation function or the autocorrelation function. For statistically homogeneous media, S_1 is simply equal to the porosity (ϕ) and S_2 depends on $\mathbf{r}$. In general, S_2 has the following asymptotic properties

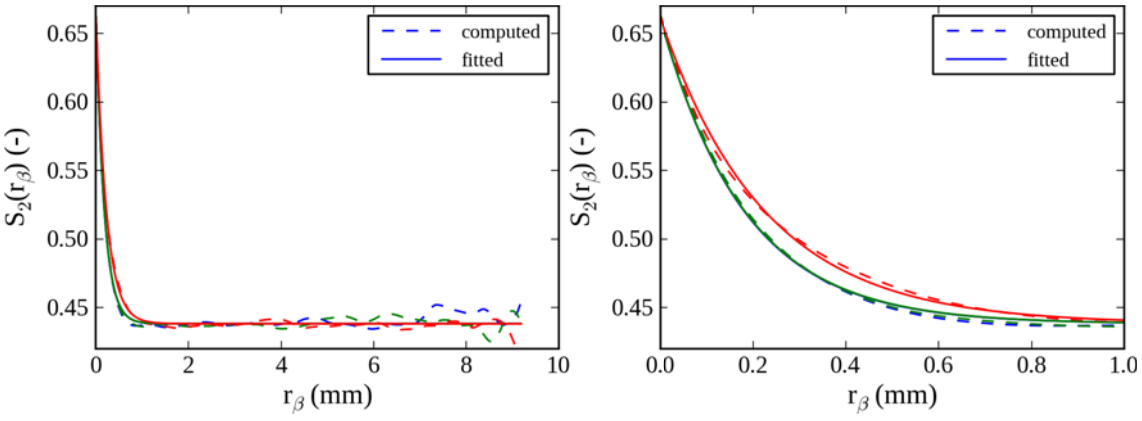

Figure 6.3: Two-point probability function $S_2(\mathbf{r})$ for the whole range of $\mathbf{r}$ (left) and magnified (right) in the x (blue), y (green) and z directions (red), obtained from the 3-D image referred as 7G in Table 6.4.2. Solid and dashed lines correspond respectively to the values computed from Eq. (6.3) and to the results of the expression $S_2(r_\beta) = (\phi - \phi^2)\ \exp(-r_\beta / l_{c_\beta}) + \phi^2$ with $\beta = (x, y, z)$.

[*Torquato*, 2002]:

$$S_2(\mathbf{r}=0) = S_1 = \phi \tag{6.4}$$

$$\lim_{\mathbf{r}\to\infty} S_2(\mathbf{r}) = \phi^2 \tag{6.5}$$

As an illustration, dashed lines in Fig. 6.3 show the two-point probability function computed over a 3-D image of a snow sample after 500 h of metamorphism (referred as image 7G in Table 6.4.2) along the x, y and z directions in blue, green and red, respectively. As proposed by *Löwe et al.* [2011, 2013], by fitting the $S_2(\mathbf{r})$ function along the coordinate axes $\beta = (x, y, z)$ to an exponential $S_2(r_\beta) = (\phi - \phi^2)\ \exp(-r_\beta/l_{c_\beta}) + \phi^2$ (solid lines in Fig. 6.3), one obtains a correlation length l_{c_β} (in μm) in the x, y, and z directions noted l_{c_x}, l_{c_y} and l_{c_z}, respectively. l_{c_z} is called the vertical component. The average value of l_{c_x} and l_{c_y} is called the horizontal component and noted $l_{c_{xy}}$. The vector $\mathbf{l}_c = (l_{c_x}, l_{c_y}, l_{c_z})$ is often used to characterize the typical sizes of the heterogeneities in the microstructure, i.e. to define the characteristic lengths of an ice grain and a pore without distinction.

6.2.2.4 Mean and Gaussian curvatures

At a given point of a 3-D object, the surface is characterized by two principal curvatures κ_1 and κ_2, which correspond to the maximum and minimum values of curvature at this point. Negative, zero and positive values of κ_1 and κ_2 define concave, flat and convex surfaces of ice, respectively. The mean curvature $\mathcal{H}$ (in m^{-1}) and Gaussian curvature $\mathcal{K}$ (in m^{-2}) are defined as:

$$\mathcal{H} = \frac{\kappa_1 + \kappa_2}{2} \tag{6.6}$$

$$\mathcal{K} = \kappa_1 \kappa_2 \tag{6.7}$$

The signs of the mean and Gaussian curvatures characterize the surface shape. For the mean curvature, negative, zero and positive values correspond to concave, flat and convex surfaces of ice, respectively. For the Gaussian curvature, negative, zero and positive values represent saddle-shaped surfaces corresponding for snow to necks and connections between ice grains, flat or cylindrical surfaces, and dome-shaped surfaces (convex or concave), respectively.

Many techniques have been proposed to estimate mean and Gaussian curvatures on either triangular or digital surfaces [*Brzoska et al.*, 1999b; *Nishikawa et al.*, 2001; *Rieger et al.*, 2002; *Zhang et al.*, 2002; *Ogawa et al.*, 2006; *Pottmann et al.*, 2009, e.g.]. Curvature estimations usually imply specific accuracy issues since these estimators are particularly sensitive to noise and digitization effects. This is mainly due to the fact that curvatures are second order derivatives obtained on a discrete grid. In our approach, the mean ($\mathcal{H}$) and Gaussian ($\mathcal{K}$) curvatures are adaptively computed from the largest relevant neighborhoods, limiting their digitization noise (see *Flin et al.*, 2004; *Brzoska et al.*, 2007; *Wang et al.*, 2012 for details). In short, we rely on the following definition for $\mathcal{H}$ and $\mathcal{K}$ [*Sethian*, 1999] where the mean curvature can be defined as the divergence of the normal vector field $\mathbf{n}(p)$ at point p:

$$\mathcal{H}(p) = \frac{\nabla \cdot \mathbf{n}(p)}{2} \tag{6.8}$$

and the Gaussian curvature as:

$$\mathcal{K}(p) = \frac{M(p)}{N(p)} \tag{6.9}$$

with

$$\begin{aligned} M(p) = & d_{,x}^2(d_{,yy}d_{,zz} - d_{,yz}^2) && (6.10)\\ & + d_{,y}^2(d_{,xx}d_{,zz} - d_{,xz}^2) && (6.11)\\ & + d_{,z}^2(d_{,xx}d_{,yy} - d_{,xy}^2) && (6.12)\\ & + 2d_{,x}d_{,y}(d_{,xz}d_{,yz} - d_{,xy}d_{,zz}) && (6.13)\\ & + 2d_{,y}d_{,z}(d_{,xy}d_{,xz} - d_{,yz}d_{,xx}) && (6.14)\\ & + 2d_{,x}d_{,z}(d_{,xy}d_{,yz} - d_{,xz}d_{,yy}) && (6.15) \end{aligned}$$

and

$$N(p) = (d_{,x}^2 + d_{,y}^2 + d_{,z}^2)^2 \tag{6.16}$$

where d is the signed distance map at p and $d_{,x}$, $d_{,y}$ and $d_{,z}$ denote the partial derivatives of d along the x, y and z coordinates, respectively. For $\mathcal{H}$ (Eq. 6.8), the normal vector field $\mathbf{n}(p)$ could also have been expressed as a partial derivative of d. However, we use a specific normal vector estimation as proposed by *Flin et al.* [2005]. Such an approach is based on an adaptive computation of the normal vector field using volumetric information obtained from the signed distance map. This gives us a precise estimation of $\mathcal{H}$ while decreasing the sensitivity of this formula to digitization effects [see *Flin et al.*, 2004]. For $\mathcal{K}$, we simply use Eqs. (6.9)–(6.16) where local estimations $\mathcal{K}(p)$ are averaged on the neighborhoods obtained for the adaptive analysis of $\mathcal{H}$ [*Wang et al.*, 2012].

6.2.3 Computations of tortuosity, effective thermal conductivity and permeability tensors

The full 3-D tensors of tortuosity $\boldsymbol{\tau}$ (dimensionless), of effective thermal conductivity $\mathbf{k}^{\text{eff}}$ (in $\mathrm{W\,m^{-1}\,K^{-1}}$) and of intrinsic permeability $\mathbf{K}^{\text{eff}}$ (in $\mathrm{m^2}$) were computed from 3-D images. For that purpose, specific boundary value problems arising from the homogenization process [*Auriault et al.*, 2009; *Calonne et al.*, 2014b] have been numerically solved on Representative Elementary Volumes (REVs) extracted from 3-D images of snow by using the software Geodict[b], based on a finite volume method [*Thoemen et al.*, 2008]. We define the REV with a side length l by Ω wherein Ω_{i} and Ω_{a} are the domains occupied by the ice and the air, respectively, and where Γ denotes the common boundary.

To compute the effective thermal conductivity tensor $\mathbf{k}^{\text{eff}}$, the following boundary value

[b]Geodict: `http://www.geodict.de`

problem was solved [*Auriault et al.*, 2009; *Calonne et al.*, 2011, 2014b]:

$$\nabla \cdot (\kappa_i(\nabla\ \mathbf{t}_\mathrm{i} + \mathbf{I})) = \mathbf{0} \quad \text{within} \quad \Omega_\mathrm{i} \tag{6.17}$$

$$\nabla \cdot (\kappa_a(\nabla\ \mathbf{t}_\mathrm{a} + \mathbf{I})) = \mathbf{0} \quad \text{within} \quad \Omega_\mathrm{a} \tag{6.18}$$

$$\mathbf{t}_\mathrm{i} - \mathbf{t}_\mathrm{a} = \mathbf{0} \quad \text{on} \quad \Gamma \tag{6.19}$$

$$(\kappa_a(\nabla\ \mathbf{t}_\mathrm{a} + \mathbf{I}) - \kappa_i(\nabla\ \mathbf{t}_\mathrm{i} + \mathbf{I})) \cdot \mathbf{n} = \mathbf{0} \quad \text{on} \quad \Gamma \tag{6.20}$$

$$\frac{1}{|\Omega|}\int_\Omega (\mathbf{t}_\mathrm{a} + \mathbf{t}_\mathrm{i})\mathrm{d}\Omega = \mathbf{0} \tag{6.21}$$

where $\mathbf{I}$ is the identity tensor, $\mathbf{n}$ is the outward vector normal to the ice surface and the two periodic vectors $\mathbf{t}_\mathrm{i}$ and $\mathbf{t}_\mathrm{a}$ are unknown. These two vectors characterize the fluctuations of the temperature field in the ice and air phase which are induced by a given macroscopic gradient of temperature ∇T applied on the REV. Finally, as in *Calonne et al.* [2011], $\kappa_a = 0.024\ \mathrm{W\,m^{-1}\,K^{-1}}$ and $\kappa_i = 2.107\ \mathrm{W\,m^{-1}\,K^{-1}}$ stand for the thermal conductivity of air and ice at 271 K respectively. The effective thermal conductivity tensor $\mathbf{k}^\mathrm{eff}$ is defined as:

$$\mathbf{k}^\mathrm{eff} = \frac{1}{|\Omega|}\left(\int_{\Omega_\mathrm{a}} \kappa_a(\nabla \mathbf{t}_\mathrm{a} + \mathbf{I})\mathrm{d}\Omega + \int_{\Omega_\mathrm{i}} \kappa_i(\nabla \mathbf{t}_\mathrm{i} + \mathbf{I})\mathrm{d}\Omega\right) \tag{6.22}$$

The tortuosity tensor of the air phase $\boldsymbol{\tau}_\mathrm{a}$ and of the ice phase $\boldsymbol{\tau}_\mathrm{i}$ are obtained by solving the same above boundary value problem (6.17)-(6.21) assuming that $\kappa_a = 1$ and $\kappa_i = 0$ for $\boldsymbol{\tau}_\mathrm{a}$, and $\kappa_a = 0$ and $\kappa_i = 1$ for $\boldsymbol{\tau}_\mathrm{i}$. These tensors are defined as:

$$\boldsymbol{\tau}_\mathrm{a} = \frac{1}{|\Omega_\mathrm{a}|}\int_{\Omega_\mathrm{a}} (\nabla \mathbf{t}_\mathrm{a} + \mathbf{I})\mathrm{d}\Omega, \quad \boldsymbol{\tau}_\mathrm{i} = \frac{1}{|\Omega_\mathrm{i}|}\int_{\Omega_\mathrm{i}} (\nabla \mathbf{t}_\mathrm{i} + \mathbf{I})\mathrm{d}\Omega \tag{6.23}$$

Let us note that for snow the air tortuosity is simply linked to the effective diffusion tensor for the water vapor by $\mathbf{D}^\mathrm{eff} = \phi D_v \boldsymbol{\tau}_\mathrm{a}$, where D_v (in $\mathrm{m^2\,s^{-1}}$) is the molecular diffusion coefficient of the vapor in air at the pore scale. If we assume that the porous medium consists of an equivalent tortuous capillary of total length l', in contrast with the REV length l, it can be shown that, by definition, $0 < \tau_\mathrm{a} \propto (l/l')^2 < 1$ [*Bear*, 1972]. Consequently, τ_a tends toward 0 or 1 when the air structure is highly tortuous or straight respectively (the same is true for τ_i and the ice structure). The tortuosity is also often defined as $\tau_\mathrm{f} \propto (l'/l)$ [*Kaempfer et al.*, 2005], so that our tortuosity definition corresponds to the inverse of τ_f^2.

The tensor $\mathbf{K}^\mathrm{eff}$ of intrinsic permeability was obtained by solving the following boundary value problem [*Calonne et al.*, 2012]:

$$\mu_a \triangle \mathbf{v}_a - \nabla \tilde{p}_a - \nabla p_a = \mathbf{0} \quad \text{within} \quad \Omega_\mathrm{a} \tag{6.24}$$

$$\nabla \cdot \mathbf{v}_a = 0 \quad \text{within} \quad \Omega_\mathrm{a} \tag{6.25}$$

$$\mathbf{v}_a = \mathbf{0} \quad \text{on} \quad \Gamma \tag{6.26}$$

where $\mathbf{v}_a$ and $\tilde{p}_a$ (with $\langle \tilde{p}_a \rangle = 0$) are the periodic unknowns which represent respectively the fluid velocity and the pressure fluctuation in a REV induced by a given macroscopic gradient of pressure ∇p_a. μ_a is the dynamic viscosity of air (in Pa s). It can be shown that $\mathbf{v}_a = -(1/\mu_a)\mathbf{b}\nabla p_a$ where $\mathbf{b}$ is a second order tensor which characterizes the variation of

the fluid velocity at the pore scale over a REV induced by a given macroscopic gradient of pressure [*Auriault et al.*, 2009]. Consequently, the permeability tensor is defined as:

$$\mathbf{K}^{\text{eff}} = \frac{1}{|\Omega|} \int_{\Omega_\text{a}} \mathbf{b} \text{d}\Omega \tag{6.27}$$

As the non-diagonal terms of the tensors $\boldsymbol{\tau}_\text{i}$, $\boldsymbol{\tau}_\text{a}$, $\mathbf{k}^{\text{eff}}$ and $\mathbf{K}^{\text{eff}}$ are negligible compared to the diagonal terms (the x, y and z axes of 3-D images correspond to the principal directions of the microstructure, z being along the direction of the gravity and of the temperature gradient), we only focus on the latter ones. In the following, we denote by $\star_z$, $\star_{xy}$ and $\star$ as the vertical component, the average of the two horizontal components ($\star_x$ and $\star_y$), and the average of the three components of any tensor $\star = (\boldsymbol{\tau}_\text{i}, \boldsymbol{\tau}_\text{a}, \mathbf{k}^{\text{eff}}$ or $\mathbf{K}^{\text{eff}})$ respectively. Moreover, for the sake of simplicity, $\star_{xy}$ and $\star$ are called the horizontal and the average components, respectively.

6.2.4 Computations of anisotropy coefficients

The anisotropy coefficient $\mathcal{A}(\star)$ was computed for each of the microstructural and physical properties mentioned above, except for density and curvatures. This coefficient is defined as the ratio between the vertical component over the horizontal one, such as $\mathcal{A}(\star) = \star_z / \star_{xy}$ where $\star = (\boldsymbol{l}_\text{SSA}$, $\boldsymbol{l}_\text{c}$, $\boldsymbol{\tau}_\text{i}$, $\boldsymbol{\tau}_\text{a}$, $\mathbf{k}$ or $\mathbf{K})$. The property is considered isotropic if it exhibits a coefficient $\mathcal{A}(\star)$ close to 1, otherwise the property is anisotropic. Note that, since SSA_{xy} characterizes the vertical surfaces while SSA_z describes the horizontal ones, we study the anisotropy coefficient of the vector $\boldsymbol{l}_\text{SSA} = (1/\text{SSA}_x,\ 1/\text{SSA}_y,\ 1/\text{SSA}_z)$ to be consistent with the other coefficients.

6.2.5 Re-adjustment in density

After sieving, the density of the snow slab exhibited slight spatial inhomogeneities ($300 \pm 15\ \text{kg}\,\text{m}^{-3}$, from macroscopic measurements with a corer). In order to focus only on the evolution of snow properties driven by the temperature gradient, readjusted values of effective thermal conductivity and permeability, k^r and K^r, were computed as if the density was homogeneous in the snow slab and equal to $294\ \text{kg}\,\text{m}^{-3}$ (average of the density values computed from 3-D images) using the regression proposed in *Calonne et al.* [2011] and *Calonne et al.* [2012], respectively, as follows:

$$k^\text{r} = \frac{k^{\text{eff}} \times k^{\text{fit}}(\rho_\text{s})}{k^{\text{fit}}(\rho_{294})} \tag{6.28}$$

$$K^\text{r} = \frac{K^{\text{eff}} \times K^{\text{fit}}(\rho_\text{s})}{K^{\text{fit}}(\rho_{294})} \tag{6.29}$$

with ρ_s the computed snow density, $\rho_{294} = 294\ \text{kg}\,\text{m}^{-3}$, $k^{\text{fit}}(\rho_\text{s}) = 2.5 \times 10^{-6}\rho_\text{s}^2 - 1.23 \times 10^{-4}\rho_\text{s} + 0.024$ and $K^{\text{fit}}(\rho_\text{s}) = 3.0 \times r_{\text{es}}^2 \exp(-0.0130 \times \rho_\text{s})$ where the equivalent sphere radius $r_{\text{es}} = 3\,/\,(\text{SSA} \times \rho_\text{i})$. This way, we obtained readjusted values for a density of $294\ \text{kg}\,\text{m}^{-3}$ of thermal conductivity (k_x^r, k_y^r, k_z^r) and of permeability (K_x^r, K_y^r, K_z^r).

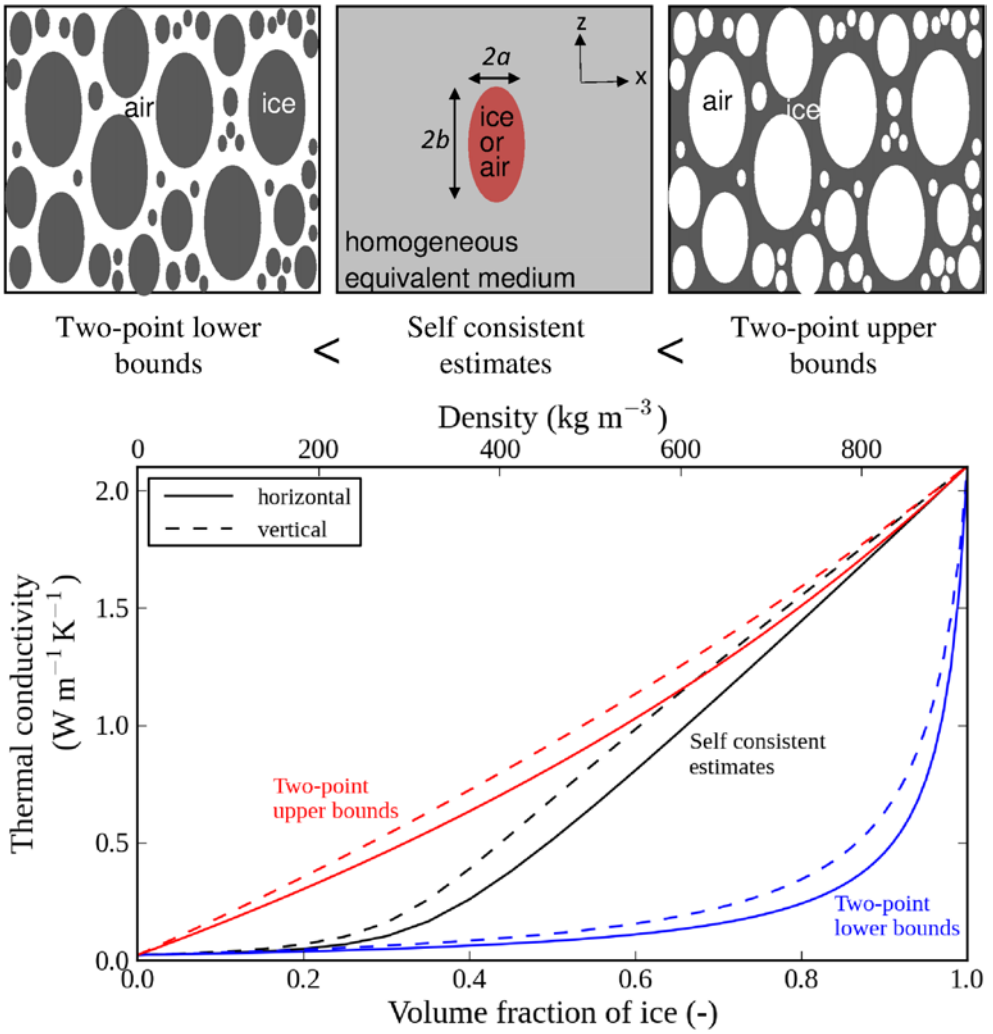

Figure 6.4: Schematic representation of the microstructure corresponding to the two-point bounds and the self consistent scheme. Effective thermal conductivity versus ice volume fraction when $b/a = 1.45$: self consistent estimates (black curves), two-points lower (blue curves) and upper (red curves) bounds.

6.2.6 Analytical estimates based on ellipsoidal inclusions

We used two analytical estimates based on ellipsoidal inclusions to estimate the physical properties of snow in the xy and z directions: the Self consistent estimates and the Dilute beds of ellipsoids. These estimates require basic microstructural information, which are the volume fraction of each phase (ϕ, $1-\phi$) and the inclusion aspect ratio and size. These latter were obtained from the 3-D images, and we chose to describe the inclusion characteristics using the correlation lengths ($l_{c_x}, l_{c_y}, l_{c_z}$).

6.2.6.1 Self consistent estimates: effective thermal conductivity and air tortuosity

The snow microstructure is considered here as a macroscopically anisotropic composite, which corresponds to an assemblage of isotropic ellipsoidal inclusions of air and ice with a

major axis collinear with the z-direction, of same aspect ratio a/b, with volume fractions ϕ, $(1-\phi)$ and thermal conductivities k_a, k_i (see Fig. 6.4). Since the correlation lengths (l_{c_x}, l_{c_y}, l_{c_z}) characterize the typical sizes of the heterogeneities (air and ice without distinction), it seems reasonable, in first order of approximation, to assume that the aspect ratio is given by $a/b = (l_{\mathrm{c}_x} + l_{\mathrm{c}_y})/(2l_{\mathrm{c}_z})$. According to the self consistent scheme [*Bruggeman*, 1935; *Hill*, 1965; *Budiansky*, 1965; *Willis*, 1977; *Torquato*, 2002], each type of inclusion is successively embedded in an homogeneous equivalent medium, i.e. an infinite matrix whose effective thermal conductivity $\mathbf{k}^{\mathrm{sc}}$ is the unknown to be calculated, which is a way to capture the connectivity of both phases. The solution of equations for an isolated inclusion then gives an implicit relation which can be solved for this effective property. In the present case, the self consistent estimate of the effective thermal conductivity $\mathbf{k}^{\mathrm{sc}}$ verifies the following implicit relation [*Torquato*, 2002]:

$$\phi(\kappa_a\mathbf{I}-\mathbf{k}^{\mathrm{sc}})\left(\mathbf{I}+\mathbf{A}[\mathbf{k}^{\mathrm{sc}}]^{-1}(\kappa_a\mathbf{I}-\mathbf{k}^{\mathrm{sc}})\right)^{-1}+(1-\phi)(\kappa_i\mathbf{I}-\mathbf{k}^{\mathrm{sc}})\left(\mathbf{I}+\mathbf{A}[\mathbf{k}^{\mathrm{sc}}]^{-1}(\kappa_i\mathbf{I}-\mathbf{k}^{\mathrm{sc}})\right)^{-1}=0 \tag{6.30}$$

with $\kappa_i = 2.107$ Wm^{-1}K^{-1} and $\kappa_a = 0.024$ Wm^{-1}K^{-1}, and where $\mathbf{A}$ is the depolarization tensor for an ellipsoid in a matrix with an effective thermal conductivity $\mathbf{k}^{\mathrm{sc}}$. When $\mathbf{k}^{\mathrm{sc}}$ is transverse isotropic, the depolarization tensor $\mathbf{A}$ is defined in the (x, y, z) frame as [*Giraud et al.*, 2007; *Kushch and Sevostianov*, 2014]:

$$\mathbf{A} = \begin{pmatrix} Q & 0 & 0 \\ 0 & Q & 0 \\ 0 & 0 & 1-2Q \end{pmatrix} \tag{6.31}$$

with

$$Q = \frac{1}{2(1-\gamma^2)}\left(1-\frac{\gamma^2}{\sqrt{\gamma^2-1}}\tan^{-1}\left(\sqrt{\gamma^2-1}\right)\right) \quad \text{if} \quad \gamma \geq 1 \tag{6.32}$$

$$Q = \frac{1}{2(1-\gamma^2)}\left(1-\frac{\gamma^2}{2\sqrt{1-\gamma^2}}\ln\left(\frac{1+\sqrt{1-\gamma^2}}{1-\sqrt{1-\gamma^2}}\right)\right) \quad \text{if} \quad \gamma \leq 1 \tag{6.33}$$

where γ is linked to the aspect ratio of the ellipsoid and anisotropy ratio of $\mathbf{k}^{\mathrm{sc}}$ by $\gamma = (a/b) \times (k^{sc}_{xy}/k^{sc}_{z})$. Thus, from Eqs. (6.30) and (6.31), the horizontal and vertical components of $\mathbf{k}^{\mathrm{sc}}$ are written:

$$k^{\mathrm{sc}}_x = k^{\mathrm{sc}}_y = k^{\mathrm{sc}}_{xy} = \frac{-(\kappa_a(\phi-Q)+\kappa_i((1-\phi)-Q))-\sqrt{\triangle_{xy}}}{2(Q-1)} \tag{6.34}$$

$$k^{\mathrm{sc}}_z = \frac{-(\kappa_a(\phi-(1-2Q))+\kappa_i((1-\phi)-(1-2Q)))-\sqrt{\triangle_z}}{2((1-2Q)-1)} \tag{6.35}$$

where

$$\triangle_{xy} = (\kappa_a(\phi-Q)+\kappa_i((1-\phi)-Q))^2 - 4(Q-1)Q\kappa_i\kappa_a \tag{6.36}$$

$$\triangle_z = (\kappa_a(\phi-(1-2Q))+\kappa_i((1-\phi)-(1-2Q)))^2 - 4(1-2Q) - 1(1-2Q)\kappa_i\kappa_a \tag{6.37}$$

The self consistent estimate of the air tortuosity tensor $\boldsymbol{\tau}^{\mathrm{sc}}_{\mathrm{a}}$ can be easily deduced from Eq. (6.30) with $\kappa_a = 1$ and $\kappa_i = 0$:

$$\boldsymbol{\tau}^{\mathrm{sc}}_{\mathrm{a}} = \phi^{-1}\mathbf{k}^{\mathrm{sc}}(\kappa_a = 1, \kappa_i = 0) \tag{6.38}$$

with, $\tau_{a_x}^{sc} = \tau_{a_y}^{sc} = \tau_{a_{xy}}^{sc} = \phi^{-1} k_{xy}^{sc}(\kappa_a = 1,\ \kappa_i = 0)$ and $\tau_{a_z}^{sc} = \phi^{-1} k_z^{sc}(\kappa_a = 1,\ \kappa_i = 0)$. Let us remark that in the particular case described above, the depolarization tensor of Eq. (6.31) is equal in both phases and Eq. (6.30) is invariant under the simultaneous interchange $\kappa_a \leftrightarrow \kappa_i$ and $\phi \leftrightarrow 1 - \phi$, meaning that each phase is treated symmetrically.

As an illustration, Figure 6.4 shows the behavior of $k_x^{sc} = k_y^{sc}$ and k_z^{sc} vs. the ice volume fraction for $b/a = 1.45$. On this figure, the two-point bounds for anisotropic composites [*Willis*, 1977] are also shown. The corresponding microstructure of the lower bounds can be viewed as ellipsoidal inclusions of ice of same aspect ratio (b/a) dispersed within the air matrix, as shown by the upper left part of Fig. 6.4. Inversely for the lower bounds, the microstructure is seen as ellipsoidal inclusions of air of same aspect ratio (b/a) dispersed within the ice matrix (see upper right part of Fig. 6.4). As expected, in each direction, the self consistent estimate lies between the bounds: at low volume fractions of ice, the self consistent estimates and the lower bounds are very close; conversely, at high volume fractions of ice, the self consistent estimates are quite similar to the upper bounds. Finally, Fig. 6.4 clearly shows the anisotropy of the effective thermal conductivity induced by the anisotropy of the microstructure. The anisotropy coefficient $\mathcal{A}(\mathbf{k}^{sc})$ is defined as k_x^{sc}/k_z^{sc} and consequently, from Eq (29) and (30), is a function of the ratio κ_i/κ_a, the porosity ϕ, and the aspect ratio b/a. In the particular case of Fig. 6.4, $\kappa_i/\kappa_a \simeq 100$ and b/a =1.45, so $\mathcal{A}(\mathbf{k}^{sc})$ depends only on the porosity and ranges from 1 to 1.6 in the whole range of ice volume fraction.

6.2.6.2 Dilute beds of spheroids: permeability

The snow is seen as a dilute dispersion of ellipsoids of ice in a matrix of air. The semi-axes of each ellipsoid are defined as: $a = (l_{c_x} + l_{c_y})/4$ and $b = l_{c_z}/2$. It can be shown [*Torquato*, 2002] that the permeability tensor estimate $\mathbf{K}^{el}$ is written in the (x, y, z) frame:

$$\mathbf{K}^{el} = \frac{2a^2}{9(1-\phi)} \begin{pmatrix} f(b/a) & 0 & 0 \\ 0 & f(b/a) & 0 \\ 0 & 0 & g(b/a) \end{pmatrix} \tag{6.39}$$

where

$$f(b/a) = \frac{3}{16\chi_b^3}\left((3\chi_b^2 - 1)\ln\left(\frac{1+\chi_b}{1-\chi_b}\right) + 2\chi_b\right) \quad \text{if} \quad b/a \geq 1 \tag{6.40}$$

$$f(b/a) = \frac{3}{8\chi_a^3}\left((1+3\chi_a^2)\tan^{-1}(\chi_a) - \chi_a\right) \quad \text{if} \quad b/a \leq 1 \tag{6.41}$$

and

$$g(b/a) = \frac{3}{8\chi_b^3}\left((1+\chi_b^2)\ln\left(\frac{1+\chi_b}{1-\chi_b}\right) - 2\chi_b\right) \quad \text{if} \quad b/a \geq 1 \tag{6.42}$$

$$g(b/a) = \frac{3}{4\chi_a^3}\left((\chi_a^2 - 1)\tan^{-1}(\chi_a) + \chi_a\right) \quad \text{if} \quad b/a \leq 1 \tag{6.43}$$

where χ_a and χ_b are linked to the aspect ratio of the ellipsoid as: $\chi_a^2 = -\chi_b^2 = (a/b)^2 - 1$. By definition, this estimation of the permeability does not depend on the spatial arrangement

of the ellipsoids, and consequently does not capture the real tortuosity of the porous media induced by the connectivity of both air and ice phases. In order to overcome this problem, the following permeability tensor estimate $\mathbf{K}^{\mathrm{di}}$ is proposed such as:

$$K_x^{\mathrm{di}} = K_y^{\mathrm{di}} = K_{xy}^{\mathrm{di}} = \tau_{\mathrm{a}_{xy}}^{\mathrm{sc}} K_{xy}^{\mathrm{el}}, \quad K_z^{\mathrm{di}} = \tau_{\mathrm{a}_z}^{\mathrm{sc}} K_z^{\mathrm{el}}. \tag{6.44}$$

where $K_{xy}^{\mathrm{el}} = K_x^{\mathrm{el}} = K_y^{\mathrm{el}}$ and K_z^{el} are the diagonal components of $\mathbf{K}^{\mathrm{el}}$ in the (x, y, z) frame (see Eq.6.39). This relation allows the recovery of an expression of the permeability similar to the one of Carman-Kozeny [*Bear*, 1972]: $K^{\mathrm{di}} \propto h(\phi)\tau_{\mathrm{a}} d_{\mathrm{c}}^2 = h(\phi) d_{\mathrm{c}}^2/\tau_{\mathrm{f}}^2$, where h is a function of the porosity and d_{c} is a characteristic length of the microstructure.

6.3 Results

6.3.1 Time evolution of microstructural and physical properties of snow

Figure 6.5 illustrates the time evolution of the snow microstructure during the experiment of temperature gradient metamorphism. 3-D images obtained from X-ray tomography are presented together with the corresponding vertical cross-section and photograph. The color coding of the 3-D images corresponds to the mean curvature field. For a better visualization of the faceted shapes, the images are presented "upside down": the top of the images corresponds to the lowest and warmest side of the physical sample. We observe qualitatively that the initial rounded grains become bigger and more angular and faceted with time. After about 200 h, depth hoar is obtained showing characteristic striations on the surface of grains (see photographs in Fig. 6.5). At the end of the experiment, the ice structure is prefentially arranged along the vertical direction, i.e. the direction of the temperature gradient, as shown by the cross-sections.

All the snow properties computed based on the 3-D images are summarized in Table 6.4.2. The time evolution of snow density, specific surface area, correlation length, tortuosity of ice and air, thermal conductivity and permeability are depicted in Fig. 6.6. The blue, green and red symbols represent the x, y and z values of the considered property, respectively. One can observe that:

- The snow density shows no significant evolution with time and the average value over the experiment is 294 kg m^{-3} (porosity of 0.68). In detail, low variations between 275 and 315 kg m^{-3} are observed from one image to another (Fig. 6.6a). As explained in Sect 6.2.5, these variations reflect the spatial heterogeneity initially present in the sieved snow layer, and not a real time evolution generated by the temperature gradient conditions.

- The average value of the SSA estimates in the three directions decreases continuously with time from 27.7 to 13.4 m^2 kg^{-1}. Between 0 and 144 h, the z estimates are slightly higher than the horizontal ones (29.2 against 26.9 m^2 kg^{-1} at 0 h). After 144 h, values in the three directions become very close to each other (Fig. 6.6b).

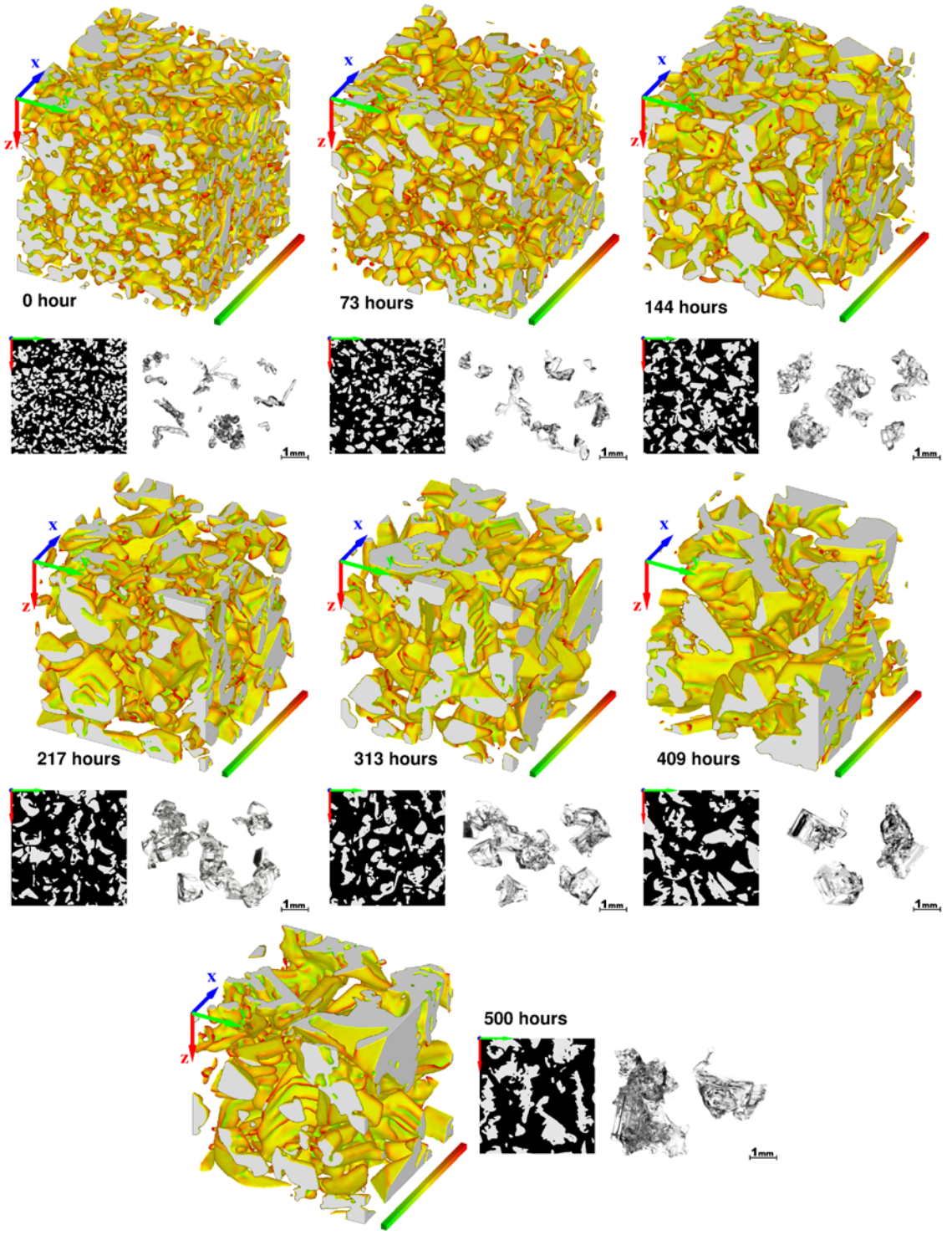

Figure 6.5: Microstructure evolution during the TG metamorphism. For each stage of the evolution, the following views are given: (i) 3-D images of the snow samples where colors represent the mean curvature of the surfaces, ranging from -36 to $+36$ mm^{-1}. Convexities, flat shapes and concavities are shown in red, yellow and green, respectively. Images have a size of 3 mm $\times$ 3 mm $\times$ 3 mm. For a better visualization of the faceted shapes, the images are presented "upside down". The arrows in blue, green and red correspond to the x, y and z directions of the images, respectively. (ii) Vertical cross-sections from 3-D images of 5.5 mm $\times$ 5.5 mm $\times$ 5.5 mm, where ice is in white and air in black. (iii) Photographs of snow grains.

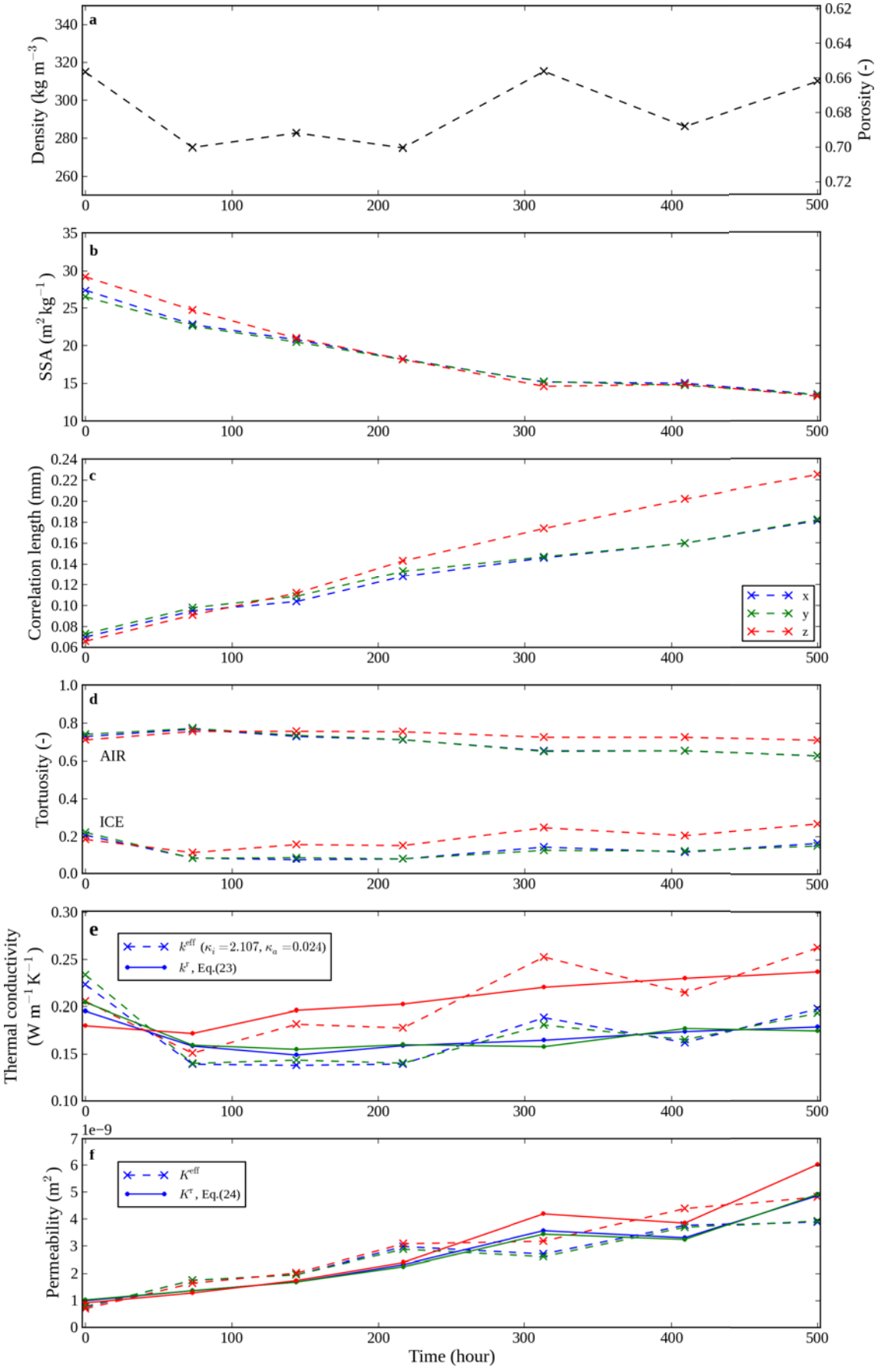

Figure 6.6: Time evolution of microstructural and physical properties of snow during the whole temperature gradient experiment. Values in the x, y and z directions are given in blue, green and red, respectively.

- The values of correlation length increase continuously during the experiment, evolving from 71 to 181 μm in the xy directions and from 68 to 228 μm in the z direction (Fig. 6.6c).

- The values of air tortuosity (~ 0.7) are around five times higher than those of ice tortuosity (~ 0.15) (Fig. 6.6d). The overall evolution of both properties is low and can be divided in two stages: the ice tortuosity decreases between 0 and 73 h and then slightly increases until the end of the experiment, while the air tortuosity shows the opposite trends during these two same periods. During the second stage, the z values stand out and become increasingly higher than the horizontal ones for both phases.

- The raw values of the effective thermal conductivity, which are referred as "computed" and depicted by the dashed lines in Fig. 6.6e, exhibit the same variations as the snow density, showing the strong relationship between these two variables. The values range between 0.14 and 0.26 $\mathrm{W\,m^{-1}\,K^{-1}}$. Solid lines in Fig. 6.6e, referred as "readjusted", show values of thermal conductivity after readjustment at a density of 294 $\mathrm{kg\,m^{-3}}$. As explained in Sect. 6.2.5, this readjustment is one way to estimate the thermal conductivity without taking into account the influence of density variations. The evolution of readjusted values is thus smoother than the one of computed values, but is as significant. Computed and readjusted values decrease from 0 to 73 h and then continuously increase until the end of the metamorphism, showing an evolution in two stages similar to the one of tortuosities. After 73 h, the z values become much higher than the xy values with time.

- The computed values of permeability range between 0.70×10^{-9} and $4.84 \times 10^{-9}\,\mathrm{m^2}$. They exhibit an opposite evolution to the one of snow density, but this dependence seems less pronounced than for the thermal conductivity. Indeed, despite the influence of density, a significant evolution is still observed during the metamorphism (dashed lines in Fig. 6.6f). Both computed and readjusted values increase over the experiment and vertical values become higher than the horizontal ones after 217 h.

Figure 6.7 shows the time evolution of the anisotropy coefficient for five snow properties. Overall, the evolution is the same for all properties: the coefficient increases from values lower than one at the beginning of the experiment to values greater than one at the end. In detail, the magnitude of the coefficients is strongly different from one variable to another. The largest evolution is shown by the coefficient of ice tortuosity $\mathcal{A}(\boldsymbol{\tau}_\mathrm{i})$, which increases from 0.86 to 1.90 between 0 and 144 h and then slightly decreases to reach 1.70 at the end of the metamorphism. The anisotropy coefficient of the thermal conductivity $\mathcal{A}(\mathbf{k}^\mathrm{eff})$ increases from 0.90 to 1.34. The largest increases of $\mathcal{A}(\boldsymbol{\tau}_\mathrm{i})$ and $\mathcal{A}(\mathbf{k}^\mathrm{eff})$ are observed between 0 and 144 h, showing that changes are almost concentrated during this period for both of the properties, as already pointed out above and shown in Fig. 6.6. The correlation length and permeability show similar values of anisotropy coefficients, which evolve from 0.96 to 1.25 and from 0.91 to 1.23, respectively. Finally, anisotropy coefficients of air tortuosity

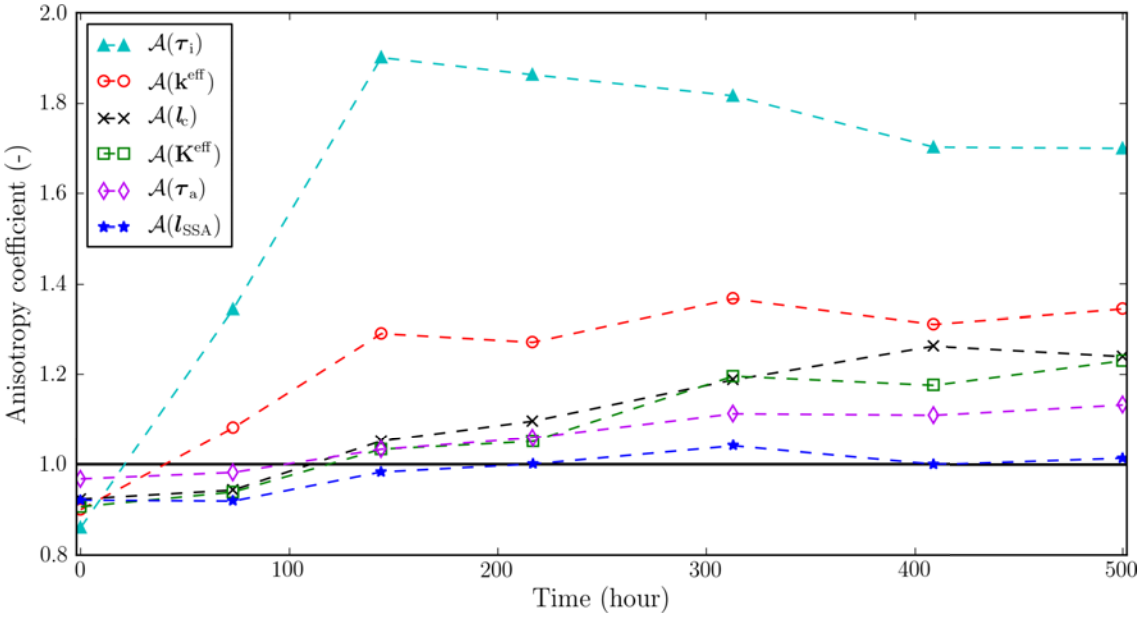

Figure 6.7: Time evolution of the anisotropy coefficient of the whole computed properties.

and of $\boldsymbol{l}_{SSA}$ are the smallest and evolve during the experiment from 0.97 to 1.13 and from 0.92 to 1.01, respectively.

The distributions of mean curvature of the upward (left) and downward (right) surfaces of ice are presented in Fig. 6.8. They are expressed in terms of occurrence ratio, which gives the ratio in % of the ice surface area that exhibits a mean curvature located in a particular range of values over the total ice surface area. The time evolution of these distributions is shown by the plots of different colors. The area-averaged and the standard deviation of the mean curvature values are given in Table 6.4.2. Initially (red color), the distribution of upward and downward surfaces are similar, with a peak of mean curvature located around 6 mm^{-1} and an occurrence ratio of $\sim 3\,\%$. With time, the area-averaged mean curvature decreases gradually, meaning that ice structures tend to become larger. At the end of the experiment (purple color), the upward and downward surfaces exhibit clearly distinct distributions: the peak of mean curvature is now located at 1 mm^{-1} (occurrence ratio of 4.2 %) for the upward ones, and at 0 mm^{-1} (occurrence ratio of 4.8 %) for the downward ones.

Using the same representation, Fig. 6.9 shows the Gaussian curvature distributions computed from the entire ice–air interface. A log scale was used to allow a better visualization of the curves. Here, we do not discern the upward and downward surfaces of ice because the Gaussian curvature distributions of these two cases are similar. Table 6.4.2 provides the time evolution of the area-averaged and standard deviation values. All the distributions are centered at 0 mm^{-2}, but become sharper over time: the maximum occurrence ratio evolves from 4.5 % to 17.3 % between 0 and 500 h and the standard deviation continuously decreases. This implies that the proportion of large, flat or cylindrical structures of ice increases. The initial distribution (red color) stands out from the others: it exhibits occurrence ratios which are small between around -50 and 50 mm^{-2} and large

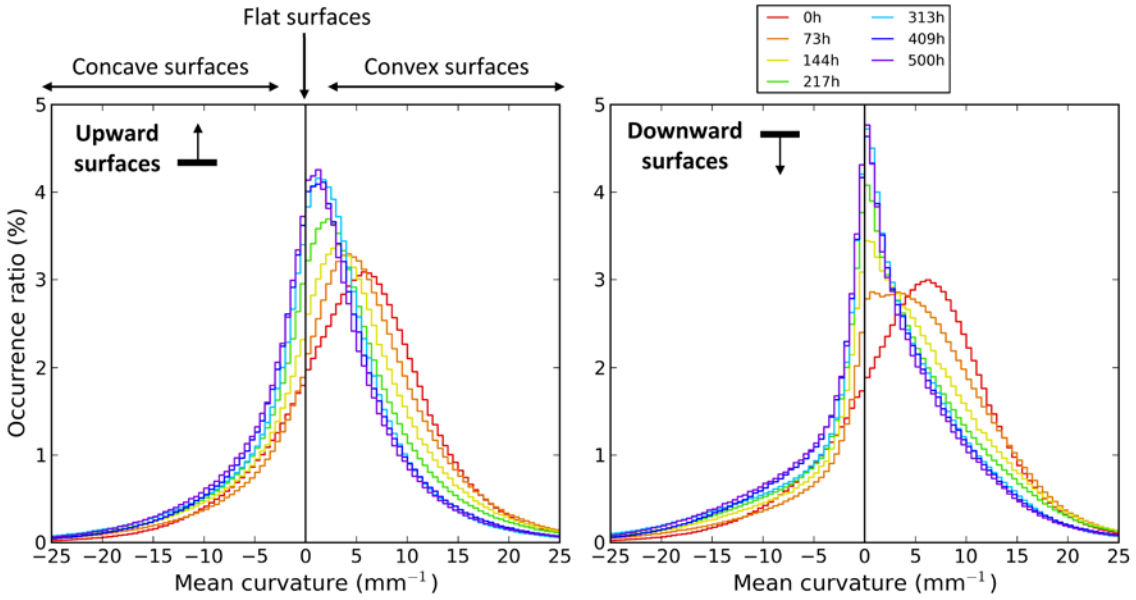

Figure 6.8: Time evolution of the mean curvature distribution computed from the upward (left) and downward (right) surfaces of the 3-D images. Each curvature class is 0.5 mm^{-1} wide.

between around -500 and -50 mm^{-2}, compared to those of other distributions. The most important changes in Gaussian curvatures of ice surfaces appear thus early after the beginning of the temperature gradient, where high negative values corresponding to small saddle-shaped structures disappear in favor of low values close to 0 mm^{-2}, which reflect large and less curved structures. Qualitatively, the same observations can be done from the 3-D images of snow at 0 (left) and 500 h (right) of metamorphism represented in Fig. 6.10 by looking at the color maps of Gaussian curvature. In the initial image, we see a lot of green color (negative Gaussian curvature) at bonds between grains, while the final image exhibits mainly yellow-based colors (nearly zero Gaussian curvatures) representing flat and large structures. The seven images of snow represented with the color map of the Gaussian curvature, as well as those of the mean curvature, are available in Appendix E.

6.3.2 Comparisons with analytical estimates

Figure 6.11 shows the comparison between the time evolution of computed values (dashed lines) and values given by analytical estimates (solid lines) of air tortuosity, effective thermal conductivity and permeability. Computed values are given in the x, y and z directions while the ones given by estimates are described in the z and xy directions (the vertical and the horizontal planes). In order to compare estimates and experiments quantitatively, we use the mean of relative differences $E(\star)$ defined as

$$E(\star) = \frac{\star_{\text{from estimate}} - \star_{\text{computed}}}{\star_{\text{computed}}}, \tag{6.45}$$

where $\star$ is a component or the anisotropy coefficient of $\boldsymbol{\tau}_a$, $\mathbf{k}^{\text{eff}}$ and $\mathbf{K}^{\text{eff}}$. $E(\star)$ is given with the associated standard deviation. For the vertical values of properties, $E(\tau_{a_z}) = 6.3 \pm 4.5\,\%$,

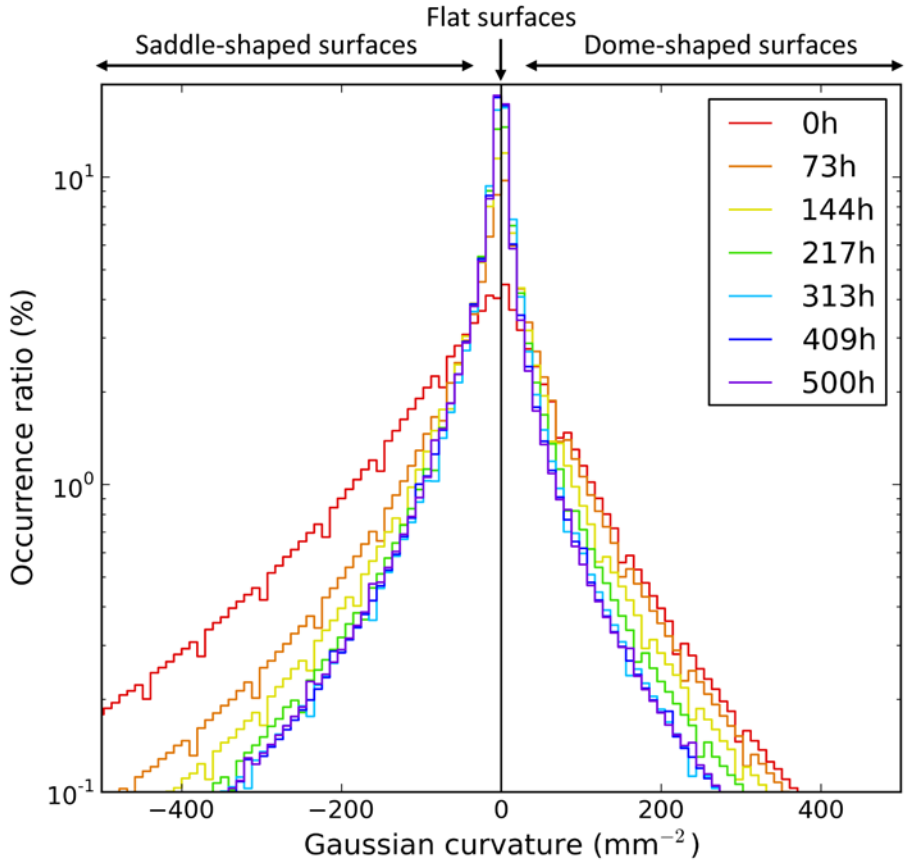

Figure 6.9: Time evolution of the Gaussian curvature distribution computed from the whole surface of the 3-D images. Each curvature class is 10 mm^{-2} wide.

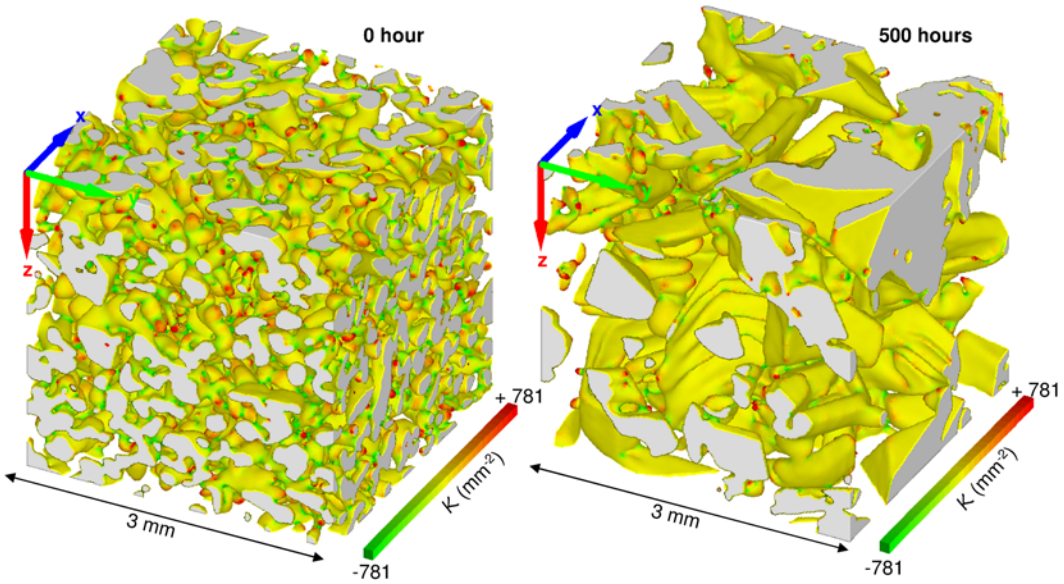

Figure 6.10: The initial (left) and final (right) 3-D images of the experiment where colors represent the Gaussian curvature of the surfaces, ranging from −781 to +781 mm^{-2}. Dome-shaped (concave or convex), flat or cylindrical and saddle-shaped surfaces are shown in red, yellow and green, respectively. Images have a size of 3 mm × 3 mm × 3 mm. For a better visualization of the faceted shapes, the images are presented "upside down". The arrows in blue, green and red correspond to the x, y and z directions of images, respectively.

$E(k_z^{\text{eff}}) = -22.6 \pm 4.32\,\%$ and $E(K_z^{\text{eff}}) = -9.6 \pm 10.9\,\%$, whereas for the horizontal ones, $E(\tau_{\text{a}_{xy}}) = 8.1 \pm 5.2\,\%$, $E(k_{xy}^{\text{eff}}) = -15.6 \pm 6.0\,\%$ and $E(K_{xy}^{\text{eff}}) = -8.1 \pm 14.7\,\%$.

Using the same representation, the time evolution of anisotropy coefficients from computed values and values given by estimates of the three above properties is shown in Fig. 6.12. For the air tortuosity, permeability and thermal conductivity, $E(\mathcal{A}(\boldsymbol{\tau}_{\text{a}})) = -1.6 \pm 0.9\,\%$, $E(\mathcal{A}(\mathbf{k}^{\text{eff}})) = -7.9 \pm 7.4\,\%$, and $E(\mathcal{A}(\mathbf{K}^{\text{eff}})) = -1.1 \pm 4.2\,\%$, respectively.

6.4 Discussion

6.4.1 Evolution of the microstructure

From the mean curvature distributions (Fig. 6.8) and the 3-D images (Fig. 6.5), we observe that the snow microstructure undergoes a strong directional faceting under a temperature gradient. At the beginning of the experiment, the top and base of ice grains are identical in shape and exhibit mainly convex surfaces, characteristic of rounded grains. With time, these regions become strongly different, showing mostly convex surfaces at the top and faceted surfaces at the bottom of the grains, which is typical of faceted crystals and depth hoar. This observation is in agreement with the results of *Flin et al.* [2006] and *Flin et al.* [2007] who show asymmetries in the mean curvature distributions of snow samples submitted to low TGs (3 and 16 $\mathrm{K\,m^{-1}}$ at -3°C) during three weeks. This asymmetric behavior can be attributed to the growth and decay properties of the ice crystal at the molecular level, where some sites are energetically more stable for the deposition or sublimation of a water molecule (see TLK or Kossel crystal models in *Markov* [1995]; *Mutaftschiev* [2001]). Thus, the convex surfaces that undergo vapor deposition grow by a layer by layer process resulting in the production of facets. Conversely, the sublimation of convex crystals preferentially leads to the generation of kink and step sites, which results in the rounding of the shapes (see e.g. *Knight* [1966]; *Flin and Brzoska* [2008] for more details). Our mean curvature results confirm the above considerations: during the experiment, the upward-oriented grain surfaces are warmer than the surrounding air and sublimate, inducing a rounding of the interface. Symetrically, the downward-oriented surfaces of the ice microstructure, colder than air, undergo vapor deposition and generate facets.

From the temporal evolution of the snow (e.g. Fig. 6.6), the metamorphism can be divided in two periods: (i) between 0 and 73 h, the microstructure, resulting from equi-temperature conditions, recrystallizes toward a new pattern of structure to adapt to the temperature gradient conditions. In particular, the small but numerous connections between grains sublimate in favor to the growth of large structures (see Gaussian curvature distributions in Fig. 6.9). During this transitional state, the ice structure becomes more tortuous (minimum value of tortuosity over the whole experiment reached at 73 h in Fig. 6.6d), because of the decrease of the links between grains. (ii) After 73 h, the structure evolves in the continuity of the pattern developed during the first stage (consolidation): grains and connections become increasingly larger especially in the gradient direction, and the ice network becomes gradually less tortuous. Our observations confirm the previous studies of *Bradley et al.* [1977], *Schneebeli et al.* [1999] and *Schneebeli and Sokratov* [2004]

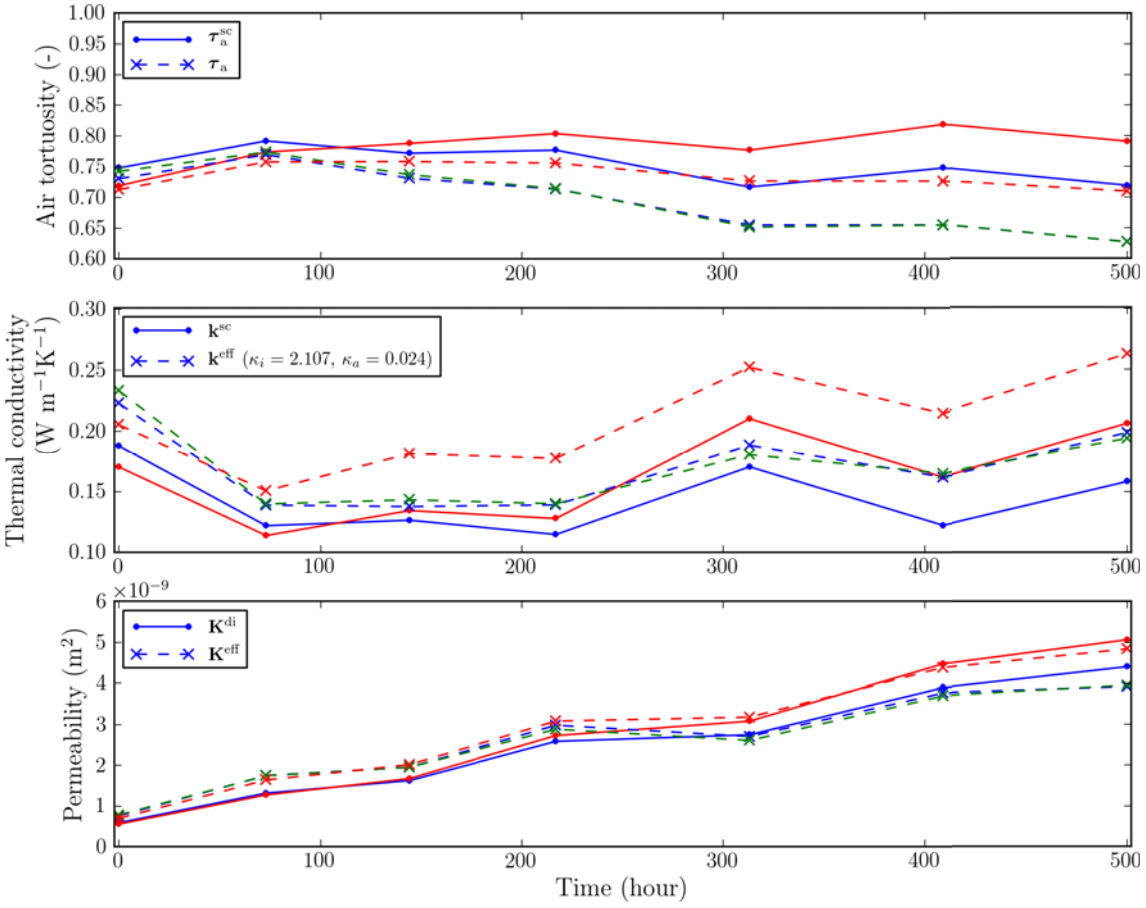

Figure 6.11: Time evolution of air tortuosity, thermal conductivity and permeability during the whole experiment. Comparison between values computed from 3-D images in the x, y and z directions (dashed lines in blue, green and red, respectively) and values given by analytical estimates in the xy and z directions (solid lines in blue and red, respectively).

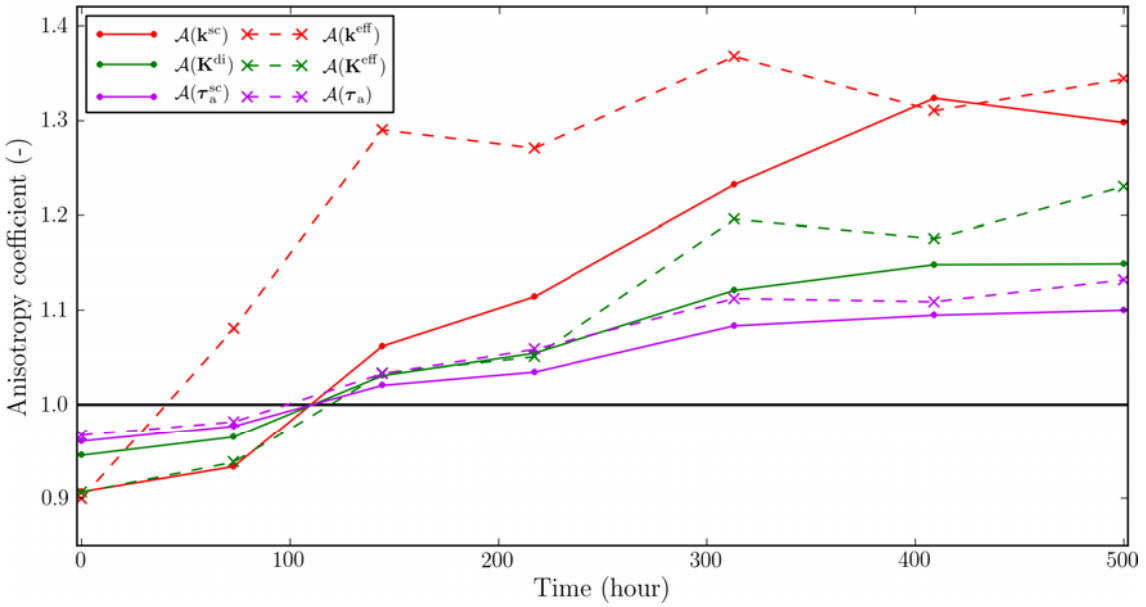

Figure 6.12: Time evolution of the anisotropy coefficients of air tortuosity, thermal conductivity and permeability. Comparison between coefficients deduced from values computed on 3-D images (dashed lines) and values given by analytical estimates (solid lines).

concerning the evolution of bonds under TG.

Because the air tortuosity is about five times higher than the ice tortuosity (see Fig. 6.6d), our snow samples can be considered as being comprised of a tortuous skeleton of ice surrounded by large channels of air in the three directions. Our initial z value of ice tortuosity of 0.19 (referred as 0A in Table 6.4.2) is quantitatively in good agreement with the work of *Kaempfer et al.* [2005] who computed from a 3-D image of rounded grains at 268 $\mathrm{kg\,m^{-3}}$ a vertical ice tortuosity of $\tau_{\mathrm{f}}^2 = 4.4$, which corresponds to 0.23 according to our tortuosity definition. In accordance with the observations of *Schneebeli and Sokratov* [2004]; *Satyawali et al.* [2008] and *Pinzer et al.* [2012], the snow density remains constant over the experiment, while grains and pores grow continuously as shown by correlation lengths and curvature distributions. It means that the microstructure is re-built without a supply or loss of mass. Moreover, the snow becomes more and more anisotropic with a structure elongated in the vertical direction, as illustrated by the anisotropy coefficients of the correlation length and of the ice tortuosity. From a thermodynamic point of view, this microstructural anisotropy can be seen as a way to decrease the vertical temperature gradient by enhancing the heat flow in that direction [*Staron et al.*, 2014].

6.4.2 Link with the physical properties

Heat conduction in snow is mostly due to the conduction of ice which conducts 100 times better than the air. Consequently, the effective thermal conductivity of snow is strongly linked to its density and to the ice tortuosity, as illustrated in Fig. 6.6. Anisotropy of thermal conductivity is lower than that of ice tortuosity because the air phase taken into account in the computation of conduction reduces this anisotropy. Air conduction cannot be neglected in the computations of snow effective conductivity even if the ratio $k_{\mathrm{i}} \,/\, k_{\mathrm{a}}$ is about 88 at 271 K, as already shown by e.g. *Calonne et al.* [2011].

We observe two distinct stages in the evolution of the effective thermal conductivity (Fig. 6.6e): a decrease between 0 and 73 h, followed by an increase until the end of the experiment. This observation is in agreement with the result of *Schneebeli and Sokratov* [2004] who also noticed a two-stage evolution of this property in roughly similar conditions (average temperature of -8°C, temperature gradient of 100 $\mathrm{K\,m^{-1}}$, snow density of 268 $\mathrm{kg\,m^{-3}}$). This behavior can be related to the evolution of the microstructure explained in Sect. 6.4.1, since (i) the destruction of connections between grains during the first period of temperature gradient limits the heat conduction in snow and (ii) the growth of large ice structures in a second time, in particular in the z direction, enhances the heat transfer.

Table 6.1: Microstructural and physical properties computed from 3-D images. Snow types are given according to the international classification [*Fierz et al.*, 2009]. "A" refers to the average value and "SD" refers to the standard deviation value.

Name		0A	1A	2A	3A	4A	5G	7G
Snow type		RG	RG	FC	DH	DH	DH	DH
Length size of 3-D image (mm)		5.9	5.9	5.9	5.9	5.9	9.7	9.2
Voxel size of 3-D image (μm)		8.4	8.4	8.4	8.4	8.4	9.7	9.7
Time under temperature gradient (h)		0	73	144	217	313	409	500
Density ρ_s ($\mathrm{kg\,m^{-3}}$)		315	275	283	275	315	286	310
Porosity ϕ (–)		0.657	0.700	0.692	0.700	0.656	0.688	0.622
Mean curvature $\mathcal{H}$ - Upward surfaces ($\mathrm{mm^{-1}}$)	Average value	4.6	4.3	3.4	2.3	1.0	1.4	0.8
	Standard deviation	8.3	9.0	9.6	8.9	8.5	8.1	8.4
Mean curvature $\mathcal{H}$ - Downward surfaces ($\mathrm{mm^{-1}}$)	Average value	4.7	4.5	3.2	2.5	1.2	1.5	0.9
	Standard deviation	8.4	9.2	9.1	9.6	9.3	8.8	9.2
Gaussian curvature $\mathcal{K}$ - All surfaces ($\mathrm{mm^{-2}}$)	Average value	-81.4	-31.2	-24.0	-19.3	-18.8	-19.0	-18.3
	Standard deviation	284.7	246.8	228.7	208.2	194.0	173.9	184.1
SSA ($\mathrm{m^2\,kg^{-1}}$)	x	27.4	22.8	20.8	18.2	15.2	15.0	13.5
	y	26.5	22.6	20.5	18.2	15.2	14.8	13.4
	z	29.2	24.7	21.0	18.2	14.6	14.9	13.3
SSA ($\mathrm{m^2\,kg^{-1}}$)	$(x+y+z)/3$	27.7	23.4	20.8	18.2	15.0	14.9	13.4
Correlation length $\mathbf{l}_c$ (μm)	x	70	95	104	128	146	160	181
	y	73	98	109	133	147	160	182
	z	66	91	112	143	174	202	225
Air tortuosity $\boldsymbol{\tau}_a$ (–)	x	0.73	0.77	0.73	0.71	0.66	0.66	0.63
	y	0.74	0.77	0.74	0.71	0.65	0.66	0.63
	z	0.71	0.76	0.76	0.76	0.73	0.73	0.71
Ice tortuosity $\boldsymbol{\tau}_i$ (–)	x	0.21	0.09	0.08	0.08	0.14	0.12	0.16
	y	0.22	0.09	0.09	0.08	0.13	0.12	0.15
	z	0.19	0.12	0.16	0.15	0.25	0.21	0.27
Thermal conductivity $\mathbf{k}^{\mathrm{eff}}$ ($\mathrm{W\,m^{-1}\,K^{-1}}$)	x	0.22	0.14	0.14	0.14	0.19	0.16	0.20
	y	0.23	0.14	0.14	0.14	0.18	0.17	0.19
	z	0.21	0.15	0.18	0.18	0.25	0.21	0.26
Permeability $\mathbf{K}^{\mathrm{eff}}$ ($\times 10^{-9}\,\mathrm{m^2}$)	x	0.76	1.75	1.95	2.98	2.71	3.77	3.92
	y	0.78	1.74	1.95	2.89	2.61	3.70	3.95
	z	0.70	1.64	2.02	3.08	3.18	4.39	4.84

As already mentioned, the intrinsic permeability is proportional to $h(\phi)\tau_a d_c^2$, where d_c is a characteristic length of the microstructure which could be linked to the correlation length or to the inverse of the specific surface area [*Calonne et al.*, 2012]. Consequently, the anisotropy of the permeability depends on both anisotropies of the air tortuosity and of the chosen characteristic length. Since the anisotropy coefficient of permeability, air tortuosity, and correlation length present similar time evolutions, while that of $\boldsymbol{l}_{SSA}$ stands out by remaining close to one (see Fig. 6.7), our results seem to show that the anisotropy of the permeability is mainly related to that of the air tortuosity and of the correlation length for snow. The fact that the permeability is related to the density and a characteristic length can explain that this property is less influenced by the density variations than the thermal conductivity as described in Sect. 6.3.1, but undergoes the same continuous increase over the experiment that is observed for the characteristic length.

Figure 6.6 shows an overall increase of the effective thermal conductivity and permeability at a constant density, underlying the role of the microstructure rearrangement [*Schneebeli and Sokratov*, 2004; *Satyawali et al.*, 2008]. Moreover, a significant vertical anisotropy is observed for both variables with coefficients until ~ 1.3. Thus, for snow subjected to a temperature gradient, the first approximation of expressing the physical properties depending on the density and on a single characteristic length for the permeability [e.g. *Shimizu*, 1970; *Yen*, 1981; *Sturm et al.*, 1997; *Calonne et al.*, 2011, 2012] should be improved by introducing for instance new microstructural parameters which could reflect the anisotropy phenomena.

6.4.3 Estimates of physical properties

The computed effective properties of snow were compared with analytical estimates based on basic information on microstructure such as the snow density and the anisotropy of heterogeneities (air and ice) through the correlation lengths. Even if the analytical estimates fail to reflect all the details of the microstructure (e.g. bonds between grains), our results clearly show that they capture the overall evolution of the considered properties with a mean of relative differences ranging from $-22.6\,\%$ to $6.3\,\%$ (see Sect. 6.3.1). These estimates do not include any fitting parameter, by contrast with the parameterization of *Löwe et al.* [2013], where the lower bounds equation (see Fig. 6.4) was adjusted to the computed data of thermal conductivity by introducing two parameters. The fitting parameters are necessary since the lower bounds equation does not take into account the connectivity of both phases, in contrast to the self consistent estimates. We compared the self-consistent estimates and the parameterization of *Löwe et al.* [2013] quantitatively; overall, both estimates are in agreement for the present data.

In both of the presently proposed estimates, the time evolution of physical properties during the metamorphism mainly depends on one parameter Q which is associated with the shape heterogeneity (pore/grain). In our case, the use of the correlation length to define Q seems relevant. Of course, future comparisons between these estimates and other set of data are needed in order to validate this approach in a large density range and other values of temperature gradients. Let us remark that these self-consistent estimates

can be improved by introducing a finer description of the snow microstructure, i.e. by considering the ice skeleton or the pore network as a complex assemblage of several classes of ellipsoidal inclusions with a given orientation, a given aspect ratio and a given volume fraction. However, these improvements will require the development of specific algorithms in order to compute, from the 3-D images, the geometric pore size/shape distribution using an anisotropic structural element like an ellipsoid. These computations are not straightforward. Finally, other relevant estimates of these effective properties can be probably obtained by introducing (i) other microstructural information in bounds or exact contrast expansions by computing three- or four-point probability functions on 3-D images [*Torquato*, 2002, 1991, 1998; *Roberts and Garboczi*, 2002] or (ii) refined variables allowing to describe the evolution of grain shapes and contacts between grains (mean and Gaussian curvatures, fabric tensor) during the metamorphism.

6.5 Conclusions

An experiment of temperature gradient (TG) metamorphism was performed in a cold room in order to monitor the evolution of the microstructural and physical properties of snow over time: seven snow samples were collected at regular intervals of time over three weeks from a snow slab subjected to a vertical temperature gradient of 43 $\mathrm{K\,m^{-1}}$. Each sample was scanned by X-ray tomography to obtain a series of 3-D images showing the microstructural evolution of the snow slab during temperature gradient metamorphism. Numerical computations were performed on these 3-D images to estimate various geometrical and physical properties of snow, such as the directional correlation lengths, the mean and Gaussian curvatures, the specific surface area, the air and ice tortuosities, the effective thermal conductivity and the intrinsic permeability. When possible, such quantities were evaluated in the x, y and z directions to monitor the evolution of their anisotropy.

The main results concerning the TG experiment can be summarized as follows: (i) As shown by many other studies, density remained almost constant during the whole experiment. (ii) The grains were continuously faceting at their bottom parts while the upper parts underwent rounding due to ice sublimation. (iii) Overall, grain and neck growths were observed during the metamorphism. (iv) The intrinsic permeability, linked mainly to the air phase, increased continuously. (v) The snow microstructure evolved in two stages: a short period of strong modifications of the ice structure due to the TG initiation (0–73 h), where the ice tortuosity and the thermal conductivity decreased, followed by a stage of consolidation of this new structure (73–500 h), where the above properties increased gradually. (vi) The anisotropy coefficients of all properties increased during the metamorphism, with larger values in the gradient direction.

These results highlight the strong interplay between microstructure and physical properties of snow, and confirm that the density alone, or any isotropic quantity, is not sufficient to describe the time evolution of physical properties during a TG metamorphism. To solve this problem, we applied analytical anisotropic estimates (self consistent estimates and dilute bed of spheroids) using microstructural parameters (directional correlation lengths)

that reflect the general shape of heterogeneities (size, anisotropy). The proposed analytical estimates, whose results were compared to those obtained by numerical computations, offer good estimations of the physical properties and anisotropy coefficients for our time series, without applying any fitting parameters.

In summary, this study presents numerical tools to quantitatively monitor snow properties using 3-D images and provides a detailed database describing snow under TG metamorphism. In particular, it provides a quantification of snow anisotropy, which is a key -but challenging- parameter to access directly with physical measurements during such a process. Used as a guideline or a validation tool, this database offers new outlooks for the development of micro and macro-scale snow models.

Chapter

7 CellIVM: a room temperature operating cryogenic cell for the in vivo monitoring of snow metamorphism by X-ray microtomography

Contents

This chapter corresponds to the paper entitled *CellIVM: a room temperature operating cryogenic cell for the in vivo monitoring of snow metamorphism by X-ray microtomography* by Calonne N., Flin F., Lesaffre B., Dufour A., Roulle J., Pugliès P., Philip A., Lahoucine F., Geindreau C., Panel J.-M., Rolland du Roscoat S., and Charrier P., submitted, 2014.

Abstract

Monitoring the 3D evolution of snow microstructure with time is crucial for a better understanding of snow metamorphism. For that purpose, we designed a new cryogenic cell that precisely controls the thermal conditions of a snow sample of about 1 cm size while it is scanned by X-ray tomography. The cell consists of a cold regulation and conduction system, and a vacuum chamber that thermally insulates the sample from outside. It operates at room temperature and is, thus, adaptable to diverse tomographic scanners to benefit from advantages in terms of imaging techniques, resolution and speed. The cell was applied to experiments of equi-temperature and temperature gradient metamorphisms. We obtained two time-lapse series where the evolution of microstructures is shown at a 7.8 μm voxel size. The typical features of each metamorphism were observed and are consistent with the temperature fields expected from heat conduction simulations, which confirms the cell's accuracy.

7.1 Introduction

Snow metamorphism strongly influences the snow properties, which are critical for applications such as snowpack stability [*Schweizer et al.*, 2003], transport of chemical species [*Grannas et al.*, 2007] and snow energy balance [*Sokratov and Barry*, 2002]. However, some of the physical mechanisms involved in metamorphism are still not fully understood and need further investigations. Three-dimensional (3D) images of snow make the quantitative study of the metamorphism possible by providing the precise evolution of the microstructures with time [e.g. *Flin et al.*, 2004; *Schneebeli and Sokratov*, 2004; *Kaempfer and Schneebeli*, 2007; *Pinzer and Schneebeli*, 2009a; *Chen and Baker*, 2010; *Srivastava et al.*, 2010; *Pinzer et al.*, 2012; *Calonne et al.*, 2014a]. Such images generally correspond to representative elementary volumes of the snow layers from which they are taken, and thus can be used to compute effective physical properties of snow arising in macroscopic models [e.g. *Calonne et al.*, 2011; *Zermatten et al.*, 2011; *Riche and Schneebeli*, 2013; *Calonne et al.*, 2012; *Löwe et al.*, 2013; *Calonne et al.*, 2014a, b; *Zermatten et al.*, 2014]. For these reasons, several methods have been developed in the last 15 years to obtain 3D images of snow by X-ray microtomography. Up to now, two different approaches have been used: a static and an in vivo approach.

The static approach aims at imaging a snow sample whose structural evolution has been stopped before the tomographic acquisition [e.g. *Brzoska et al.*, 1999a; *Coléou et al.*, 2001; *Flin et al.*, 2004; *Heggli et al.*, 2009; *Calonne et al.*, 2014a]. To do so, the impregnation technique is generally used: the porosity of the snow sample is filled by a product that is liquid below 0°C, and the whole is then refrozen at a lower temperature. The impregnation has two effects: its stops the metamorphism and consolidates the sample for further transportation, or machining of subsamples. This method is intended to preserve exactly the sampled microstructure until the tomography. It is thus especially appropriate for the sampling of snow specimens on the field. With this approach, the metamorphism of a homogeneous snow slab can be monitored by imaging different snow samples collected at several time intervals in the slab [*Flin et al.*, 2004; *Srivastava et al.*, 2010; *Calonne et al.*,

2014a]. However, this approach is not suited to time-lapse imaging, since each stage of the metamorphism correspond to a different sample. The tomography takes place either in a cold-room or in an ambient temperature room. In the latter case, this approach requires a cryogenic cell to protect the snow sample from outside's conditions during the scan. A precise control of the temperature is not needed, the goal being only to keep the sample in a sufficently cold environment to prevent any phase change of the considered materials during a scan. This is one of the main advantages of the static method: it can be used on various X-ray scanners operating at room temperature by using a quite simple cryogenic cell.

The in vivo approach consists in scanning the same non-impregnated sample that undergoes structural evolutions under specific conditions of metamorphism [e.g. *Schneebeli and Sokratov*, 2004; *Pinzer and Schneebeli*, 2009a; *Chen and Baker*, 2010]. The main difficulty of this approach is the precise control of the temperature conditions within a small snow sample for long time periods. To facilitate this temperature control, the whole experiment occurs, up to now, in cold room and the sample is scanned by a dedicated cold-room tomograph. Even in cold room, the use of a cryogenic cell [*Pinzer and Schneebeli*, 2009b] is generally required to precisely control the temperature conditions at the boundaries of the sample during the experiment. The in vivo approach has some drawbacks inherent to the use of laboratory tomographs, which may induce several limitations in term of imaging technology. However, this approach gives access to the grain to grain evolution of a same snow sample by time-lapse tomography. Such time series of 3D images provide important information on the ice growth processes and the vapor transfers involved [*Pinzer et al.*, 2012], and are crucial for microscopic models of metamorphism [e.g. *Flin et al.*, 2003; *Kaempfer and Plapp*, 2009].

We designed a new cryogenic cell that is suited to the in vivo approach, but operates at room temperature. This cell, called Cell for In Vivo Monitoring (CellIVM), includes the main advantages of the above approaches: (1) It enables the grain to grain evolution of a same snow sample during several days of metamorphism by precisely controlling the temperature conditions at the boundaries of the sample. (2) It can be adapted to a large panel of scanners operating at room temperature, including those of synchrotron instruments. This provides new opportunities, in terms of imaging techniques, resolutions and speeds [e.g. *Rolland du Roscoat et al.*, 2011; *Nguyen-Thi et al.*, 2012] to the in vivo study of snow metamorphism.

7.2 Description of the cryogenic cell (CellIVM)

This work was motivated by the need to monitor snow metamorphism by time-lapse microtomography with a scanner operating at room temperature. For that purpose, we designed the CellIVM to precisely impose the temperature conditions at the top and bottom of the sample while its lateral sides are thermally insulated from the outside. Specific requirements for the cell's design concerned the X-ray absorption properties of the materials that must ensure a good contrast of the air and ice on the reconstructed

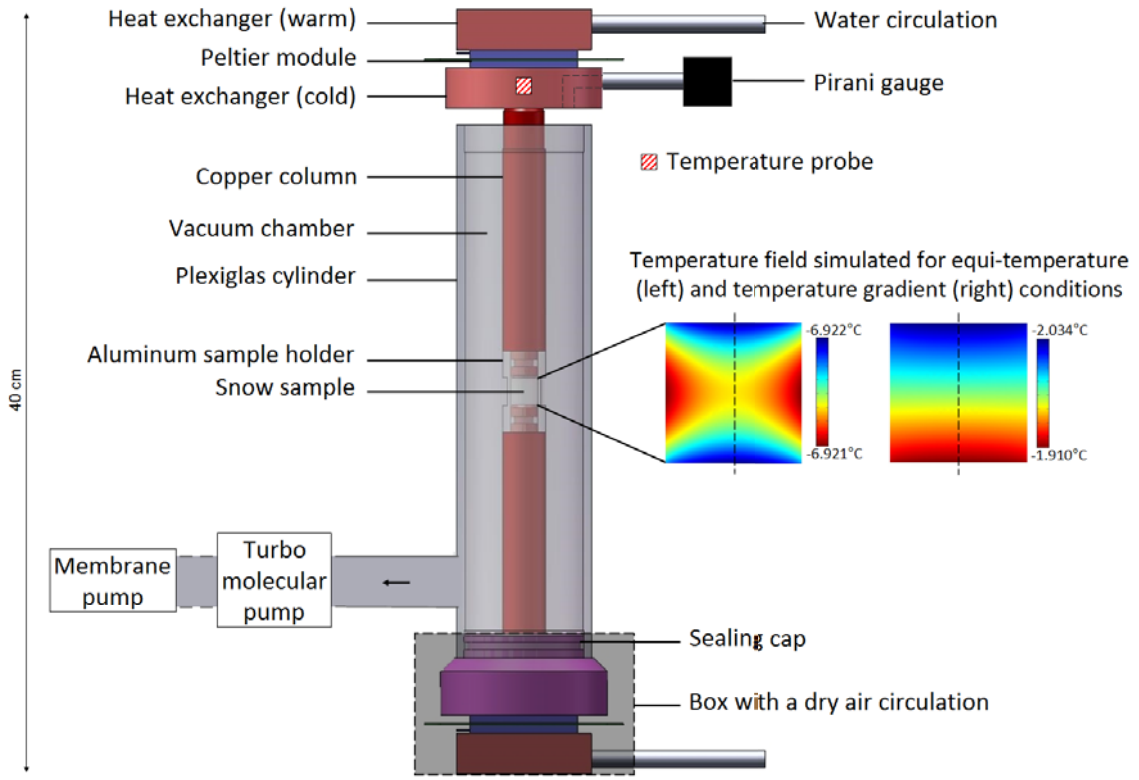

Figure 7.1: Schematic of the CellIVM and simulations of the temperature field within the snow sample. All the components situated on both extremities of the snow sample are strictly identical, with the exception of the vacuum pumping system located at the base of the Plexiglas cylinder and the vacuum gauge located in the upper part. For a sake of clarity, the box and the sealing cap of the upper part of the cell are not illustrated.

images, the size of the snow sample that must be large enough to be representative, and the geometrical arrangement of the cell that must enable a 360° rotation during a tomographic acquisition. In addition, the snow sample must be protected from heating and frosting during its installation within the cell for the tomography, and the setting up must be fast (see Section 7.4). Figure 7.1 presents a schematic of the CellIVM, which can be decomposed into three functional parts: (1) a system of cold production and regulation that controls the temperature gradient (TG) imposed to the sample, (2) a removable conduction system that conducts cold to the sample and protects it during its installation into the cell, and (3) a vacuum system that insulates the sample from outside.

The first part consists of two strictly identical systems that impose a vertical TG through the sample holder. The temperatures of the heat exchangers (cold part) are measured using four-wire Pt100 temperature probes and regulated by Peltier modules (thermoelectric cooler Kryotherm TB-2-(199-199)-0.8) via a controller (Meerstetter TEC-1122). The Pt100 probes were calibrated and have a precision of ± 0.03°C between 0 and -10°C. The temperature settings of the Peltier modules are ensured by the controller with a precision of about ± 0.01°C. The warm parts of the Peltier modules are continuously cooled by a water circulation at around 20°C through the heat exchangers to avoid overheating of the modules. The heat exchangers are in copper to facilitate the heat conduction. The

Peltier modules and the exchangers are grouped in a box where a dry air circulation flows continuously to prevent condensation or deposition of the ambient water vapor above the considered cold surfaces. The cold is conducted from the extremities of the CellIVM to the snow sample by a removable conduction system.

The conduction system consists of an aluminium cylinder inserted between two identical copper columns of 1.6 cm diameter and 14 cm height, which are themselves in contact with the heat exchangers (cold part). Their contact surfaces were finely polished to obtain a good thermal contact. The aluminum sample holder can contain a snow sample of 1 cm diameter and 1 cm height and conducts cold along the lateral sides of the sample. This lateral conduction contributes to obtain a uniform TG within the sample. Aluminum was chosen for its relatively high thermal conduction and low X-ray absorption properties. The sample holder is of 3 cm length and of 0.3 cm thick, except at its central part where it is of 0.1 cm thick to minimize the absorption of the X-rays through the aluminum. It fits into the copper columns along 1 cm to enhance the cold conduction between these two components, and which also stabilizes the assembly. In addition, the external surfaces of the aluminum sample holder were polished to decrease the surface emissivity and limit the infrared radiation from the outside to the snow sample.

The third part of the CellIVM consists of a vacuum system that thermally insulates the snow sample from the tomograph room. For that, a Plexiglas cylinder of internal diameter of 4.4 cm surrounds the sample holder, creating a chamber. While the cell is operating, the air remaining in the chamber is permanently pumped at the base of the Plexiglas cylinder by a turbo-molecular pump (Pfeiffer TMU065) connected to a membrane pump (Vacuubrand MZ2D). A Pirani gauge provides an estimation of the air pressure in the chamber by measuring the pressure via a short tube of 0.5 cm diameter placed at the upper part of the system. The measured pressure usually reaches values around 0.1 Pa quickly after starting the pumping system, leading to a thermal conductivity of air of around 0.0015 $Wm^{-1}K^{-1}$ (reduced by ~ 28 compared to that at atmospheric pressure). This value was estimated using the equation given by *Potkay et al.* [2007] and assuming that 0.1 Pa is representative of the pressure in the vacuum chamber. The tightness of the vacuum chamber is ensured by sealing caps equipped of o-rings, which connect the Plexiglas extremities to the heat exchangers, and by o-rings between the aluminum sample holder and the copper columns, which isolate the snow sample. The turbo-molecular pump is connected to the vacuum chamber by around 30 cm of vacuum tube, and cooled by a 20°C water circulation. The membrane pump is installed outside the tomograph cabin to prevent heating of the air, and connected to the turbo pump by a flexible vacuum tube.

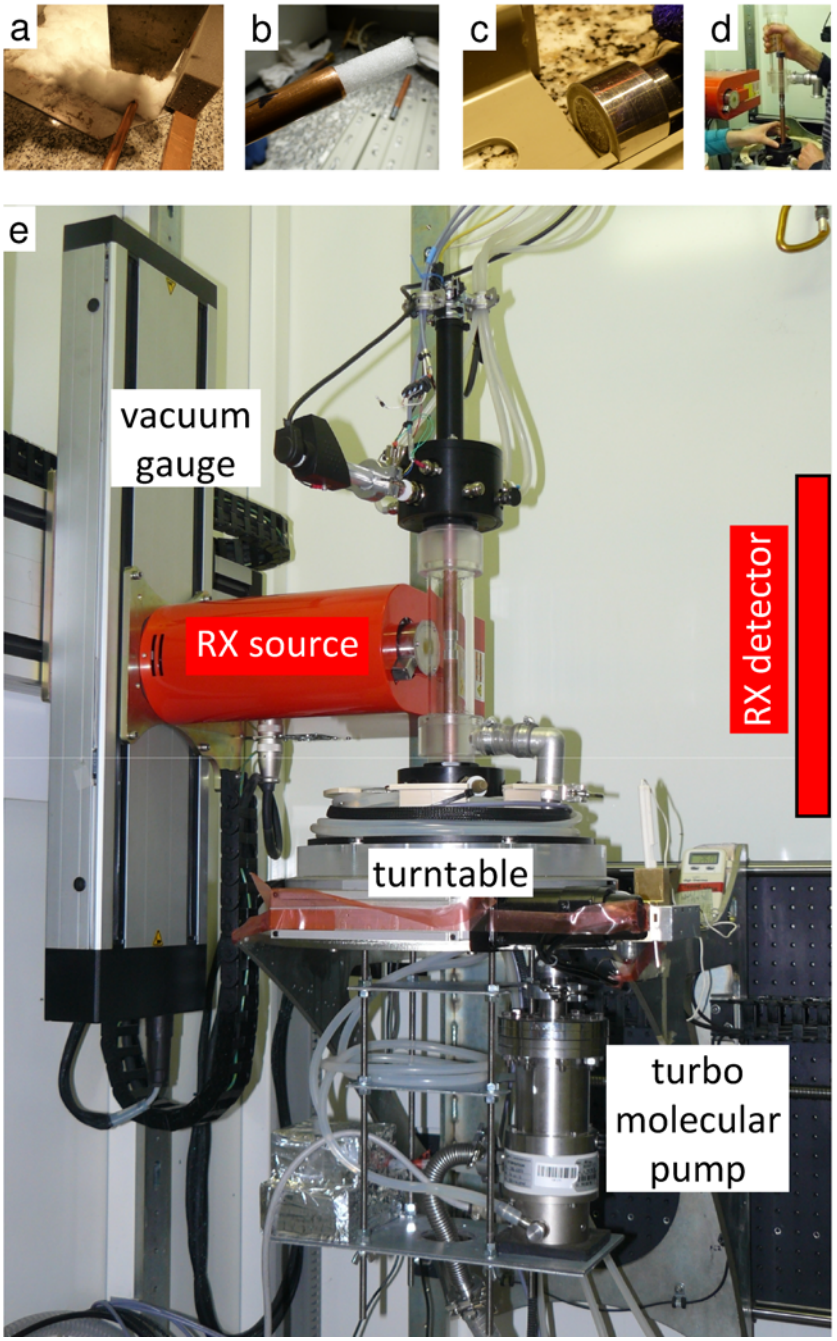

Figure 7.2: Photographs of the experiment: (a) Snow coring into a snow layer; (b) Cylindrical snow sample; (c) Core insertion into the aluminum sample holder; (d) Installation of the sample into the cryogenic cell; (e) Overview of the cryogenic cell installed in the tomograph cabin (RX-solutions) of the 3SR lab.

7.3 Temperature field simulations

Measurements of temperature close to the snow sample are not performed since they are complex to design and may perturb locally the temperature field. We thus carried out a series of heat conduction simulations, using the finite element code ComsolMultiphysics, to evaluate the temperature field inside the cryogenic cell and the snow sample depending

on the imposed thermal boundary conditions at the heat exchangers (cold part). All the components of the cell shown in Figure 7.1 were defined as an axisymmetric solid model. The thermal conductivity of copper, aluminum, Plexiglas and air at around 0.1 Pa were taken equal to 390, 200, 0.2 and 0.0015 $\mathrm{W\,m^{-1}\,K^{-1}}$, respectively. In order to reflect the temperature field of the snow sample, we used an effective thermal conductivity corresponding to low-density snow of 0.2 $\mathrm{W\,m^{-1}\,K^{-1}}$ [*Calonne et al.*, 2011]. We imposed the temperature of the heat exchanger at the top (T_{top}) and base (T_{base}) of the system, as well as the temperature of the tomograph cabin (T_{room}). The contacts between the different components were assumed to be perfect. The heat transfer by radiation and air convection were neglected.

Figure 7.1 shows two results of the temperature simulations of the snow sample. The left temperature field was simulated for isothermal conditions, with $T_{\mathrm{top}} = T_{\mathrm{base}} =$ -7°C and $T_{\mathrm{room}} = 20$°C. The simulated field is slightly influenced by the outside with temperature values comprised between -6.921 and -6.922°C, leading to a maximum temperature difference in the sample of 0.001°C. The analysis of the field leads to a maximum TG of the order of 0.2 $\mathrm{K\,m^{-1}}$. This value is far below the minimal TG of 3 $\mathrm{K\,m^{-1}}$ for which temperature gradient effects can be observed [*Flin et al.*, 2007]. Under such conditions, the sample is thus expected to undergo isothermal metamorphism as presented by *Kaempfer and Schneebeli* [2007].

The right temperature field of the sample shown in Figure 7.1 was simulated for TG conditions, where $T_{\mathrm{top}} =$ -2.2°C, $T_{\mathrm{base}} =$ -1.8°C and $T_{\mathrm{room}} = 20$°C. The TG between the two heat exchangers is thus of 1.4 $\mathrm{K\,m^{-1}}$. At the top and base of the snow sample, the temperature are of -2.034 and -1.910°C, respectively, leading to a local TG through the snow sample of 12 $\mathrm{K\,m^{-1}}$. In practice, we use such simulations to determine the temperature settings to apply to the Peltier modules in order to impose a given local TG for our experiments. In the figure, the influence of the outside temperature is not observable on the field's shape: the iso-temperature levels in the sample are perpendicular to the gradient. Under such conditions, an uniform TG metamorphism is thus expected to occur.

7.4 Application to snow metamorphism

To check the accuracy of the CellIVM, time-lapse X-ray tomography was carried out at the 3SR laboratory to monitor the equi-temperature metamorphism and the temperature gradient (TG) metamorphism of a snow sample. In what follows, we describe for both metamorphisms the experimental process, from the sampling to the tomography, as well as the 3D images and vertical cross-sections obtained.

7.4.1 Equi-temperature metamorphism

The snow sample was prepared in cold-room following the method below (see Figure 7.2a-c for illustrations). First, two layers of ice of around 1.5 mm thickness were created at the extremity of the copper columns to provide a constant source (or sink) of water vapor

during the metamorphism. A cylindrical snow core of 1 cm diameter and 0.7 cm length was sampled from a natural snow layer collected near Grenoble, France, consisting of decomposed and fragmented precipitation particles (DF) and rounded grains (RG) at around 160 $\mathrm{kg\,m^{-3}}$. The aluminum sample holder was mounted on the lower copper column, ready to receive the snow sample. The sample was carefully inserted into the aluminum sample holder, and then isolated from outside by fitting the upper copper column into the sample holder. The set was put in a copper holster and placed in isothermal conditions at -7°C in a freezer waiting for the tomography.

CellIVM was installed into the tomographic cabin (RX-solutions) as shown in Figure 7.2e. The turbo-molecular pump was fixed below the turntable of the tomograph. CellIVM was screwed to the turntable via a platform where the water and air tubes of the lower part of the cell were initially wounded. The tubes of the upper part of the cell were initially twisted and attached at the top of the cabin. Indeed, both upper and lower tubes unwind during tomography, which facilitates the rotation process.

Before the sample installation, the temperature of the upper and lower heat exchangers were both set to -7°C. The snow sample was set up in the CellIVM following a process where the aluminum sample holder is in direct contact with the ambient air only few seconds (Figure 7.2d). Moreover, the copper columns constitute an important cold mass that protects the snow sample from heating. Immediately after, the vacuum pumping system was started and operated until the end of the experiment.

We performed time-lapse tomography to monitor the equi-temperature metamorphism of the prepared snow sample over 28 hours. The temperature settings at the top and base of the cell were maintained at -7°C. The first tomograph was obtained 1 hour after the beginning of the isothermal conditions to ensure stabilized thermal conditions. Throughout the metamorphism, the snow sample was regularly scanned at a resolution of 7.8 μm via the software X-Act. We used a voltage of 80 kV and a current intensity of 120 μm, leading to a scan duration of 2 hours. These parameters ensure the best compromise between the quality of radiographies and the duration of the scan. Note that this latter should be defined depending on the rate of the sample evolution. The scan duration is not an issue with the equi-temperature metamorphism whose evolutions are slow. We obtained 1200 radiographies per scan covering 360° rotation around the vertical axis of the sample. The number of pixel of the X-ray detector was 1920×1536. The software DigiCT was used to reconstruct horizontal cross-sections of the snow samples from radiographies. 3D images of around $6 \times 6 \times 6$ $\mathrm{mm^3}$ of the snow microstructure were finally obtained after image processing.

Figure 7.3 shows $1 \times 1 \times 1$ $\mathrm{mm^3}$ sub-volumes of the snow sample at the beginning and after 28 hours of equi-temperature metamorphism. No significant change occur during this period. Nevertheless, through a grain to grain comparison, the initial structure exhibits convex surfaces in red which are no longer present at t = 28 h, meaning that these surfaces have been preferentially sublimated. In the same time, the initial concave surfaces in green become less numerous at t = 28 h, which indicates that vapor deposition occurred in this area. Qualitatively, the general evolution is a slight rounding of the ice structure, which is

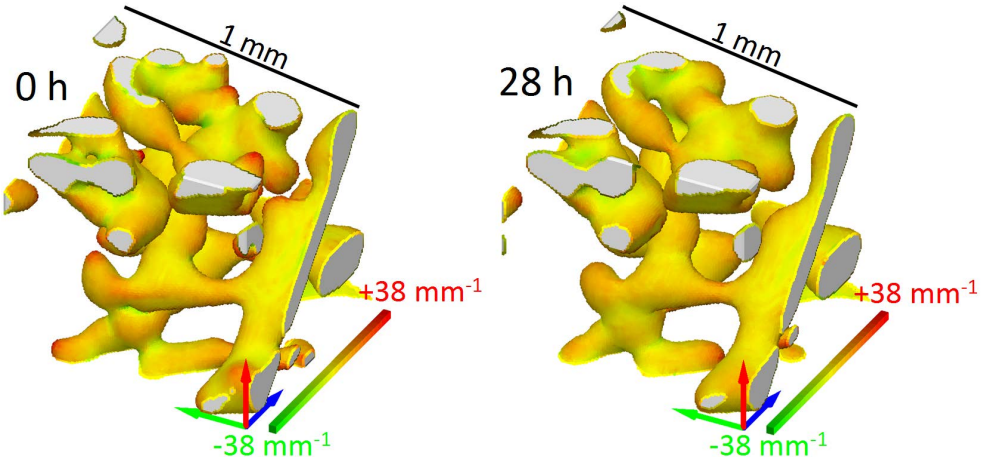

Figure 7.3: Sub-volumes of 3D images of the snow sample undergoing an equi-temperature metamorphism. The color map indicates the mean curvature scale, where convexities, flat shapes and concavities are shown in red, yellow and green, respectively. The red arrows are pointing downward of the physical sample. The voxel size is of 7.8 μm.

typical of the equi-temperature metamorphism and in agreement with previous studies [*Flin et al.*, 2004; *Kaempfer and Schneebeli*, 2007]. This observation is in accordance with the simulated temperature field and validates the control of the TG through the sample.

7.4.2 Temperature gradient metamorphism

The preparation of the snow sample and its setting up into the CellIVM followed basically the same protocol presented in section 7.4.1. Time-lapse tomography was carried out to monitor the TG metamorphism of the prepared snow sample over 105 hours. The temperature settings of the Peltier modules at the top and base were set to -2.2°C and -1.8°C, respectively. From similar simulations to those presented in section 7.3, but considering additional ice layers of thermal conductivity of 2.1 $\mathrm{W\,m^{-1}\,K^{-1}}$ at the top and base of the snow sample, we estimated a local TG of 18 $\mathrm{K\,m^{-1}}$ through the sample. As for the equi-temperature metamorphism, the first tomograph was acquired 1 hour after starting the TG to ensure stabilized thermal conditions. The parameters of tomography were the same as those given in section 7.4.1. The TG was chosen sufficiently moderate to enable a 2 hour duration scan.

The structural evolution of the snow sample is illustrated by vertical cross-sections (Figure 7.4a) and 1×1×1 $\mathrm{mm^3}$ sub-volumes of 3D images (Figure 7.4b). The ice layer at the top and the bottom of the snow sample are visible in the right cross section. With time, the ice matrix appears to move gradually downward, with sublimation at the top and deposition at the bottom of the ice structures. The initial DF/RG evolves to faceted crystals (FC), characterized by faceted shapes and angular surfaces. Such planar or convex zones (yellow or red surfaces on 3D images, respectively), can be easily detected after 31 hours of TG. These observations are consistent with the simulated value of 18 $\mathrm{K\,m^{-1}}$ through snow, as well as with previous studies [e.g. *Flin and Brzoska*, 2008].

Figure 7.4c shows the final structure of the whole snow sample reached after 105

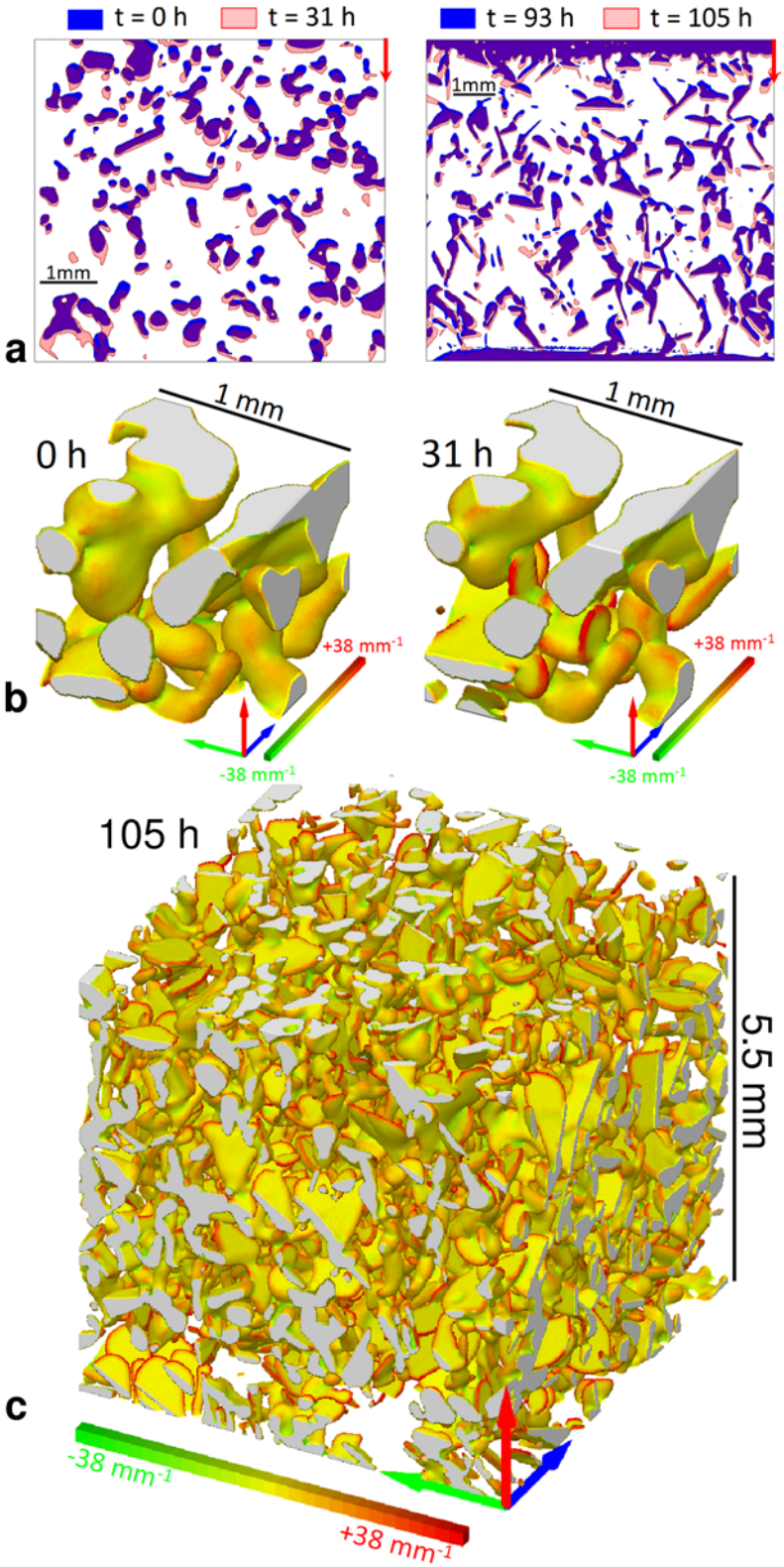

Figure 7.4: (a) Vertical cross sections, (b) sub-volumes and (c) whole volume of 3D images of the snow sample undergoing a TG metamorphism at different times. All the red arrows are oriented toward the bottom of the physical sample. The left and right cross-sections are represented using different magnifications. The 3D images are colored with respect to the mean curvature scale and represented upside down for a better visualization of the facets. The voxel size is of 7.8 μm.

hours of TG at an average temperature of -2°C. The ice structure exhibits several plate shapes that indicate that the ice growth has been faster along preferential directions of the crystals. This may be linked to the dependence of the ice crystal growth with temperature. Indeed, at -2°C, the prismatic faces of the ice crystal grow faster than the basal faces, leading to plate shaped crystals [*Kuroda and Lacmann*, 1982; *Furukawa and Wettlaufer*, 2007]. Moreover, most of the "lateral" sides of the plates are rounded more than faceted. This observation is also a typical feature of the ice evolution just above -2°C and has been already reported by *Colbeck* [1983b] and *Furukawa and Kohata* [1993]: close to the melting point, the basal faces of the crystals remain plane while the prismatic faces are rounded, even under a TG. The above considerations validate the temperature control of the CellIVM because the snow evolution is in agreement with the temperature conditions expected from simulations, and also with the evolutions reported in the literature for similar conditions.

7.5 Conclusion and outlooks

We developed a new cryogenic cell (CellIVM) that is suited to the in vivo monitoring of snow metamorphism, and which operates at room temperature. For this last reason, the CellIVM is adaptable to a large panel of tomographic scanners, including those of synchrotron instruments, which has several advantages in terms of speed, resolution, and imaging techniques [e.g. *Rolland du Roscoat et al.*, 2011; *Nguyen-Thi et al.*, 2012]. CellIVM controls precisely the temperature conditions at the boundaries of the sample by combining (1) a system of cold regulation and conduction that forces the temperature at the top and bottom of the sample, and (2) a vacuum system that insulates the sample from outside. Thus, the type and regime of metamorphism can be imposed on a snow sample over several days, making it possible to monitor its grain to grain evolution by time-lapse tomography at room temperature.

Experiments of equi-temperature and TG metamorphisms were monitored using the CellIVM installed in the 3SR tomograph (RX-solutions). We obtained a time series of 3D images for both experiments where the structural evolution of snow is observable at a 7.8 μm voxel size. A typical rounding of the shapes was observed during equi-temperature metamorphism at -8°C while TG metamorphism of 18 $\mathrm{K\,m^{-1}}$ at -2°C exhibited specific patterns of rounded plates, as reported in the literature. All these observations are consistent with the temperature fields expected from heat conduction simulations and confirm the accuracy of the cell. Further work will focus on the quantitative analysis of the above 3D series to compute local growth rates, and compare them to those predicted by microscale models.

Conclusion Part III

This part was dedicated to monitor the evolution of snow as a function of time, i.e. during the metamorphism, using a static approach in Chapter 6 and an in vivo approach in Chapter 7. The main objective was to contribute to a better understanding of the physics of dry snow metamorphisms at the pore scale using 3D images of snow, as well as of the link between the microstructure and the effective properties arising in the macroscopic description of the transport phenomena.

In Chapter 6, we presented the time evolution of microstructural and effective properties of snow estimated from 3-D images, during a temperature gradient metamorphism.The main contributions of the study are summarized hereafter.

- The typical process of faceting at the base of the grains and rounding at the top are clearly captured by the mean curvature distributions of the ice surfaces.
- A significant anisotropic behavior of the microstructural and physical properties develops in parallel with time.
- The study highlights the strong interplay between microstructure and physical properties of snow, and confirms that the density alone, or any isotropic quantity, is not sufficient to estimate finely the effective properties of all snow types.
- Analytical estimates (Self consistent estimates and Dilutes bed of spheroids) are presented as a way to capture the anisotropy of the microstructure through the correlation lengths. They offer good estimates of the effective properties and of their anisotropy for our experiment.

Used as a guideline or a validation tool, the presented database offers new outlooks for the development of micro and macro-scale snow models.

To monitor the in vivo evolution of a same snow sample with time by tomography, we developed a new cryogenic cell presented in Chapter 7. The mains points of this new cell are summarized as follows.

- The cell controls precisely the temperature conditions at the boundaries of the sample by combining a system of cold regulation and conduction and a vacuum system. The type and regime of metamorphism can thus be imposed on the snow sample.
- The time series of 3D images of isothermal and temperature gradient metamorphisms show the typical features reported in literature and confirm the accuracy of the cell.
- The cell operates at room temperature and not in a cold room. Advantages in terms of imaging techniques, resolution, speed, are thus now accessible to the in vivo study of snow.

This work has potential impacts on all the communities linked to cryo-imaging. For snow and ice, implications concern snow metamorphism modeling, ice crystal growth, heat and vapor transfer processes, 3D mappings of ice crystalline orientations by DCT, etc.

Conclusion and perspectives

The overall objective of the thesis was to contribute to a better understanding of dry snow metamorphism and the physics involved at both microscopic and macroscopic scales. For that purpose, the work was based on theoretical modeling (upscaling methods), experimentation (tomography, instrumentation, cold-room manipulations), and numerical simulation (Geodict, ComsolMultiphysics). In the following, we recall the main results obtained during the thesis and propose some perspectives.

Macroscopic model of heat and vapor transport by homogenization

A first part of our work was dedicated to derive the macroscopic equivalent models of heat and water vapor transfers through a snow layer from the physics at the pore scale using the homogenization of multiple scale expansions. Under the condition of separation of scales, the models are obtained without any prerequisite at the macroscopic scale and are intrinsic to the geometry of the medium and the phenomenon. The domain of validity of the model is given by the order of magnitude of the dimensionless numbers with respect to the separation of scales. These numbers characterize the relative influence of the physical phenomena at the pore scale. The heat and vapor transfers at the pore scale were described by conduction, diffusion, and forced convection, coupled to phase changes.

We have shown that the macroscopic models of heat and vapor transfers through a snow layer mainly depend on the intensity of the air flow, i.e. on the order of magnitude of the pore Reynolds number and the Péclet numbers, and on the temperature gradient imposed to the layer, i.e. on the order of magnitude of dimensionless numbers [W] and [H], that characterize the phase change process at the air/ice interface.

One of the advantages of the homogenization method is that all terms of the macroscopic description (balance equations, etc) are perfectly defined. In particular, this method provides the definition of:

- the effective properties (effective diffusion tensor, effective thermal conductivity tensor, intrinsic permeability tensor, etc) arising in the macroscopic models of transport. More precisely, the effective properties can be estimated by solving specific boundary value problems over representative elementary volumes of snow. Let us remark that,

although the macroscopic heat and vapor transfers are described by two coupled equations, these effective properties are obtained by solving uncoupled problems, except in the case of the dispersion tensor. This theoretical result shows that the effective diffusion tensor is not enhanced by the phase change process at the air/ice interface, as suggested by several studies.

- the macroscopic source terms of heat and vapor, induced by sublimation/deposition at the pore scale. We have shown that the mass transfer coefficient introduced by *Albert and McGilvary* [1992] depends only on temperature, in the case of our models.

The macroscopic models presented here were derived from a given microscopic description. If the physical description at the pore scale is modified or enriched by new processes, such as natural convection, anisotropic crystal growth, transfers in unsaturated wet snow, etc, one can follow the presented method to derive the corresponding equivalent macroscopic model. Moreover, the presented models were derived assuming a good separation of scales, $\varepsilon = l/L = 5 \times 10^{-3}$, where l and L are the characteristic lengths of the microstructure and of the snow layer, respectively. Different separation of scales could be considered and may lead to different macroscopic models. The particular case of a poor separation of scales might typically appear for very thin snow layers or for snow layers submitted to very large temperature gradients. In that case, the macroscopic model could be derived by investigating the following superior order of approximation in the asymptotic analysis [*Boutin*, 1996; *Auriault et al.*, 2005].

The most direct perspective of this work is the evaluation of the proposed model with respect to macroscopic field or laboratory measurements. This comparative study should include, in addition to macroscopic measurements (temperature, etc), 3D images of representative elementary volumes of snow to estimate the effective properties required in the macroscopic model.

Another perspective might be related to the improvement of snowpack models, such as Crocus, the one developed at the CEN. Based on our study, the description of the transport phenomena could be enriched or modified. Work could especially concern the simulation of the vapor transfer, which is not described in likely most of the current models, and might be useful to reflect that snow density can sometimes evolve because of a strong vapor transfer [*Gallet et al.*, 2014].

Effective properties of transport phenomena

In the second part, we studied the relationship between the effective properties involved in the heat and vapor transfers at the macro-scale and the snow microstructure, including snow density. The properties under consideration were the effective tensor of vapor diffusion, the effective thermal conductivity tensor, and the intrinsic permeability tensor. We estimated these effective tensors by solving the specific boundary value problems arising from the homogenization method over representative elementary volumes. Those volumes

were extracted from about thirty 3D images of snow spanning the full range of seasonal snow types and density.

Overall, the effective properties are strongly related to snow density, as already pointed out by previous studies, but also exhibits an anisotropic behavior, which can be significant especially for depth hoar and faceted crystal as expected. Analytical estimates (Self consistent estimates and Dilute beds of spheroids) are presented as a way to capture the anisotropic behavior of effective properties. These analytical estimates are based on basic information of the microstructure: density and anisotropy of the heterogeneities.

The effective properties are defined using the homogenization method by uncoupled boundary value problems. Our estimates of properties from 3D images reflect strictly the phenomena under consideration. In contrast, this is not easily possible with macroscopic measurements where the obtained estimates often result from all the physical processes involved. For example, our results show that the vapor diffusion is not enhanced in snow compared to the vapor diffusion in a free air space, as mentioned by previous studies, whose a number of which are based on controversial measurements.

The significant dataset of snow properties can be useful to future microscopic and macroscopic studies. For example, our estimates of effective thermal conductivity based on 3D images were used in the work of *Hagenmuller et al.* [2014] to evaluate the relationship of a new microstructural indicator, namely the minimum cut density, with respect to physical properties. Used as a guideline or a validation tool, the presented database also offers new outlooks for the development of macro-scale snow models. For example, *Domine et al.* [2013] implemented the regression curve of permeability proposed in this thesis into the macroscopic model Crocus. They obtained a good agreement between simulated and observed snow permeability. In the work of *Carmagnola et al.* [2014], our time series of specific surface area was used to guide its implementation in the Crocus model.

A possible further work concerns the presented analytical estimates, which should be compared to other experimental results whose conditions differ from those shown in the thesis. To this end, we are now analyzing a new time series of 3D images of a temperature gradient metamorphism (different temperature, temperature gradient, and initial snow density) obtained during the master internship of Alexandre Philip (*Observation in vivo d'une métamorphose de gradient de température par imagerie 3D à l'aide d'une cellule cryogénique et caractérisation quantitative*) that I co-supervised.

To complete our study of the effective properties of transport, similar numerical computations can be carried out to estimate the effective dispersion tensor arising in the macroscopic models, from the 3D images. These simulations, which are not straightforward, require solving a boundary value problem that involves the convection effects at the pore scale.

Monitoring of dry snow metamorphisms

The last contribution of the thesis concerned the monitoring of the microstructure evolution during dry snow metamorphism using 3D images of snow. Two different approaches

were used: (i) a static approach to monitor the evolution of a snow slab by collecting different snow samples at regular time intervals, and (ii) an in vivo approach to monitor the grain to grain evolution of a same snow sample by time lapse tomography. The latter one is the result of a significant instrumental development carried out during the thesis, to design a new cryogenic cell. This cell is able to operate at room temperature conditions and not only, as until now, in a cold-room [*Schneebeli and Sokratov*, 2004; *Pinzer and Schneebeli*, 2009a; *Chen and Baker*, 2010].

3D imaging of snow is a critical tool to study the snow metamorphism at the microscopic scale. For example, the process of faceting and rounding at the base and top of the ice grains, which is a challenging effect to model, can be captured by the mean curvature distributions of the ice surfaces. Furthermore, the in vivo method gives access to the grain to grain evolution of snow in 3D. Such data can be used to evaluate the physical description that is taken into account in the microscopic models of dry snow metamorphism, i.e. to compare the simulated evolution versus the observed one. This way, the description can be adjusted.

Because the two approaches operate at room temperature, they can be adapted to a large panel of tomographic scanners, including those on synchrotron instruments. Advantages in terms of imaging techniques, resolution, speed, are thus accessible and open the way to more refined studies. For snow and ice, implications concern snow metamorphism model, ice crystal growth, heat and vapor transfer processes, 3D mappings of ice crystalline orientations by diffraction contrast tomography [*Ludwig et al.*, 2009; *Rolland du Roscoat et al.*, 2011], etc.

Concerning the faceting/rounding processes, a study is currently in progress using the new cryogenic cell. We acquired 3D images of the in vivo evolution of an air bubble of diameter 0.3 mm in a block of single ice crystal under temperature gradient conditions by time lapse tomography at a resolution of 7.8 μm. The analysis of the tomographic data is still in progress but first results are shown in Figure i: at the beginning of the experiment, the air bubble is roughly spherical, while after 95 hours, facets at the top of the bubble are observable. Such 3D images can be used as guidelines and validation data for the micro-scale models that would be used to simulate the faceting/rounding processes.

Following the same in vivo method, an experimental work about the anisotropy of the ice crystal growth could be carried out to better understand its relationship with temperature and supersaturation. On this topic, a preliminary study has been initiated during my three-month stay (JSPS summer program 2012) at the Institute of Low Temperature Science at Sapporo, Japan, in collaboration with Y. Furukawa. During this stay, we monitored the growth of a negative crystal (air cavity in a single ice crystal) in 2D using time-lapse optical microscopy. Thanks to a hollow needle inserted in the crystal, the "growth" was driven by an air pumping system that continuously creates an under-saturation of vapor in the air cavity and thus forces the sublimation of ice (see Figure ii). We obtained preliminary results of the influence of the temperature and under-saturation on the preferential growth of basal or prismatic faces of the ice crystal. 3D images would provide more quantitative

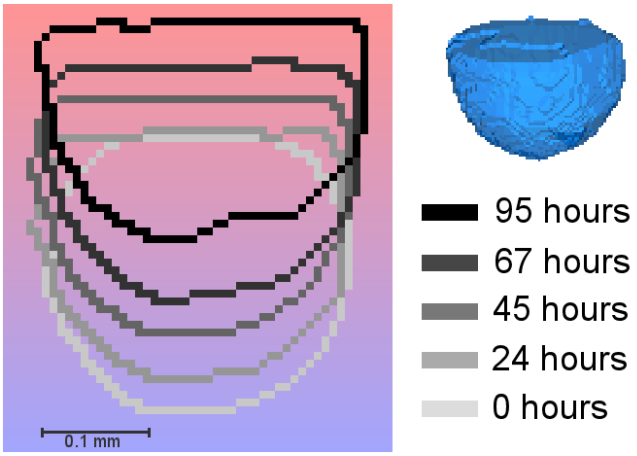

Figure i: Time evolution of the morphology of the air bubble in a single ice crystal submitted to a temperature gradient of around 50 $\mathrm{K\,m^{-1}}$, based on vertical cross-sections from tomographic data. The contour of the bubble interface is shown at different times. A 3D view of the bubble after 95 hours is also provided.

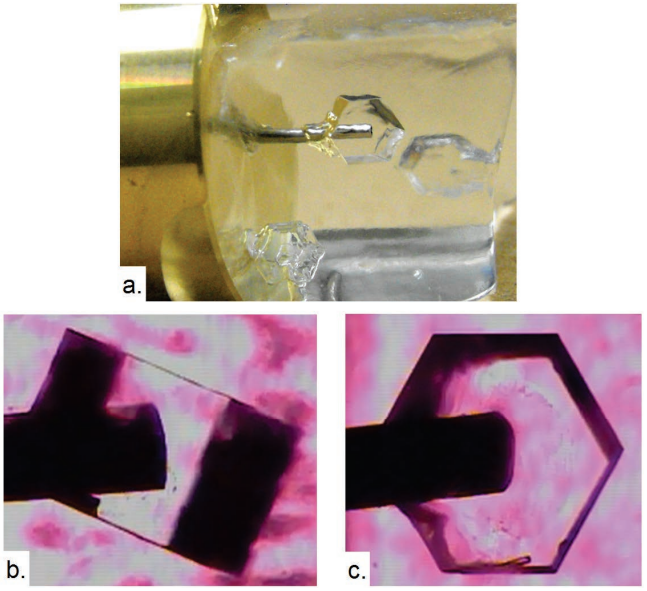

Figure ii: a. Picture of the needle of the air pumping system inserted in the single ice crystal. The tip of the needle is surrounded by a negative crystal. Picture of the prismatic (b.) and basal (c.) face of a negative crystal. The needle has a diameter of 0.8 mm.

measurements that could be also compared to the results given by numerical simulations.

Similarly, in the framework of the DigitalSnow ANR project in which we are involved, we are trying to develop a 3D model for the dry snow metamorphism at the pore scale. The goal is to simulate the microstructural evolution under isothermal or temperature gradient conditions, starting from a given 3D image of snow and using a phase field approach as presented by *Kaempfer and Plapp* [2009]. This development will benefit from comparative studies between simulated and observed evolutions using notably the time series of 3D images obtained during the thesis.

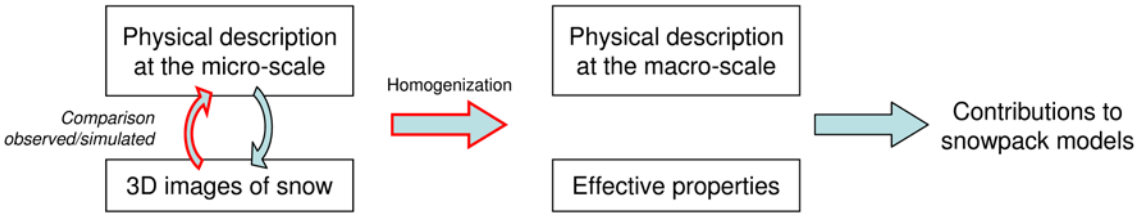

Figure iii: Schematic of thesis approach for the study of snow physcis.

In conclusion, the approach used in the thesis can be illustrated by the schematic of Figure 7.5. As mentioned above, studies using 3D images of snow can bring new insights concerning the physics of dry snow metamorphism at the pore scale. A way to precisely guide the description of such physics is to compare the 3D microstructures of snow given by micro-scale models and by tomographic observations. The modification of the physics at the pore scale may have an influence on the physics at a larger scale. Based on the physical description at micro-scale and 3D images of snow, the equivalent macroscopic model can be derived using the homogenization method, and the effective properties arising in this model can be estimated. Results may help improving the macroscopic snowpack models. In this approach, the thesis has mainly contributed to the understanding of the micro-scale physics using 3D images, and to the transition to the macro-scale including the effective properties estimations, as represented by the arrows with a red contour.

Conclusion et perspectives (en français)

L'objectif général de la thèse était de contribuer à l'amélioration de nos connaissances sur les métamorphoses de la neige sèche et la physique impliquée, à l'échelle microscopique et macroscopique. Pour ce faire, le travail s'est basé sur de la modélisation théorique (méthodes de changement d'échelle), de l'expérimentation (tomographie, instrumentation, manipulations en chambre froide), et de la simulation numérique (Geodict, ComsolMultiphysics). Les principaux résultats obtenus au cours de la thèse sont rappelés dans ce qui suit et quelques perspectives sont proposées.

Modélisation macroscopique du transport de chaleur et de vapeur par homogénéisation

La première partie de notre travail a été consacrée à la détermination des modèles équivalents macroscopiques de transfert de chaleur et de vapeur d'eau à travers une couche de neige à partir de la physique à l'échelle des pores, en utilisant la méthode d'homogénéisation basée sur les développements asymptotiques à échelles multiples. Sous la condition de séparation d'échelles, les modélisations sont obtenues sans aucun prérequis préalable à l'échelle macroscopique et sont intrinsèques à la géométrie du matériau et du phénomène. Le domaine de validité de la modélisation est donné par l'ordre de grandeur des nombres sans dimension par rapport à la séparation d'échelles. Ces nombres caractérisent l'influence relative des phénomènes physiques à l'échelle des pores. Dans cette thèse, le transfert à micro-échelle de chaleur et de vapeur est décrit par la conduction, la diffusion et la convection forcée, couplée aux changements de phase.

Nous avons montré que le modèle macroscopique décrivant les phénomènes de transfert dépend principalement de l'intensité de l'écoulement d'air imposé à la couche de neige, i.e. de l'ordre de grandeur du nombre de Reynolds des pores et des nombres de Péclet, ainsi que de son gradient de température, i.e. de l'ordre de grandeur des nombres sans dimension [W] et [H], qui caractérisent le changement de phase à l'interface air/glace.

Un des avantages de la méthode d'homogénéisation est de définir parfaitement tous les termes de la description macroscopique (équations de bilan...). En particulier, cette méthode permet de définir :

- les propriétés effectives (tenseur de diffusion effectif, tenseur de conductivité thermique effective, tenseur de perméabilité intrinsèque...) impliquées dans les modélisations macroscopiques du transport. Ces propriétés effectives peuvent être estimées en résolvant des problèmes aux limites spécifiques sur des volumes élémentaires représentatifs de neige. Notons que, bien que le transfert macroscopique de chaleur et de vapeur soit décrit par deux équations couplées, les propriétés effectives sont, quant-à-elles, obtenues en résolvant des problèmes non couplés, sauf dans le cas du tenseur effectif de dispersion. Dans le cas présent, nos développements ont montré que le tenseur effectif de diffusion de vapeur n'est donc pas influencé par le changement de phase à l'interface air/glace, tel que suggéré par plusieurs études.

- les termes sources macroscopiques de chaleur et de vapeur, induits par la sublimation/déposition à l'échelle des pores. On a montré ainsi que le coefficient de transfert de masse introduit par *Albert and McGilvary* [1992] ne dépend que de la température, au moins dans le cas de nos modèles.

Les modèles macroscopiques présentés dans cette thèse ont été obtenus à partir d'une description microscopique donnée. Si cette description physique à l'échelle des pores est modifiée ou enrichie par de nouveaux phénomènes, tels que la convection naturelle, la croissance cristalline anisotrope, les transferts en neige humide non-saturée..., la méthode proposée peut être suivie afin d'obtenir la modélisation macroscopique équivalente correspondante. D'autre part, les modèles présentés ont été obtenus pour une bonne séparation d'échelles, $\varepsilon = l/L = 5 \times 10^{-3}$, où l et L sont respectivement les longueurs caractéristiques de la microstructure et de la couche de neige. Différentes séparations d'échelles pourraient être bien sûr considérées et conduire à des modélisations macroscopiques différentes. En particulier, le cas plus complexe d'une faible séparation d'échelles pourrait se produire pour de très fines couches de neige ou des couches soumises à de très forts gradients de température. Dans ce cas, la modélisation macroscopique pourrait être obtenue en examinant l'ordre d'approximation supérieur suivant dans l'analyse asymptotique [*Boutin*, 1996; *Auriault et al.*, 2005].

La perspective la plus directe de ce travail est l'évaluation du modèle macro-échelle des phénomènes de transport proposé en utilisant des mesures macroscopiques de terrain ou de laboratoire. Cette étude comparative devrait inclure, en plus des mesures macroscopiques (température...), l'obtention d'images 3D de volumes élémentaires représentatifs de neige afin d'estimer les propriétés effectives nécessaires à la modélisation macroscopique.

Une autre perspective pourrait être liée à l'amélioration des modèles de manteau neigeux, comme le modèle Crocus développé au CEN. Leur description des phénomènes de transport pourrait être en effet enrichie ou modifiée en s'aidant de notre étude. Ce travail pourrait concerner en particulier le transfert de vapeur, qui n'est pas inclus dans la plupart des modèles actuels, mais dont la simulation semble pourtant nécessaire pour refléter certaines situations du manteau neigeux où les profils

de masse volumique de la neige dépendent du transport de vapeur d'eau [*Gallet et al.*, 2014].

Propriétés effectives liées aux phénomènes de transport

Dans un second temps, le travail de thèse a porté sur la relation entre les propriétés effectives, impliquées dans les transferts de chaleur et de vapeur à macro-échelle, et la microstructure de la neige, masse volumique incluse. On a étudié en particulier le tenseur de diffusion effectif, le tenseur de conductivité thermique effective, et le tenseur de perméabilité intrinsèque. Ces tenseurs effectifs ont été estimés en résolvant les problèmes aux limites spécifiques issus du processus d'homogénéisation sur des volumes élémentaires représentatifs de neige. Ces volumes ont été extraits d'une trentaine d'images 3D de neige reflétant toute la gamme de types de neige saisonnière et de masse volumique.

Dans l'ensemble, les propriétés effectives de la neige sont étroitement liées à la masse volumique, comme déjà souligné par des études antérieures, mais présentent également un comportement anisotrope, qui peut être significatif notamment pour le givre de profondeur et les cristaux facettés. Afin de décrire ce comportement anisotrope des propriétés effectives, des estimations analytiques (Modèle auto-cohérent et Modèle de réseau dilué de sphéroïdes) ont été présentées. Ces estimations sont basées sur des informations simples de la microstructure que sont la masse volumique et l'anisotropie des hétérogénéités.

Chaque propriété effective est en générale obtenue par la résolution d'un problème aux limites issu du processus d'homogénéisation qui est découplé des autres phénomènes physiques (sauf dans le cas de la dispersion). Ainsi, l'estimation de ces propriétés à partir d'images 3D reflète donc strictement le phénomène considéré. Ce découplage n'est pas aussi simple lorsque l'on effectue des mesures macroscopiques des propriétés. C'est pourquoi les estimations obtenues sont souvent le résultat de plusieurs processus physiques mis en jeu lors de la mesure. Nos estimations permettent, par exemple, de montrer que la diffusion de la vapeur n'est pas augmentée dans la neige par rapport à celle dans l'air libre, contrairement à ce que montrent plusieurs études expérimentales.

Le large jeu de données de propriétés de la neige que constitue ce travail peut être utile à de futures études microscopiques et macroscopiques. A titre d'exemple, nos estimations de conductivité thermique effective à partir d'images 3D ont été utilisées dans le travail de *Hagenmuller et al.* [2014] pour évaluer la relation d'un nouveau paramètre micro-structural, à savoir la masse volumique de coupe minimale (minimum cut density), par rapport à différentes propriétés physiques. Cette base de donnée peut également servir d'outil pour guider le développement des modèles de manteau neigeux à macro-échelle ou les valider. Par exemple, *Domine et al.* [2013] ont implémenté l'équation de régression de la perméabilité intrinsèque proposée dans cette thèse dans le modèle de manteau neigeux Crocus. Ils obtiennent un bon accord entre la perméabilité de la neige simulée et celle mesurée sur le terrain. Enfin, dans le travail de *Carmagnola et al.* [2014], notre série temporelle de surface spécifique de la neige (SSA) a été utilisée pour guider la mise en œuvre de la description de la SSA dans le modèle Crocus.

Parmi les travaux à poursuivre, il serait intéressant de comparer les estimations

analytiques présentées à d'autres résultats expérimentaux obtenus dans des conditions différentes de celles étudiées dans la thèse. Dans cette optique, nous sommes en train d'analyser une nouvelle série temporelle d'images 3D acquise au cours d'une métamorphose de gradient de température (température, gradient de température, masse volumique de la neige initiale différente) obtenue lors du stage de master d'Alexandre Philip (*Observation in vivo d'une métamorphose de gradient de température par imagerie 3D à l'aide d'une cellule cryogénique et caractérisation quantitative*) que j'ai co-encadré.

D'autre part, l'étude des propriétés effectives liées aux phénomènes de transport pourrait être complétée par l'estimation du tenseur effectif de dispersion, qui apparaît dans les modèles macroscopiques lorsque la convection est importante. Néanmoins ces estimations à partir d'images 3D ne sont pas triviales et nécessitent de résoudre un problème aux limites qui implique les effets de convection à l'échelle des pores.

Suivi des métamorphoses de la neige sèche

La dernière contribution de cette thèse concerne le suivi de l'évolution de la microstructure au cours des métamorphoses de la neige sèche par imagerie 3D. Deux approches différentes ont été utilisées: (i) une approche statique, qui a permis de suivre l'évolution d'une couche de neige en prélevant des échantillons de cette couche à intervalles de temps réguliers, et (ii) une approche in vivo, où le suivi de l'évolution grains à grains d'un même échantillon de neige par tomographies successives est réalisé. Cette dernière approche a été rendue possible grâce à un travail de développement instrumental réalisé au cours de la thèse, afin de concevoir une nouvelle cellule cryogénique. Cette cellule fonctionne à température ambiante et non, comme les cellules présentées jusqu'à présent [*Schneebeli and Sokratov*, 2004; *Pinzer and Schneebeli*, 2009a; *Chen and Baker*, 2010], en chambre froide uniquement.

L'imagerie 3D de la neige est un outil essentiel pour étudier les métamorphoses de la neige à l'échelle microscopique. A titre d'exemple, le processus de facettage et d'arrondissement à la base et au sommet des grains de glace, difficile à prendre en compte dans les modèles micro-échelle, a pu être décrit par les distributions de courbure moyenne de la surface air/glace. D'autre part, la méthode in vivo donne accès à l'évolution grains à grains de la neige en 3D. Ces données peuvent être utilisées pour évaluer la description physique prise en compte dans les modélisations microscopiques des métamorphoses de la neige sèche : en partant d'une même image 3D initiale, l'évolution de la microstructure simulée et de celle observée peuvent être comparées.

Les cellules cryogéniques utilisées pour les deux approches de suivi des métamorphoses fonctionnent à température ambiante. Elles sont donc adaptables à un large panel de tomographes, y compris ceux de type synchrotron, qui peuvent présenter différents avantages en termes de techniques d'imagerie, de résolution, de vitesse d'acquisition... Ainsi, des études fines des métamorphoses de la neige sont envisageables, tel que l'étude de la croissance anisotrope du cristal de glace, l'étude des processus de facettage/arrondissement de la surface de glace, l'obtention de la cartographie 3D de l'orientation cristalline de la glace par tomographie par contraste de diffraction [*Ludwig et al.*, 2009; *Rolland du Roscoat*

et al., 2011], etc. Toutes ces études ont des implications concernant l'amélioration de la modélisation micro-échelle des métamorphoses de la neige.

En ce qui concerne les processus de facettage/d'arrondissement, un travail est actuellement en cours avec la nouvelle cellule cryogénique. Une série d'images 3D de l'évolution in vivo d'une bulle d'air d'un diamètre de 0,3 mm contenue dans un bloc de glace monocristallin sous un gradient de température a été acquise par tomographies successives à une résolution de 7,8 μm. L'analyse des données est toujours en cours, mais les premiers résultats sont présentés dans la Figure i : au début de l'expérience, la bulle d'air est à peu près sphérique, tandis qu'après 95 heures d'évolution, des facettes au sommet de la bulle sont observables. Ces images 3D pourront être utilisées pour guider ou valider les modèles à micro-échelle qui souhaiteraient simuler les processus de facettage/d'arrondissement du cristal de glace.

Toujours en utilisant la méthode in vivo, une étude expérimentale sur l'anisotropie de la vitesse de croissance des cristaux de glace pourrait être réalisée afin de mieux comprendre sa relation avec la température et la sursaturation. Sur ce sujet, un premier travail a été initié lors de mon séjour de trois mois (programme d'été 2012 de la JSPS) à l'Institute of Low Temperature Science à Sapporo, au Japon, en collaboration avec Y. Furukawa. Pendant ce séjour, nous avons suivi la croissance d'un cristal négatif (cavité d'air dans un monocristal de glace) en 2D par acquisition d'images successives avec un microscope optique. Grâce à une aiguille creuse insérée dans le cristal de glace, la "croissance" du cristal négatif est générée par un système de pompage qui crée en permanence une sous-saturation de vapeur dans la cavité d'air et entraîne ainsi la sublimation de la glace (voir Figure ii). Des résultats préliminaires de l'influence de la température et de la sous-saturation sur la croissance préférentielle des faces basales ou prismatiques du cristal de glace ont été obtenus. Des images 3D de ces phénomènes fourniraient des résultats plus précis, et pourraient, entre autres, être comparées à des résultats issus de modélisations.

De même, dans le cadre du projet ANR DigitalSnow dans lequel nous sommes impliqués, nous essayons de développer un modèle 3D pour les métamorphoses de la neige sèche à l'échelle des pores. Le but est de simuler l'évolution de la microstructure sous des conditions isothermes ou de gradient de température, à partir d'une image 3D donnée de neige, et en utilisant une approche de champ de phase telle que présentée par *Kaempfer and Plapp* [2009]. Ce développement pourra bénéficier d'études comparatives entre les évolutions simulées et observées à l'aide, notamment, de la série temporelle d'images 3D obtenue au cours de la thèse.

En conclusion, l'approche de travail utilisée dans cette thèse peut être illustrée par le schéma de la Figure 7.5. Les études basées sur des images 3D de neige contribuent à éclaircir certaines problématiques concernant la physique des métamorphoses de la neige sèche à l'échelle des pores. La description de cette physique peut être guidée notamment en comparant des microstructures 3D de neige obtenues par simulations à micro-échelle et par observations tomographiques. La modification de la physique à l'échelle des pores a potentiellement une influence sur la physique à plus grande échelle, notamment à

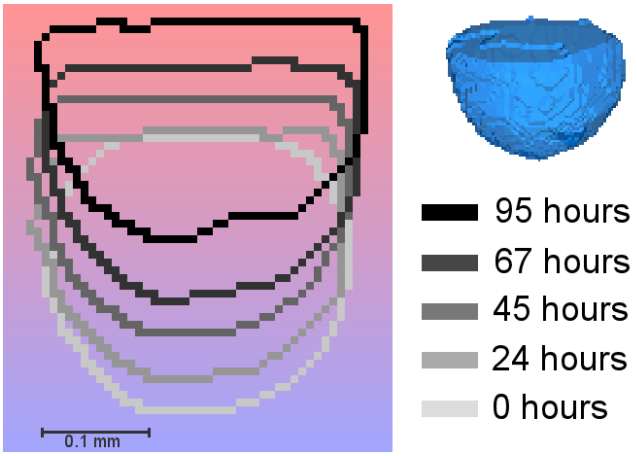

Figure i: Evolution temporelle de la morphologie d'une bulle d'air incluse dans un monocristal de glace soumis à un gradient de température d'environ 50 $\mathrm{K\,m^{-1}}$, à partir de coupes verticales issues des données tomographiques. Le contour de l'interface de la bulle est montré à différents temps. Une vue 3D de la bulle après 95 heures d'évolution est aussi illustrée.

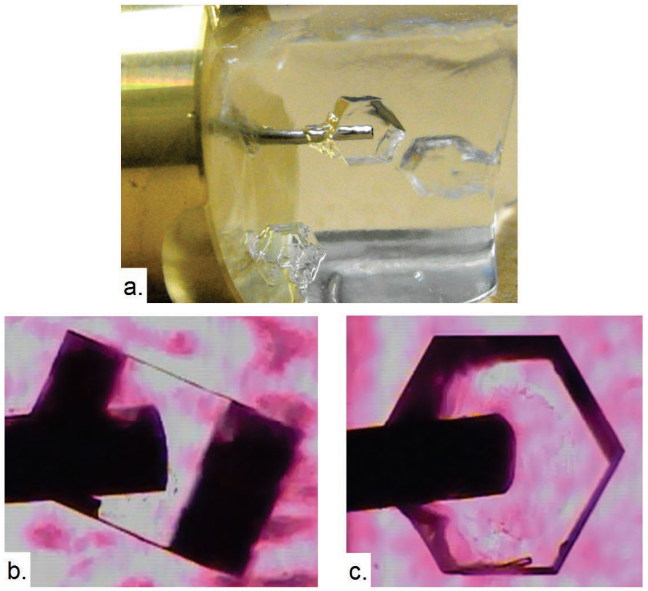

Figure ii: a. Image de l'aiguille du système de pompage d'air, introduite dans le monocristal de glace. Le bout de l'aiguille est entouré par un cristal négatif. Photo d'une face prismatique (b.) et basale (c) du cristal négatif. L'aiguille a un diamètre de 0,8 mm.

l'échelle d'une couche de neige. L'homogénéisation permet de déterminer la modélisation macroscopique équivalente à partir d'une description physique à micro-échelle. A l'aide d'images 3D de neige, les propriétés effectives impliquées dans cette modélisation peuvent être estimées. Ces développements théoriques ainsi que l'estimation des propriétés effectives peuvent contribuer à l'amélioration des modèles macroscopiques de manteau neigeux. Dans cette approche, la thèse a principalement contribué à la compréhension de la physique à micro-échelle en utilisant des images 3D, et à la transition vers la macro-échelle, y compris l'estimation des propriétés effectives, comme représenté par les flèches de contour rouge.

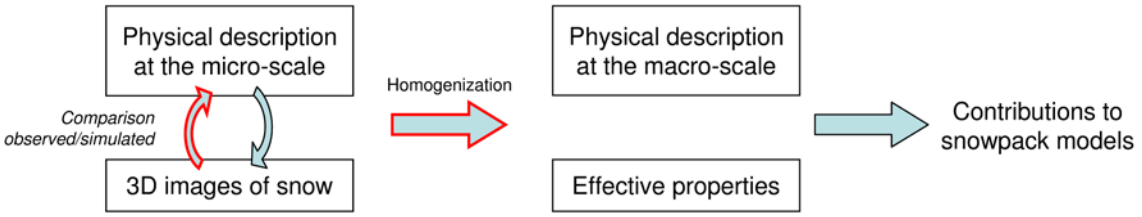

Figure iii: Illustration schématique de l'approche générale de la thèse pour l'étude de la physique de la neige.

List of publications resulting from this thesis

Peer-reviewed publications

- Calonne N., F. Flin, B. Lesaffre, A. Dufour, J. Roulle, P. Puglièse, A. Philip, F. Lahoucine, C. Geindreau, J.-M. Panel, S. Rolland du Roscoat, and P. Charrier, A room temperature operating cryogenic cell for the in vivo monitoring of snow metamorphism by X-ray microtomography, submitted.

- Hagenmuller, P., N. Calonne, G. Chambon, F. Flin, C. Geindreau, and M. Naaim. Characterization of the snow microstructural bonding system through the minimum cut density, Cold Regions Science and Technology, 108, 72-79, doi: 10.1016/j.coldregions.2014.09.002, 2014.

- Calonne, N., C. Geindreau, and F. Flin, Macroscopic modeling for heat and water vapor transfer in dry snow by homogenization, Journal of Physical Chemistry B, published in ASAP version, doi:10.1021/jp5052535, 2014.

- Calonne, N., F. Flin, C. Geindreau, B. Lesaffre, and S. Rolland du Roscoat, Study of a temperature gradient metamorphism of snow from 3-D images: time evolution of microstructures, physical properties and their associated anisotropy, The Cryosphere Discuss., 8, 1407-1451, doi:10.5194/tcd-8-1407-2014, 2014.

- Calonne, N., C. Geindreau, F. Flin, S. Morin, B. Lesaffre, S. Rolland du Roscoat, P. Charrier, 3D image-based numerical computations of snow permeability: links to specific surface area, density, and microstructural anisotropy, The Cryosphere, 6, 939–951, doi:10.5194/tc-6-939-2012, 2012.

- Calonne, N., F. Flin, S. Morin, B. Lesaffre, S. Rolland du Roscoat, C. Geindreau, Numerical and experimental investigations of the effective thermal conductivity of snow, Geophys. Res. Lett., 38, L23501, doi:10.1029/2011GL049234, 2011.

Other publications

- Hagenmuller, P., G. Chambon, B. Lesaffre, F. Flin, N. Calonne, and M. Naaim, Energybased binary segmentation of snow microtomographic images, Proceedings of the 1st International Conference on Tomography of Materials and Structures (ICTMS), Ghent, Belgium, 2013.

International conferences

- Calonne, N., C. Geindreau, F. Flin, B. Lesaffre and S. Rolland du Roscoat, Towards the macroscopic modeling of dry snow metamorphism using an upscaling method, 13th International Conference on the Physics and Chemistry of Ice, Hanover, USA, 17 -20 March 2014, talk.

- Calonne, N., C. Geindreau, F. Flin, B. Lesaffre and S. Rolland du Roscoat, About the relationship between microstructural and effective physical properties of snow computed on 3D images: comparison with measurements and models, AGU 2013, San Francisco, USA, 9 -13 December 2013, invited poster.

- Calonne, N., F. Flin, B. Lesaffre, A. Dufour, J. Roulle, P. Puglièse, A. Philip, F. Lahoucine, S. Rolland du Roscoat and C. Geindreau, A room temperature operating cryogenic cell for in vivo monitoring of dry snow metamorphism by X-ray microtomography, AGU 2013, San Francisco, USA, 9 - 13 December 2013, poster.

- Calonne, N., F. Flin, C. Geindreau, B. Lesaffre and S. Rolland du Roscoat, Study of a temperature gradient metamorphism of snow from 3D images : time evolution of microstructures, physical properties and their associated anisotropy, International Snow Science Workshop 2013, Grenoble - Chamonix Mt Blanc, France, 7 - 11 October 2013, poster.

- Calonne, N., Y. Furukawa, C. Geindreau, and F. Flin, Study of the ice crystal growth and decay in air, JSPS Summer Program 2012 - Poster Session, Sokendai, Japan, 14 June 2012, poster.

- Calonne, N., F. Flin, S. Morin, B. Lesaffre, S. Rolland du Roscoat, C. Geindreau, 3D image-based numerical simulations and experimental measurements of the effective thermal conductivity of snow, Micro-DICE Conference 2011, Grenoble, France, 7 - 9 November 2011, talk.

- Calonne, N., F. Flin, S. Morin, C. Geindreau, S. Rolland du Roscoat, B. Lesaffre, C. Carmagnola, F. Domine, On the relationships between key physical properties of snow at the microstructure scale, IUGG 2011 Conference, IACS Symposium, Melbourne, Australia, 28 June - 7 July 2011, poster.

Seminars

- Calonne, N., F. Flin, B. Lesaffre, S. Rolland du Roscoat, and C. Geindreau, Study of a temperature gradient metamorphism of snow from 3-D images: time evolution of microstructures, physical properties and their associated anisotropy, Seminar at Institute for snow and avalanche research, Davos, Switzerland, 25 April 2014, talk.

- Calonne, N., F. Flin, B. Lesaffre, S. Rolland du Roscoat, and C. Geindreau, Métamorphose de la neige sèche : de la microstructure aux propriétés macroscopiques, Rencontre DySCo 2014 (Dynamics of complex systems), Les 2 Alpes, 27 – 28 March 2014, talk.

Bibliography

Akitaya, E., Studies of depth hoar, *Low. Temp. Sci., Series A*, *26*, 1 – 67, 1974.

Albert, M., Some numerical experiments on firn ventilation with heat transfer, *Annals of Glaciology*, *18*, 161–165, 1993.

Albert, M., and W. McGilvary, Thermal effects due to air flow and vapor transport in dry snow, *J. Glaciol*, *38*(129), 273–281, 1992.

Albert, M., C. Shuman, Z. Courville, R. Bauer, M. Fahnestock, and T. Scambos, Extreme firn metamorphism: impact of decades of vapor transport on near-surface firn at a low-accumulation glazed site on the east antarctic plateau, *Ann. Glaciol.*, *39*(1), 73–78, doi:10.3189/172756404781814041, 2004.

Albert, M. R., Effects of snow and firn ventilation on sublimation rates, *Ann. Glaciol.*, *35*(1), 52–56, doi:10.3189/172756402781817194, 2002.

Albert, M. R., and J. P. Hardy, Ventilation experiments in seasonal snow cover, *IAHS Publications-Series of Proceedings and Reports-Intern Assoc Hydrological Sciences*, *228*, 41–50, 1995.

Albert, M. R., and E. F. Shultz, Snow and firn properties and air-snow transport processes at Summit, Greenland, *Atmos. Environ.*, *36*, 2789–2797, 2002.

Albert, M. R., E. F. Shultz, and F. E. Perron, Snow and firn permeability at siple dome, antarctica, *Ann. Glaciol.*, *31*(1), 353–356, doi:10.3189/172756400781820273, 2000.

Arakawa, H., K. Izumi, K. Kawashima, and T. Kawamura, Study on quantitative classification of seasonal snow using specific surface area and intrinsic permeability, *Cold. Reg. Sci. Technol.*, *59*, 163–168, doi:10.1016/j.coldregions.2009.07.00, 2009.

Arakawa, H., K. Izumi, K. Kawashima, and Y. Ishii, Relationship between intrinsic permeability and microstructure of seasonal snow cover, in *SEPPYO*, vol. 72, pp. 311–321, Japanese Society of Snow and Ice, (in Japanese with English abstract), 2010.

Armstrong, R., and E. Brun, *Snow and climate: physical processes, surface energy exchange and modeling*, Cambridge Univ. Pr., 2008.

Arnaud, L., V. Lipenkov, J.-M. Barnola, M. Gay, P. Duval, et al., Modelling of the densification of polar firn: characterization of the snow-firn transition, *Annals of Glaciology*, *26*, 39–44, 1998.

Arnaud, L., G. Picard, N. Champollion, F. Domine, J. Gallet, E. Lefebvre, M. Fily, and J. Barnola, Measurement of vertical profiles of snow specific surface area with a 1 cm resolution using infrared reflectance: instrument description and validation, *Journal of Glaciology*, *57*(201), 17–29, 2011.

Arns, C., M. Knackstedt, W. V. Pinczewski, and N. S. Martys, Virtual permeametry on microtomographic images, *Journal of Petroleum Science and Engineering*, *45*(1–2), 41–46, doi:10.1016/j.petrol.2004.05.001,2004, 2004.

Arns, C. H., M. A. Knackstedt, W. V. Pinczewsk, and W. B. Lindquist, Accurate estimation of transport properties from microtomographic images, *Geophysical research letters*, *28*(17), 3361–3364, doi:10.1029/2001GL012987, 2001.

Arons, E. M., and S. C. Colbeck, Geometry of heat and mass transfer in dry snow: a review of theory and experiment, *Rev. Geophys.*, *33*(4), 463 – 493, doi:10.1029/95RG02073, 1995.

Auriault, J., Heterogeneous periodic and random media. Are the equivalent macroscopic descriptions similar?, *Int. J. Eng. Sci.*, *49*, 806–808, 2011.

Auriault, J.-L., Heterogeneous medium. is an equivalent description possible?, *Int. J. Engng. Sci.*, *29*, 785 – 795, 1991.

Auriault, J.-L., and P. Adler, Taylor dispersion in porous media: analysis by multiple scale expansions, *Advances in Water Resources*, *18*(4), 217–226, 1995.

Auriault, J.-L., C. Geindreau, and C. Boutin, Filtration law in porous media with poor separation of scales, *Transport in porous media*, *60*(1), 89–108, 2005.

Auriault, J.-L., C. Boutin, and C. Geindreau., *Homogenization of Coupled Phenomena in Heterogenous Media*, Wiley-ISTE, London, 2009.

Bader, H., Mineralogische und strukturelle charakterisierung des schnees und seiner metamorphose, in *Der Schnee und seine Metamorphose*, edited by H. Bader et al., pp. 1–61, Kümmerly & Frey, Bern, Beiträge zur Geologie der Schweiz, Geotechnische Serie Hydrologie 3, 1939.

Barrett, J. W., H. Garcke, and R. Nürnberg, Numerical computations of faceted pattern formation in snow crystal growth, *Physical Review E*, *86*(1), 011,604, 2012.

Bartelt, P., and M. Lehning, A physical SNOWPACK model for the Swiss avalanche warning: Part I: numerical model, *Cold Reg. Sci. Technol.*, *35*(3), 123–145, 2002.

Batchelor, G. K., and R. W. O'Brien, Thermal and electrical conduction through a granular material, *Proc. R. Soc. London A*, *355*, 313 – 333, 1977.

Bear, J., *Dynamics of Fluids in Porous Media*, Dover, 1972.

Beckmann, W., and R. Lacmann, Interface kinetics of the growth and evaporation of ice single crystals from the vapour phase: Ii. measurements in a pure water vapour environment, *Journal of Crystal Growth*, *58*(2), 433–442, 1982.

Bensoussan, A., J.-L. Lions, and G. Papanicolaou, *Asymptotic Analysis for periodic structures*, North Holland, 1978.

Bentley, W., Snow crystals, *National Geography*, *43*, 103–112, 1904.

Bernard, D., D. Gendron, J.-M. Heintz, S. Bordère, and J. Etourneau, First direct 3d visualisation of microstructural evolutions during sintering through x-ray computed microtomography, *Acta Materialia*, *53*(1), 121 – 128, doi:DOI:10.1016/j.actamat.2004.09.027, 2005.

Berryman, J. G., Planar spatial correlations, anisotropy, and specific surface area of stationary random porous media, *Journal of Applied Physics*, *83*, 1998.

Boone, A., and P. Etchevers, An intercomparison of three snow schemes of varying complexity coupled to the same land-surface model: Local scale evaluation at an Alpine site, *J. Hydrometeorol.*, *2*, 374 – 394, 2001.

Bornert, M., T. Bretheau, and P. Gilormini, *Homogénéisation en mécanique des matériaux, Tome 1: Matériaux aléatoires élastiques et milieux périodiques*, Hermes Science Publications, 2001.

Boutin, C., Microstructural effects in elastic composites, *International Journal of Solids and Structures*, *33*(7), 1023–1051, 1996.

Boutin, C., Study of permeability by periodic and self consistent homogenisation, *Eur. J. Mech. A/Solids*, *19*, 603–632, 2000.

Boutin, C., and C. Geindreau, Periodic homogenization and consistent estimates of transport parameters through sphere and polyhedron packings in the whole porosity range, *Phys. Rev. E*, *82*(1), 036,313–1 – 036,313–18, 2010.

Bradley, C., R. Brown, and T. Williams, Gradient metamorphism, zonal weakening of the snow-pack and avalanche initiation, *J. Glaciol.*, *19*, 335–342, 1977.

Brucker, L., G. Picard, L. Arnaud, J.-M. Barnola, M. Schneebeli, H. Brunjail, E. Lefebvre, and M. Fily, Modeling time series of microwave brightness temperature at Dome C, Antarctica, using vertically resolved snow temperature and microstructure measurements, *J. Glaciol.*, *57 (201)*, 171 – 182, 2011.

Bruggeman, D., The calculation of various physical constants of heterogeneous substances. i. the dielectric constants and conductivities of mixtures composed of isotropic substances, *Ann. Phys*, *24*(132), 636–679, 1935.

Brun, E., and F. Touvier, Etude expérimentale de la convection thermique dans la neige, *Journal de Physique*, *48*(C1), 257–262, 1987.

Brun, E., E. Martin, V. Simon, C. Gendre, and C. Coléou, An energy and mass model of snow cover suitable for operational avalanche forecasting, *J. Glaciol.*, *35*(121), 333 – 342, 1989.

Brun, E., P. David, M. Sudul, and G. Brunot, A numerical model to simulate snow-cover stratigraphy for operational avalanche forecasting, *J. Glaciol.*, *38*(128), 13 – 22, 1992.

Brzoska, J.-B., C. Coléou, and B. Lesaffre, Thin-sectioning of wet snow after flash-freezing, *Journal of Glaciology*, *44*(146), 54–62, 1998.

Brzoska, J.-B., C. Coléou, B. Lesaffre, S. Borel, O. Brissaud, W. Ludwig, E. Boller, and J. Baruchel, 3D visualization of snow samples by microtomography at low temperature, *ESRF Newsletter*, *32*, 22–23, 1999a.

Brzoska, J.-B., B. Lesaffre, C. Coléou, K. Xu, and R. A. Pieritz, Computation of 3D curvatures on a wet snow sample, *Eur. Phys. J. AP*, *7*, 45–57, (10.1051/epjap:1999198), 1999b.

Brzoska, J.-B., F. Flin, and N. Ogawa, Using Gaussian curvature for the 3D segmentation of snow grains from microtomographic data, in *Physics and Chemistry of Ice*, edited by W. Kuhs, Special Publication Nr 311, pp. 125–132, RSC Publishing, Cambridge, UK, proceedings of the 11th International Conference on the Physics and Chemistry of Ice held at Bremerhaven, Germany on 23-28 July 2006, 2007.

Brzoska, J.-B., F. Flin, and J. Barckicke, Explicit iterative computation of diffusive vapour field in the 3-D snow matrix: preliminary results for low flux metamorphism, *Ann. Glaciol.*, *48*, 13–18, doi:10.3189/172756408784700798, 2008.

Budiansky, B., On the elastic moduli of some heterogeneous materials, *J. Mech. Phys. Solids*, *13*, 223–227, 1965.

Calonne, N., F. Flin, S. Morin, B. Lesaffre, S. Rolland du Roscoat, and C. Geindreau, Numerical and experimental investigations of the effective thermal conductivity of snow, *Geophys. Res. Lett.*, *38*, L23,501, doi:10.1029/2011GL049234, 2011.

Calonne, N., C. Geindreau, F. Flin, S. Morin, B. Lesaffre, S. Rolland du Roscoat, and P. Charrier, 3-d image-based numerical computations of snow permeability: links to specific surface area, density, and microstructural anisotropy, *The Cryosphere*, *6*(5), 939–951, doi:10.5194/tc-6-939-2012, 2012.

Calonne, N., F. Flin, C. Geindreau, B. Lesaffre, and S. Rolland du Roscoat, Study of a temperature gradient metamorphism of snow from 3-D images: time evolution of microstructures, physical properties and their associated anisotropy, *The Cryosphere Discussions*, *8*, 1407–1451, 2014a.

Calonne, N., C. Geindreau, and F. Flin, Macroscopic modeling for heat and water vapor transfer in dry snow by homogenization, *The Journal of Physical Chemistry B*, doi: 10.1021/jp5052535, 2014b.

Calonne, N., et al., A room temperature operating cryogenic cell for the in vivo monitoring of snow metamorphism by X-ray microtomography, submitted, 2014c.

Carmagnola, C. M., S. Morin, M. Lafaysse, F. Domine, B. Lesaffre, Y. Lejeune, G. Picard, and L. Arnaud, Implementation and evaluation of prognostic representations of the optical diameter of snow in the surfex/isba-crocus detailed snowpack model, *The Cryosphere*, *8*(2), 417–437, doi:10.5194/tc-8-417-2014, 2014.

Chen, S., and I. Baker, Evolution of individual snowflakes during metamorphism, *J. Geophys. Res.*, *115*(D21), D21,114–, 2010.

Christon, M., P. J. Burns, and R. A. Sommerfeld, Quasi-steady temperature gradient metamorphism in idealized, dry snow, *Numerical Heat Transfer Part A - Applications*, *25*, 259–278, doi:10.1080/10407789408955948, 1994.

Colbeck, S., The vapor diffusion coefficient for snow, *Water resources research*, *29*(1), 109–115, 1993.

Colbeck, S. C., A theory for water flow through a layered snowpack, *Water Resour. Res.*, *11*(2), 261–266, doi:10.1029/WR011i002p00261, 1975.

Colbeck, S. C., An analysis of water flow in dry snow, *Water Resour. Res.*, *12*(3), 523–527, doi:10.1029/WR012i003p00523, 1976.

Colbeck, S. C., Theory of metamorphism of dry snow, *J. Geophys. Res.*, *88*(C9), 5475–5482, (10.1029/0JGREA0000880000C9005475000001), 1983a.

Colbeck, S. C., Ice crystal morphology and growth rates at low supersaturations and high temperatures, *J. Appl. Phys.*, *54*(5), 2677–2682, 1983b.

Colbeck, S. C., Air movement in snow due to windpumping, *J. Glaciol.*, *35*, 209 – 213, 1989.

Colbeck, S. C., A model of wind pumping for layered snow, *J. Glaciol.*, *43*, 60 – 65, 1997.

Coléou, C., B. Lesaffre, J.-B. Brzoska, W. Ludwig, and E. Boller, Three-dimensional snow images by X-ray microtomography, *Ann. Glaciol.*, *32*, 75–81, doi:10.3189/172756401781819418, 2001.

Conger, S. M., and D. M. McClung, Comparison of density cutters for snow profile observations, *J. Glaciol*, *55 (189)*, 163 – 169, 2009.

Courville, Z., M. Albert, M. Fahnestock, L. Cathles, and C. Shuman, Impacts of an accumulation hiatus on the physical properties of firn at a low-accumulation polar site, *Journal of Geophysical Research: Earth Surface (2003–2012)*, *112*(F2), 2007.

Courville, Z., M. Hörhold, M. Hopkins, and M. Albert, Lattice-boltzmann modeling of the air permeability of polar firn, *J. Geophys. Res.*, *115*(F4), F04,032, doi:10.1029/2009JF001549, 2010.

De Quervain, M., Snow structure, heat and mass flux through snow, *The Role of Snow and Ice in Hydrology*, pp. 203–226, 1973.

Dominé, F., T. Lauzier, A. Cabanes, L. Legagneux, W. F. Kuhs, K. Techmer, and T. Heinrichs, Snow metamorphism as revealed by scanning electron microscopy, *Microscopy research and technique*, *62*(1), 33–48, 2003.

Domine, F., M. Albert, T. Huthwelker, H. W. Jacobi, A. A. Kokhanovsky, M. Lehning, G. Picard, and W. R. Simpson, Snow physics as relevant to snow photochemistry, *Atmos. Chem. Phys.*, *8*, 171 – 208, 2008.

Domine, F., J. Bock, S. Morin, and G. Giraud, Linking the effective thermal conductivity of snow to its shear strength and density, *J. Geophys. Res.*, *116*, F04,027, doi:10.1029/2011JF002000, 2011.

Domine, F., S. Morin, E. Brun, M. Lafaysse, and C. M. Carmagnola, Seasonal evolution of snow permeability under equi-temperature and temperature-gradient conditions, *The Cryosphere*, *7*(6), 1915–1929, doi:10.5194/tc-7-1915-2013, 2013.

Ene, H., and E. Sanchez-Palencia, Equations et phénomènes de surface pour écoulement dans un modèle de milieu poreux, *J. de Mécanique*, *14*, 73–108, 1975.

Erbe, E. F., A. Rango, J. Foster, E. G. Josberger, C. Pooley, and W. P. Wergin, Collecting, shipping, storing, and imaging snow crystals and ice grains with low-temperature scanning electron microscopy, *Microscopy research and technique*, *62*(1), 19–32, 2003.

Ferreol, B., and D. Rothman, Lattice-Boltzmann simulations of flow through Fontainebleau sandstone, *Transport in Porous Media*, *20*(1–2), 3–20, doi:10.1007/BF00616923, 1995.

Fierz, C., R. L. Armstrong, Y. Durand, P. Etchevers, E. Greene, D. M. McClung, K. Nishimura, P. K. Satyawali, and S. A. Sokratov, *The international classification for seasonal snow on the ground*, IHP-VII Technical Documents in Hydrology n 83, IACS Contribution n 1, 2009.

Flin, F., and J.-B. Brzoska, The temperature gradient metamorphism of snow: vapour diffusion model and application to tomographic images, *Ann. Glaciol.*, *49*, 17–21, doi:10.3189/172756408787814834, 2008.

Flin, F., J.-B. Brzoska, B. Lesaffre, C. Coléou, and R. A. Pieritz, Full three-dimensional modelling of curvature-dependent snow metamorphism: first results and comparison with experimental tomographic data, *J. Phys. D: Appl. Phys.*, *36*, A49–A54, doi:10.1088/0022-3727/36/10A/310, 2003.

Flin, F., J.-B. Brzoska, B. Lesaffre, C. Coléou, and R. A. Pieritz, Three-dimensional geometric measurements of snow microstructural evolution under isothermal conditions, *Ann. Glaciol.*, *38*, 39–44, doi:10.3189/172756404781814942, 2004.

Flin, F., J.-B. Brzoska, R. Pieritz, B. Lesaffre, C. Coléou, and Y. Furukawa, A tentative model for the temperature gradient snow metamorphism and its first validations on x-ray microtomographic data, in *Proceedings of the 8th International Conference on X-ray Microscopy, XRM2005*, edited by S. Aoki, Y. Kagoshima, and Y. Suzuki, Conference Series 7, pp. 306–308, Institute of Pure and Applied Physics, Tokyo, Japan, ISBN 4-900526-21-5, 2006.

Flin, F., J.-B. Brzoska, R. Pieritz, B. Lesaffre, C. Coléou, and Y. Furukawa, The temperature gradient metamorphism of snow: Model and first validations using X-ray microtomographic images, in *P. C. I.*, edited by W. Kuhs, Special Publication Nr 311, pp. 181–189, RSC Publishing, Cambridge, UK, proceedings of the 11th International Conference on the Physics and Chemistry of Ice held at Bremerhaven, Germany on 23-28 July 2006, 2007.

Flin, F., B. Lesaffre, A. Dufour, L. Gillibert, A. Hasan, S. Rolland du Roscoat, S. Cabanes, and P. Pugliese, On the Computations of Specific Surface Area and Specific Grain Contact Area from Snow 3D Images, in *Physics and Chemistry of Ice*, edited by Y. Furukawa, pp. 321–328, Hokkaido University Press, Sapporo, JP, proceedings of the 12th International Conference on the Physics and Chemistry of Ice held at Sapporo, Japan on 5-10 September 2010, 2011.

Flin, F., et al., Adaptive estimation of normals and surface area for discrete 3-D objects: application to snow binary data from X-ray tomography, *I.E.E.E. Trans. Image. Process.*, *14*(5), 585–596, doi:10.1109/TIP.2005.846021, 2005.

Freitag, J., U. Dobrindt, and J. Kipfstuhl, A new method for predicting transport properties of polar firn with respect to gases on the pore-space scale, *Ann. Glaciol.*, *35*(1), 538–544, doi:10.3189/172756402781816582, 2002.

Freitag, J., F. Wilhelms, and S. Kipfstuhl, Microstructure-dependent densification of polar firn derived from x-ray microtomography, *J. Glaciol.*, *50*(169), 243–250, doi:10.3189/172756504781830123, 2004.

Fukuzawa, T., and E. Akitaya, Depth-hoar crystal growth in the surface layer under high temperature gradient, *Annals of Glaciology*, *18*, 39–45, 1993.

Furukawa, Y., and S. Kohata, Temperature dependence of the growth form of negative crystal in an ice single crystal and evaporation kinetics for its surfaces, *J. Cryst. Growth*, *129*, 571–581, 1993.

Furukawa, Y., and J. S. Wettlaufer, Snow and ice crystals, *Physics Today*, *60*(12), 70–71, 2007.

Furukawa, Y., M. Yamamoto, and T. Kuroda, Ellipsometric study of the transition layer on the surface of an ice crystal, *Journal of crystal growth*, *82*(4), 665–677, 1987.

Gallet, J.-C., F. Domine, C. S. Zender, and G. Picard, Measurement of the specific surface area of snow using infrared reflectance in an integrating sphere at 1310 and 1550 nm, *The Cryosphere*, *3*, 167 – 182, doi:10.5194/tc-3-167-2009, 2009.

Gallet, J.-C., F. Domine, J. Savarino, M. Dumont, and E. Brun, The growth of sublimation crystals and surface hoar on the antarctic plateau, *The Cryosphere*, *8*(4), 1205–1215, 2014.

Gay, M., M. Fily, C. Genthon, M. Frezzotti, H. Oerter, and J.-G. Winther, Snow grain-size measurements in antarctica, *Journal of Glaciology*, *48*(163), 527–535, 2002.

Geindreau, C., and J.-L. Auriault, Transport phenomena in saturated porous media under liquid-solid phase change, *Arch. Mech.*, *53*, 385–420, 2001.

Geindreau, C., and J.-L. Auriault, Magnetohydrodynamic flows in porous media, *Journal of fluid mechanics*, *466*, 343–363, 2002.

Giraud, A., C. Gruescu, D. Do, F. Homand, and D. Kondo, Effective thermal conductivity of transversely isotropic media with arbitrary oriented ellipsoidal inhomogeneities, *International Journal of Solids and Structures*, *44*(9), 2627–2647, 2007.

Gonda, T., and T. Koike, Growth rates and growth forms of ice crystals grown from the vapor phase, *Journal of Crystal Growth*, *56*(2), 259–264, 1982.

Good, W., Thin sections, serial cuts and 3-D analysis of snow, in *International Association of Hydrological Sciences Publication*, vol. 162, pp. 35–48, (Symposium at Davos 1986 – *Avalanche Formation, Movement and Effects*), 1987.

Grannas, A. M., A. E. Jones, J. Dibb, and et al., An overview of snow photochemistry: evidence, mechanisms and impacts, *Atmos. Chem. Phys.*, *7*, 4329 – 4373, 2007.

Grenfell, T., and S. Warren, Representation of a nonspherical ice particle by a collection of independent spheres for scattering and absorption of radiation, *Journal of Geophysical Research*, *104*(D24), 31,697–31,709, doi:10.1029/2000JC000414, 1999.

Hagenmuller, P., G. Chambon, B. Lesaffre, F. Flin, and M. Naaim, Energy-based binary segmentation of snow microtomographic images, *J. Glaciol.*, *59*(217), 859–873, doi: 10.3189/2013JoG13J035, 2013.

Hagenmuller, P., N. Calonne, G. Chambon, F. Flin, C. Geindreau, and M. Naaim, Characterization of the snow microstructural bonding system through the minimum cut density, *Cold Regions Science and Technology*, *108*(0), 72 – 79, doi:http://dx.doi.org/10.1016/j.coldregions.2014.09.002, 2014.

Hashin, Z., Assessment of self consistent scheme approximation : Conductivity of particulate composites, *J. Comp. Mater.*, *2*, 284–304, 1968.

Heggli, M., E. Frei, and M. Schneebeli, Snow replica method for three-dimensional X-ray microtomographic imaging, *Journal of Glaciology*, *55*(192), 631–639, 2009.

Hill, R., A self consistent mechanics of composite materials, *J. Mech. Phys. Solids*, *13*, 213–222, 1965.

Hobbs, P. V., and B. J. Mason, The sintering and adhesion of ice, *Philosophical Magazine*, *9*(98), 181–197, 1964.

Hörhold, M. W., M. R. Albert, and J. Freitag, The impact of accumulation rate on anisotropy and air permeability of polar firn at a high-accumulation site, *J. Glaciol.*, *55*(192), 625–630, doi:10.3189/002214309789471021, 2009.

Jordan, R., A one-dimensional temperature model for a snow cover: technical documentation for SNTHERM.89., *Tech. Rep. 91-16*, U.S. Army Cold Regions Research and Engineering Laboratory, 1991.

Jordan, R., E. Andreas, and A. Makshtas, Heat budget of snow-covered sea ice at north pole 4, *J. Geophys. Res.*, *104*(C4), 7785–7806, 1999a.

Jordan, R. E., J. P. Hardy, F. E. Perron, and D. J. Fisk, Air permeability and capillary rise as measures of the pore structure of snow: an experimental and theoretical study, *Hydrol. Proc.*, *13*(12-13), 1733–1753, doi:10.1002/(SICI)1099-1085(199909)13:12/13<1733::AID-HYP863>3.0.CO;2-2, 1999b.

Kaempfer, T., and M. Schneebeli, Observation of isothermal metamorphism of new snow and interpretation as a sintering process, *J. Geophys. Res.*, *112*, D24,101, doi:10.1029/2007JD009047, 2007.

Kaempfer, T., M. Schneebeli, and S. Sokratov, A microstructural approach to model heat transfer in snow, *Geophys. Res. Lett.*, *32*(21), L21,503, doi:10.1029/2005GL023873, 2005.

Kaempfer, T. U., and M. Plapp, Phase-field modeling of dry snow metamorphism, *Phys. Rev. E*, *79*, 031,502, doi:10.1103/PhysRevE.79.031502, 2009.

Kamata, Y., and A. Sato, Water vapor transport in snow under temperature gradient condition, in *11th International Conference on the Physics and Chemistry of Ice (PCI-2006)*, p. 106, 2006.

Kanit, T., S. Forest, I. Galliet, V. Mounoury, and D. Jeulin, Determination of the size of the representative elementary volume element for random composites: statistical and numerical approach, *Int. J. Solids Struct.*, *40 (13 -14)*, 3647–3679, doi:10.1016/S0020-7683(03)00143-4, 2003.

Katsushima, T., T. Kumakura, and Y. Takeuchi, A multiple snow layer model including a parameterization of vertical water channel process in snowpack, *Cold Reg. Sci. Technol.*, *59*(2-3), 143–151, 2009.

Kingery, W. D., Regelation, surface diffusion and ice sintering, *J. Appl. Phys.*, *31*(5), 833–838, 1960.

Knight, C. A., Formation of crystallographic etch pits on ice and its application to the study of hailstones, *J. Appl. Meteor.*, *5*, 710–714, 1966.

Koivu, V., M. Decain, C. Geindreau, K. Mattila, J.-F. Bloch, and M. Kataja, Transport properties of heterogeneous materials. Combining computerised x-ray micro-tomography and direct numerical simulations, *Inte. Comput. Fluid Dyn.*, *10*(1), 713–721, 2009.

Kuroda, T., and R. Lacmann, Growth kinetics of ice from the vapour phase and its growth forms, *Journal of Crystal Growth*, *56*(1), 189–205, 1982.

Kuroiwa, D., A study of ice sintering, *Tellus*, *13*, 252–259, 1961.

Kushch, V. I., and I. Sevostianov, Dipole moments, property contribution tensors and effective conductivity of anisotropic particulate composites, *International Journal of Engineering Science*, *74*, 15–34, 2014.

Lasseux, D., A. A. Arani, and A. Ahmadi, On the stationary macroscopic inertial effects for one phase flow in ordered and disordered porous media, *Physics of Fluids (1994-present)*, *23*(7), 073,103, 2011.

Lehning, M., P. Bartelt, B. Brown, T. Russi, U. Stöckli, and M. Zimmerli, Snowpack model calculations for avalanche warning based upon a new network of weather and snow stations, *Cold Regions Science and Technology*, *30*(1), 145–157, 1999.

Lehning, M., P. Bartelt, B. Brown, and C. Fierz, A physical snowpack model for the swiss avalanche warning: Part iii: Meteorological forcing, thin layer formation and evaluation, *Cold Regions Science and Technology*, *35*(3), 169–184, 2002a.

Lehning, M., P. Bartelt, B. Brown, C. Fierz, and P. Satyawali, A physical SNOWPACK model for the Swiss avalanche warning. part II: snow microstructure., *Cold Reg. Sci. Technol.*, *35*(3), 147 – 167, doi:10.1016/S0165-232X(02)00073-3, 2002b.

Lehning, M., I. Völksch, D. Gustafsson, T. A. Nguyen, M. Stähli, and M. Zappa, Alpine3d: a detailed model of mountain surface processes and its application to snow hydrology, *Hydrol. Process.*, *20*(10), 2111–2128, doi:10.1002/hyp.6204, 2006.

Lesaffre, B., E. Pougatch, and E. Martin, Objective determination of snow-grain characteristics from images, *Ann. Glaciol.*, *26*, 112–118, 1998.

Lesaffre, B., J.-B. Broska, C. Coléou, F. Flin, and R. Pieritz, Images tridimensionnelles de neige : des prélévements in situ aux fichiers de données volumiques. application à une expérience de métamorphose d' isothermie, *Tech. rep.*, CNRM-GAME CEN, Météo France - CNRS, 2004.

Libbrecht, K., and M. Rickerby, Measurements of growth rates of (0001) ice crystal surfaces, *arXiv preprint arXiv:1110.5828*, 2011.

Libbrecht, K. G., Growth rates of the principal facet of ice between -10°C and -40°C, *Journal of Crystal Growth*, *247*, 530–540, (10.1016/S0022-0248(02)01996-6), 2003.

Libbrecht, K. G., The physics of snow crystals, *Rep. Prog. Phys.*, *68*, 855–895, doi:doi:10.1088/0034-4885/68/4/R03, 2005.

Libbrecht, K. G., and H. M. Arnold, Measurements of ice crystal growth rates in air at -5°C and -10°C, *arXiv:0912.2518v1*, 2009.

Löwe, H., J. Spiegel, and M. Schneebeli, Interfacial and structural relaxations of snow under isothermal conditions, *J. Glaciol.*, *57*, 203, 2011.

Löwe, H., F. Riche, and M. Schneebeli, A general treatment of snow microstructure exemplified by an improved relation for thermal conductivity, *The Cryosphere*, *7*(5), 1473–1480, doi:10.5194/tc-7-1473-2013, 2013.

Luciano, G. L., and M. R. Albert, Bidirectional permeability measurements of polar firn, *Ann. Glaciol.*, *35*(1), 63–66, doi:10.3189/172756402781817095, 2002.

Ludwig, W., P. Reischig, A. King, M. Herbig, E. M. Lauridsen, G. Johnson, T. J. Marrow, and J. Y. Buffière, Three-dimensional grain mapping by x-ray diffraction contrast tomography and the use of friedel pairs in diffraction data analysis, *Review of Scientific Instruments*, *80*(3), 033905, doi:10.1063/1.3100200, 2009.

Lundy, C. C., M. Q. Edens, and R. L. Brown, Measurement of snow density and microstructure using computed tomography, *Journal of Glaciology*, *48*(161), 312–316, doi:doi:10.3189/172756502781831485, 2002.

Maeno, N., and T. Ebinuma, Pressure sintering of ice and its implication to the densification of snow at polar glaciers and ice sheets, *J. Phys. Chem.*, *87*(21), 4103–4110, 1983.

Marbouty, D., An experimental study of temperature-gradient metamorphism, *J. Glaciol.*, *26*, 303–312, 1980.

Markov, I. V., *Crystal growth for beginners*, World Scientific Publishing Co. Pte. Ltd, Singapore, 1995.

Marshall, H.-P., and J. B. Johnson, Accurate inversion of high-resolution snow penetrometer signals for microstructural and micromechanical properties, *J. Geophys. Res.*, *114*, F04,016, doi:10.1029/2009JF001269, 2009.

Martys, N., and H. D. Chen, Simulation of multicomponent fluids in complex three-dimensional geometries by the lattice boltzmann method, *Phys. Rev. E*, *53*(1), 743–750, doi:10.1103/PhysRevE.53.743, 1996.

Massman, W., A review of the molecular diffusivities of H_2O, CO_2, CH_4, CO, O_3, SO_2, NH_3, N_2O, NO, and NO_2 in air, O_2 and N_2 near STP, *Atmospheric Environment*, *32*(6), 1111–1127, doi:http://dx.doi.org/10.1016/S1352-2310(97)00391-9, 1998.

Matzl, M., and M. Schneebeli, Measuring specific surface area of snow by near-infrared photography, *J. Glaciol.*, *52*, 558 – 564, 2006.

Matzl, M., and M. Schneebeli, Stereological measurement of the specific surface area of seasonal snow types: Comparison to other methods, and implications for mm-scale vertical profiling, *Cold Reg. Sci. Technol.*, *64*(1), 1 – 8, doi:10.1016/j.coldregions.2010.06.006, 2010.

Mei, C. C., and J. L. Auriault, The effect of inertia on flow through porous medium, *J. Fluid. Mech.*, *222*, 647–663, 1991.

Miller, D., and E. Adams, A microstructural dry-snow metamorphism model for kinetic crystal growth, *J. Glaciol.*, *55*, 194, 2009.

Miller, D. A., E. E. Adams, and R. L. Brown, A microstructural approach to predict dry snow metamorphism in generalized thermal conditions, *Cold Regions Science and Technology*, *37*, 213–226, 2003.

Morin, S., F. Domine, L. Arnaud, and G. Picard, In-situ monitoring of the time evolution of the effective thermal conductivity of snow, *Cold Regions Sci. Tech.*, *64*(2), 73 – 80, doi:10.1016/j.coldregions.2010.02.008, 2010.

Mutaftschiev, B., *The atomistic nature of crystal growth*, Springer series in material science, Berlin, 2001.

Nakaya, U., *Snow crystals: natural and artificial*, Harvard University Press, 1954.

Nelson, J., and C. Knight, Snow crystal habit changes explained by layer nucleation, *Journal of the atmospheric sciences*, *55*(8), 1452–1465, 1998.

Neumann, T. A., Effects on firn ventilation on geochemistry of polar snow, Phd thesis, University of Washington, 2003.

Neumann, T. A., M. R. Albert, C. Engel, Z. Courville, and F. Perron, Sublimation rate and the mass-transfer coefficient for snow sublimation, *International Journal of Heat and Mass Transfer*, *52*(1), 309–315, 2009.

Nguyen-Thi, H., L. Salvo, R. H. Mathiesen, L. Arnberg, B. Billia, M. Suery, and G. Reinhart, On the interest of synchrotron x-ray imaging for the study of solidification in metallic alloys, *Comptes Rendus Physique*, *13*(3), 237–245, 2012.

Nishikawa, Y., T. Koga, T. Hashimoto, and H. Jinnai, Measurements of interfacial curvatures of bicontinuous structure from three-dimensional digital images. 2. a sectioning and fitting method, *Langmuir*, *17*, 3254–3265, 2001.

Ogawa, N., F. Flin, and J.-B. Brzoska, Representation of two curvatures of surface and its application to snow physics, *Memoirs of the Hokkaido Institute of Technology*, *34*, 81–87, 2006.

Painter, T. H., N. P. Molotch, M. Cassidy, M. Flanner, and K. Steffen, Contact spectroscopy for determination of stratigraphy of optical grain size, *J. Glaciol*, *53*, 121 – 127, 2006.

Pfeffer, W. T., and R. Mrugala, Temperature gradient and initial snow density as controlling factors in the formation and structure of hard depth hoar, *Journal of Glaciology*, *48*(163), 485–494, 2002.

Pielmeier, C., and M. Schneebeli, Stratigraphy and changes in hardness of snow measured by hand, ramsonde and snow micro penetrometer: a comparison with planar sections, *Cold Reg. Sci. Technol.*, *37*, 393–405, 2003.

Pinzer, B., and M. Schneebeli, Snow metamorphism under alternating temperature gradients: Morphology and recrystallization in surface snow, *Geophysical Research Letters*, *36*(23), L23,503, 2009a.

Pinzer, B., and M. Schneebeli, Breeding snow: an instrumented sample holder for simultaneous tomographic and thermal studies, *Measurement Science and Technology*, *20*(9), 095,705, 2009b.

Pinzer, B., M. Schneebeli, and T. Kaempfer, Vapor flux and recrystallization during dry snow metamorphism under a steady temperature gradient as observed by time-lapse micro-tomography, *The Cryosphere*, *6*, 1141–1155, 2012.

Pitman, D., and B. Zuckerman, Effective thermal conductivity of snow at -88°C, -27°C and -5°C, *J. Appl. Phys.*, *38*, 2698–2699, 1967.

Potkay, J. A., G. R. Lambertus, R. D. Sacks, and K. D. Wise, A low-power pressure-and temperature-programmable micro gas chromatography column, *Journal of Microelectromechanical Systems*, *16*(5), 1071–1079, 2007.

Pottmann, H., J. Wallner, Q.-X. Huang, and Y.-L. Yang, Integral invariants for robust geometry processing, *Computer Aided Geometric Design*, *26*(1), 37–60, 2009.

Powers, D., K. O'Neill, and S. C. Colbeck, Theory of natural convection in snow, *J. Geophys. Res.*, *90*(D6), 10,641–10,649, 1985.

Raymond, C., and K. Tusima, Grain coarsening of water-saturated snow, *J. Glaciol.*, *22*(86), 83–105, 1979.

Riche, F., and M. Schneebeli, Microstructural change around a needle probe to measure thermal conductivity of snow, *J. Glaciol.*, *56*(199), 871–876, doi:10.3189/002214310794457164, 2010.

Riche, F., and M. Schneebeli, Thermal conductivity of snow measured by three independent methods and anisotropy considerations, *The Cryosphere*, *7*(1), 217–227, 2013.

Rieger, B., F. J. Timmermans, and L. J. van Vliet, Estimation of curvature on surfaces in 3d grey-value images, in *Proc ASCI 2002, 8th annual conf. of the advanced school for computing and imaging*, pp. 170–177, 2002.

Roberts, A., and E. J. Garboczi, Computation of the linear elastic properties of random porous materials with a wide variety of microstructure, *Proceedings of the Royal Society of London. Series A: Mathematical, Physical and Engineering Sciences*, *458*(2021), 1033–1054, 2002.

Rolland du Roscoat, S., M. Decain, X. Thibault, C. Geindreau, and J.-F. Bloch, Estimation of microstructural properties from synchrotron X-ray microtomography and determination of the REV in paper materials, *Acta Materialia*, *55 (8)*, 2841–2850, doi:10.1016/j.actamat.2006.11.050, 2007.

Rolland du Roscoat, S., M. Decain, C. Geindreau, X. Thibault, and J.-F. Bloch, Microstructural analysis of paper using synchrotron X-ray microtomography: numerical estimation of the permeability and effective thermal conductivity, *Appita Journal*, *61*(4), 286–290, 2008.

Rolland du Roscoat, S., A. King, A. Philip, P. Reischig, W. Ludwig, F. Flin, and J. Meyssonnier, Analysis of snow microstructure by means of x-ray diffraction contrast tomography, *Advanced Engineering Materials*, *13*(3), 128–135, doi:10.1002/adem.201000221, 2011.

Saito, Y., *Statistical physics of crystal growth*, vol. 2, World Scientific, 1996.

Sanchez-Palencia, E., Non-homogeneous media and vibration theory, in *Lectures Notes in Physics, Vol. 127.*, vol. 127, Springer-Verlag, Berlin, 1980.

Satyawali, P., Diffusivity and vapor flow into snow during phase change, *Annals of Glaciology*, *31*(1), 445–450, 2000.

Satyawali, P., N. Sinha, and D. Sethi, Double-microtoming technique for snow studies, *Canadian journal of physics*, *81*(1-2), 529–537, 2003.

Satyawali, P. K., and A. K. Singh, Dependence of thermal conductivity of snow on microstructure, *Journal of Earth System Sciences*, *117*(4), 465 – 475, 2008.

Satyawali, P. K., A. K. Singh, S. K. Dewali, P. Kumar, and V. Kumar, Time dependence of snow microstructure and associated effective thermal conductivity, *Ann. Glaciol.*, *49*, 43 – 50, 2008.

Sazaki, G., S. Zepeda, S. Nakatsubo, M. Yokomine, and Y. Furukawa, Quasi-liquid layers on ice crystal surfaces are made up of two different phases, *Proceedings of the National Academy of Sciences*, *109*(4), 1052–1055, 2012.

Schneebeli, M., Three-dimensional snow: How snow really looks like, in *Proceedings of International Snow Science Workshop*, pp. 407–408, 2000.

Schneebeli, M., and S. A. Sokratov, Tomography of temperature gradient metamorphism of snow and associated changes in heat conductivity, *Hydrol. Process.*, *18*(18), 3655 – 3665, doi:10.1002/hyp.5800, 2004.

Schneebeli, M., C. Pielmeier, and J. B. Johnson, Measuring snow microstructure and hardness using a high resolution penetrometer, *Cold Reg. Sci. Technol.*, *30 (1–3)*, 101–114, doi:10.1016/S0165-232X(99)00030-0, 1999.

Schweizer, J., B. Jamieson, and M. Schneebeli, Snow avalanche formation, *Reviews of Geophysics*, *41*(4), 2003.

Sergent, C., E. Martin, and C. Ancey, *Guide Neige et Avalanche - Connaissances, Pratiques, & Sécurité. Chapitre 3. Les métamorphoses de la neige, propriétés physiques et mécaniques*, EPFL, Lausanne, 1998.

Sethian, J. A., *Level set methods and fast marching methods: evolving interfaces in computational geometry, fluid mechanics, computer vision, and materials science*, vol. 3, Cambridge university press, 1999.

Shertzer, R. H., and E. E. Adams, Anisotropic thermal conductivity model for dry snow, *Cold Reg. Sci. Technol.*, *69*(2), 122 – 128, doi:10.1016/j.coldregions.2011.09.005, 2011.

Shimizu, H., Air permeability of deposited snow, *Contributions from the Institute of Low Temperature Science*, *A22*, 1–32, 1970.

Skjetne, E., and J.-L. Auriault, High-velocity laminar and turbulent flow in porous media, *Transport in porous media*, *36*(2), 131–147, 1999.

Sokratov, S. A., and R. G. Barry, Intraseasonal variation in the thermoinsulation effect of snow cover on soil temperatures and energy balance, *Journal of Geophysical Research: Atmospheres (1984–2012)*, *107*(D10), ACL–13, 2002.

Sokratov, S. A., and N. Maeno, Effective water vapor diffusion coefficient of snow under a temperature gradient, *Water resources research*, *36*(5), 1269–1276, 2000.

Sommerfeld, R. A., and J. E. Rocchio, Permeability measurements on new and equitemperature snow, *Water Resour. Res.*, *29*(8), 2485–2490, 1993.

Spanne, P., J. F. Thovert, C. J. Jacquin, W. B. Lindquist, K. W. Jones, and P. M. Adler, Synchrotron computed microtomography of porous media: topology and transports, *Physical review letters*, *73*(14), 2001–2004, doi:10.1103/PhysRevLett.73.2001, 1994.

Srivastava, P., P. Mahajan, P. Satyawali, and V. Kumar, Observation of temperature gradient metamorphism in snow by x-ray computed microtomography: measurement of microstructure parameters and simulation of linear elastic properties, *Annals of Glaciology*, *51*(54), 73–82, 2010.

Staron, P. J., E. E. Adams, and D. A. Miller, Nonequilibrium thermodynamics of kinetic metamorphism in snow, *Cold Regions Science and Technology*, *97*(0), 60 – 71, doi: http://dx.doi.org/10.1016/j.coldregions.2013.10.007, 2014.

Sturm, M., and J. B. Johnson, Natural convection in the subarctic snow cover, *J. Geophys. Res.*, *96*(B7), 11,657–11,671, 1991.

Sturm, M., J. Holmgren, M. König, and K. Morris, The thermal conductivity of seasonal snow, *J. Glaciol.*, *43*(143), 26 – 41, 1997.

Sun, S., J. Jin, and Y. Xue, A simple snow-atmosphere-soil transfer model, *Journal of Geophysical Research: Atmospheres (1984–2012)*, *104*(D16), 19,587–19,597, 1999.

Theile, T., and M. Schneebeli, Algorithm to decompose three-dimensional complex structures at the necks: tested on snow structures, *IET Image Processing*, *5*(2), 132–140, 2011.

Thoemen, H., T. Walther, and A. Wiegmann, 3D simulation of macroscopic heat and mass transfer properties from the microstructure of wood fibre networks, *Comp. Sci. Techn.*, *68*(3–4), 608 – 616, doi:10.1016/j.compscitech.2007.10.014, 2008.

Torquato, S., Random heterogeneous media: microstructure and improved bounds on effective properties, *Applied mechanics reviews*, *44*(2), 37–76, 1991.

Torquato, S., Effective stiffness tensor of composite media: Ii. applications to isotropic dispersions, *Journal of the Mechanics and Physics of Solids*, *46*(8), 1411–1440, 1998.

Torquato, S., *Random Heterogeneous Materials: Microstructure and Macroscopic Properties*, 2002.

Vetter, R., S. Sigg, H. Singer, D. Kadau, H. Herrmann, and M. Schneebeli, Simulating isothermal aging of snow, *EPL (Europhysics Letters)*, *89*, 26,001, doi:10.1209/0295-5075/89/26001, 2010.

Vionnet, V., E. Brun, S. Morin, A. Boone, E. Martin, S. Faroux, P. L. Moigne, and J.-M. Willemet, The detailed snowpack scheme Crocus and its implementation in SURFEX v7.2, *Geosci. Model. Dev.*, *5*, 773–791, doi:10.5194/gmd-5-773-2012, 2012.

Waldner, P. A., M. Schneebeli, U. Schultze-Zimmermann, and H. Flühler, Effect of snow structure on water flow and solute transport, *Hydrol. Proc.*, *18*(7), 1271–1290, 2004.

Wallace, J. M., and P. V. Hobbs, *Atmospheric science: an introductory survey*, vol. 92, Academic press, 2006.

Wang, X., and I. Baker, Observation of the microstructural evolution of snow under uniaxial compression using x-ray computed microtomography, *Journal of Geophysical Research: Atmospheres*, *118*(22), 12–371, 2013.

Wang, X., L. Gillibert, F. Flin, and D. Coeurjolly, Curvature-driven volumetric segmentation of binary shapes: an application to snow microstructure analysis, in *21st International Conference on Pattern Recognition, Tsukuba, Japan*, poster, 2012.

Wergin, W. P., A. Rango, E. F. Erbe, and C. A. Murphy, Low temperature sem of precipitated and metamorphosed snow crystals collected and transported from remote sites, *Microscopy and Microanalysis*, *2*(03), 99–112, 1996.

Wettlaufer, J., and M. G. Worster, Premelting dynamics, *Annu. Rev. Fluid Mech.*, *38*, 427–452, 2006.

Whitaker, S., Advances in theory of fluid motion in porous media, *Industrial & engineering chemistry*, *61*(12), 14–28, 1969.

Whitaker, S., *The method of volume averaging*, vol. 13, Springer, 1998.

Wiegmann, A., Computation of the permeability of porous materials from their microstructure by fff- stokes, *Fraunhofer ITWMKaiserslautern, Technical Report 129*, 2007.

Willis, J., Bounds and self-consistent estimates for the overall properties of anisotropic composites, *Journal of the Mechanics and Physics of Solids*, *25*(3), 185–202, 1977.

Yamaguchi, S., T. Katsushima, A. Sato, and T. Kumakura, Water retention curve of snow with different grain sizes, *Cold Reg. Sci. Technol.*, *64*(2), 87 – 93, doi:10.1016/j.coldregions.2010.05.008, 2010.

Yen, Y.-C., Review of the thermal properties of snow, ice and sea ice, *Tech. Rep. 81-10*, Cold Regions Research and Engineering Laboratory, Hanover, NH, 1981.

Yosida, Z., H. Oura, D. Kuroiwa, T. Huzioka, K. Kojima, S. Aoki, and S. Kinosita, Physical studies on deposited snow: I thermal properties, *Tech. Rep. 7*, Institute of Low Temperature Science, Hokkaido University, Sapporo, Japan, 1955.

Zermatten, E., S. Haussener, M. Schneebeli, and A. Steinfeld, Tomography-based determination of permeability and dupuit-forchheimer coefficient of characteristic snow samples, *J. Glaciol.*, *57*(205), 811–816, doi:10.3189/002214311798043799, 2011.

Zermatten, E., M. Schneebeli, H. Arakawa, and A. Steinfeld, Tomography-based determination of porosity, specific area and permeability of snow and comparison with measurements, *Cold Reg. Sci. Technol.*, *97*(0), 33 – 40, doi:10.1016/j.coldregions.2013.09.013, 2014.

Zhang, Y., J. Paik, A. Koschan, M. A. Abidi, and D. Gorsich, Simple and efficient algorithm for part decomposition of 3-D triangulated models based on curvature analysis, in *Proceedings of the 2002 International Conference on Image Processing*, vol. 3, pp. III–273–III–276, IEEE, 2002.

Appendix

A Appendix of Chapter 2

Appendix A1

Taking into account the order of magnitude of the dimensionless numbers in the Case 1, $\left[\mathrm{F}_i^T\right] = \mathcal{O}\left(\left[\mathrm{F}_a^T\right]\right) = \mathcal{O}\left([\mathrm{F}_a^\rho]\right) = \mathcal{O}(\varepsilon^2)$, $[\mathrm{K}] = \mathcal{O}\left(1\right), [\mathrm{H}] = \mathcal{O}\left(\varepsilon^2\right), [\mathrm{W}] = \mathcal{O}\left(\varepsilon^2\right)$, the dimensionless microscopic description (Equations (10)-(15) in the manuscript) becomes:

$$\varepsilon^2 \rho_i^* C_i^* \frac{\partial T_i^*}{\partial t^*} - \mathrm{div}^*(\kappa_i^* \mathbf{grad}^* T_i^*) = 0 \quad \text{in } \Omega_i \tag{A.1}$$

$$\varepsilon^2 \rho_a^* C_a^* \frac{\partial T_a^*}{\partial t^*} - \mathrm{div}^*(\kappa_a^* \mathbf{grad} T_a^*) = 0 \quad \text{in } \Omega_a \tag{A.2}$$

$$\varepsilon^2 \frac{\partial \rho_v^*}{\partial t^*} - \mathrm{div}^*(D_v^* \mathbf{grad}^* \rho_v^*) = 0 \quad \text{in } \Omega_a \tag{A.3}$$

$$T_i^* = T_a^* \quad \text{on } \Gamma \tag{A.4}$$

$$\kappa_i^* \mathbf{grad}^* T_i^* \cdot \mathbf{n_i} - \kappa_a^* \mathbf{grad}^* T_a^* \cdot \mathbf{n_i} = \varepsilon^2 L_{sg}^* \mathbf{w}^* \cdot \mathbf{n_i} \quad \text{on } \Gamma \tag{A.5}$$

$$D_v^* \mathbf{grad}^* \rho_v^* \cdot \mathbf{n_i} = \varepsilon^2 \rho_i^* \mathbf{w}^* \cdot \mathbf{n_i} \quad \text{on } \Gamma. \tag{A.6}$$

This set of equations is completed by the Hertz-Knudsen equation and the Clausius Clapeyron's law (Equation (8) and (9) in the manuscript) expressed in dimensionless form as:

$$w_n^* = \mathbf{w}^* \cdot \mathbf{n_i} = \frac{1}{\beta^*}\left[\frac{\rho_v^* - \rho_{vs}^*(T_a^*)}{\rho_{vs}^*(T_a^*)} - d_0^* K^*\right] \quad \text{on } \Gamma \tag{A.7}$$

$$\rho_{vs}^*(T_a^*) = \rho_{vs}^{\mathrm{ref}*}(T^{\mathrm{ref}*}) \exp\left[\frac{L_{sg}^* m^*}{\rho_i^* k^*}\left(\frac{1}{T^{\mathrm{ref}*}} - \frac{1}{T_a^*}\right)\right] \tag{A.8}$$

Heat transfer

Introducing asymptotic expansions for T_i^* and T_a^* in the relations (A.1, A.2, A.4, A.5) give at the lowest order:

$$\mathrm{div}_{y^*}(\kappa_i^* \mathbf{grad}_{y^*} T_i^{*(0)}) = 0 \quad \text{in } \Omega_i \tag{A.9}$$

$$\mathrm{div}_{y^*}(\kappa_a^* \mathbf{grad}_{y^*} T_a^{*(0)}) = 0 \quad \text{in } \Omega_a \tag{A.10}$$

$$T_i^{*(0)} = T_a^{*(0)} \quad \text{on } \Gamma \tag{A.11}$$

$$(\kappa_i^* \mathbf{grad}_{y^*} T_i^{*(0)} - \kappa_a^* \mathbf{grad}_{y^*} T_a^{*(0)}) \cdot \mathbf{n_i} = 0 \quad \text{on } \Gamma \tag{A.12}$$

where the unknowns $T_i^{*(0)}(\mathbf{x}^*, \mathbf{y}^*, t)$ and $T_a^{*(0)}(\mathbf{x}^*, \mathbf{y}^*, t)$ are $\mathbf{y}^*$-periodic. It can be shown [*Auriault et al.*, 2009] that the obvious solution of the above boundary value problem is given by:

$$T_i^{*(0)} = T_a^{*(0)} = T^{*(0)}(\mathbf{x}^*, t). \tag{A.13}$$

At the first order, the temperature is independent of the microscopic dimensionless variable $\mathbf{y}^*$, i.e. we have only one temperature field. Taking into account these results, equations (A.1, A.2, A.4, A.5) of order ε give the following second-order problem:

$$\mathrm{div}_{y^*}(\kappa_i^*(\mathbf{grad}_{y^*} T_i^{*(1)} + \mathbf{grad}_{x^*} T^{*(0)})) = 0 \quad \text{in } \Omega_i \tag{A.14}$$

$$\mathrm{div}_{y^*}(\kappa_a^*(\mathbf{grad}_{y^*} T_a^{*(1)} + \mathbf{grad}_{x^*} T^{*(0)})) = 0 \quad \text{in } \Omega_a \tag{A.15}$$

$$T_i^{*(1)} = T_a^{*(1)} \quad \text{on } \Gamma \tag{A.16}$$

$$(\kappa_i^*(\mathbf{grad}_{y^*} T_i^{*(1)} + \mathbf{grad}_{x^*} T^{*(0)}) - \kappa_a^*(\mathbf{grad}_{y^*} T_a^{*(1)} + \mathbf{grad}_{x^*} T^{*(0)})) \cdot \mathbf{n_i} = 0 \quad \text{on } \Gamma \tag{A.17}$$

where the unknowns $T_i^{*(1)}(\mathbf{x}^*, \mathbf{y}^*, t)$ and $T_a^{*(1)}(\mathbf{x}^*, \mathbf{y}^*, t)$ are $\mathbf{y}^*$-periodic and the macroscopic gradient $\mathbf{grad}_{x^*} T^{*(0)}$ is given. The solution of the above boundary value problem appears as a linear function of the macroscopic gradient, modulo an arbitrary function $\widetilde{T}^{*(1)}(\mathbf{x}^*, t)$ [*Auriault et al.*, 2009]:

$$T_i^{*(1)}(\mathbf{x}^*, \mathbf{y}^*, t) = \mathbf{t}_i^*(\mathbf{y}^*) \cdot \mathbf{grad}_{x^*} T^{*(0)} + \widetilde{T}_i^{*(1)} \tag{A.18}$$

$$T_a^{*(1)}(\mathbf{x}^*, \mathbf{y}^*, t) = \mathbf{t}_a^*(\mathbf{y}^*) \cdot \mathbf{grad}_{x^*} T^{*(0)} + \widetilde{T}_a^{*(1)} \tag{A.19}$$

where $\mathbf{t}_i^*(\mathbf{y}^*)$ and $\mathbf{t}_a^*(\mathbf{y}^*)$ are two periodic vectors which characterize the fluctuation of temperature in both phases at the pore scale. Introducing (A.18) and (A.19) in the set (A.14)-(A.17), these two vectors are solution of the following boundary value problem in a compact form:

$$\mathrm{div}_{y^*}(\kappa_i^*(\mathbf{grad}_{y^*} \mathbf{t}_i^* + \mathbf{I})) = 0 \quad \text{in } \Omega_i \tag{A.20}$$

$$\mathrm{div}_{y^*}(\kappa_a^*(\mathbf{grad}_{y^*} \mathbf{t}_a^* + \mathbf{I})) = 0 \quad \text{in } \Omega_a \tag{A.21}$$

$$\mathbf{t}_i^* = \mathbf{t}_a^* \quad \text{on } \Gamma \tag{A.22}$$

$$(\kappa_i^*(\mathbf{grad}_{y^*} \mathbf{t}_i^* + \mathbf{I}) - \kappa_a^*(\mathbf{grad}_{y^*} \mathbf{t}_a^* + \mathbf{I})) \cdot \mathbf{n_i} = 0 \quad \text{on } \Gamma \tag{A.23}$$

$$\frac{1}{|\Omega|} \int_\Omega (\mathbf{t}_\mathrm{a}^* + \mathbf{t}_\mathrm{i}^*) \mathrm{d}\Omega = \mathbf{0} \tag{A.24}$$

This latter equation is introduced to ensure the uniqueness of the solution. Finally, the third order problem is given by the equations (A.1, A.2, A.4, A.5) of order ε^2:

$$\begin{aligned} \rho_i^* C_i^* \frac{\partial T^{*(0)}}{\partial t^*} - \mathrm{div}_{y^*}(\kappa_i^*(\mathbf{grad}_{y^*} T_i^{*(2)} + \mathbf{grad}_{x^*} T_i^{*(1)})) \\ -\mathrm{div}_{x^*}(\kappa_i^*(\mathbf{grad}_{y^*} T_i^{*(1)} + \mathbf{grad}_{x^*} T^{*(0)})) = 0 \quad \text{in } \Omega_i \\ \rho_a^* C_a^* \frac{\partial T^{*(0)}}{\partial t^*} - \mathrm{div}_{y^*}(\kappa_a^*(\mathbf{grad}_{y^*} T_a^{*(2)} + \mathbf{grad}_{x^*} T_a^{*(1)})) \end{aligned} \tag{A.25}$$

$$-\mathrm{div}_{x^*}(\kappa_a^*(\mathbf{grad}_{y^*}T_a^{*(1)} + \mathbf{grad}_{x^*}T^{*(0)})) = 0 \quad \text{in } \Omega_a \tag{A.26}$$

$$T_i^{*(2)} = T_a^{*(2)} \quad \text{on } \Gamma \tag{A.27}$$

$$(\kappa_i^*(\mathbf{grad}_{y^*}T_i^{*(2)} + \mathbf{grad}_{x^*}T_i^{*(1)}) - \kappa_a^*(\mathbf{grad}_{y^*}T_a^{*(2)} + \mathbf{grad}_{x^*}T_a^{*(1)})) \cdot \mathbf{n_i} = L_{sg}^* w_n^{*(0)} \quad \text{on } \Gamma \tag{A.28}$$

where the unknowns $T_i^{*(2)}(\mathbf{x}^*, \mathbf{y}^*, t)$ and $T_a^{*(2)}(\mathbf{x}^*, \mathbf{y}^*, t)$ are $\mathbf{y}^*$-periodic and $w_n^{*(0)}(\mathbf{x}^*, \mathbf{y}^*, t)$ is the normal interface velocity at the zero order due to the phase change given by the Hertz-Knudsen equation (A.7) and the Clausius Clapeyron's law (A.8).

Water vapor transfer

Introducing asymptotic expansions for ρ_v^* in the relations (A.3, A.6) give at the lowest order

$$\mathrm{div}_{y^*}(D_v^* \mathbf{grad}_{y^*}\rho_v^{*(0)}) = 0 \quad \text{in } \Omega_a \tag{A.29}$$

$$D_v^* \mathbf{grad}_{y^*}\rho_v^{*(0)} \cdot \mathbf{n_i} = 0 \quad \text{on } \Gamma. \tag{A.30}$$

where the unknown $\rho_v^{*(0)}(\mathbf{x}^*, \mathbf{y}^*, t)$ is $\mathbf{y}^*$-periodic. It can be shown[*Auriault et al.*, 2009] that the solution of the above boundary value problem is given by:

$$\rho_v^{*(0)} = \rho_v^{*(0)}(\mathbf{x}^*, t). \tag{A.31}$$

At the first order, the water vapor density is independent of the microscopic dimensionless variable $\mathbf{y}^*$. Taking into account these results, the second-order problem is given by the equations (A.3, A.6) of order ε:

$$\mathrm{div}_{y^*}(D_v^*(\mathbf{grad}_{y^*}\rho_v^{*(1)} + \mathbf{grad}_{x^*}\rho_v^{*(0)})) = 0 \quad \text{in } \Omega_a \tag{A.32}$$

$$D_v^*(\mathbf{grad}_{y^*}\rho_v^{*(1)} + \mathbf{grad}_{x^*}\rho_v^{*(0)}) \cdot \mathbf{n_i} = 0 \quad \text{on } \Gamma. \tag{A.33}$$

where the unknown $\rho_v^{*(1)}(\mathbf{x}^*, \mathbf{y}^*, t)$ is $\mathbf{y}^*$-periodic and the macroscopic gradient $\mathbf{grad}_{x^*}\rho_v^{*(0)}$ is given. The solution of the above boundary value problem appears as a linear function of the macroscopic gradient, modulo an arbitrary function $\widetilde{\rho}_v^{*(1)}(\mathbf{x}^*, t)$ [*Auriault et al.*, 2009]:

$$\rho_v^{*(1)}(\mathbf{x}^*, \mathbf{y}^*, t) = \mathbf{g}_v^*(\mathbf{y}^*) \cdot \mathbf{grad}_{x^*}\rho_v^{*(0)} + \widetilde{\rho}_v^{*(1)}(\mathbf{x}^*, t) \tag{A.34}$$

where $\mathbf{g}_v^*(\mathbf{y}^*)$ is a periodic vector which characterizes the fluctuation of water vapor density in the air phase at the pore scale. Introducing (A.34) in the set (A.32)-(A.33), this vector is solution of the following boundary value problem in a compact form:

$$\mathrm{div}_{y^*}(D_v^*(\mathbf{grad}_{y^*}\mathbf{g}_v^* + \mathbf{I})) = 0 \quad \text{in } \Omega_a \tag{A.35}$$

$$D_v^*(\mathbf{grad}_{y^*}\mathbf{g}_v^* + \mathbf{I}) \cdot \mathbf{n_i} = 0 \quad \text{on } \Gamma \tag{A.36}$$

$$\frac{1}{|\Omega|}\int_{\Omega_a} \mathbf{g}_v^* \mathrm{d}\Omega = \mathbf{0} \tag{A.37}$$

This latter equation is introduced to ensure the uniqueness of the solution. Finally, the third order problem is given by the equations (A.3, A.6) of order ε^2:

$$\frac{\partial \rho_v^{*(0)}}{\partial t^*} - \mathrm{div}_{y^*}(D_v^*(\mathbf{grad}_{y^*}\rho_v^{*(2)} + \mathbf{grad}_{x^*}\rho_v^{*(2)}))$$

$$-\mathrm{div}_{x^*}(D_v^*(\mathbf{grad}_{y^*}\rho_v^{*(1)} + \mathbf{grad}_{x^*}\rho_v^{*(1)})) = 0 \quad \text{in } \Omega_i \tag{A.38}$$

$$D_v^*(\mathbf{grad}_{y^*}\rho_v^{*(2)} + \mathbf{grad}_{x^*}\rho_v^{*(2)}) \cdot \mathbf{n_i} = \rho_i^* w_n^{*(0)} \quad \text{on } \Gamma \tag{A.39}$$

where the unknown $\rho_v^{*(2)}(\mathbf{x}^*, \mathbf{y}^*, t)$ is $\mathbf{y}^*$-periodic and $w_n^{*(0)}(\mathbf{x}^*, \mathbf{y}^*, t)$ is the normal interface velocity due to the phase change at the zero order given by the Hertz-Knudsen equation (A.7) and the Clausius Clapeyron's law (A.8).

Expression of $w_n^{*(0)}$

Introducing the asymptotic development of T_a^* in the Clausius Clapeyron's law, we get:

$$\rho_{vs}^*(T_a^*) = \rho_{vs}^{\mathrm{ref}*}(T^{\mathrm{ref}*}) \exp\left[\frac{L_{sg}^* m^*}{\rho_i^* k^*}\left(\frac{1}{T^{\mathrm{ref}*}} - \frac{1}{(T^{*(0)} + \varepsilon T_a^{*(1)} + ...)}\right)\right] \tag{A.40}$$

which can be put in the form:

$$\rho_{vs}^*(T_a^*) = \rho_{vs}^{\mathrm{ref}*}(T^{\mathrm{ref}*}) \exp\left[\frac{L_{sg}^* m^*}{\rho_i^* k^*}\left(\frac{1}{T^{\mathrm{ref}*}} - \frac{1}{T^{*(0)}}\right)\right]\left(1 + \varepsilon \frac{L_{sg}^* m^*}{\rho_i^* k^*} \frac{T_a^{*(1)}}{(T^{*(0)})^2} + ...\right) \tag{A.41}$$

This relation shows that the asymptotic development of the Clausius-Clapeyron's law is written:

$$\rho_{vs}^*(T_a^*) = \rho_{vs}^{*(0)}(\mathbf{x}^*, t) + \varepsilon \rho_{vs}^{*(1)}(\mathbf{x}^*, \mathbf{y}^*, t) + ... \tag{A.42}$$

where the first term $\rho_{vs}^{*(0)}$, which depends on $T^{*(0)}(\mathbf{x}^*, t)$ only, is defined as:

$$\rho_{vs}^{*(0)}(T^{*(0)}) = \rho_{vs}^{\mathrm{ref}*}(T^{\mathrm{ref}*}) \exp\left[\frac{L_{sg}^* m^*}{\rho_i^* k^*}\left(\frac{1}{T^{\mathrm{ref}*}} - \frac{1}{T^{*(0)}}\right)\right] \tag{A.43}$$

Introducing the asymptotic development of ρ_v^* and ρ_{vs}^* (see Eq.A.42) in the Hertz-Knudsen equation (A.7), we get:

$$w_n^* = \mathbf{w}^* \cdot \mathbf{n_i} = \frac{1}{\beta^*}\left[\left(\frac{\rho_v^{*(0)} + \varepsilon \rho_v^{*(1)} + ...}{\rho_{vs}^{*(0)} + \varepsilon \rho_{vs}^{*(1)} + ...} - 1\right) - d_0^* K^*\right] \tag{A.44}$$

which can be also put in the form:

$$w_n^* = \mathbf{w}^* \cdot \mathbf{n_i} = \frac{1}{\beta^*}\left[\left(\frac{\rho_v^{*(0)}}{\rho_{vs}^{*(0)}} + \varepsilon\, \frac{\rho_v^{*(1)}\rho_{vs}^{*(0)} - \varepsilon \rho_v^{*(0)}\rho_{vs}^{*(1)}}{(\rho_{vs}^{*(0)})^2} + ... - 1\right) - d_0^* K^*\right] \tag{A.45}$$

This relation shows that the asymptotic development of the Hertz-Knudsen equation is written:

$$w_n^* = \mathbf{w}^* \cdot \mathbf{n_i} = w_n^{*(0)}(\mathbf{x}^*, t) + \varepsilon w_n^{*(1)}(\mathbf{x}^*, \mathbf{y}^*, t) + ... \tag{A.46}$$

where the first term $w_n^{*(0)}$ is written:

$$w_n^{*(0)} = \frac{1}{\beta^*}\left[\frac{\rho_v^{*(0)} - \rho_{vs}^{*(0)}(T^{*(0)})}{\rho_{vs}^{*(0)}(T^{*(0)})} - d_0^* K^*\right] \tag{A.47}$$

The relations (A.47) and (A.43) show that the normal velocity $w_n^{*(0)}$ arising in the boundary conditions (A.28) and (A.39) does not depend on $\mathbf{y}^*$.

Macroscopic equivalent description

Consequently, integrating (A.25) over Ω_i and (A.26) over Ω_a, and then using the divergence theorem, the periodicity condition, and the boundary conditions (A.28) lead to the first order dimensionless macroscopic description for the heat transfer:

$$(\rho C)^{\text{eff}*}\frac{\partial T^{*(0)}}{\partial t^*} - \text{div}_{x^*}(\mathbf{k}^{\text{eff}*}\mathbf{grad}_{x^*}\ T^{*(0)}) = -\text{SSA}_V L^*_{sg} w_n^{*(0)} \tag{A.48}$$

where $\text{SSA}_\text{V} = |\Gamma|/|\Omega|$ is the specific surface area, $(\rho C)^{\text{eff}*}$ and $\mathbf{k}^{\text{eff}*}$ are the dimensionless effective thermal capacity and the effective dimensionless conductivity respectively, defined as:

$$(\rho C)^{\text{eff}*} = (1-\phi)\rho_i^* C_i^* + \phi\rho_a^* C_a^* \tag{A.49}$$

$$\mathbf{k}^{\text{eff}*} = \frac{1}{|\Omega|}\left(\int_{\Omega_\text{a}} \kappa_a^*(\mathbf{grad}_{y^*}\mathbf{t}_a^*(\mathbf{y}^*) + \mathbf{I})\text{d}\Omega + \int_{\Omega_\text{i}} \kappa_i^*(\mathbf{grad}_{y^*}\mathbf{t}_i^*(\mathbf{y}^*) + \mathbf{I})\text{d}\Omega\right) \tag{A.50}$$

where ϕ is the porosity. Similarly, integrating (A.38) over Ω_a, and then using the divergence theorem, the periodicity condition, and the boundary conditions (A.39) lead to the first order dimensionless macroscopic description for the water vapor transfer:

$$\phi\frac{\partial \rho_v^{*(0)}}{\partial t} - \text{div}_{x^*}(\mathbf{D}^{\text{eff}*}\mathbf{grad}_{x^*}\rho_v^{*(0)}) = -\text{SSA}_V \rho_i^* w_n^{*(0)} \tag{A.51}$$

where $\text{SSA}_\text{V} = |\Gamma|/|\Omega|$ is the surface area and $\mathbf{D}^{\text{eff}*}$ is the dimensionless effective diffusion tensor defined as:

$$\mathbf{D}^{\text{eff}*} = \frac{1}{|\Omega|}\int_{\Omega_a} D_v^*(\mathbf{grad}_{y^*}\ \mathbf{g}_v^*(\mathbf{y}^*) + \mathbf{I})\text{d}\Omega \tag{A.52}$$

Appendix A2

Table A.1: Normalized values of the x, y and z components of the effective vapor diffusion tensor $\mathbf{D}^{\text{eff}}$ computed on 35 3D images of snow [*Calonne et al.*, 2011, 2012, 2014a], together with snow type and density.

Image	Type	Density ($\mathrm{kg\,m^{-1}}$)	D_x^{eff}/D_v	D_y^{eff}/D_v	D_z^{eff}/D_v
Fr	PP	124.9	7.27e-01	7.34e-01	7.07e-01
I01	PP	102.9	7.54e-01	7.63e-01	7.47e-01
I03	PP	123.3	7.27e-01	7.42e-01	7.38e-01
I04	PP	113.4	7.70e-01	7.65e-01	7.54e-01
I08	DF	147.7	7.39e-01	7.23e-01	7.20e-01
I15	RG	172.7	7.01e-01	7.06e-01	6.97e-01
I19	RG	192.5	6.72e-01	6.77e-01	6.68e-01
I21	RG	198.6	6.67e-01	6.74e-01	6.50e-01
I23	RG	256.3	5.89e-01	5.81e-01	5.67e-01
P03	PP	134.6	7.49e-01	7.49e-01	7.22e-01
P04	DF	157.6	7.27e-01	7.40e-01	6.59e-01
P06	RG	354.5	4.47e-01	4.53e-01	4.28e-01
P07	RG	280.1	5.58e-01	5.59e-01	4.79e-01
P08	RG	379.0	4.21e-01	4.23e-01	3.80e-01
P09	RG	396.1	3.93e-01	4.03e-01	3.55e-01
P10	RG	396.1	3.94e-01	3.93e-01	3.73e-01
P11	RG	413.7	3.74e-01	3.72e-01	3.50e-01
P14	RG	359.8	4.40e-01	4.38e-01	4.25e-01
P15	RG	315.5	5.06e-01	4.70e-01	4.99e-01
0A	RG	314.8	4.80e-01	4.88e-01	4.68e-01
1A	FC	275.0	5.39e-01	5.42e-01	5.31e-01
2A	DH	282.7	5.06e-01	5.10e-01	5.25e-01
3A	DH	274.8	5.00e-01	5.00e-01	5.29e-01
4A	DH	315.3	4.30e-01	4.28e-01	4.77e-01
5A-G	DH	286.1	4.59e-01	4.59e-01	5.09e-01
7A-G	DH	309.9	4.15e-01	4.15e-01	4.70e-01
E2b	DH	262.7	5.50e-01	5.42e-01	5.66e-01
grad3	DH	369.2	2.92e-01	2.87e-01	3.72e-01
H00	RG	430.6	3.50e-01	3.48e-01	3.41e-01
H01	MF	544.1	1.82e-01	1.64e-01	1.74e-01
H1-2	MF	512.9	2.39e-01	2.37e-01	2.35e-01
H02	MF	502.6	2.46e-01	2.52e-01	2.60e-01
H03	MF	495.1	2.62e-01	2.61e-01	2.56e-01
H05-G	MF	472.8	2.75e-01	2.79e-01	2.91e-01
Chamair	MF	522.3	2.41e-01	2.30e-01	2.30e-01

Appendix

B Appendix of Chapter 3

Asymptotic analysis: Case B1

Taking into account the order of magnitude of the dimensionless numbers in the Case B1, $\left[\mathrm{F_i^T}\right] = \mathcal{O}\left(\left[\mathrm{F_a^T}\right]\right) = \mathcal{O}\left([\mathrm{F_a^\rho}]\right) = \mathcal{O}(\varepsilon^2)$, $[\mathrm{Re}] = \mathcal{O}\left(\left[\mathrm{Pe^T}\right]\right) = \mathcal{O}\left([\mathrm{Pe^\rho}]\right) = \mathcal{O}(\varepsilon)$, $[\mathrm{Q}] = \mathcal{O}\left(\varepsilon^{-1}\right)$, $[\mathrm{N}] = \mathcal{O}\left(\varepsilon^{-1}\right)$, $[\mathrm{M}] = \mathcal{O}\left(\varepsilon^2\right)$, $[\mathrm{K}] = \mathcal{O}\left(1\right), [\mathrm{H}] = \mathcal{O}\left(\varepsilon^2\right), [\mathrm{W}] = \mathcal{O}\left(\varepsilon^2\right)$, the dimensionless microscopic description (Equations (**??**)-(2.17)) becomes:

$$\varepsilon\rho_a^*{\mathbf{v_a}}^*\,\mathbf{grad}^*\,{\mathbf{v_a}}^* = \mu_a^*\Delta^*{\mathbf{v_a}}^* - \varepsilon^{-1}\mathbf{grad}^*\,p_a^* \quad \text{in } \Omega_a \tag{B.1}$$

$$\mathrm{div}^*\,{\mathbf{v_a}}^* = 0 \quad \text{in } \Omega_a \tag{B.2}$$

$$\varepsilon^2\rho_i^*C_i^*\frac{\partial T_i^*}{\partial t^*} - \mathrm{div}^*(\kappa_i^*\mathbf{grad}^*T_i^*) = 0 \quad \text{in } \Omega_i \tag{B.3}$$

$$\varepsilon^2\rho_a^*C_a^*\frac{\partial T_a^*}{\partial t^*} + \varepsilon\rho_a^*C_a^*{\mathbf{v_a}}^*\cdot\mathbf{grad}^*\,T_a^* - \mathrm{div}^*(\kappa_a^*\mathbf{grad}^*T_a^*) = 0 \quad \text{in } \Omega_a \tag{B.4}$$

$$\varepsilon^2\frac{\partial \rho_v^*}{\partial t^*} + \varepsilon{\mathbf{v_a}}^*\cdot\mathbf{grad}^*\,\rho_v^* - \mathrm{div}^*(D_v^*\mathbf{grad}^*\rho_v^*) = 0 \quad \text{in } \Omega_a \tag{B.5}$$

$$T_i^* = T_a^* \quad \text{on } \Gamma \tag{B.6}$$

$${\mathbf{v_a}}^*\cdot\mathbf{t_i} = 0 \quad \text{on } \Gamma \tag{B.7}$$

$$\rho_a^*(\varepsilon^2\mathbf{w}^* - {\mathbf{v_a}}^*)\cdot\mathbf{n_i} = -\varepsilon\rho_i^*\mathbf{w}^*\cdot\mathbf{n_i} \quad \text{on } \Gamma \tag{B.8}$$

$$\kappa_i^*\mathbf{grad}^*T_i^*\cdot\mathbf{n_i} - \kappa_a^*\mathbf{grad}^*T_a^*\cdot\mathbf{n_i} = \varepsilon^2L_{sg}^*\mathbf{w}^*\cdot\mathbf{n_i} \quad \text{on } \Gamma \tag{B.9}$$

$$D_v^*\mathbf{grad}^*\rho_v^*\cdot\mathbf{n_i} = \varepsilon^2\rho_i^*\mathbf{w}^*\cdot\mathbf{n_i} \quad \text{on } \Gamma. \tag{B.10}$$

This set of equations is completed by the Hertz-Knudsen equation and the Clausius Clapeyron's law, Eq. (2.8) and (2.9), expressed in dimensionless form as:

$$w_n^* = \mathbf{w}^*\cdot\mathbf{n_i} = \frac{1}{\beta^*}\left[\frac{\rho_v^* - \rho_{vs}^*(T_a^*)}{\rho_{vs}^*(T_a^*)} - d_0^*K^*\right] \quad \text{on } \Gamma \tag{B.11}$$

$$\rho_{vs}^*(T_a^*) = \rho_{vs}^{\mathrm{ref}*}(T^{\mathrm{ref}*})\exp\left[\frac{L_{sg}^*m^*}{\rho_i^*k^*}\left(\frac{1}{T^{\mathrm{ref}*}} - \frac{1}{T_a^*}\right)\right] \tag{B.12}$$

Fluid flow

Introducing asymptotic expansions for $\mathbf{v}_a^*$ and p_a^* in the relations (B.1) give at the lowest order ε^{-1}:

$$\mathbf{grad}_{y^*}\, p_a^{*(0)} = 0 \quad \text{in } \Omega_a \tag{B.13}$$

where the unknown $p_a^{*(0)}(\mathbf{x}^*, \mathbf{y}^*)$ is $\mathbf{y}^*$-periodic. It can be shown [*Auriault et al.*, 2009] that this relation implies that:

$$p_a^{*(0)} = p_a^{*(0)}(\mathbf{x}^*). \tag{B.14}$$

At the first order, the pressure is independent of the microscopic dimensionless variable $\mathbf{y}^*$, i.e. constant over a period or REV. Taking into account these results, equations (B.1, B.2, B.7, B.8) of order ε^0 give the following second-order problem:

$$\mu_a^* \Delta_{y^*} {\mathbf{v_a}}^{*(0)} - \mathbf{grad}_{y^*}\, p_a^{*(1)} - \mathbf{grad}_{x^*}\, p_a^{*(0)} = 0 \quad \text{in } \Omega_a \tag{B.15}$$

$$\mathrm{div}_{y^*}\, {\mathbf{v_a}}^{*(0)} = 0 \quad \text{in } \Omega_a \tag{B.16}$$

$${\mathbf{v_a}}^{*(0)} \cdot \mathbf{t_i} = 0 \quad \text{on } \Gamma \tag{B.17}$$

$${\mathbf{v_a}}^{*(0)} \cdot \mathbf{n_i} = 0 \quad \text{on } \Gamma \tag{B.18}$$

where $\mathbf{v}_a^{*(1)}(\mathbf{x}^*, \mathbf{y}^*)$ and $p_a^{*(1)}(\mathbf{x}^*, \mathbf{y}^*)$ are the $\mathbf{y}^*$-periodic unknowns, which represent respectively the fluid velocity and the pressure fluctuation in a REV induced by a given macroscopic gradient of pressure $\mathbf{grad}_{x^*} p_a^{*(0)}$. It can be shown that ${\mathbf{v_a}}^{*(0)}$ and $p_a^{*(1)}$ are linear function of $\mathbf{grad}_{x^*} p_a^{*(0)}$, and $p_a^{*(1)}$ is expressed modulo an arbitrary function $\widetilde{p}_a^{*(1)}(\mathbf{x}^*)$ [*Auriault et al.*, 2009]:

$$p_a^{*(1)}(\mathbf{x}^*, \mathbf{y}^*) = \mathbf{b}^*(\mathbf{y}^*) \cdot \mathbf{grad}_{x^*} p_a^{*(0)} + \widetilde{p}_a^{*(1)}(\mathbf{x}^*) \tag{B.19}$$

$$\mathbf{v}_a^{*(0)}(\mathbf{x}^*, \mathbf{y}^*) = \mathbf{k}^*(\mathbf{y}^*) \cdot \mathbf{grad}_{x^*} p_a^{*(0)} \tag{B.20}$$

where $\mathbf{k}^*(\mathbf{y}^*)$ is a second order tensor and $\mathbf{b}^*(\mathbf{y}^*)$ is a y^*-periodic vector and average zero over the REV, $\langle \mathbf{b}^* \rangle = 0$. This latter condition ensure the uniqueness of $\mathbf{b}^*$. $\mathbf{b}^*$ characterizes the fluctuation of pressure at the pore scale induced by the macroscopic gradient. Introducing (B.19) and (B.20) in the set (B.15)-(B.17), the tensor $\mathbf{k}^*(\mathbf{y}^*)$ and vector $\mathbf{b}^*(\mathbf{y}^*)$ are solution of the following boundary value problem in a compact form:

$$\mu_a^* \Delta_{y^*} \mathbf{k}^* - \mathbf{grad}_{y^*}\, \mathbf{b}^* - \mathbf{I} = 0 \quad \text{in } \Omega_a \tag{B.21}$$

$$\mathbf{grad}_{y^*}\, \mathbf{k}^* = 0 \quad \text{in } \Omega_a \tag{B.22}$$

$$\mathbf{k}^* = 0 \quad \text{on } \Gamma \tag{B.23}$$

At the next order, equations (B.2, B.7, B.8) are written.

$$\mathrm{div}_{x^*}\, {\mathbf{v_a}}^{*(0)} + \mathrm{div}_{y^*}\, {\mathbf{v_a}}^{*(1)} = 0 \quad \text{in } \Omega_a \tag{B.24}$$

$${\mathbf{v_a}}^{*(1)} \cdot \mathbf{t_i} = 0 \quad \text{on } \Gamma \tag{B.25}$$

$$\rho_a^* {\mathbf{v_a}}^{*(1)} \cdot \mathbf{n_i} = -\rho_i^* \mathbf{w}^{*(0)} \cdot \mathbf{n_i} \quad \text{on } \Gamma \tag{B.26}$$

where the unknown $\mathbf{v}_a^{*(1)}(\mathbf{x}^*, \mathbf{y}^*)$ is $\mathbf{y}^*$-periodic. Integrating equation (B.24) over Ω_a and then using the divergence theorem, boundary condition (B.26) and the periodicity condition, the dimensionless macroscopic mass balance takes the form

$$\mathrm{div}_{x^*}(\langle \mathbf{v}_a^{*(0)} \rangle) + \left(1 - \frac{\rho_i^*}{\rho_a^*}\right) \mathrm{SSA}_V \; w_n^{*(0)} = 0 \tag{B.27}$$

where

$$\langle \mathbf{v}_a^{*(0)} \rangle = -\frac{\mathbf{K}^{\mathrm{eff}*}}{\mu_a^*} \mathbf{grad}_{x^*} \; p_a^{*(0)} \tag{B.28}$$

$$\mathbf{K}^{\mathrm{eff}*} = \frac{1}{|\Omega|} \int_{\Omega_\mathrm{a}} \mathbf{k} \, \mathrm{d}\Omega. \tag{B.29}$$

and $w_n^{*(0)}(\mathbf{x}^*, \mathbf{y}^*, t)$ is the normal interface velocity at the zero order due to the phase change given by the Hertz-Knudsen equation (B.67) and the Clausius Clapeyron's law (B.66).

Heat transfer

Introducing asymptotic expansions for T_i^* and T_a^* in the relations (B.3, B.4, B.6, B.9) give at the lowest order ε^0:

$$\mathrm{div}_{y^*}(\kappa_i^* \mathbf{grad}_{y^*} T_i^{*(0)}) = 0 \quad \text{in } \Omega_i \tag{B.30}$$

$$\mathrm{div}_{y^*}(\kappa_a^* \mathbf{grad}_{y^*} T_a^{*(0)}) = 0 \quad \text{in } \Omega_a \tag{B.31}$$

$$T_i^{*(0)} = T_a^{*(0)} \quad \text{on } \Gamma \tag{B.32}$$

$$(\kappa_i^* \mathbf{grad}_{y^*} T_i^{*(0)} - \kappa_a^* \mathbf{grad}_{y^*} T_a^{*(0)}) \cdot \mathbf{n_i} = 0 \quad \text{on } \Gamma \tag{B.33}$$

where the unknowns $T_i^{*(0)}(\mathbf{x}^*, \mathbf{y}^*, t)$ and $T_a^{*(0)}(\mathbf{x}^*, \mathbf{y}^*, t)$ are $\mathbf{y}^*$-periodic. It can be shown [*Auriault et al.*, 2009] that the obvious solution of the above boundary value problem is given by:

$$T_i^{*(0)} = T_a^{*(0)} = T^{*(0)}(\mathbf{x}^*, t). \tag{B.34}$$

At the first order, the temperature is independent of the microscopic dimensionless variable $\mathbf{y}^*$, i.e. we have only one temperature field. Taking into account these results, equations (B.3, B.4, B.6, B.9), of order ε give the following second-order problem:

$$\mathrm{div}_{y^*}(\kappa_i^*(\mathbf{grad}_{y^*} T_i^{*(1)} + \mathbf{grad}_{x^*} T^{*(0)})) = 0 \quad \text{in } \Omega_i \tag{B.35}$$

$$\mathrm{div}_{y^*}(\kappa_a^*(\mathbf{grad}_{y^*} T_a^{*(1)} + \mathbf{grad}_{x^*} T^{*(0)})) = 0 \quad \text{in } \Omega_a \tag{B.36}$$

$$T_i^{*(1)} = T_a^{*(1)} \quad \text{on } \Gamma \tag{B.37}$$

$$(\kappa_i^*(\mathbf{grad}_{y^*} T_i^{*(1)} + \mathbf{grad}_{x^*} T^{*(0)}) - \kappa_a^*(\mathbf{grad}_{y^*} T_a^{*(1)} + \mathbf{grad}_{x^*} T^{*(0)})) \cdot \mathbf{n_i} = 0 \quad \text{on } \Gamma \tag{B.38}$$

where the unknowns $T_i^{*(1)}(\mathbf{x}^*, \mathbf{y}^*, t)$ and $T_a^{*(1)}(\mathbf{x}^*, \mathbf{y}^*, t)$ are $\mathbf{y}^*$-periodic and the macroscopic gradient $\mathbf{grad}_{x^*} T^{*(0)}$ is given. The solution of the above boundary value problem appears as a linear function of the macroscopic gradient, modulo an arbitrary function $\widetilde{T}^{*(1)}(\mathbf{x}^*, t)$ [*Auriault et al.*, 2009]:

$$T_i^{*(1)}(\mathbf{x}^*, \mathbf{y}^*, t) = \mathbf{t}_i^*(\mathbf{y}^*) \cdot \mathbf{grad}_{x^*} T^{*(0)} + \widetilde{T}_i^{*(1)} \tag{B.39}$$

$$T_a^{*(1)}(\mathbf{x}^*,\mathbf{y}^*,t) = \mathbf{t}_a^*(\mathbf{y}^*)\cdot\mathbf{grad}_{x^*}T^{*(0)} + \widetilde{T}_a^{*(1)} \tag{B.40}$$

where $\mathbf{t}_i^*(\mathbf{y}^*)$ and $\mathbf{t}_a^*(\mathbf{y}^*)$ are two periodic vectors which characterize the fluctuation of temperature in both phases at the pore scale. Introducing (B.39) and (B.40) in the set (B.35)-(B.38), these two vectors are solution of the following boundary value problem in a compact form:

$$\mathrm{div}_{y^*}(\kappa_i^*(\mathbf{grad}_{y^*}\mathbf{t}_i^* + \mathbf{I})) = 0 \quad \text{in } \Omega_i \tag{B.41}$$

$$\mathrm{div}_{y^*}(\kappa_a^*(\mathbf{grad}_{y^*}\mathbf{t}_a^* + \mathbf{I})) = 0 \quad \text{in } \Omega_a \tag{B.42}$$

$$\mathbf{t}_i^* = \mathbf{t}_a^* \quad \text{on } \Gamma \tag{B.43}$$

$$(\kappa_i^*(\mathbf{grad}_{y^*}\mathbf{t}_i^* + \mathbf{I}) - \kappa_a^*(\mathbf{grad}_{y^*}\mathbf{t}_a^* + \mathbf{I}))\cdot\mathbf{n_i} = 0 \quad \text{on } \Gamma \tag{B.44}$$

$$\frac{1}{|\Omega|}\int_\Omega (\mathbf{t}_\mathrm{a}^* + \mathbf{t}_\mathrm{i}^*)\mathrm{d}\Omega = \mathbf{0} \tag{B.45}$$

This latter equation is introduced to ensure the uniqueness of the solution. Finally, the third order problem is given by the equations (B.3, B.4, B.6, B.9) of order ε^2:

$$\rho_i^* C_i^* \frac{\partial T^{*(0)}}{\partial t^*} - \mathrm{div}_{y^*}(\kappa_i^*(\mathbf{grad}_{y^*}T_i^{*(2)} + \mathbf{grad}_{x^*}T_i^{*(1)}))$$

$$-\mathrm{div}_{x^*}(\kappa_i^*(\mathbf{grad}_{y^*}T_i^{*(1)} + \mathbf{grad}_{x^*}T^{*(0)})) = 0 \quad \text{in } \Omega_i \tag{B.46}$$

$$\rho_a^* C_a^* \frac{\partial T^{*(0)}}{\partial t^*} + \rho_a^* C_a^* \mathbf{v}_a^{*(0)}\cdot(\mathbf{grad}_{x^*}T^{*(0)} + \mathbf{grad}_{y^*}T_a^{*(1)})$$

$$-\mathrm{div}_{y^*}(\kappa_a^*(\mathbf{grad}_{y^*}T_a^{*(2)} + \mathbf{grad}_{x^*}T_a^{*(1)})) - \mathrm{div}_{x^*}(\kappa_a^*(\mathbf{grad}_{y^*}T_a^{*(1)} + \mathbf{grad}_{x^*}T^{*(0)})) = 0 \quad \text{in } \Omega_a \tag{B.47}$$

$$T_i^{*(2)} = T_a^{*(2)} \quad \text{on } \Gamma \tag{B.48}$$

$$(\kappa_i^*(\mathbf{grad}_{y^*}T_i^{*(2)} + \mathbf{grad}_{x^*}T_i^{*(1)}) - \kappa_a^*(\mathbf{grad}_{y^*}T_a^{*(2)} + \mathbf{grad}_{x^*}T_a^{*(1)}))\cdot\mathbf{n_i} = L_{sg}^* w_n^{*(0)} \quad \text{on } \Gamma \tag{B.49}$$

where the unknowns $T_i^{*(2)}(\mathbf{x}^*,\mathbf{y}^*,t)$ and $T_a^{*(2)}(\mathbf{x}^*,\mathbf{y}^*,t)$ are $\mathbf{y}^*$-periodic, $\mathbf{v}_a^{*(0)}(\mathbf{x}^*,\mathbf{y}^*,t)$ is given by the equation (B.20) (and verifies the relations (B.16) and B.18) and $w_n^{*(0)}(\mathbf{x}^*,\mathbf{y}^*,t)$ is the normal interface velocity at the zero order due to the phase change given by the Hertz-Knudsen (B.67) and the Clausius Clapeyron's law (B.66). Consequently, integrating (B.46) over Ω_i and (B.47) over Ω_a, and then using the divergence theorem, the periodicity condition, and the boundary conditions (B.49) lead to the first order dimensionless macroscopic description for the heat transfer:

$$(\rho C)^{\mathrm{eff}*}\frac{\partial T^{*(0)}}{\partial t^*} + \rho_a^* C_a^* \langle \mathbf{v}_a^{*(0)}\rangle\cdot\mathbf{grad}_{x^*}T^{*(0)} - \mathrm{div}_{x^*}(\mathbf{k}^{\mathrm{eff}*}\mathbf{grad}_{x^*}\ T^{*(0)}) = \mathrm{SSA}_V L_{sg}^* w_n^{*(0)} \tag{B.50}$$

where $\mathrm{SSA_V} = |\Gamma|/|\Omega|$ is the specific surface area, $(\rho C)^{\mathrm{eff}*}$ and $\mathbf{k}^{\mathrm{eff}*}$ are the dimensionless effective thermal capacity and the effective dimensionless conductivity respectively, defined as:

$$(\rho C)^{\mathrm{eff}*} = (1-\phi)\rho_i^* C_i^* + \phi\rho_a^* C_a^* \tag{B.51}$$

$$\mathbf{k}^{\mathrm{eff}*} = \frac{1}{|\Omega|}\left(\int_{\Omega_\mathrm{a}} \kappa_a^*(\mathbf{grad}_{y^*}\mathbf{t}_a^*(\mathbf{y}^*) + \mathbf{I})\mathrm{d}\Omega + \int_{\Omega_\mathrm{i}} \kappa_i^*(\mathbf{grad}_{y^*}\mathbf{t}_i^*(\mathbf{y}^*) + \mathbf{I})\mathrm{d}\Omega\right) \tag{B.52}$$

where ϕ is the porosity.

Water vapor transfer

Introducing asymptotic expansions for ρ_v^* in the relations (B.5, B.10) give at the lowest order (ε^0)

$$\mathrm{div}_{y^*}(D_v^* \mathbf{grad}_{y^*} \rho_v^{*(0)}) = 0 \quad \text{in } \Omega_a \tag{B.53}$$

$$D_v^* \mathbf{grad}_{y^*} \rho_v^{*(0)} \cdot \mathbf{n_i} = 0 \quad \text{on } \Gamma. \tag{B.54}$$

where the unknown $\rho_v^{*(0)}(\mathbf{x}^*, \mathbf{y}^*, t)$ is $\mathbf{y}^*$-periodic. It can be shown [*Auriault et al.*, 2009] that the solution of the above boundary value problem is given by:

$$\rho_v^{*(0)} = \rho_v^{*(0)}(\mathbf{x}^*, t). \tag{B.55}$$

At the first order, the water vapor density is independent of the microscopic dimensionless variable $\mathbf{y}^*$. Taking into account these results, the second-order problem is given by the equations (B.5, B.10) of order ε:

$$\mathrm{div}_{y^*}(D_v^*(\mathbf{grad}_{y^*} \rho_v^{*(1)} + \mathbf{grad}_{x^*} \rho_v^{*(0)})) = 0 \quad \text{in } \Omega_a \tag{B.56}$$

$$D_v^*(\mathbf{grad}_{y^*} \rho_v^{*(1)} + \mathbf{grad}_{x^*} \rho_v^{*(0)}) \cdot \mathbf{n_i} = 0 \quad \text{on } \Gamma. \tag{B.57}$$

where the unknown $\rho_v^{*(1)}(\mathbf{x}^*, \mathbf{y}^*, t)$ is $\mathbf{y}^*$-periodic and the macroscopic gradient $\mathbf{grad}_{x^*} \rho_v^{*(0)}$ is given. The solution of the above boundary value problem appears as a linear function of the macroscopic gradient, modulo an arbitrary function $\widetilde{\rho}_v^{*(1)}(\mathbf{x}^*, t)$ [*Auriault et al.*, 2009]:

$$\rho_v^{*(1)}(\mathbf{x}^*, \mathbf{y}^*, t) = \mathbf{g}_v^*(\mathbf{y}^*) \cdot \mathbf{grad}_{x^*} \rho_v^{*(0)} + \widetilde{\rho}_v^{*(1)}(\mathbf{x}^*, t) \tag{B.58}$$

where $\mathbf{g}_v^*(\mathbf{y}^*)$ is a periodic vector which characterizes the fluctuation of water vapor density in the air phase at the pore scale. Introducing (B.58) in the set (B.56)-(B.57), this vector is solution of the following boundary value problem in a compact form:

$$\mathrm{div}_{y^*}(D_v^*(\mathbf{grad}_{y^*} \mathbf{g}_v^* + \mathbf{I})) = 0 \quad \text{in } \Omega_a \tag{B.59}$$

$$D_v^*(\mathbf{grad}_{y^*} \mathbf{g}_v^* + \mathbf{I}) \cdot \mathbf{n_i} = 0 \quad \text{on } \Gamma \tag{B.60}$$

$$\frac{1}{|\Omega|} \int_{\Omega_a} \mathbf{g}_v^* \mathrm{d}\Omega = \mathbf{0} \tag{B.61}$$

This latter equation is introduced to ensure the uniqueness of the solution. Finally, the third order problem is given by the equations (B.5, B.10) of order ε^2:

$$\frac{\partial \rho_v^{*(0)}}{\partial t^*} + \mathbf{v}_a^{*(0)} \cdot (\mathbf{grad}_{x^*} \rho_v^{*(0)} + \mathbf{grad}_{y^*} \rho_v^{*(1)}) - \mathrm{div}_{y^*}(D_v^*(\mathbf{grad}_{y^*} \rho_v^{*(2)} + \mathbf{grad}_{x^*} \rho_v^{*(2)}))$$

$$-\mathrm{div}_{x^*}(D_v^*(\mathbf{grad}_{y^*} \rho_v^{*(1)} + \mathbf{grad}_{x^*} \rho_v^{*(1)})) = 0 \quad \text{in } \Omega_i \tag{B.62}$$

$$D_v^*(\mathbf{grad}_{y^*} \rho_v^{*(2)} + \mathbf{grad}_{x^*} \rho_v^{*(2)}) \cdot \mathbf{n_i} = \rho_i^* w_n^{*(0)} \quad \text{on } \Gamma \tag{B.63}$$

where the unknown $\rho_v^{*(2)}(\mathbf{x}^*, \mathbf{y}^*, t)$ is $\mathbf{y}^*$-periodic, $\mathbf{v}_a^{*(0)}(\mathbf{x}^*, \mathbf{y}^*, t)$ is given by the equation (B.20) (and verifies the relations (B.16) and (B.18)) and and $w_n^{*(0)}(\mathbf{x}^*, \mathbf{y}^*, t)$ is the normal interface velocity due to the phase change at the zero order given by the Hertz-Knudsen equation (B.67) and the Clausius Clapeyron's law (B.66). Integrating (B.62) over Ω_a, and

then using the divergence theorem, the periodicity condition, and the boundary conditions (B.63) lead to the first order dimensionless macroscopic description for the water vapor transfer:

$$\phi\frac{\partial\rho_v^{*(0)}}{\partial t}+\langle\mathbf{v}_a^{*(0)}\rangle\cdot\mathbf{grad}_{x^*}\rho_v^{*(0)}-\mathrm{div}_{x^*}(\mathbf{D}^{*\mathrm{eff}}\mathbf{grad}_{x^*}\rho_v^{*(0)})=-\mathrm{SSA}_V\rho_i^*w_n^{*(0)} \tag{B.64}$$

where $\mathrm{SSA_V}=|\Gamma|/|\Omega|$ is the surface area and $\mathbf{D}^{*\mathrm{eff}}$ is the dimensionless effective diffusion tensor defined as:

$$\mathbf{D}^{\mathrm{eff}*}=\frac{1}{|\Omega|}\int_{\Omega_a}D_v^*(\mathbf{grad}_{y^*}\ \mathbf{g}_v^*(\mathbf{y}^*)+\mathbf{I})\mathrm{d}\Omega \tag{B.65}$$

Expression of $w_n^{*(0)}$

The asymptotic analysis for the the Clausius Clapeyron's law and the Hertz-Knudsen equation are presented in *Calonne et al.* [2014b]. They obtained

$$\rho_{vs}^{*(0)}(T^{*(0)})=\rho_{vs}^{\mathrm{ref}*}(T^{\mathrm{ref}*})\exp\left[\frac{L_{sg}^*m^*}{\rho_i^*k^*}\left(\frac{1}{T^{\mathrm{ref}*}}-\frac{1}{T^{*(0)}}\right)\right] \tag{B.66}$$

$$w_n^{*(0)}=\frac{1}{\beta^*}\left[\frac{\rho_v^{*(0)}-\rho_{vs}^{*(0)}(T^{*(0)})}{\rho_{vs}^{*(0)}(T^{*(0)})}-d_0^*K^*\right] \tag{B.67}$$

The relations (B.67) and (B.66) show that the normal velocity $w_n^{*(0)}$ arising in the boundary conditions (B.49) and (B.63) does not depend on $\mathbf{y}^*$.

Asymptotic analysis: Case C1

Taking into account the order of magnitude of the dimensionless numbers in the Case C1, $\left[\mathrm{F_i^T}\right]=\mathcal{O}\left(\left[\mathrm{F_a^T}\right]\right)=\mathcal{O}\left([\mathrm{F_a^\rho}]\right)=\mathcal{O}(\varepsilon)$, $[\mathrm{Re}]=\mathcal{O}\left(\left[\mathrm{Pe^T}\right]\right)=\mathcal{O}\left([\mathrm{Pe^\rho}]\right)=\mathcal{O}\left(1\right)$, $[\mathrm{Q}]=\mathcal{O}\left(\varepsilon^{-1}\right)$, $[\mathrm{N}]=\mathcal{O}\left(\varepsilon^{-1}\right)$, $[\mathrm{M}]=\mathcal{O}\left(\varepsilon^{3}\right)$, $[\mathrm{K}]=\mathcal{O}\left(1\right),[\mathrm{H}]=\mathcal{O}\left(\varepsilon^{2}\right),[\mathrm{W}]=\mathcal{O}\left(\varepsilon^{2}\right)$, the dimensionless microscopic description (Equations (**??**)-(2.17)) becomes:

$$\rho_a^*\mathbf{v_a}^*\,\mathbf{grad}^*\,\mathbf{v_a}^*=\mu_a^*\Delta^*\mathbf{v_a}^*-\varepsilon^{-1}\mathbf{grad}^*\,p_a^*\quad\text{in }\Omega_a \tag{C.1}$$

$$\mathrm{div}^*\,\mathbf{v_a}^*=0\quad\text{in }\Omega_a \tag{C.2}$$

$$\varepsilon^2\rho_i^*C_i^*\frac{\partial T_i^*}{\partial t^*}-\mathrm{div}^*(\kappa_i^*\mathbf{grad}^*T_i^*)=0\quad\text{in }\Omega_i \tag{C.3}$$

$$\varepsilon^2\rho_a^*C_a^*\frac{\partial T_a^*}{\partial t^*}+\rho_a^*C_a^*\mathbf{v_a}^*\cdot\mathbf{grad}^*\,T_a^*-\mathrm{div}^*(\kappa_a^*\mathbf{grad}^*T_a^*)=0\quad\text{in }\Omega_a \tag{C.4}$$

$$\varepsilon^2\frac{\partial\rho_v^*}{\partial t^*}+\mathbf{v_a}^*\cdot\mathbf{grad}^*\,\rho_v^*-\mathrm{div}^*(D_v^*\mathbf{grad}^*\rho_v^*)=0\quad\text{in }\Omega_a \tag{C.5}$$

$$T_i^*=T_a^*\quad\text{on }\Gamma \tag{C.6}$$

$$\mathbf{v_a}^*\cdot\mathbf{t_i}=0\quad\text{on }\Gamma \tag{C.7}$$

$$\rho_a^*(\varepsilon^2\mathbf{w}^*-\mathbf{v_a}^*)\cdot\mathbf{n_i}=-\varepsilon\rho_i^*\mathbf{w}^*\cdot\mathbf{n_i}\quad\text{on }\Gamma \tag{C.8}$$

$$\kappa_i^*\mathbf{grad}^*T_i^*\cdot\mathbf{n_i}-\kappa_a^*\mathbf{grad}^*T_a^*\cdot\mathbf{n_i}=\varepsilon^2L_{sg}^*\mathbf{w}^*\cdot\mathbf{n_i}\quad\text{on }\Gamma \tag{C.9}$$

$$D_v^* \mathbf{grad}^* \rho_v^* \cdot \mathbf{n_i} = \varepsilon^2 \rho_i^* \mathbf{w}^* \cdot \mathbf{n_i} \quad \text{on } \Gamma. \tag{C.10}$$

This set of equations is completed by the Hertz-Knudsen equation and the Clausius Clapeyron's law, Eq. (2.8) and (2.9), expressed in dimensionless form as:

$$w_n^* = \mathbf{w}^* \cdot \mathbf{n_i} = \frac{1}{\beta^*} \left[\frac{\rho_v^* - \rho_{vs}^*(T_a^*)}{\rho_{vs}^*(T_a^*)} - d_0^* K^* \right] \quad \text{on } \Gamma \tag{C.11}$$

$$\rho_{vs}^*(T_a^*) = \rho_{vs}^{\text{ref}*}(T^{\text{ref}*}) \exp \left[\frac{L_{sg}^* m^*}{\rho_i^* k^*} \left(\frac{1}{T^{\text{ref}*}} - \frac{1}{T_a^*} \right) \right] \tag{C.12}$$

Fluid flow

As in the case B1, introducing asymptotic expansions for $\mathbf{v}_a^*$ and p_a^* in the relations (C.1) give at the lowest order ε^{-1}:

$$\mathbf{grad}_{y^*} p_a^{*(0)} = 0 \quad \text{in } \Omega_a, \tag{C.13}$$

where the unknown $p_a^{*(0)}(\mathbf{x}^*, \mathbf{y}^*)$ is $\mathbf{y}^*$-periodic. It can be shown [*Auriault et al.*, 2009] that this relation implies that:

$$p_a^{*(0)} = p_a^{*(0)}(\mathbf{x}^*). \tag{C.14}$$

At the first order, the pressure is independent of the microscopic dimensionless variable $\mathbf{y}^*$, i.e. constant over a period or REV. Taking into account these results, equations (C.1, C.2, C.7, C.8) of order ε^0 give now the following second-order problem:

$$\mu_a^* \Delta_{y^*} {\mathbf{v_a}}^{*(0)} - \mathbf{grad}_{y^*} p_a^{*(1)} - \mathbf{grad}_{x^*} p_a^{*(0)} = \rho_a^* {\mathbf{v_a}}^{*(0)} \mathbf{grad}_{y^*}^* {\mathbf{v_a}}^{*(0)} \quad \text{in } \Omega_a \tag{C.15}$$

$$\text{div}_{y^*} {\mathbf{v_a}}^{*(0)} = 0 \quad \text{in } \Omega_a \tag{C.16}$$

$${\mathbf{v_a}}^{*(0)} \cdot \mathbf{t_i} = 0 \quad \text{on } \Gamma \tag{C.17}$$

$${\mathbf{v_a}}^{*(0)} \cdot \mathbf{n_i} = 0 \quad \text{on } \Gamma \tag{C.18}$$

where $\mathbf{v}_a^{*(1)}(\mathbf{x}^*, \mathbf{y}^*)$ and $p_a^{*(1)}(\mathbf{x}^*, \mathbf{y}^*)$ are the $\mathbf{y}^*$-periodic unknowns. By contrast to the Case B1, the equation (C.15) is strongly non linear. Consequently, ${\mathbf{v_a}}^{*(0)}$ appears as non linear function $\mathbf{f}$ of the macroscopic pressure gradient $\mathbf{grad}_{x^*} p_a^{*(0)}$, of $\mathbf{y}^*$ and the fluid properties (ρ_a^* μ_a^*) , (see [*Auriault et al.*, 2009] and references here in for more details):

$$\mathbf{v}_a^{*(0)}(\mathbf{x}^*, \mathbf{y}^*) = -\mathbf{f}(\mathbf{grad}_{x^*} p_a^{*(0)}, \mathbf{y}^*, \rho_a^*, \mu_a^*) \tag{C.19}$$

A similar relation stands for the pressure $p_a^{*(1)}(\mathbf{x}^*, \mathbf{y}^*)$. At the next order, equations (C.2, C.7, C.8) are written.

$$\text{div}_{x^*} {\mathbf{v_a}}^{*(0)} + \text{div}_{y^*} {\mathbf{v_a}}^{*(1)} = 0 \quad \text{in } \Omega_a \tag{C.20}$$

$${\mathbf{v_a}}^{*(1)} \cdot \mathbf{t_i} = 0 \quad \text{on } \Gamma \tag{C.21}$$

$${\mathbf{v_a}}^{*(1)} \cdot \mathbf{n_i} = 0 \quad \text{on } \Gamma \tag{C.22}$$

where the unknown $\mathbf{v}_a^{*(1)}(\mathbf{x}^*, \mathbf{y}^*)$ is $\mathbf{y}^*$-periodic. Let us remark that the equation (C.22) does not present a left term as in the case B1, since now $[\mathrm{M}] = \mathcal{O}(\varepsilon^3)$. As in the Case

B1, integrating equation (C.20) over Ω_a and then using the divergence theorem, boundary condition (C.22) and the periodicity condition, the dimensionless macroscopic mass balance takes the form

$$\mathrm{div}_{x^*}(\langle \mathbf{v}_a^{*(0)} \rangle) = 0 \tag{C.23}$$

where the dimensionless macroscopic flow law is written:

$$\langle \mathbf{v}_a^{*(0)} \rangle = -\frac{1}{|\Omega|} \int_{\Omega_a} \mathbf{f}(\mathbf{grad}_{x^*} p_a^{*(0)}, \mathbf{y}^*, \rho_a^*, \mu_a^*), \mathrm{d}\Omega = -\mathbf{F}(\mathbf{grad}_{x^*} p_a^{*(0)}, \text{microstructure}, \rho_a^*, \mu_a^*) \tag{C.24}$$

Heat transfer

Introducing asymptotic expansions for T_i^* and T_a^* in the relations (C.3, C.4, C.6, C.9) give at the lowest order ε^0:

$$\mathrm{div}_{y^*}(\kappa_i^* \mathbf{grad}_{y^*} T_i^{*(0)}) = 0 \quad \text{in } \Omega_i \tag{C.25}$$

$$\rho_a^* C_a^* \mathbf{v}_a^{*(0)} \cdot \mathbf{grad}_{y^*} T^{*(0)} - \mathrm{div}_{y^*}(\kappa_a^* \mathbf{grad}_{y^*} T_a^{*(0)}) = 0 \quad \text{in } \Omega_a \tag{C.26}$$

$$T_i^{*(0)} = T_a^{*(0)} \quad \text{on } \Gamma \tag{C.27}$$

$$(\kappa_i^* \mathbf{grad}_{y^*} T_i^{*(0)} - \kappa_a^* \mathbf{grad}_{y^*} T_a^{*(0)}) \cdot \mathbf{n_i} = 0 \quad \text{on } \Gamma \tag{C.28}$$

where the unknowns $T_i^{*(0)}(\mathbf{x}^*, \mathbf{y}^*, t)$ and $T_a^{*(0)}(\mathbf{x}^*, \mathbf{y}^*, t)$ are $\mathbf{y}^*$-periodic. It can be shown [*Auriault et al.*, 2009; *Geindreau and Auriault*, 2002] that the solution of the above boundary value problem is given by:

$$T_i^{*(0)} = T_a^{*(0)} = T^{*(0)}(\mathbf{x}^*, t). \tag{C.29}$$

At the first order, the temperature is independent of the microscopic dimensionless variable $\mathbf{y}^*$, i.e. we have only one temperature field. Taking into account these results, equations (C.3, C.4, C.6, C.9), of order ε give the following second-order problem:

$$\rho_i^* C_i^* \frac{\partial T^{*(0)}}{\partial t^*} - \mathrm{div}_{y^*}(\kappa_i^*(\mathbf{grad}_{y^*} T_i^{*(1)} + \mathbf{grad}_{x^*} T^{*(0)})) = 0 \quad \text{in } \Omega_i \tag{C.30}$$

$$\begin{aligned} &\rho_a^* C_a^* \frac{\partial T^{*(0)}}{\partial t^*} + \rho_a^* C_a^* \mathbf{v}_a^{*(0)} \cdot (\mathbf{grad}_{x^*} T^{*(0)} + \mathbf{grad}_{y^*} T_a^{*(1)}) \\ &-\mathrm{div}_{y^*}(\kappa_a^*(\mathbf{grad}_{y^*} T_a^{*(1)} + \mathbf{grad}_{x^*} T^{*(0)})) = 0 \quad \text{in } \Omega_a \end{aligned} \tag{C.31}$$

$$T_i^{*(1)} = T_a^{*(1)} \quad \text{on } \Gamma \tag{C.32}$$

$$(\kappa_i^*(\mathbf{grad}_{y^*} T_i^{*(1)} + \mathbf{grad}_{x^*} T^{*(0)}) - \kappa_a^*(\mathbf{grad}_{y^*} T_a^{*(1)} + \mathbf{grad}_{x^*} T^{*(0)})) \cdot \mathbf{n_i} = 0 \quad \text{on } \Gamma \tag{C.33}$$

where the unknowns $T_i^{*(1)}(\mathbf{x}^*, \mathbf{y}^*, t)$ and $T_a^{*(1)}(\mathbf{x}^*, \mathbf{y}^*, t)$ are $\mathbf{y}^*$-periodic and the macroscopic gradient $\mathbf{grad}_{x^*} T^{*(0)}$ is given. $\mathbf{v}_a^{*(0)}$ is given by the relation (C.19). Integrating (C.30) over Ω_i and (C.31) over Ω_a and taking into account the condition of periodicity, the boundary condition (C.33) and the relation (C.19), we obtain the following first order macroscopic description:

$$(\rho C)^{\mathrm{eff}*} \frac{\partial T^{*(0)}}{\partial t^*} + \rho_a^* C_a^* \langle \mathbf{v}_a^{*(0)} \rangle \cdot \mathbf{grad}_{x^*} T^{*(0)} = 0 \tag{C.34}$$

where $\langle \mathbf{v}_a^{*(0)} \rangle$ and $(\rho C)^{\mathrm{eff}*}$ are given by the relations (C.24) and (B.51) respectively. As expected, the convection alone is present at the first order of approximation.

The first correction of this macroscopic model will bring the into play diffusion. Using the relation (C.34), the boundary value problem can be put in the form :

$$-\beta^*\langle \mathbf{v}_a^{*(0)}\rangle \cdot \mathbf{grad}_{x^*} T^{*(0)} - \mathrm{div}_{y^*}(\kappa_i^*(\mathbf{grad}_{y^*} T_i^{*(1)} + \mathbf{grad}_{x^*} T^{*(0)})) = 0 \quad \text{in } \Omega_i \tag{C.35}$$

$$-\gamma^*\langle \mathbf{v}_a^{*(0)}\rangle \cdot \mathbf{grad}_{x^*} T^{*(0)} + \rho_a^* C_a^* \mathbf{v}_a^{*(0)} \cdot (\mathbf{grad}_{x^*} T^{*(0)} + \mathbf{grad}_{y^*} T_a^{*(1)})$$
$$-\mathrm{div}_{y^*}(\kappa_a^*(\mathbf{grad}_{y^*} T_a^{*(1)} + \mathbf{grad}_{x^*} T^{*(0)})) = 0 \quad \text{in } \Omega_a \tag{C.36}$$

$$T_i^{*(1)} = T_a^{*(1)} \quad \text{on } \Gamma \tag{C.37}$$

$$(\kappa_i^*(\mathbf{grad}_{y^*} T_i^{*(1)} + \mathbf{grad}_{x^*} T^{*(0)}) - \kappa_a^*(\mathbf{grad}_{y^*} T_a^{*(1)} + \mathbf{grad}_{x^*} T^{*(0)})) \cdot \mathbf{n_i} = 0 \quad \text{on } \Gamma \tag{C.38}$$

where $\beta^* = (\rho_a^* C_a^*)(\rho_i^* C_i^*)/\rho C)^{\mathrm{eff}*}$ and $\gamma^* = (\rho_a^* C_a^*)^2/\rho C)^{\mathrm{eff}*}$. Consequently, the solution of the above boundary value problem (C.35) -(C.38) appears as a linear function of the macroscopic gradient of temperature, modulo an arbitrary function $\widetilde{T}^{*(1)}(\mathbf{x}^*, t)$ [*Auriault et al.*, 2009; *Geindreau and Auriault*, 2002]: and is written

$$T_i^{*(1)}(\mathbf{x}^*, \mathbf{y}^*, t) = \mathbf{m}_i^*(\mathbf{y}^*, \mathbf{grad}_{x^*} p_a^{*(0)}) \cdot \mathbf{grad}_{x^*} T^{*(0)} + \widetilde{T}_i^{*(1)} \tag{C.39}$$

$$T_a^{*(1)}(\mathbf{x}^*, \mathbf{y}^*, t) = \mathbf{m}_a^*(\mathbf{y}^*, \mathbf{grad}_{x^*} p_a^{*(0)}) \cdot \mathbf{grad}_{x^*} T^{*(0)} + \widetilde{T}_a^{*(1)} \tag{C.40}$$

where $\mathbf{m}_i^*(\mathbf{y}^*, \mathbf{grad}_{x^*} p_a^{*(0)})$ and $\mathbf{m}_a^*(\mathbf{y}^*, \mathbf{grad}_{x^*} p_a^{*(0)})$ are two periodic vectors which characterize the fluctuation of temperature in both phases at the pore scale. They also depend on the velocity field at the first order and hence on the macroscopic pressure gradient $\mathbf{grad}_{x^*} p_a^{*(0)}$. Introducing (C.39) and (C.40) in the set (C.35)-(C.38), these two vectors are solution of the following boundary value problem in a compact form:

$$-\beta\langle \mathbf{v}_a^{*(0)}\rangle - \mathrm{div}_{y^*}(\kappa_i^*(\mathbf{grad}_{y^*} \mathbf{m}_i^* + \mathbf{I})) = 0 \quad \text{in } \Omega_i \tag{C.41}$$

$$(-\gamma + \rho_a^* C_a^*)\langle \mathbf{v}_a^{*(0)}\rangle + \mathbf{v}_a^{*(0)} \cdot \mathbf{grad}_{y^*} \mathbf{m}_a^* - \mathrm{div}_{y^*}(\kappa_a^*(\mathbf{grad}_{y^*} \mathbf{m}_a^* + \mathbf{I})) = 0 \quad \text{in } \Omega_a \tag{C.42}$$

$$\mathbf{m}_i^* = \mathbf{m}_a^* \quad \text{on } \Gamma \tag{C.43}$$

$$(\kappa_i^*(\mathbf{grad}_{y^*} \mathbf{m}_i^* + \mathbf{I}) - \kappa_a^*(\mathbf{grad}_{y^*} \mathbf{m}_a^* + \mathbf{I})) \cdot \mathbf{n_i} = 0 \quad \text{on } \Gamma \tag{C.44}$$

$$\frac{1}{|\Omega|}\int_\Omega (\mathbf{m}_\mathrm{a}^* + \mathbf{m}_\mathrm{i}^*) \mathrm{d}\Omega = \mathbf{0} \tag{C.45}$$

This latter equation is introduced to ensure the uniqueness of the solution. Finally, the third order problem is given by the equations (C.3, C.4, C.6, C.9) of order ε^2:

$$\rho_i^* C_i^* \frac{\partial T^{*(1)}}{\partial t^*} - \mathrm{div}_{y^*}(\kappa_i^*(\mathbf{grad}_{y^*} T_i^{*(2)} + \mathbf{grad}_{x^*} T_i^{*(1)}))$$
$$-\mathrm{div}_{x^*}(\kappa_i^*(\mathbf{grad}_{y^*} T_i^{*(1)} + \mathbf{grad}_{x^*} T^{*(0)})) = 0 \quad \text{in } \Omega_i \tag{C.46}$$

$$\rho_a^* C_a^* \frac{\partial T^{*(1)}}{\partial t^*} + \rho_a^* C_a^* \mathbf{v}_a^{*(0)} \cdot (\mathbf{grad}_{y^*} T^{*(2)} + \mathbf{grad}_{x^*} T^{*(1)}) + \rho_a^* C_a^* \mathbf{v}_a^{*(1)} \cdot (\mathbf{grad}_{y^*} T^{*(1)} + \mathbf{grad}_{x^*} T^{*(0)})$$
$$-\mathrm{div}_{y^*}(\kappa_a^*(\mathbf{grad}_{y^*} T_a^{*(2)} + \mathbf{grad}_{x^*} T_a^{*(1)})) - \mathrm{div}_{x^*}(\kappa_a^*(\mathbf{grad}_{y^*} T_a^{*(1)} + \mathbf{grad}_{x^*} T^{*(0)})) = 0 \quad \text{in } \Omega_a \tag{C.47}$$

$$T_i^{*(2)} = T_a^{*(2)} \quad \text{on } \Gamma \tag{C.48}$$

$$(\kappa_i^*(\mathbf{grad}_{y^*}T_i^{*(2)}+\mathbf{grad}_{x^*}T_i^{*(1)})-\kappa_a^*(\mathbf{grad}_{y^*}T_a^{*(2)}+\mathbf{grad}_{x^*}T_a^{*(1)}))\cdot\mathbf{n_i}=L_{sg}^*w_n^{*(0)}\quad\text{on }\Gamma \tag{C.49}$$

where the unknowns $T_i^{*(2)}(\mathbf{x}^*,\mathbf{y}^*,t)$ and $T_a^{*(2)}(\mathbf{x}^*,\mathbf{y}^*,t)$ are $\mathbf{y}^*$-periodic. The fluid velocity $v_a^{*(0)}(\mathbf{x}^*,\mathbf{y}^*,t)$ is given by the equation (C.19) (and verifies the relation (C.16)) and $v_a^{*(1)}(\mathbf{x}^*,\mathbf{y}^*,t)$ verifies the relations (C.21) and (C.22). Finally, $w_n^{*(0)}(\mathbf{x}^*,\mathbf{y}^*,t)$ is the normal interface velocity due to the phase change at the zero order given by the Hertz-Knudsen equation (B.67) and the Clausius Clapeyron's law (B.66). Integrating (C.46) over Ω_i and (C.47) over Ω_a, and then using the divergence theorem, the periodicity condition, and the boundary conditions (C.49) lead to the first order correction:

$$\begin{aligned}(\rho C)^{\text{eff}*}\frac{\partial T^{*(1)}}{\partial t^*}+\rho_a^*C_a^*\langle\mathbf{v}_a^{*(0)}\rangle\cdot\mathbf{grad}_{x^*}\widetilde{T}_i^{*(1)}+&+\rho_a^*C_a^*\langle\mathbf{v}_a^{*(1)}\rangle\cdot\mathbf{grad}_{x^*}T_i^{*(0)}\\ -\text{div}_{x^*}(\mathbf{k}^{\text{disp}*}\mathbf{grad}_{x^*}\,T^{*(0)})&=\text{SSA}_V L_{sg}^*w_n^{*(0)}\end{aligned} \tag{C.50}$$

where $\mathbf{k}^{\text{dips}*}$ is the effective thermal dispersion tensor respectively, defined as:

$$\mathbf{k}^{\text{disp}*}=\frac{1}{|\Omega|}\left(\int_{\Omega_\text{a}}\kappa_a^*(\mathbf{grad}_{y^*}\mathbf{m}_a^*(\mathbf{y}^*)+\mathbf{I})+\mathbf{v}_a^{*(0)}\otimes\mathbf{m}_a^*\text{d}\Omega+\int_{\Omega_\text{i}}\kappa_i^*(\mathbf{grad}_{y^*}\mathbf{m}_i^*(\mathbf{y}^*)+\mathbf{I})\text{d}\Omega\right) \tag{C.51}$$

Finally, we can define:

$$\langle T^*\rangle=T^{*(0)}+\varepsilon\widetilde{T}^{*(1)},\quad\langle\mathbf{v}_a^*\rangle=\langle\mathbf{v}_a^{*(0)}\rangle+\varepsilon\langle\mathbf{v}_a^{*(1)}\rangle \tag{C.52}$$

where $\langle\cdot\rangle$ represent the mean over the REV respectively. Thus, adding equations (C.34) and (C.50) multiplied by ε, we get the following dimensionless macroscopic description at the second order of approximation:

$$(\rho C)^{\text{eff}*}\frac{\partial\langle T^*\rangle}{\partial t^*}+\rho_a^*C_a^*\langle\mathbf{v}_a^*\rangle\cdot\mathbf{grad}_{x^*}\langle T^*\rangle-\text{div}_{x^*}(\varepsilon\mathbf{k}^{\text{disp}*}\mathbf{grad}_{x^*}\langle T^*\rangle)=\text{SSA}_V L_{sg}^*w_n^{*(0)} \tag{C.53}$$

Water vapor transfer

Introducing asymptotic expansions for ρ_v^* in the relations (C.5, C.10) give at the lowest order (ε^0)

$$\mathbf{v}_a^{*(0)}\cdot\mathbf{grad}_{y^*}\rho_v^{*(0)}-\text{div}_{y^*}(D_v^*\mathbf{grad}_{y^*}\rho_v^{*(0)})=0\quad\text{in }\Omega_a \tag{C.54}$$

$$D_v^*\mathbf{grad}_{y^*}\rho_v^{*(0)}\cdot\mathbf{n_i}=0\quad\text{on }\Gamma. \tag{C.55}$$

where the unknown $\rho_v^{*(0)}(\mathbf{x}^*,\mathbf{y}^*,t)$ is $\mathbf{y}^*$-periodic. It can be shown[*Auriault et al.*, 2009] that the solution of the above boundary value problem is given by:

$$\rho_v^{*(0)}=\rho_v^{*(0)}(\mathbf{x}^*,t). \tag{C.56}$$

At the first order, the water vapor density is independent of the microscopic dimensionless variable $\mathbf{y}^*$. Taking into account these results, the second-order problem is given by the equations (C.5, C.10) of order ε:

$$\frac{\partial\rho_v^{*(0)}}{\partial t^*}+\mathbf{v}_a^{*(0)}\cdot(\mathbf{grad}_{y^*}\rho_v^{*(1)}+\mathbf{grad}_{x^*}\rho_v^{*(0)})-\text{div}_{y^*}(D_v^*(\mathbf{grad}_{y^*}\rho_v^{*(1)}+\mathbf{grad}_{x^*}\rho_v^{*(0)}))=0\quad\text{in }\Omega_a \tag{C.57}$$

$$D_v^*(\mathbf{grad}_{y^*}\rho_v^{*(1)} + \mathbf{grad}_{x^*}\rho_v^{*(0)}) \cdot \mathbf{n_i} = 0 \quad \text{on } \Gamma. \tag{C.58}$$

where the unknown $\rho_v^{*(1)}(\mathbf{x}^*, \mathbf{y}^*, t)$ is $\mathbf{y}^*$-periodic and the macroscopic gradient $\mathbf{grad}_{x^*}\rho_v^{*(0)}$ is given. $\mathbf{v}_a^{*(0)}$ is given by the relation (C.19) (and verifies the relations (C.16) and (C.18)). Integrating (C.57) over Ω_a and taking into account the condition of periodicity, the boundary condition (C.58) and the relation (C.19), we obtain the following first order macroscopic description:

$$\phi\frac{\partial\rho_v^{*(0)}}{\partial t^*} + \langle\mathbf{v}_a^{*(0)}\rangle \cdot \mathbf{grad}_{x^*}\rho_v^{*(0)} = 0 \tag{C.59}$$

where $\langle\mathbf{v}_a^{*(0)}\rangle$ is given by the relation (C.24).

As for the temperature, the convection alone is present at the first order of approximation. Using the relation (C.59), the boundary value problem (refrvd2C) - (C.58) is written:

$$-\phi^{-1}\langle\mathbf{v}_a^{*(0)}\rangle \cdot \mathbf{grad}_{x^*}\rho_v^{*(0)} + \mathbf{v}_a^{*(0)} \cdot (\mathbf{grad}_{y^*}\rho_v^{*(1)} + \mathbf{grad}_{x^*}\rho_v^{*(0)})$$
$$-\mathrm{div}_{y^*}(D_v^*(\mathbf{grad}_{y^*}\rho_v^{*(1)} + \mathbf{grad}_{x^*}\rho_v^{*(0)})) = 0 \quad \text{in } \Omega_a \tag{C.60}$$

$$D_v^*(\mathbf{grad}_{y^*}\rho_v^{*(1)} + \mathbf{grad}_{x^*}\rho_v^{*(0)}) \cdot \mathbf{n_i} = 0 \quad \text{on } \Gamma. \tag{C.61}$$

The solution of the above boundary value problem appears as a linear function of the macroscopic gradient of the water vapor, modulo an arbitrary function $\widetilde{\rho}_v^{*(1)}(\mathbf{x}^*, t)$ [*Auriault et al.*, 2009]:

$$\rho_v^{*(1)}(\mathbf{x}^*, \mathbf{y}^*, t) = \mathbf{h}_v^*(\mathbf{y}^*, \mathbf{grad}_{x^*}p_a^{*(0)}) \cdot \mathbf{grad}_{x^*}\rho_v^{*(0)} + \widetilde{\rho}_v^{*(1)}(\mathbf{x}^*, t) \tag{C.62}$$

where $\mathbf{h}_v^*(\mathbf{y}^*, \mathbf{grad}_{x^*}p_a^{*(0)})$ is a periodic vector which characterizes the fluctuation of water vapor density in the air phase at the pore scale which depends on the intensity of the flow and thus on $\mathbf{grad}_{x^*}p_a^{*(0)}$. Introducing (C.62) in the set (C.60)-(C.61), this vector is solution of the following boundary value problem in a compact form:

$$(-\phi^{-1}\langle\mathbf{v}_a^{*(0)}\rangle + \mathbf{v}_a^{*(0)}) + \mathbf{v}_a^{*(0)} \cdot \mathbf{grad}_{y^*}\mathbf{h}_v^* - \mathrm{div}_{y^*}(D_v^*(\mathbf{grad}_{y^*}\mathbf{h}_v^* + \mathbf{I})) = 0 \quad \text{in } \Omega_a \tag{C.63}$$

$$D_v^*(\mathbf{grad}_{y^*}\mathbf{h}_v^* + \mathbf{I}) \cdot \mathbf{n_i} = 0 \quad \text{on } \Gamma \tag{C.64}$$

$$\frac{1}{|\Omega|}\int_{\Omega_a}\mathbf{h}_v^*\mathrm{d}\Omega = \mathbf{0} \tag{C.65}$$

This latter equation is introduced to ensure the uniqueness of the solution. Finally, the third order problem is given by the equations (C.5, C.10) of order ε^2:

$$\frac{\partial\rho_v^{*(1)}}{\partial t^*} + \mathbf{v}_a^{*(0)} \cdot (\mathbf{grad}_{y^*}\rho_v^{*(2)} + \mathbf{grad}_{x^*}\rho_v^{*(1)}) + \mathbf{v}_a^{*(1)} \cdot (\mathbf{grad}_{y^*}\rho_v^{*(1)} + \mathbf{grad}_{x^*}\rho_v^{*(0)})$$
$$-\mathrm{div}_{y^*}(D_v^*(\mathbf{grad}_{y^*}\rho_v^{*(2)} + \mathbf{grad}_{x^*}\rho_v^{*(1)})) - \mathrm{div}_{x^*}(D_v^*(\mathbf{grad}_{y^*}\rho_v^{*(1)} + \mathbf{grad}_{x^*}\rho_v^{*(0)})) = 0 \quad \text{in } \Omega_a \tag{C.66}$$

$$D_v^*(\mathbf{grad}_{y^*}\rho_v^{*(2)} + \mathbf{grad}_{x^*}\rho_v^{*(1)}) \cdot \mathbf{n_i} = \rho_i^* w_n^{*(0)} \quad \text{on } \Gamma \tag{C.67}$$

where the unknown $\rho_v^{*(2)}(\mathbf{x}^*, \mathbf{y}^*, t)$ is $\mathbf{y}^*$-periodic. The fluid velocity $v_a^{*(0)}(\mathbf{x}^*, \mathbf{y}^*, t)$ is given by the equation (C.19) (and verifies the relation (C.16)) and $v_a^{*(1)}(\mathbf{x}^*, \mathbf{y}^*, t)$ verifies the

relations (C.21) and (C.22). Finally, $w_n^{*(0)}(\mathbf{x}^*, \mathbf{y}^*, t)$ is the normal interface velocity due to the phase change at the zero order given by the Hertz-Knudsen equation (B.67) and the Clausius Clapeyron's law (B.66). Integrating (C.66) over Ω_a, and then using the divergence theorem, the periodicity condition, and the boundary conditions (C.67) lead to the first order correction :

$$\phi \frac{\partial \rho_v^{*(1)}}{\partial t} + \langle \mathbf{v}_a^{*(0)} \rangle \cdot \mathbf{grad}_{x^*} \widetilde{\rho}_v^{*(1)} + \langle \mathbf{v}_a^{*(1)} \rangle \cdot \mathbf{grad}_{x^*} \rho_v^{*(0)}$$

$$-\mathrm{div}_{x^*}(\mathbf{D}^{\mathrm{disp}*} \mathbf{grad}_{x^*} \rho_v^{*(0)}) = -\mathrm{SSA}_V \rho_i^* w_n^{*(0)} \tag{C.68}$$

where $\mathrm{SSA_V} = |\Gamma|/|\Omega|$ is the surface area and $\mathbf{D}^{\mathrm{disp}*}$ is the dimensionless effective dispersion tensor for the water vapor defined as:

$$\mathbf{D}^{\mathrm{disp}*} = \frac{1}{|\Omega|} \int_{\Omega_a} D_v^* (\mathbf{grad}_{y^*}\ \mathbf{h}_v^*(\mathbf{y}^*) + \mathbf{I}) + \mathbf{v}_a^{*(0)} \otimes \mathbf{h}_v^* \mathrm{d}\Omega \tag{C.69}$$

Finally, we can define:

$$\langle \rho_v^* \rangle_a = \rho_v^{*(0)} + \varepsilon \widetilde{\rho}_v^{*(1)}, \quad \langle \mathbf{v}_a^* \rangle = \langle \mathbf{v}_a^{*(0)} \rangle + \varepsilon \langle \mathbf{v}_a^{*(1)} \rangle \tag{C.70}$$

where $\langle \cdot \rangle_a$ and $\langle \cdot \rangle$ represent the mean over the air phase and over the REV respectively. Thus, adding equations (C.59) and (C.68) multiplied by ε, we get the following dimensionless macroscopic description at the second order of approximation:

$$\phi \frac{\partial \langle \rho_v^* \rangle_a}{\partial t} + \langle \mathbf{v}_a^* \rangle \cdot \mathbf{grad}_{x^*} \langle \rho_v^* \rangle_a - \mathrm{div}_{x^*}(\varepsilon \mathbf{D}^{*\mathrm{disp}} \mathbf{grad}_{x^*} \langle \rho_v^* \rangle_a) = -\mathrm{SSA}_V \rho_i^* w_n^{*(0)} \tag{C.71}$$

Appendix

C Appendix of Chapter 4

General Information

In the following, we provide the list and related information for all the samples used in this study. For each snow type [Fierz et al., 2009], a typical microtomographic sample is presented together with its main results in terms of effective thermal conductivity.

- Figures x.1: 3D images of the snow sample. The color coding of the images corresponds to the curvature field, which allows an easy representation of the 3D structure from planar images.
- Figures x.2: Estimations of the REV (the smallest fraction of the sample volume from which a variable representative of the whole can be determined) with respect to the thermal conductivity. It is estimated by calculating values of the thermal conductivity from several sub-volumes of increasing sizes. The REV is reached as soon as values remain constant when sub-volumes of calculations increase.
- Tables x.1: Numerical values of the diagonal terms of the effective thermal conductivity. For all the images of the study, the non diagonal terms are 100 times lower than the diagonal values and can be neglected.

List of the 30 Samples Used in the Study

Sample name	Snow type	Voxel size (μm)	Remarks	Main References
Fr	PP	4.91	Sampled at Col de Porte[1], 14 February 2002.	This study
I01	PP	4.91	Sampled at Col de Porte, 15 h after the snowfall.	Flin et al., 2004
I03	PP	4.91	62 h after the snowfall, under isothermal conditions at –2°C.	Flin et al., 2004
I04	PP	4.91	81 h after the snowfall, under isothermal conditions at –2°C.	Flin et al., 2004
I08	DF	4.91	297 h after the snowfall, under isothermal conditions at –2°C.	Flin et al., 2004
I15	RG	4.91	806 h after the snowfall, under isothermal conditions at –2°C.	Flin et al., 2004
I19	RG	4.91	1381 h after the snowfall, under isothermal conditions at –2°C.	Flin et al., 2004
I21	RG	4.91	1694 h after the snowfall, under isothermal conditions at –2°C.	Flin et al., 2004
I23	RG	4.91	2026 h after the snowfall, under isothermal conditions at –2°C.	Flin et al., 2004
P03	PP	8.48	Girose glacier[2], 20 cm depth, 17 March 2009.	Flin et al., 2011
P04	DF	8.588	Girose glacier, 40 cm depth, 17 March 2009.	Flin et al., 2011
P06	RG	6.158	Girose glacier, 60 cm depth, 17 March 2009.	Flin et al., 2011
P07	RG	8.609	Girose glacier, 70 cm depth, 17 March 2009.	Flin et al., 2011
P08	RG	8.552	Girose glacier, 100 cm depth, 17 March 2009.	Flin et al., 2011
P09	RG	6.158	Girose glacier, 120 cm depth, 17 March 2009.	Flin et al., 2011
P10	RG	6.103	Girose glacier, 165 cm depth, 17 March 2009.	Flin et al., 2011
P11	RG	8.588	Girose glacier, 65 cm depth, 1 March 2009.	Flin et al., 2011
P14	RG	6.154	Girose glacier, 80 cm depth, 1 March 2009.	Flin et al., 2011
P15	RG	6.158	Girose glacier, 170 cm depth, 1 March 2009.	Flin et al., 2011
H00	RG	8.609	Sieved snow, followed by isothermal conditions.	Flin et al., 2011
H01	MF	8.609	Grain coarsening of water-saturated snow and drainage after 1h.	Flin et al., 2011
H1-2	MF	8.590	Grain coarsening of water-saturated snow and drainage after 6h.	Flin et al., 2011
H02	MF	8.590	Grain coarsening of water-saturated snow and drainage after 24h.	Flin et al., 2011
H03	MF	8.609	Grain coarsening of water-saturated snow and drainage after 48h.	Flin et al., 2011
H05	MF	8.590	Grain coarsening of water-saturated snow and drainage after 142h.	Flin et al., 2011
Chamair	MF	10	Grain coarsening of water-saturated snow and drainage.	Coléou et al., 2001
E2b	FC	4.91	3 weeks under a TG = 16 K m^{-1}, T_{mean} = -3°C, sampled in the middle of the layer.	Flin et al., 2008
3A	DH	8.400	9 days under a TG = 43 K m^{-1}, T_{mean} = -4°C, sampled in the middle of the layer.	This study
4A	DH	8. 397	13 days under a TG = 43 K m^{-1}, T_{mean} = -4°C, sampled in the middle of the layer.	This study
Grad3	DH	10	8 days under a TG = 100 K m^{-1}, T_{mean} = -5°C.	Coléou et al., 2001

Table 1: List of the snow samples used in the present work. Snow type is defined according to the International Classification for Seasonal Snow on the Ground [*Fierz et al., 2009*]: PP, Precipitation Particles; DF, Decomposing and Fragmented precipitation particles; RG, Rounded Grains; FC, Faceted Crystals; DH, Depth Hoar; MF, Melt Forms. Lines with gray background correspond to samples for which detailed information is provided below.

[1] 1325 m altitude, Chartreuse range, France.
[2] 3200 m altitude, Ecrins range, France.

Sample *Fr* - Precipitation Particles (PP)

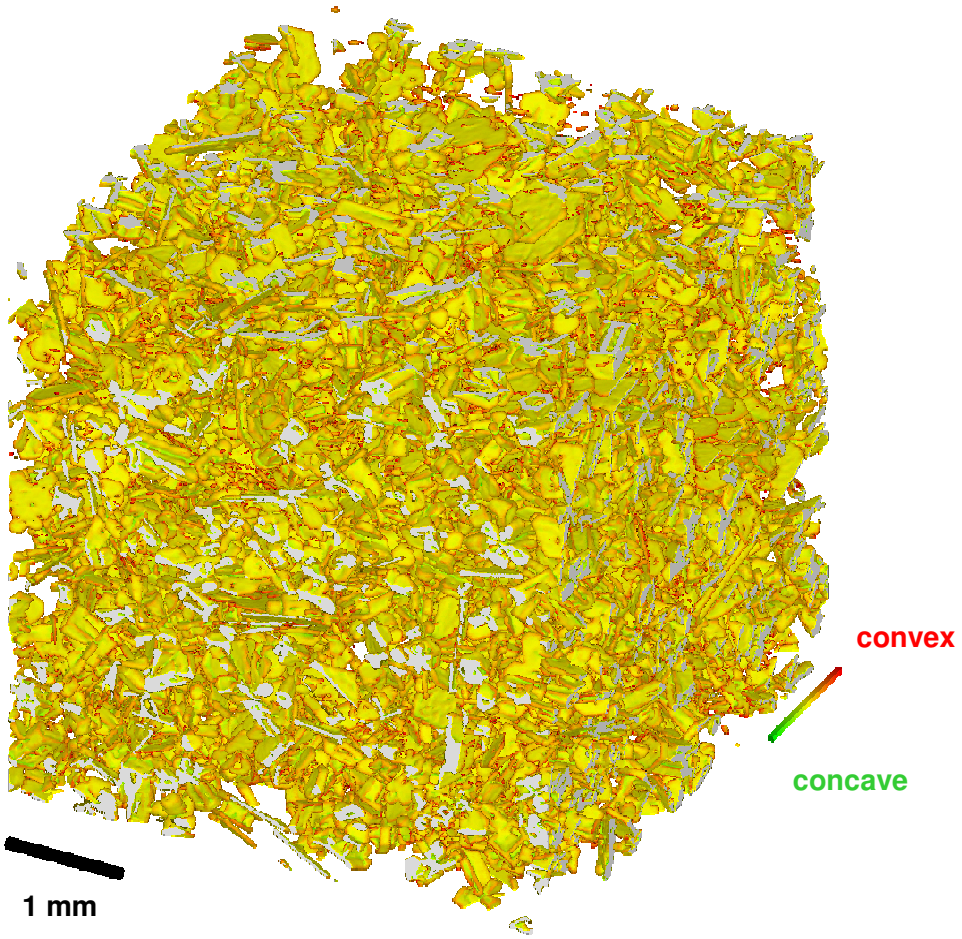

Figure 1.1: 3D visualization of the microtomographic image (size = 1192^3 voxels, 1 vox. = 4.91 µm).

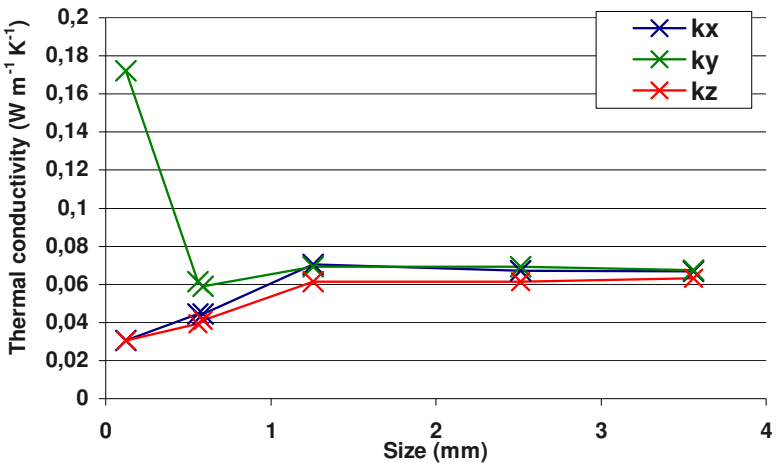

Figure 1.2:
Dependency of $\mathbf{k^{eff}}$ estimates with sample size.

REV (mm)	**2.5**
Density (kg m^{-3})	**124.9**
$k^{eff}x$ (W m^{-1} K^{-1})	**0.067**
$k^{eff}y$ (W m^{-1} K^{-1})	**0.067**
$k^{eff}z$ (W m^{-1} K^{-1})	**0.063**

Table 1.1:
Estimated REV, density and $\mathbf{k^{eff}}$ values.

Sample *P04* - Decomposing and Fragmented precipitation particles (DF)

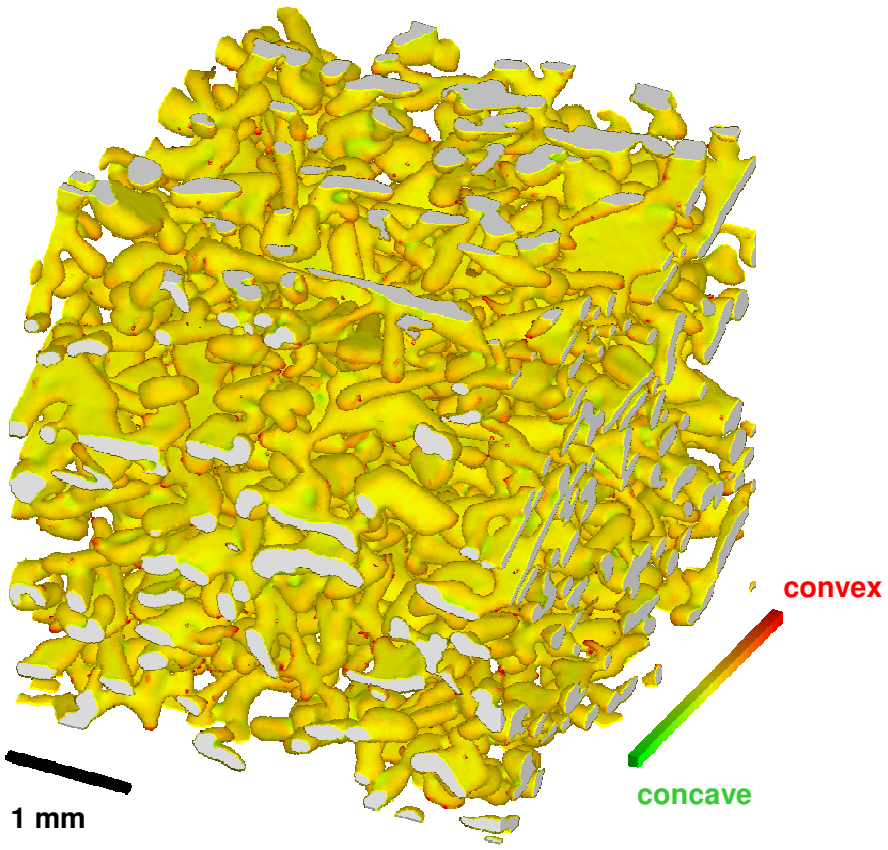

Figure 2.1: 3D visualization of the microtomographic image (size = 512^3 voxels, 1 vox. = 8.588 µm).

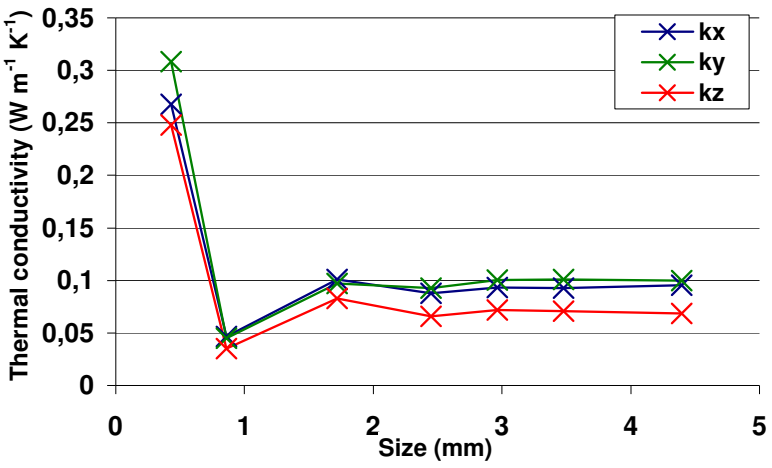

Figure 2.2:
Dependency of $\mathbf{k^{eff}}$ estimates with sample size.

REV (mm)	**3**
Density (kg m^{-3})	**157.6**
k^{eff}_x (W m^{-1} K^{-1})	**0.095**
k^{eff}_y (W m^{-1} K^{-1})	**0.100**
k^{eff}_z (W m^{-1} K^{-1})	**0.068**

Table 2.1:
Estimated REV, density and $\mathbf{k^{eff}}$ values.

Sample *P11* - Rounded Grains (RG)

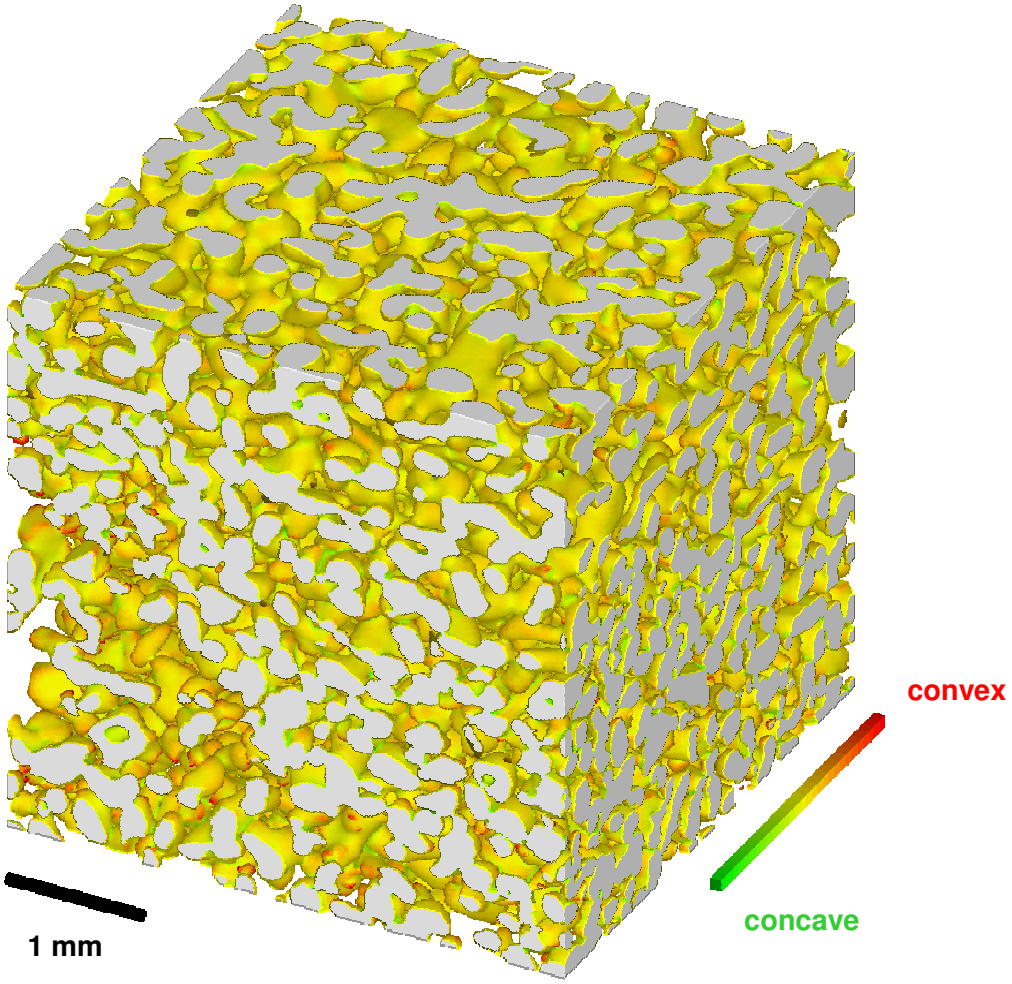

Figure 3.1: 3D visualization of the microtomographic image (size = 512^3 voxels, 1 vox. = 8.588 µm).

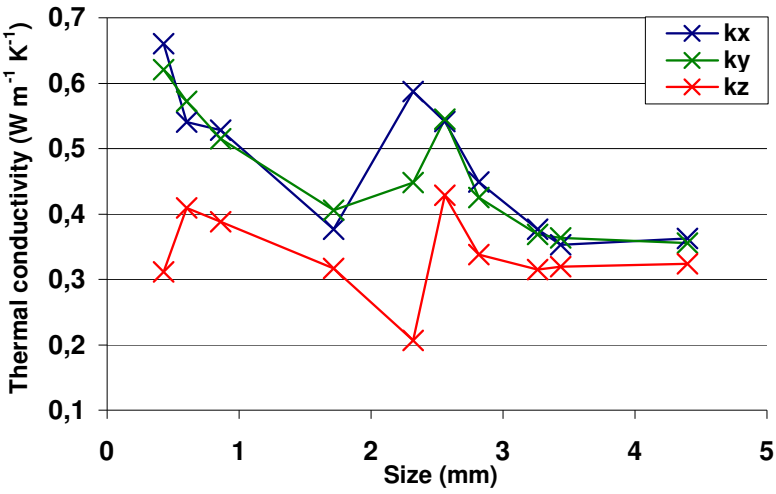

Figure 3.2:
Dependency of $\mathbf{k^{eff}}$ estimates with sample size.

REV (mm)	**4**
Density (kg m^{-3})	**413.7**
k^{eff}_x (W m^{-1} K^{-1})	**0.363**
k^{eff}_y (W m^{-1} K^{-1})	**0.356**
k^{eff}_z (W m^{-1} K^{-1})	**0.324**

Table 3.1:
Estimated REV, density and $\mathbf{k^{eff}}$ values.

Sample *H02* - Melt Forms (MF)

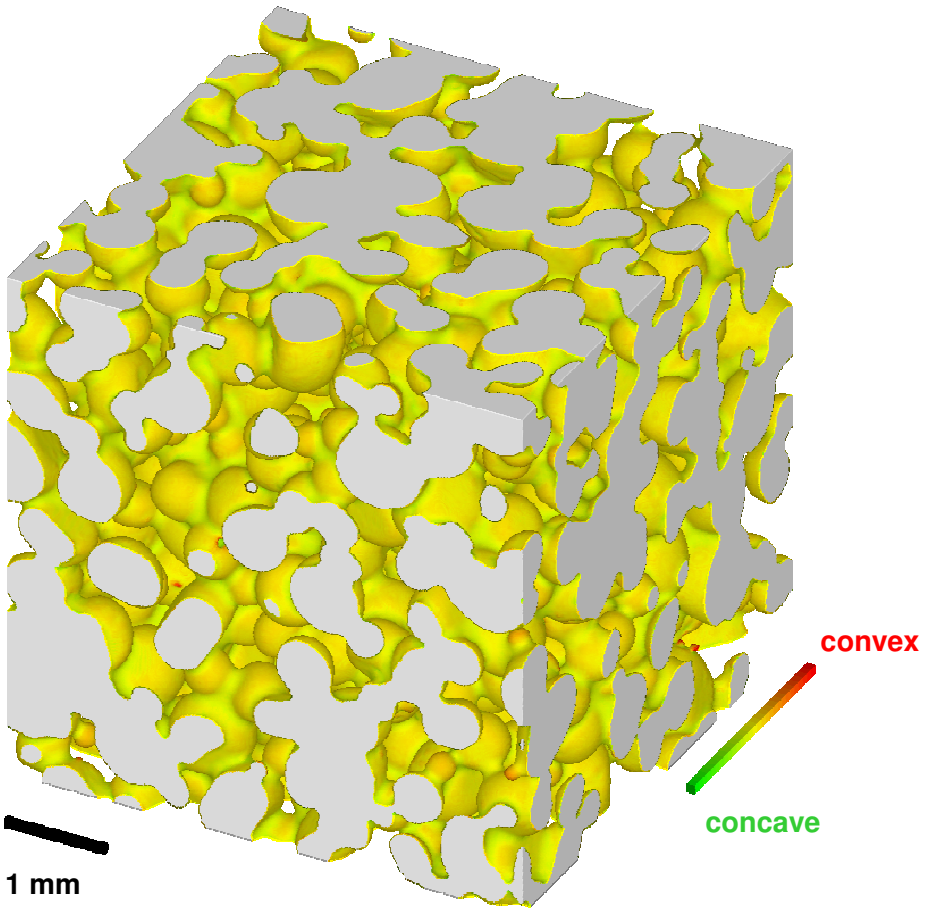

Figure 4.1: 3D visualization of the microtomographic image (size = 651^3 voxels, 1 vox. = 8.590 µm).

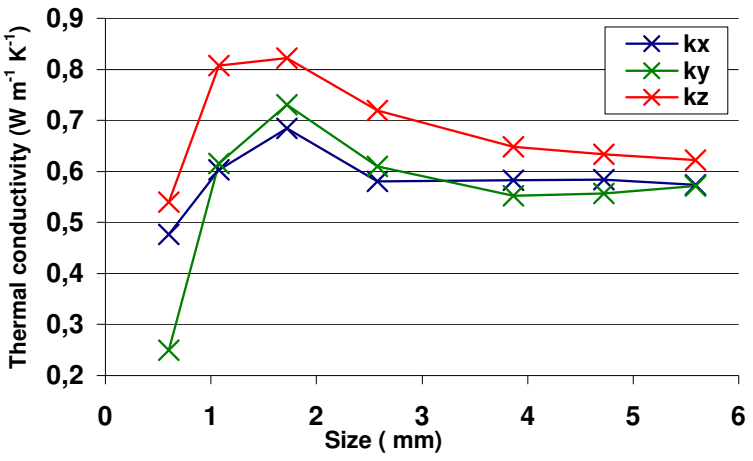

Figure 4.2:
Dependency of $\mathbf{k}^{\mathbf{eff}}$ estimates with sample size.

REV (mm)	**5.5**
Density (kg m^{-3})	**502.6**
k^{eff}_x (W m^{-1} K^{-1})	**0.574**
k^{eff}_y (W m^{-1} K^{-1})	**0.571**
k^{eff}_z (W m^{-1} K^{-1})	**0.623**

Table 4.1:
Estimated REV, density and $\mathbf{k}^{\mathbf{eff}}$ values.

Sample *E2b* – Faceted Crystals (FC)

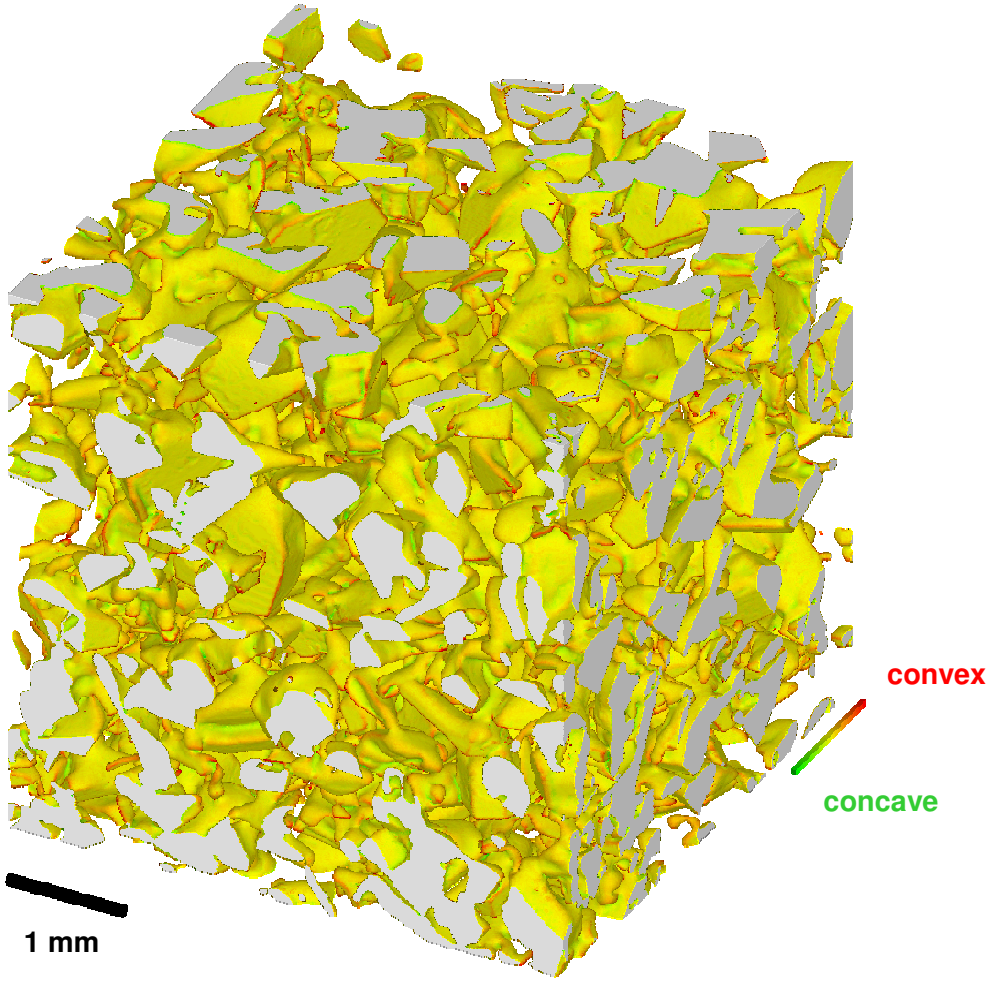

Figure 5.1: 3D visualization of the microtomographic image (size = 1200^3 voxels, 1 vox. = 4.91 µm).

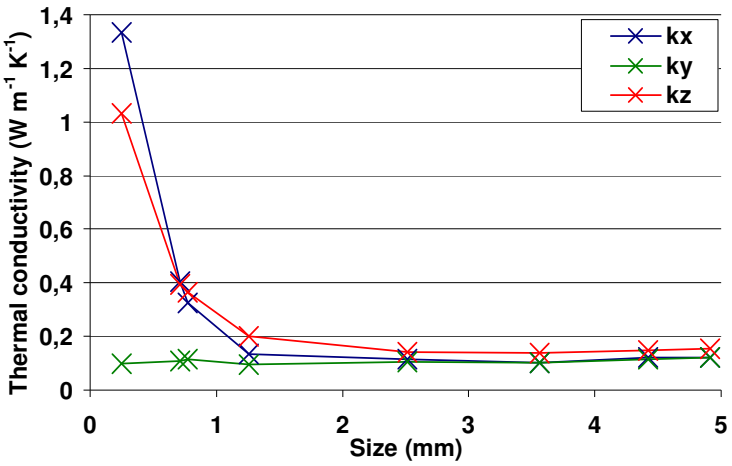

Figure 5.2:
Dependency of $\mathbf{k^{eff}}$ estimates with sample size.

REV (mm)	**3**
Density (kg m^{-3})	**262.7**
k^{eff}_x (W m^{-1} K^{-1})	**0.123**
k^{eff}_y (W m^{-1} K^{-1})	**0.121**
k^{eff}_z (W m^{-1} K^{-1})	**0.154**

Table 5.1:
Estimated REV, density and $\mathbf{k^{eff}}$ values.

Sample *Grad3* – Depth Hoar (DH)

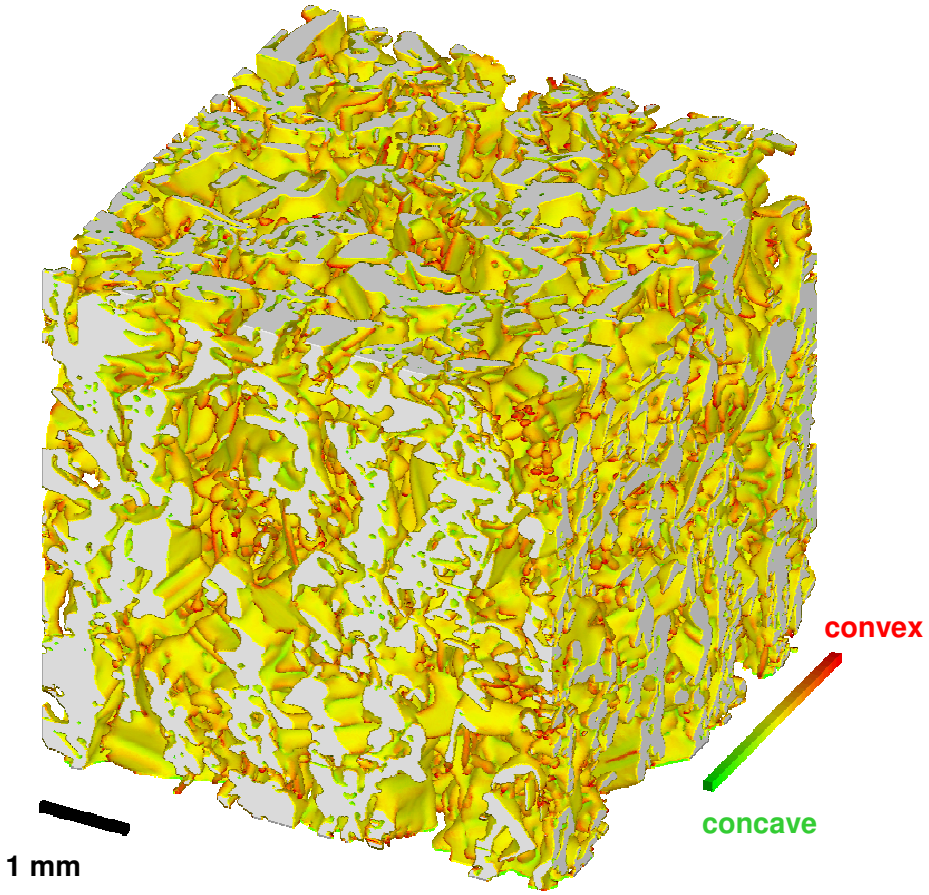

Figure 6.1: 3D visualization of the microtomographic image (size = 600^3 voxels, 1 vox. = 10 µm).

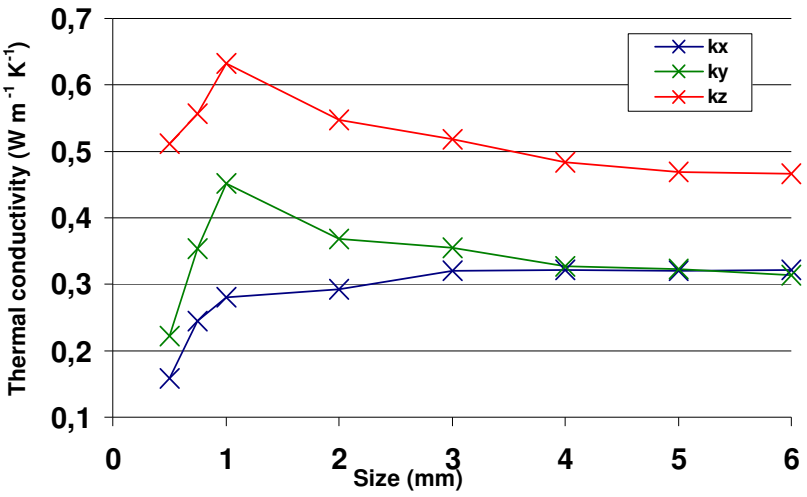

Figure 6.2:
Dependency of $\mathbf{k}^{\mathbf{eff}}$ estimates with sample size.

REV (mm)	**5**
Density (kg m^{-3})	**369.2**
k^{eff}_x (W m^{-1} K^{-1})	**0.322**
k^{eff}_y (W m^{-1} K^{-1})	**0.314**
k^{eff}_z (W m^{-1} K^{-1})	**0.466**

Table 6.1:
Estimated REV, density and $\mathbf{k}^{\mathbf{eff}}$ values.

Appendix

D Appendix of Chapter 5

General Information

In the following, we provide the list of the samples used in this study with related information (Table 1) and values of permeability, density and specific surface area (Table 2). For each snow type [Fierz et al., 2009], a typical microtomographic sample is presented together with its REV estimate in term of permeability:

- Figures 1.a – 6.a: 3-D images of the snow sample. The color levels of the images correspond to the fluid velocity (intensity) computed for a pressure drop of $2\text{x}10^{-2}$ Pa along the vertical direction (z) and a dynamic viscosity of air of $1.8\text{x}10^{-5}$ Pa s^{-1}. The ice grains are represented in white.

- Figures 1.b – 6.b: Estimations of the REV (the smallest fraction of the sample volume from which a variable representative of the whole can be determined) with respect to the permeability. The REV is estimated by calculating values of permeability from several sub-volumes of increasing sizes. It is reached as soon as values remain constant when sub-volumes of calculations increase. For each figure, the permeability value computed on the largest volume size corresponds to that given in Table 2.

List of the 35 Samples Used in the Study

Sample name	Snow type	Voxel size (μm^3)	Remarks	Main References
Fr	PP	4.91	Sampled at Col de Porte[1], 14 February 2002.	Calonne et al., 2011
I01	PP	4.91	Sampled at Col de Porte, 15 h after the snowfall.	Flin et al., 2004
I03	PP	4.91	62 h after the snowfall, under isothermal conditions at –2°C.	Flin et al., 2004
I04	PP	4.91	81 h after the snowfall, under isothermal conditions at –2°C.	Flin et al., 2004
I08	DF	4.91	297 h after the snowfall, under isothermal conditions at –2°C.	Flin et al., 2004
I15	RG	4.91	806 h after the snowfall, under isothermal conditions at –2°C.	Flin et al., 2004
I19	RG	4.91	1381 h after the snowfall, under isothermal conditions at –2°C.	Flin et al., 2004
I21	RG	4.91	1694 h after the snowfall, under isothermal conditions at –2°C.	Flin et al., 2004
I23	RG	4.91	2026 h after the snowfall, under isothermal conditions at –2°C.	Flin et al., 2004
P03	PP	8.48	Girose glacier[2], 20 cm depth, 17 March 2009.	Flin et al., 2011
P04	DF	8.588	Girose glacier, 40 cm depth, 17 March 2009.	Flin et al., 2011
P06	RG	6.158	Girose glacier, 60 cm depth, 17 March 2009.	Flin et al., 2011
P07	RG	8.609	Girose glacier, 70 cm depth, 17 March 2009.	Flin et al., 2011
P08	RG	8.552	Girose glacier, 100 cm depth, 17 March 2009.	Flin et al., 2011
P09	RG	6.158	Girose glacier, 120 cm depth, 17 March 2009.	Flin et al., 2011
P10	RG	6.103	Girose glacier, 165 cm depth, 17 March 2009.	Flin et al., 2011
P11	RG	8.588	Girose glacier, 65 cm depth, 1 March 2009.	Flin et al., 2011
P14	RG	6.154	Girose glacier, 80 cm depth, 1 March 2009.	Flin et al., 2011
P15	RG	6.158	Girose glacier, 170 cm depth, 1 March 2009.	Flin et al., 2011
H00	RG	8.609	Sieved snow, followed by isothermal conditions.	Flin et al., 2011
H01	MF	8.609	Grain coarsening of water-saturated snow and drainage after 1h.	Flin et al., 2011
H1-2	MF	8.590	Grain coarsening of water-saturated snow and drainage after 6h.	Flin et al., 2011
H02	MF	8.590	Grain coarsening of water-saturated snow and drainage after 24h.	Flin et al., 2011
H03	MF	8.609	Grain coarsening of water-saturated snow and drainage after 48h.	Flin et al., 2011
H05-G	MF	9.46	Grain coarsening of water-saturated snow and drainage after 142h.	Flin et al., 2011
Chamair	MF	10	Grain coarsening of water-saturated snow and drainage.	Coléou et al., 2001
E2b	FC	4.91	3 weeks under a TG = 16 K m^{-1}, T_{mean} = -3°C, sampled in the middle of the layer.	Flin et al., 2008
0A	RG	8.392	Sieved snow, following by isothermal conditions.	This study
1A	RG	8.395	3 days under a TG = 43 K m^{-1}, T_{mean} = -4°C, sampled in the middle of the layer.	This study
2A	FC	8.373	6 days under a TG = 43 K m^{-1}, T_{mean} = -4°C, sampled in the middle of the layer.	This study
3A	DH	8.400	9 days under a TG = 43 K m^{-1}, T_{mean} = -4°C, sampled in the middle of the layer.	Calonne et al., 2011
4A	DH	8. 397	13 days under a TG = 43 K m^{-1}, T_{mean} = -4°C, sampled in the middle of the layer.	Calonne et al., 2011
5A-G	DH	9.655	17 days under a TG = 43 K m^{-1}, T_{mean} = -4°C, sampled in the middle of the layer.	This study
7A-G	DH	9.672	21 days under a TG = 43 K m^{-1}, T_{mean} = -4°C, sampled in the middle of the layer.	This study
Grad3	DH	10	8 days under a TG = 100 K m^{-1}, T_{mean} = -5°C.	Coléou et al., 2001

Table 1: List of the 35 snow samples used in the present work. Snow type is defined according to the International Classification for Seasonal Snow on the Ground [*Fierz et al., 2009*]: PP, Precipitation Particles; DF, Decomposing and Fragmented precipitation particles; RG, Rounded Grains; FC, Faceted Crystals; DH, Depth Hoar; MF, Melt Forms. Lines with gray background correspond to samples for which detailed information is provided below.

[1] 1325 m altitude, Chartreuse range, France.
[2] 3200 m altitude, Ecrins range, France.

Computed Values for the 35 Samples Used in the Study

Sample name	Snow type	K^{eff}_x x 10^{-9} (m^2)	K^{eff}_y x 10^{-9} (m^2)	K^{eff}_z x 10^{-9} (m^2)	SSA (m^2 kg^{-1})	Density (kg m^{-3})
Fr	PP	3.58	3.77	3.69	55.30	120.49
I01	PP	3.83	2.22	3.33	55.79	102.90
I03	PP	3.79	3.93	4.03	41.37	123.34
I04	PP	4.23	4.16	4.06	42.48	113.43
I08	DF	4.60	4.38	4.79	29.32	147.71
I15	RG	4.54	4.70	4.79	23.32	172.76
I19	RG	4.73	4.82	4.84	19.90	192.48
I21	RG	4.73	4.93	4.36	19.23	198.62
I23	RG	2.82	2.62	2.47	17.24	256.30
P03	PP	2.42	2.38	2.06	50.91	134.55
P04	DF	6.14	6.38	4.62	25.36	157.54
P06	RG	0.64	0.65	0.59	21.59	354.51
P07	RG	2.45	2.44	1.83	17.15	280.05
P08	RG	1.09	1.08	0.96	14.57	379.00
P09	RG	1.26	1.29	1.04	12.29	396.14
P10	RG	1.55	1.68	1.38	10.46	396.07
P11	RG	0.46	0.45	0.40	20.76	413.75
P14	RG	0.90	0.88	0.80	18.13	352.68
P15	RG	1.54	1.54	1.73	16.09	315.54
H00	RG	0.45	0.44	0.43	17.34	431.36
H01	MF	0.48	0.45	0.48	6.99	550.93
H1-2	MF	0.75	0.75	0.74	7.69	503.80
H02	MF	1.22	1.22	1.27	6.18	471.70
H03	MF	1.80	1.88	1.73	5.25	498.11
H05-G	MF	3.96	4.57	4.87	3.78	471.70
Chamair	MF	0.57	0.51	0.54	8.49	525.90
E2b	FC	5.71	4.87	5.62	15.43	239.70
0A	RG	0.76	0.78	0.70	27.68	314.81
1A	RG	1.75	1.74	1.64	23.37	275.01
2A	FC	1.95	1.95	2.02	20.75	282.71
3A	DH	2.98	2.89	3.08	18.18	274.82
4A	DH	2.71	2.61	3.18	15.19	315.36
5A-G	DH	3.77	3.70	4.39	14.89	284.09
7A-G	DH	3.92	3.95	4.84	13.42	311.23
Grad3	DH	0.65	0.63	1.06	21.84	369.18

Table 2: List of the snow samples and types with the corresponding computed values of the permeability in the x, y and z direction (K^{eff}_x, K^{eff}_y and K^{eff}_z), the Specific Surface Area (SSA) and the density. All these values were computed on the largest volume available of each sample, which is at least equal to the REV of the three variables. Snow type is defined according to the International Classification for Seasonal Snow on the Ground [Fierz et al., 2009]: PP, Precipitation Particles; DF, Decomposing and Fragmented precipitation particles; RG, Rounded Grains; FC, Faceted Crystals; DH, Depth Hoar; MF, Melt Forms. Lines with gray background correspond to samples for which detailed information is provided below.

Sample *Fr* - Precipitation Particles (PP)

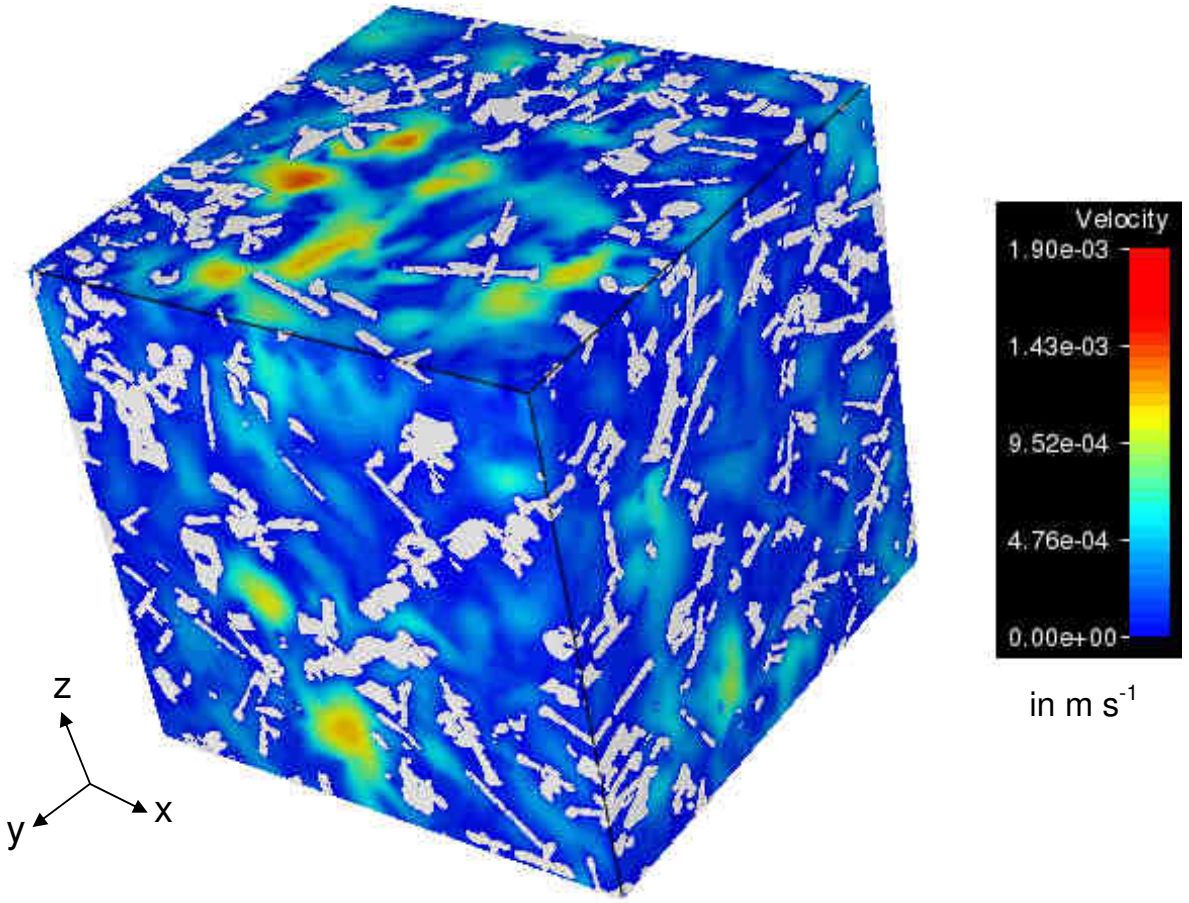

Figure 1.a: 3-D visualization of the fluid velocity for a pressure drop along z direction (size = 750^3 voxels, 1 vox. = 4.91 µm).

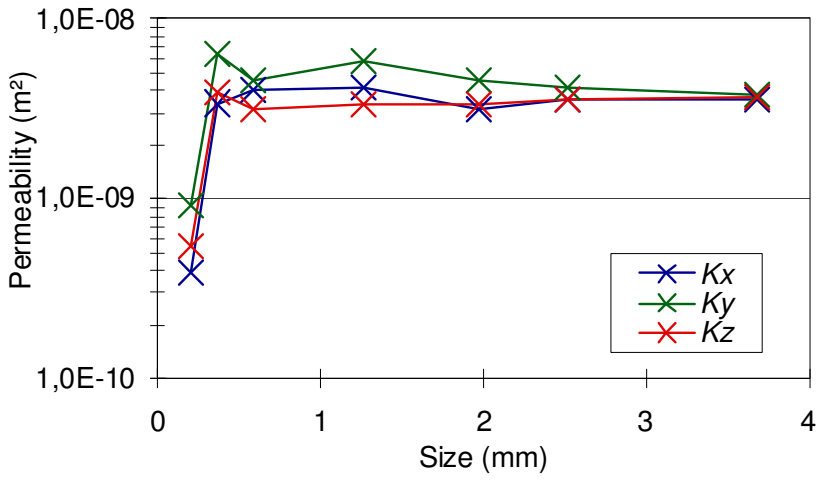

Figure 1.b:
Dependency of $\mathbf{K^{eff}}$ estimates with sample size.

Sample *P04* - Decomposing and Fragmented precipitation particles (DF)

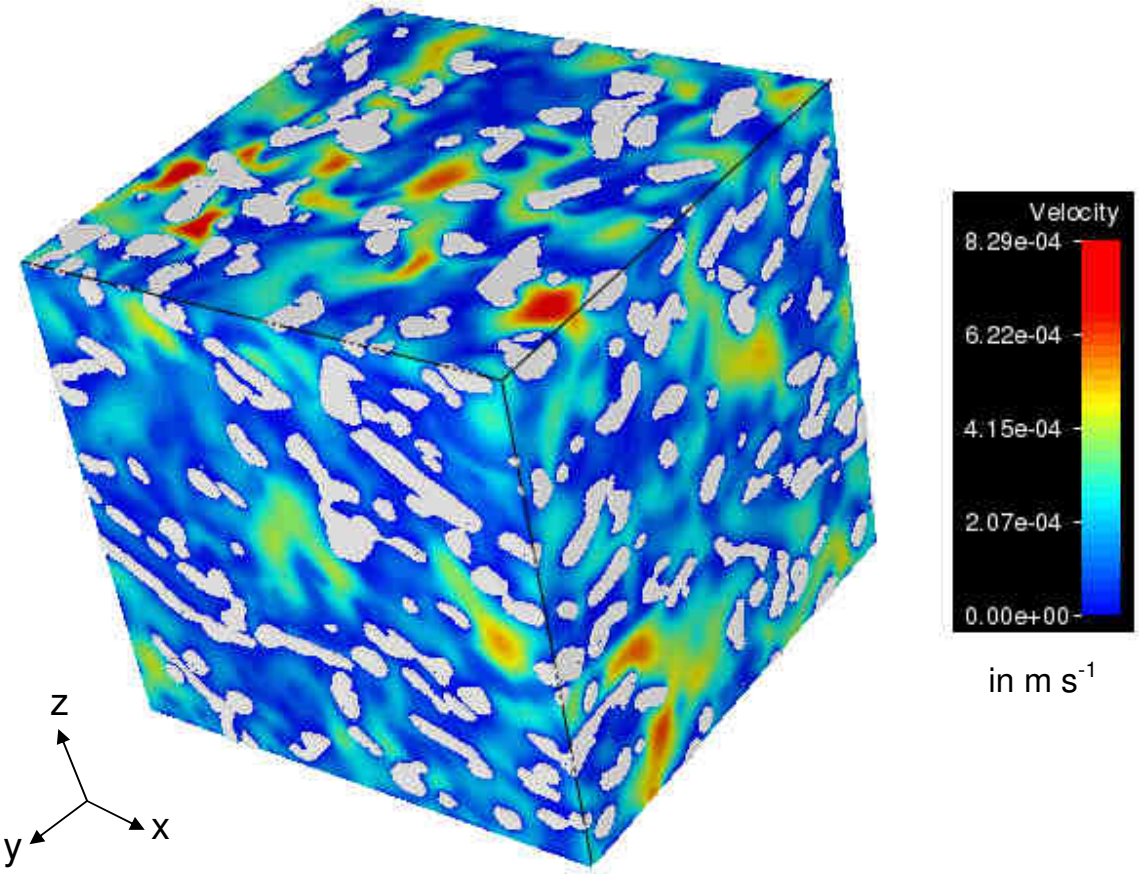

Figure 2.a: 3-D visualization of the fluid velocity for a pressure drop along z direction (size = 512^3 voxels, 1 vox. = 8.588 µm).

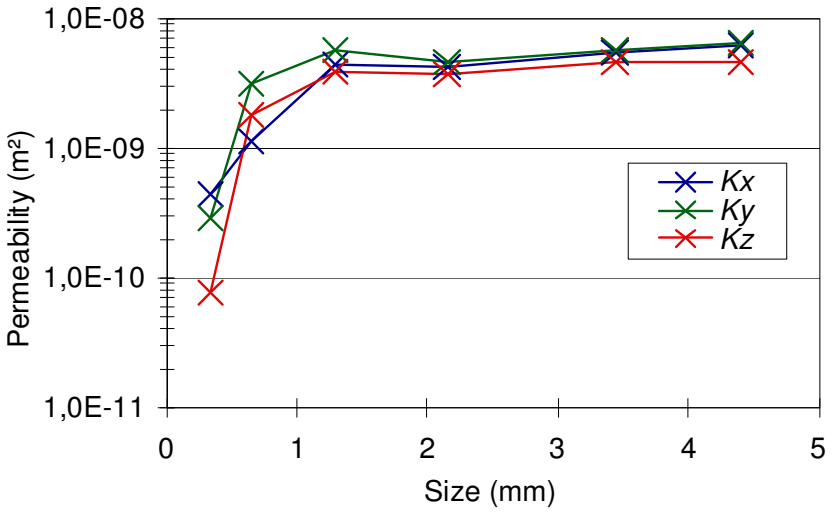

Figure 2.b:
Dependency of $\mathbf{K}^{\mathbf{eff}}$ estimates with sample size.

Sample *P11* - Rounded Grains (RG)

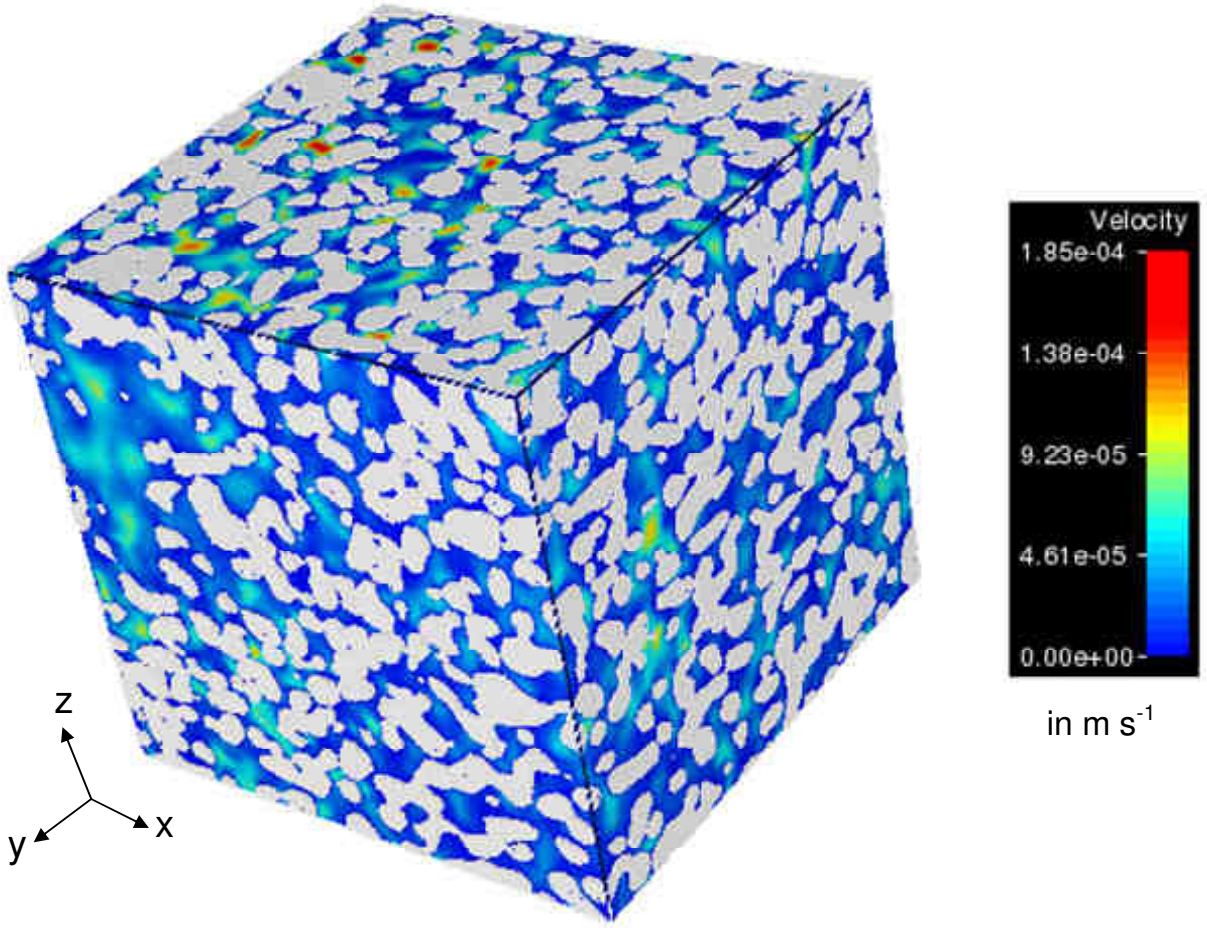

Figure 3.a: 3-D visualization of the fluid velocity for a pressure drop along z direction (size = 512^3 voxels, 1 vox. = 8.588 µm).

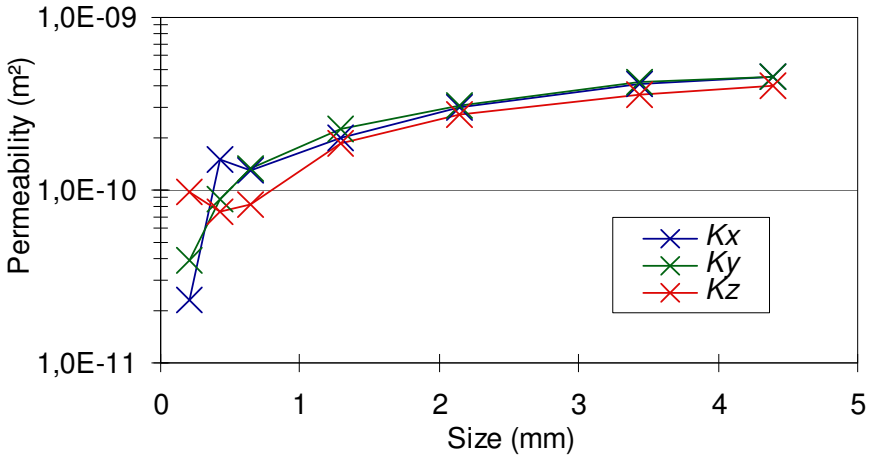

Figure 3.b:
Dependency of $\mathbf{K}^{\mathbf{eff}}$ estimates with sample size.

Sample *H02* - Melt Forms (MF)

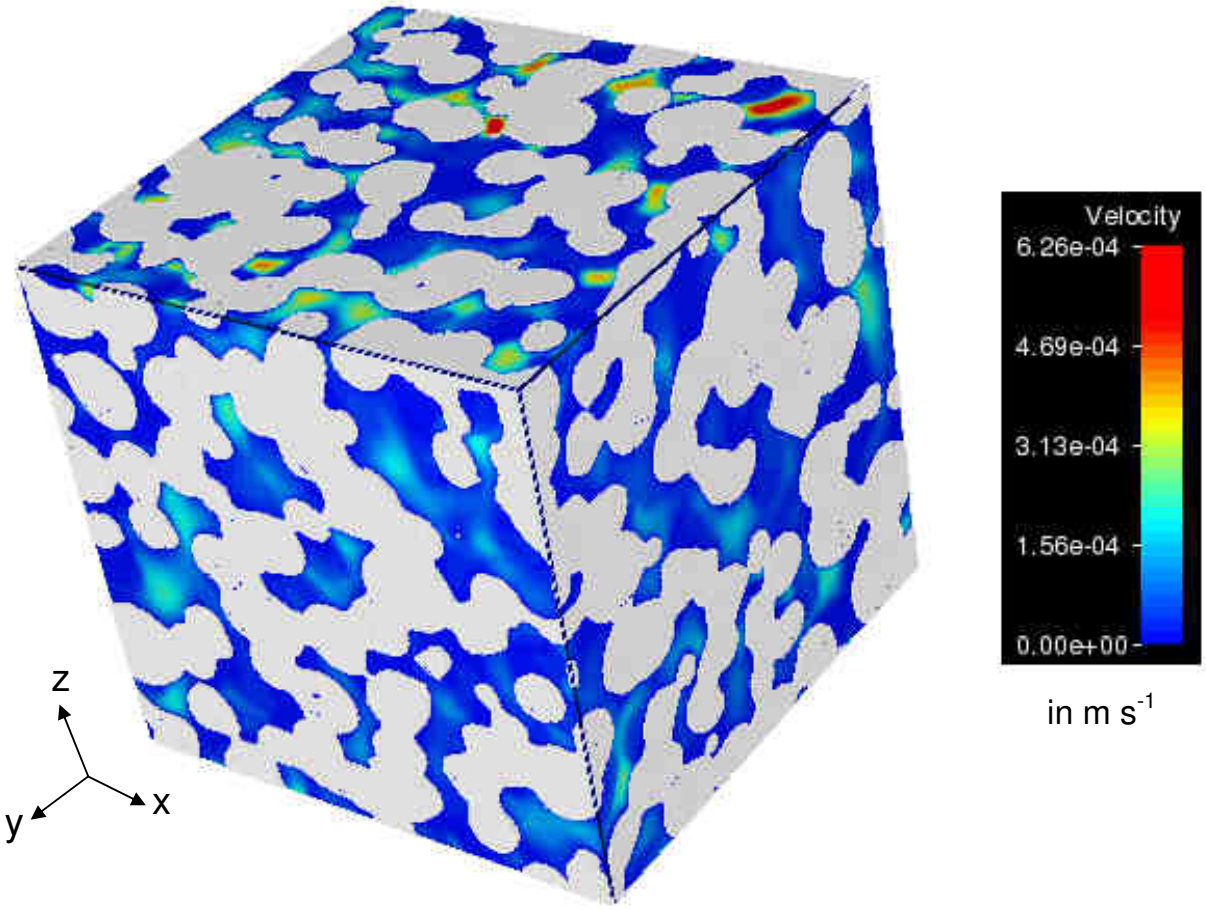

Figure 4.a: 3-D visualization of the fluid velocity for a pressure drop along z direction (size = 651^3 voxels, 1 vox. = 8.590 µm).

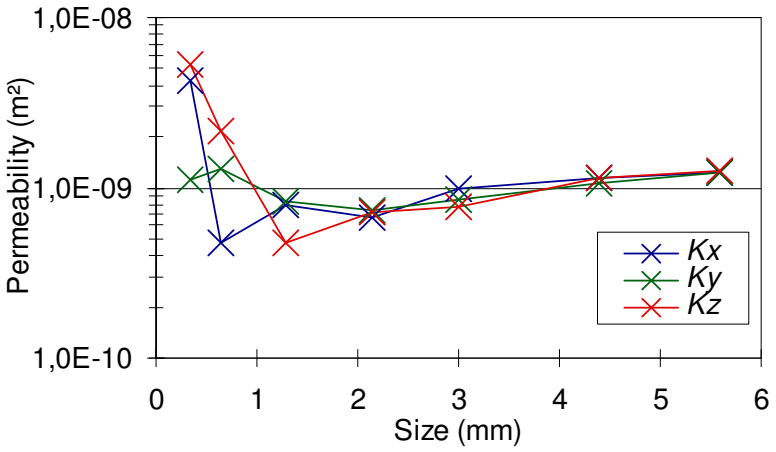

Figure 4.b:
Dependency of $\mathbf{K^{eff}}$ estimates with sample size.

Sample *E2b* – Faceted Crystals (FC)

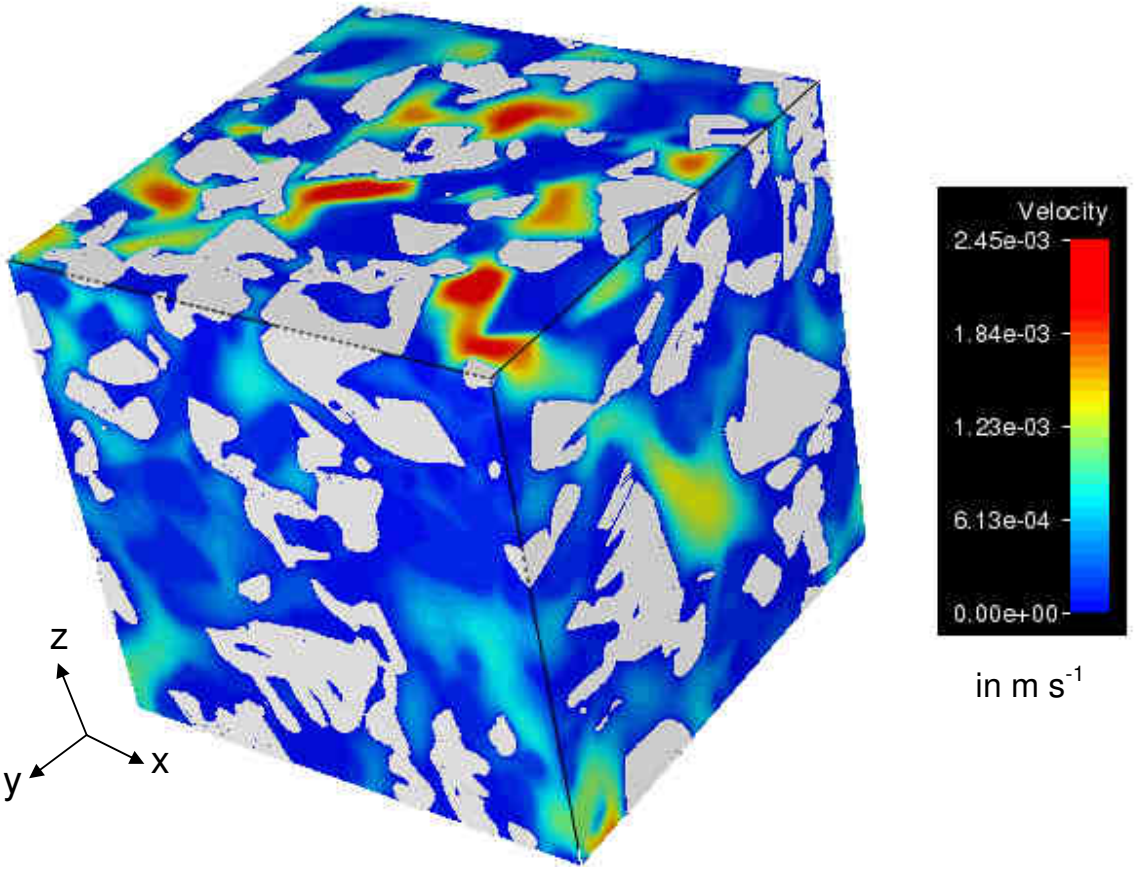

Figure 5.a: 3-D visualization of the fluid velocity for a pressure drop along z direction (size = 750^3 voxels, 1 vox. = 4.91 µm).

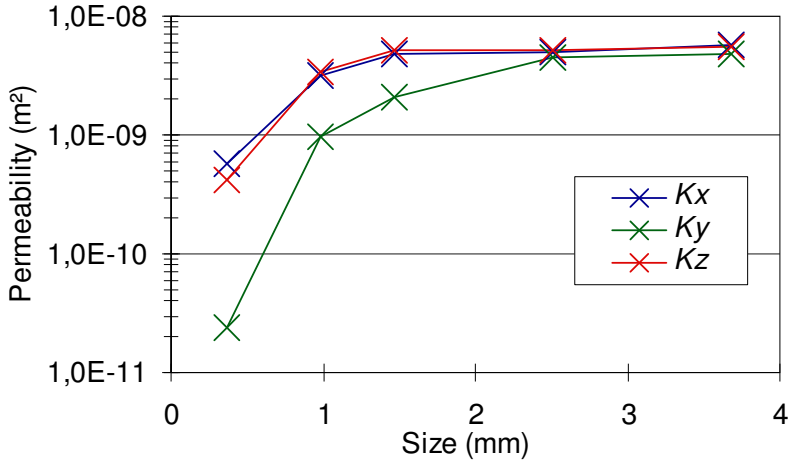

Figure 5.b:
Dependency of $\mathbf{K^{eff}}$ estimates with sample size.

Sample *Grad3* – Depth Hoar (DH)

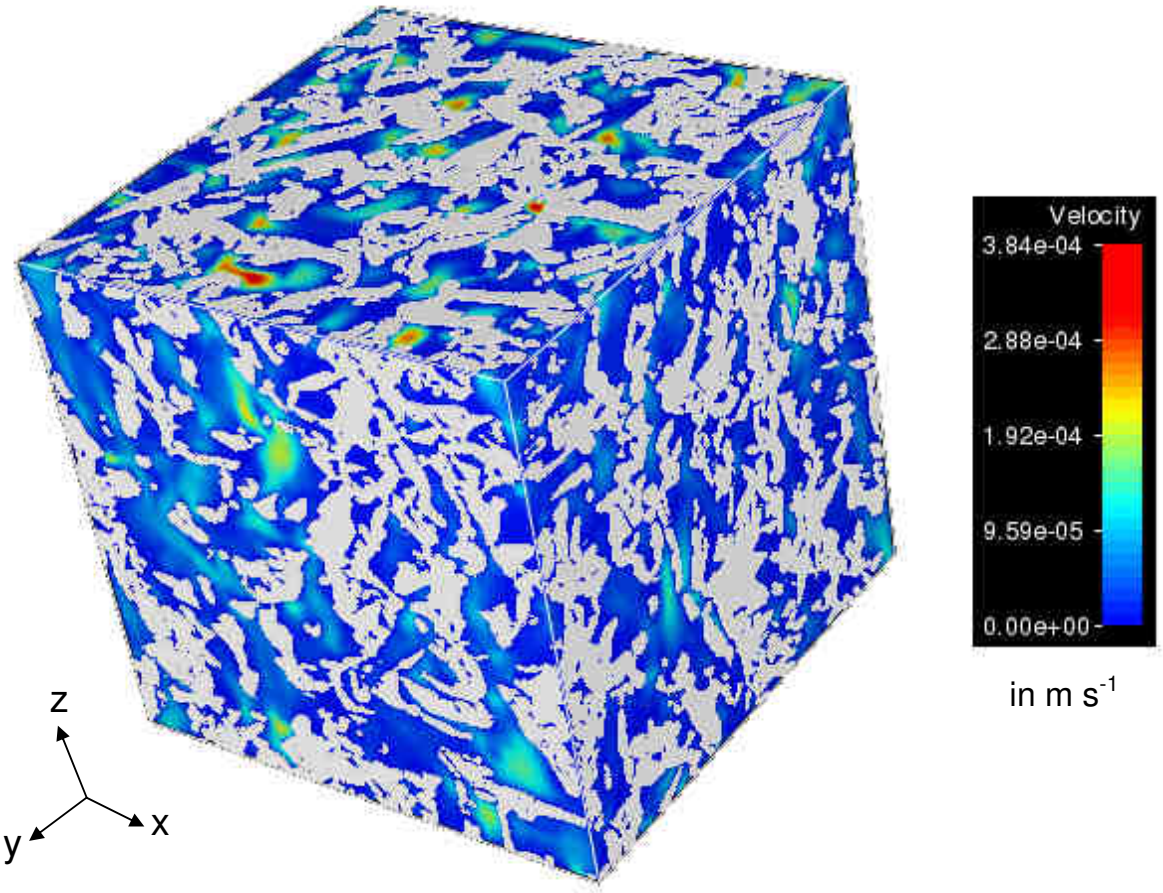

Figure 6.a: 3-D visualization of the fluid velocity for a pressure drop along z direction (size = 600^3 voxels, 1 vox. = 10 µm).

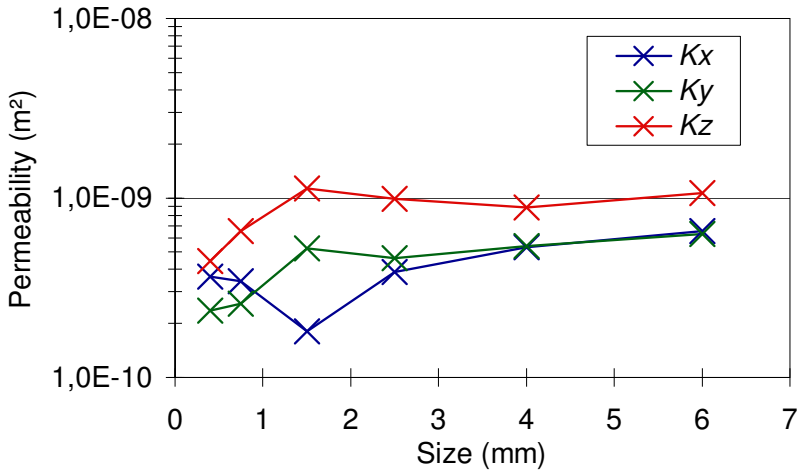

Figure 6.b:
Dependency of $\mathbf{K^{eff}}$ estimates with sample size.

Appendix

E Appendix of Chapter 6

General Information

In the following, we provide the 3-D visualizations of the seven images of snow samples used in our study. Images are cubic and have a size of 5.5 x 5.5 x 5.5 mm^3. For a better visualization of the facetted shapes, the images are presented "upside down": the top (respectively, the base) of the images corresponds to the lowest (highest) and warmest (coolest) side of the physical sample. The arrows in blue, green and red correspond to the x-, y- and z-directions of the images, respectively, z being along the direction of gravity. The color code is defined as follows:

- Figures 1.a – 7.a: Colors represent the mean curvature of surfaces ranging from -36 to +36 mm^{-1} such as the convexities, flat shapes and concavities are shown in red, yellow and green, respectively.
- Figures 1.b – 7.b: Colors represent the Gaussian curvature of surfaces ranging from -781 to +781 mm^{-2}, such as the dome-shaped (concave or convex), flat or cylindrical and saddle-shaped surfaces are shown in red, yellow and green, respectively.

Sample 0A – Rounded Grains (RG)

0 hour under
temperature gradient.

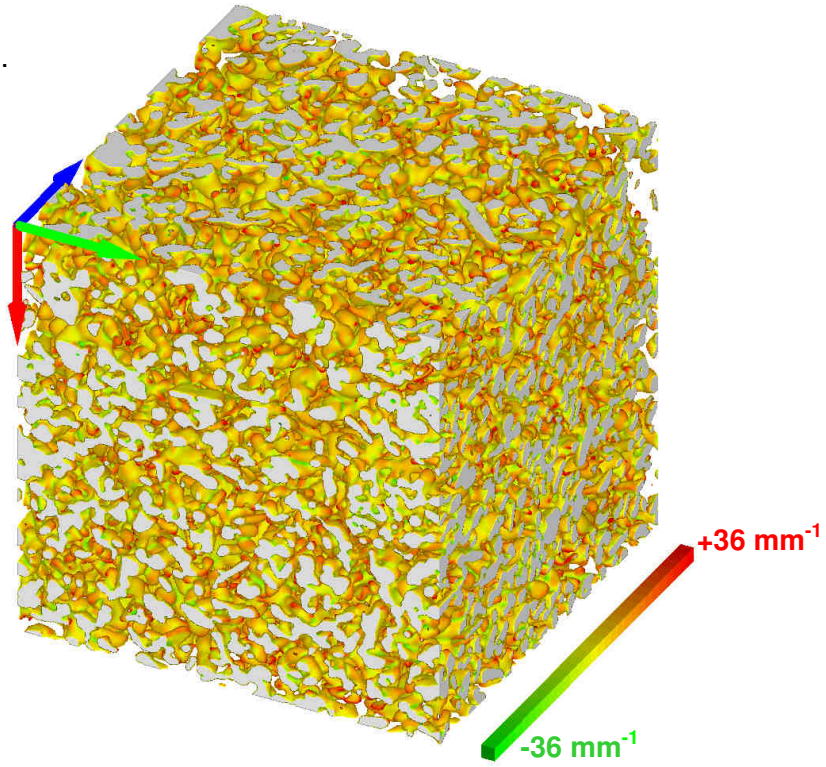

Figure 1.a: Mean curvature.

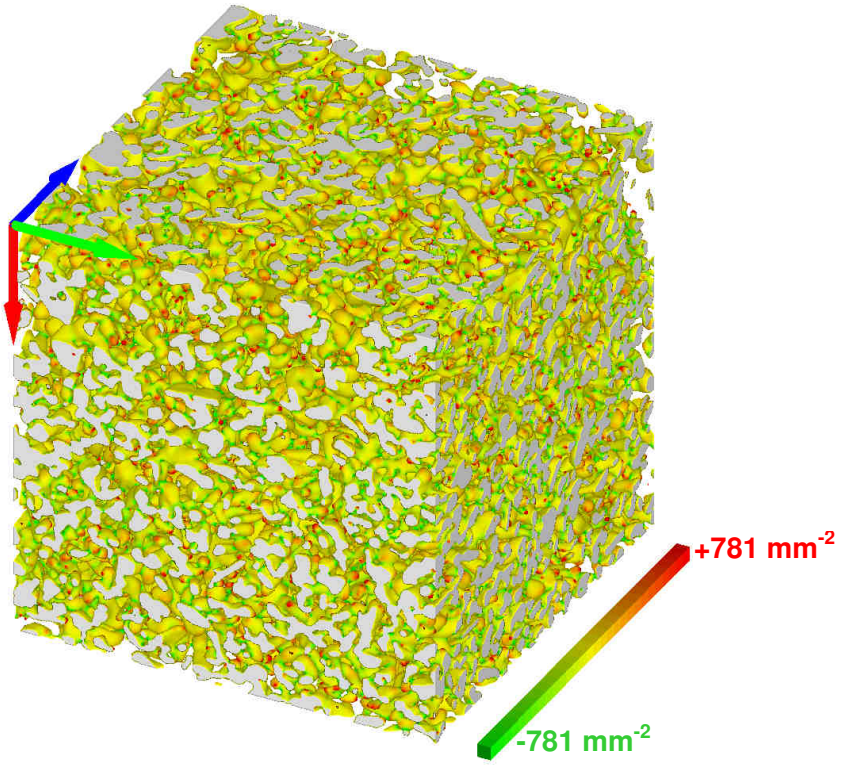

Figure 1.b: Gaussian curvature.

Sample 1A – Rounded Grains (RG)

73 hours under
temperature gradient.

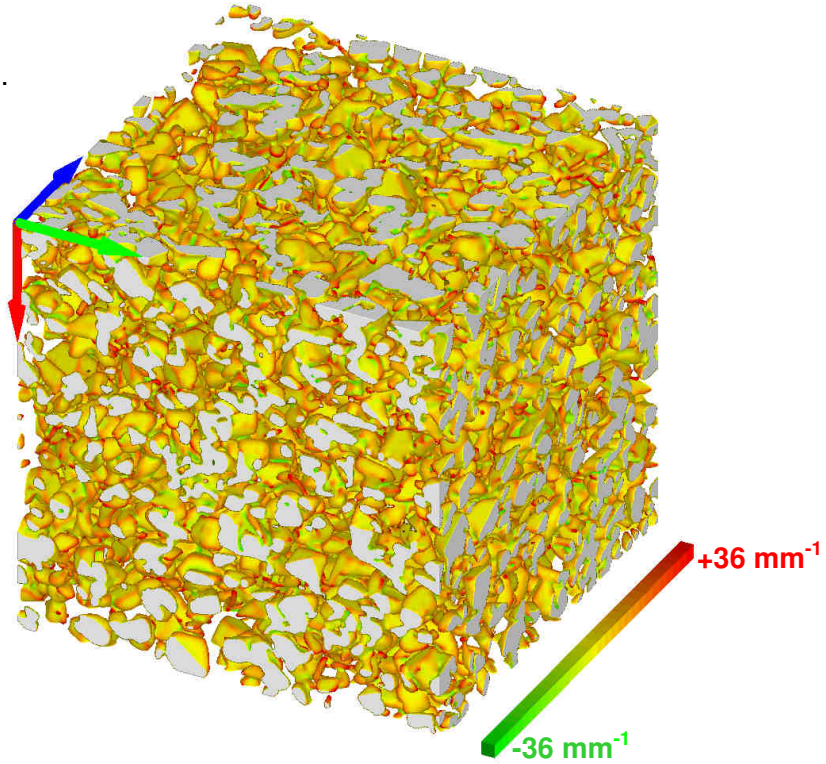

Figure 2.a: Mean curvature.

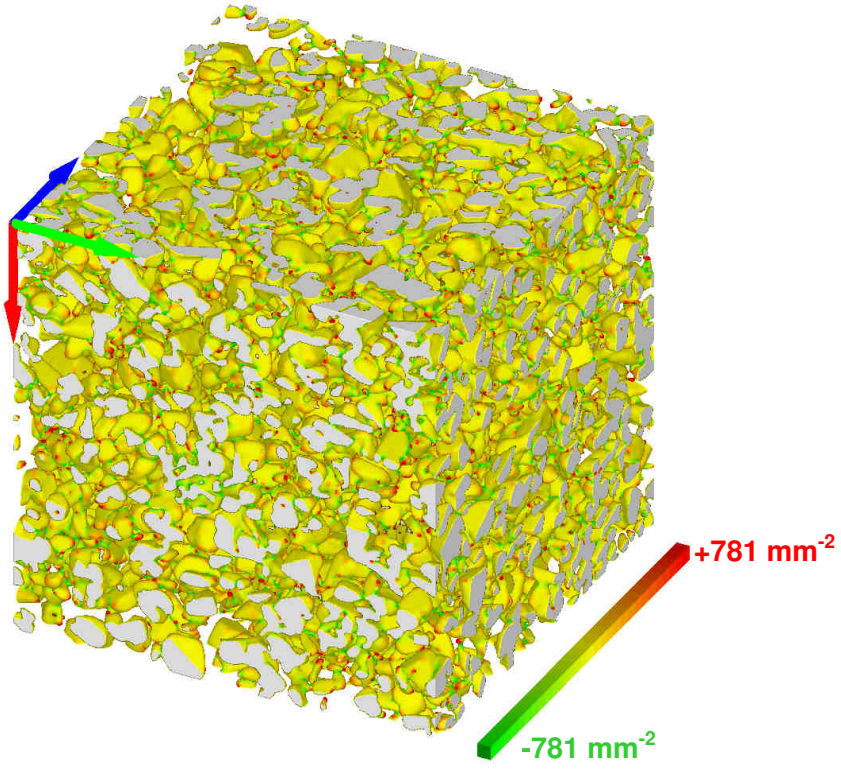

Figure 2.b: Gaussian curvature.

Sample 2A – Facetted Crystals (FC)

144 hours under temperature gradient.

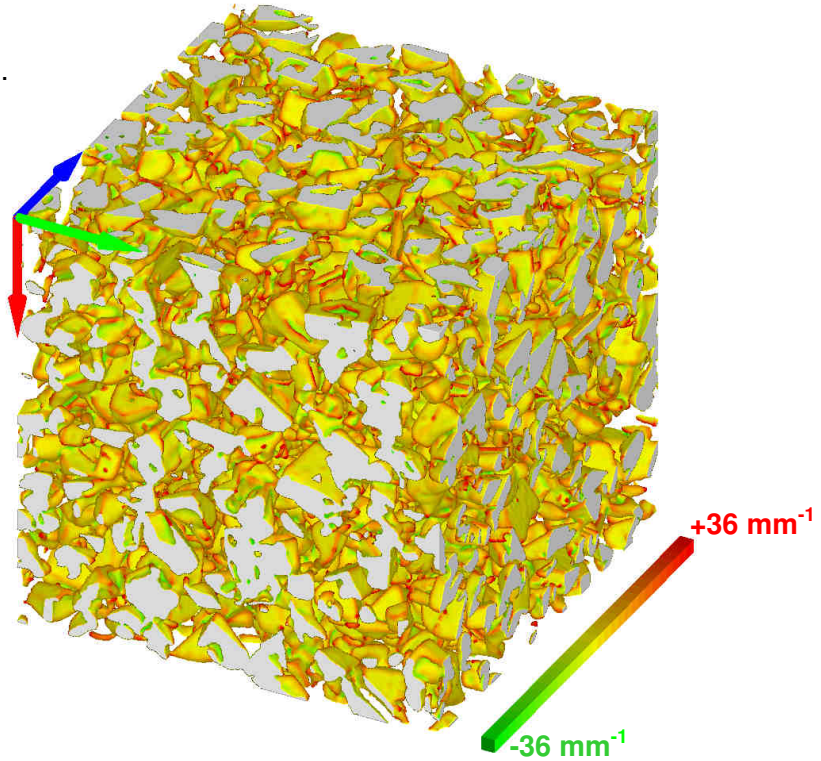

Figure 3.a: Mean curvature.

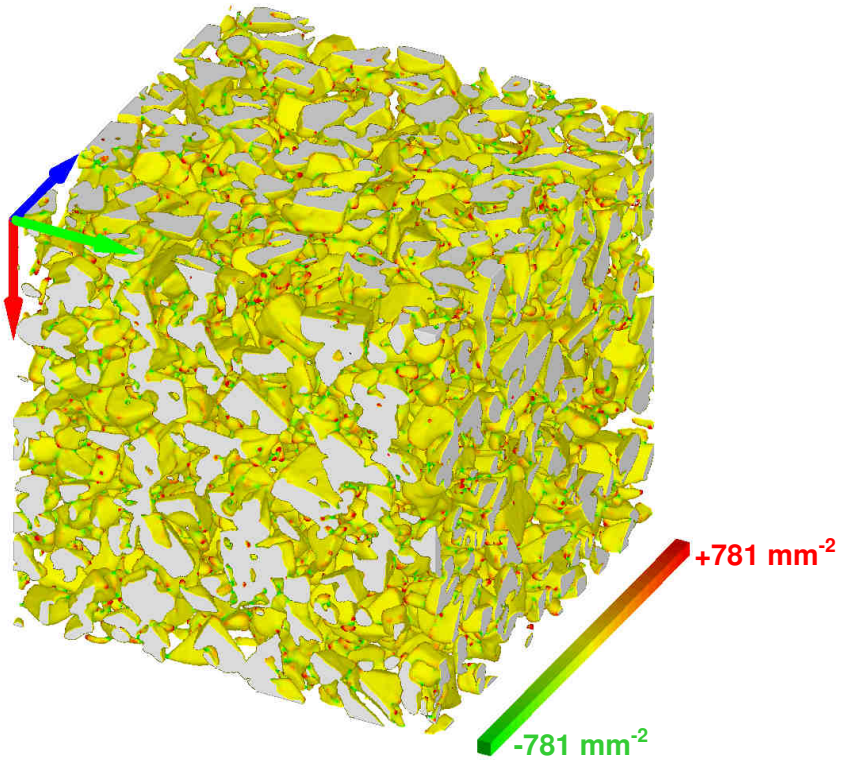

Figure 3.b: Gaussian curvature.

Sample 3A – Depth Hoar (DH)

217 hours under temperature gradient.

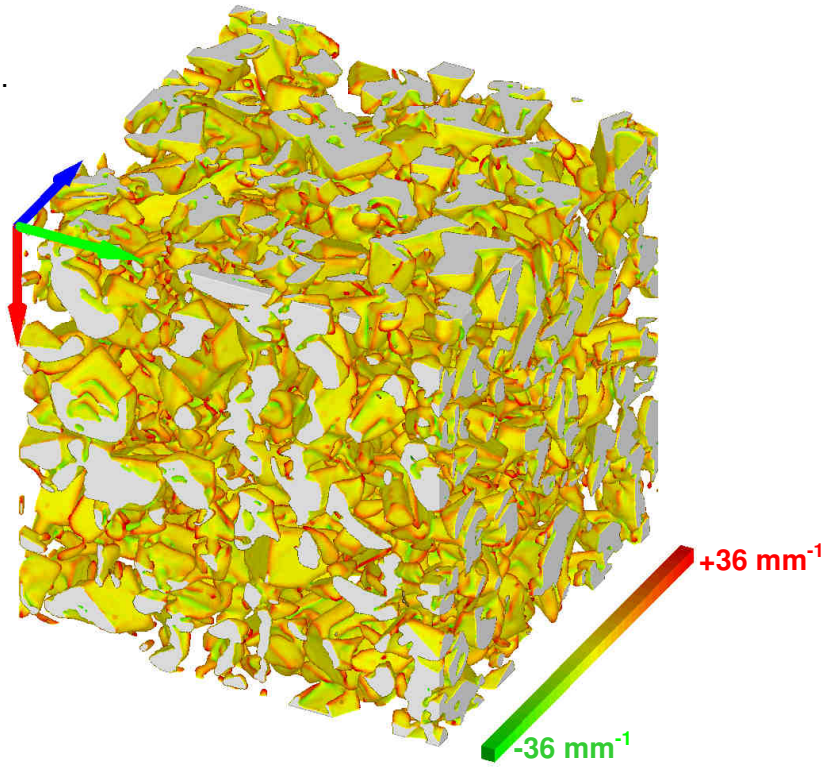

Figure 4.a: Mean curvature.

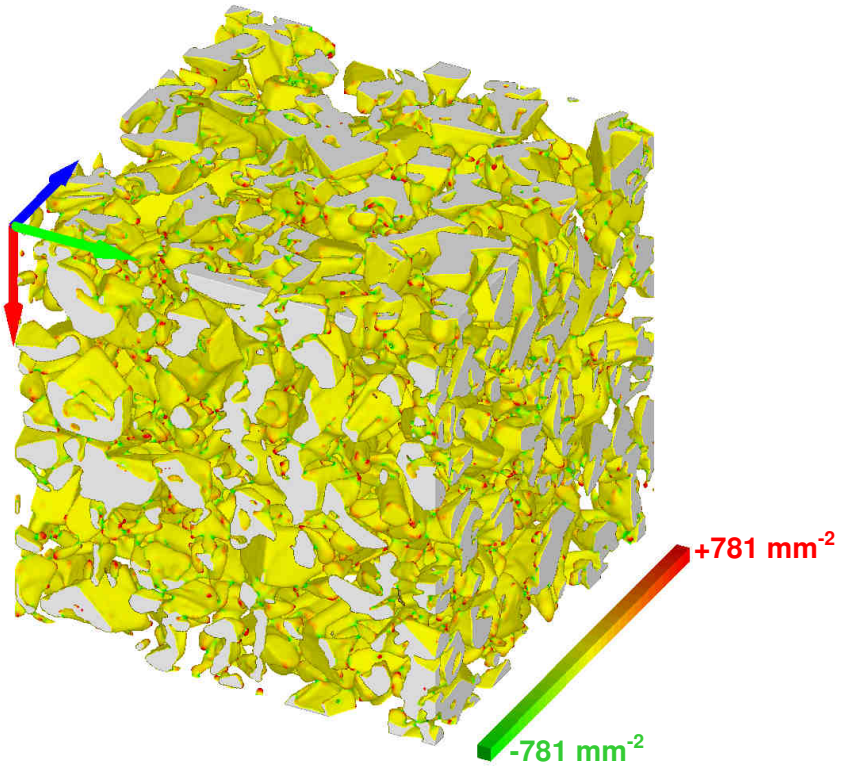

Figure 4.b: Gaussian curvature.

Sample 4A – Depth Hoar (DH)

313 hours under temperature gradient.

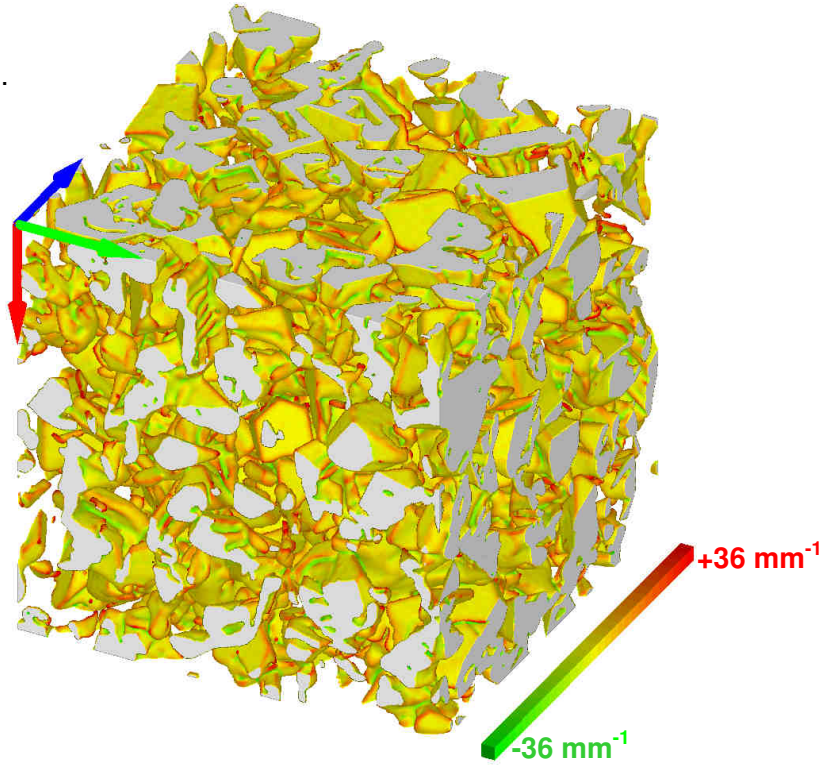

Figure 5.a: Mean curvature.

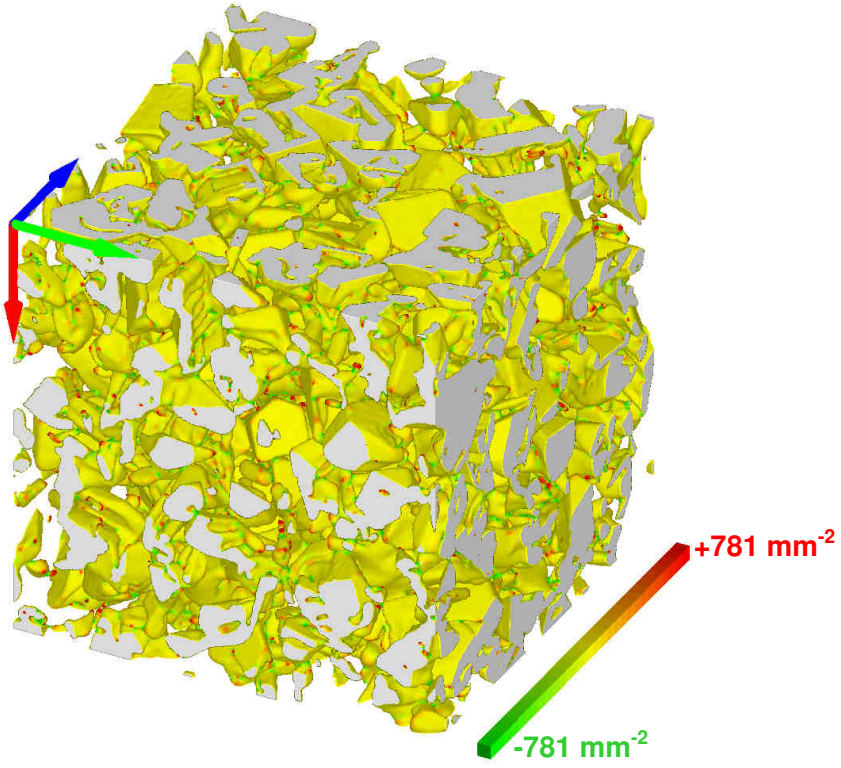

Figure 5.b: Gaussian curvature.

Sample 5G – Depth Hoar (DH)

409 hours under temperature gradient.

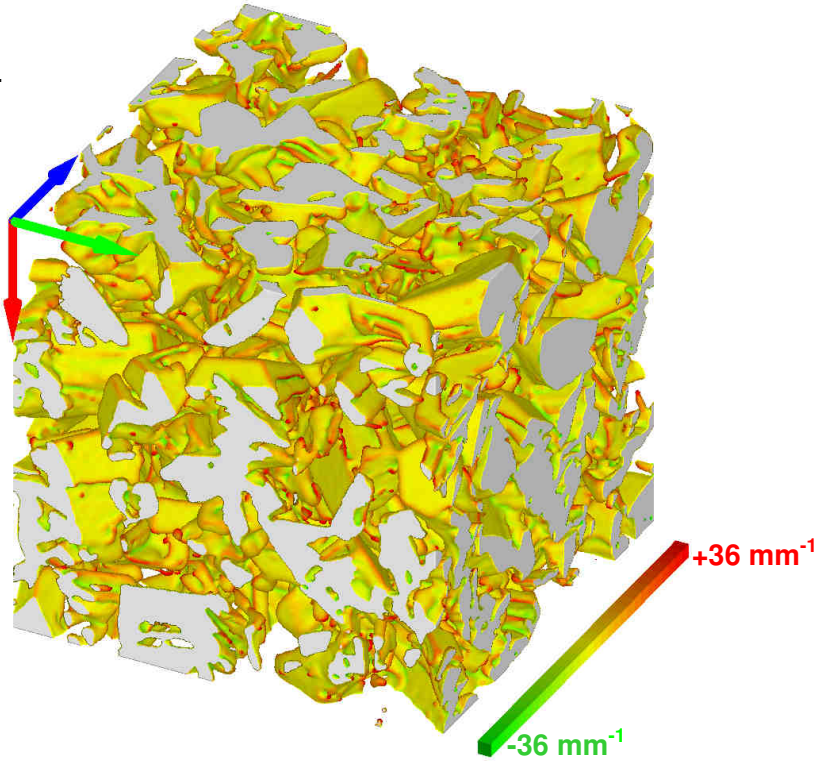

Figure 6.a: Mean curvature.

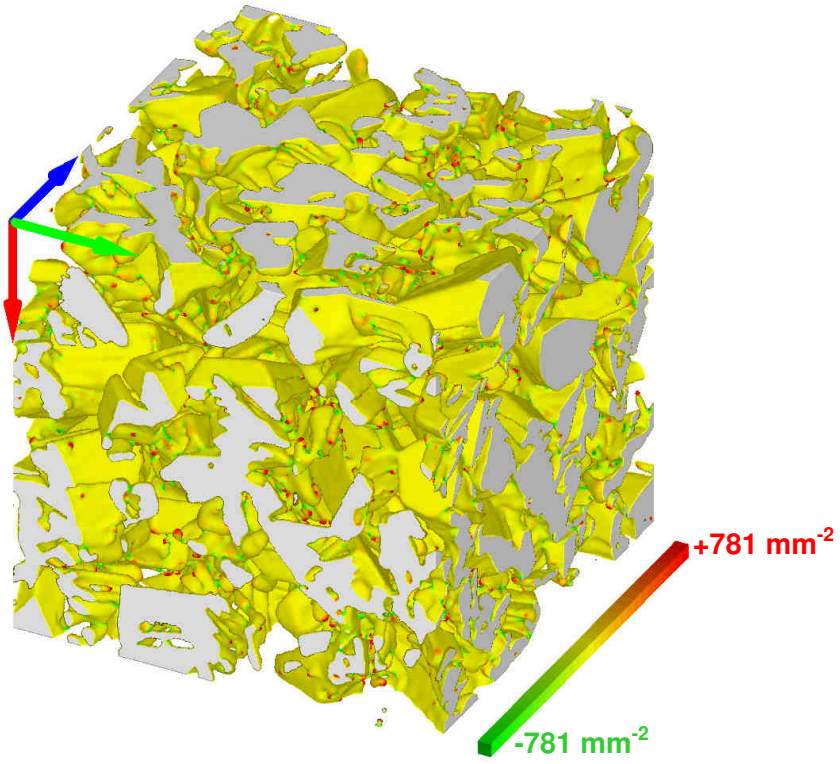

Figure 6.b: Gaussian curvature.

Sample 7G – Depth Hoar (DH)

500 hours under temperature gradient.

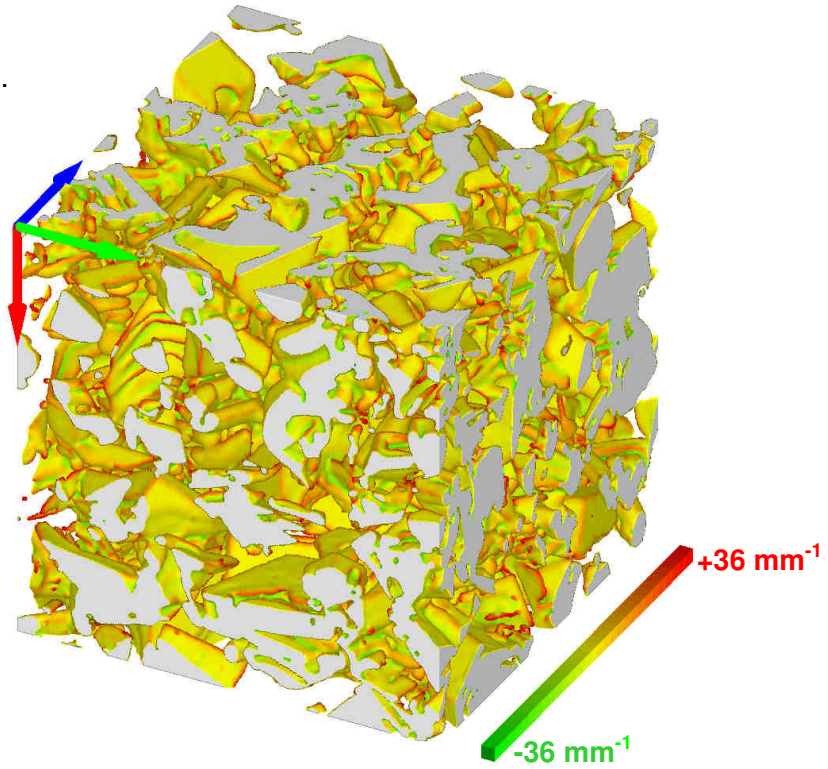

Figure 7.a: Mean curvature.

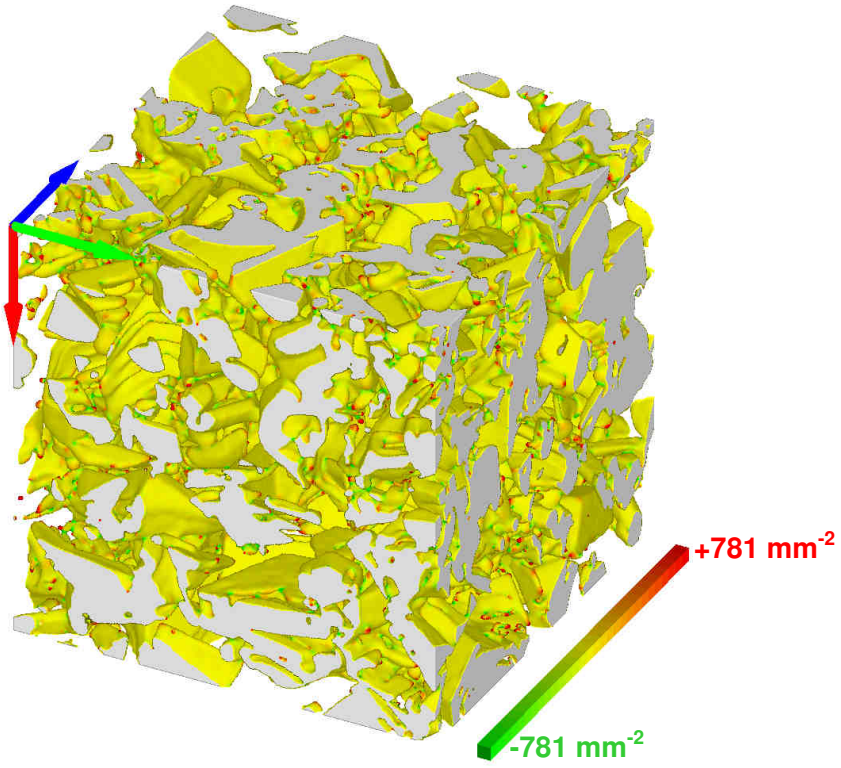

Figure 7.b: Gaussian curvature.